Quantum Degeneracy and Interactions in the ^{87}Rb -^{40}K Bose-Fermi Mixture

by

Jonathan Michael Goldwin

B.Sc. Physics and Mathematics,

University of Wisconsin – Madison, 1999

A thesis submitted to the

Faculty of the Graduate School of the

University of Colorado in partial fulfillment

of the requirements for the degree of

Doctor of Philosophy

Department of Physics

2005

This thesis entitled:
Quantum Degeneracy and Interactions in the ^{87}Rb -^{40}K Bose-Fermi Mixture
written by Jonathan Michael Goldwin
has been approved for the Department of Physics

Deborah S. Jin

Jun Ye

Date

The final copy of this thesis has been examined by the signatories, and we find that both the content and the form meet acceptable presentation standards of scholarly work in the above mentioned discipline.

Goldwin, Jonathan Michael (Ph.D., Physics)

Quantum Degeneracy and Interactions in the ^{87}Rb -^{40}K Bose-Fermi Mixture

Thesis directed by Associate Professor Deborah S. Jin

An apparatus for producing dilute-gas quantum degenerate Bose-Fermi mixtures is presented. The experiment uses forced evaporative cooling to obtain a nearly pure ^{87}Rb Bose-Einstein condensate immersed in a gas of sympathetically cooled ^{40}K atoms at 0.2 times the Fermi temperature. The design, construction, and operation of the apparatus are described in detail. The onset of quantum degeneracy is characterized and contrasted between species, revealing the effects of quantum statistics on the bulk properties of the gases.

The apparatus is then used to study the interactions between species in ultracold non-degenerate mixtures. Measurements of rethermalization rates are used to determine the elastic scattering cross-section between species. From these measurements the magnitude of the inter-species s-wave scattering length is determined. The scattering length is central to characterizing a variety of static and dynamic properties of the mixture. The apparatus is additionally used to study for the first time Feshbach resonances in the collisions between ^{87}Rb and ^{40}K atoms. These resonances present a means for experimentally tuning the scattering length between species to any desired value. Prospects for future experiments exploiting this real-time control over the interactions are discussed.

Dedication

For my parents.

Acknowledgements

I would like to acknowledge the contributions of a number of people to the work described in this thesis. It is the nature of the JILA quantum gas collaboration that literally dozens of people will at one time or another contribute ideas to each experiment.

The first word of thanks must go to Debbie, who took me in with only my eagerness to work as a credential. She spent many hours in the lab with me when I started, and gave me considerable freedom later on. I can only hope that her clear thinking, intense focus, and ability to distill problems to their essence has rubbed off on me over time. Secondary advisor credits go to Eric Cornell and Carl Wieman, who have invested considerable time and effort into creating the work environment that exists here today. Their earnest desire to educate, combined with vast reserves of experience, imagination, and scientific rigor, has led to a unique place for graduate students to develop our skills.

Somewhere between our advisors and the other contributors to these experiments must come Shin Inouye. Shin was a post-doc with us from a time when we were still optimizing our MOTs through our recent observation of Feshbach resonances. In fact Shin was involved with nearly all of the experiments described in this thesis, and contributed a considerable amount of technical expertise to the design of the experiment. More importantly, Shin always encouraged me to reduce problems in the lab to something like the "spherical cow" approximation,

in order to quickly estimate which things I should worry about and which could be safely neglected.

The various measurements in this thesis were performed in conjunction with (in order of appearance) Scott Papp, Michele Olsen, and Jianying Lang. Bonna Newman also made important early contributions to the design and construction of the experiment, as did Brett DePaola, who was able to assist us via the JILA visiting fellows program, and Ashley Carter, who spent a semester with us under the OSEP program at CU. Chris Ticknor and John Bohn provided invaluable theoretical support. Other people contributing to our experiment at one time or another include Brian DeMarco (who showed me, in addition to other things, how to trigger a 'scope), Steve Gensemer, Tom Loftus, Cindy Regal and Markus Greiner. A general word of thanks goes out to the large number of students, post-docs, and visiting fellows who have worked their way through the quantum gas collaboration during my time. I would also like to acknowledge stimulating discussions on the joys and tribulations of ^{87}Rb -^{40}K mixtures with Giacomo Roati of the LENS group, as well as with Christian Ospelkaus of the University of Hamburg, and Thilo Stöferle of the ETH in Zürich.

Much electronics expertise was provided by James Fung-A-Fat and Terry Brown. Mechanical engineering (and beyond) was provided by Hans Green, Blaine Horner, Todd Asnicar, and Tom Foote. Computing expertise from Joel Frahm, James McKown, and Pete Ruprecht has been crucial, as has the hard work of Pam Leland, Ed and Randall Holliness, Brian Lynch, and Maryly Dole.

Finally on a personal note I would like to thank my parents for their undying support over all these years. And I am especially grateful to Mary Ellen Flynn for her love and support, which have weathered the *Sturm und Drang* of this work with much grace and understanding.

Contents

Chapter

Tables

Table

Figures

Figure

Chapter 1

Introduction

> That the impossible should be asked of me, good, what else could be asked of me? But the absurd! Of me whom they have reduced to reason.
>
> - Samuel Beckett, *The Unnamable*

This thesis describes some of the first experiments probing and manipulating the cross-species interactions in an ultracold dilute gas mixture of Bosons and Fermions. To date most systems of this type have been used as practical tools, bypassing the Pauli exclusion principle in order to cool gases of fermionic atoms to only a fraction of the Fermi temperature. Bose-Fermi mixtures, however, additionally allow us to study a variety of many-body quantum mechanical systems of interest to condensed matter physics, with the degree of control and relative theoretical simplicity of atomic gases. In our systems interactions between atoms are typically short-range and two-body in nature, impurities are absent, and smooth, regular, time-dependent trapping potentials are easily generated in the lab. Furthermore, through the use of Feshbach resonances, the interactions may be controlled in real time in the experiments.

In this thesis I describe the design, construction, and operation of an experimental apparatus we have built for trapping and cooling to quantum degeneracy a dilute-gas mixture composed of ^{87}Rb (boson) and ^{40}K (fermion) atoms. It is shown that such a mixture can be cooled using relatively standard techniques until a nearly pure Bose-Einstein condensate coexists with a quantum degenerate gas of fermions at around 20% of the Fermi temperature. I will describe measurements we have made of the s-wave elastic collision cross-section between ^{87}Rb and ^{40}K atoms in the ultracold, but non-degenerate regime. These measurements give us important information on the interactions between species in quantum degenerate mixtures. Finally, I will present our most recent work where we have identified a number of inter-species Feshbach resonances in the ^{87}Rb -^{40}K system. These resonances represent, in principle, a means for exerting complete real-time control over the interactions between species. This kind of control may allow us to study a significant number of exciting new phenomena in the future.

A more detailed overview of this thesis is given in Section 1.3. Before proceeding, however, I would like to give some motivation for our interest in quantum degenerate atomic Fermi gases and Bose-Fermi mixtures.

1.1 I See Fermions

It is a peculiar fact of the quantum mechanical world that all of the constituents of the ordinary matter and light around us fall into one of two categories — they are either bosons or fermions. Bosons and fermions are distinguished on the one hand by their quantum mechanical spin, which takes on integer values for bosons and half-integer values for fermions. On the other hand the differences between bosons and fermions can become manifest even in the absence of spin-dependent forces. The bulk properties of ensembles of identical particles can be strikingly different depending on which family the particles belong to. The

behavior of groups of identical fermions underlies the rich variety of elements in the periodic table, and the concerted efforts of identical bosons have brought us the laser.

The experiments described in this thesis aim to study and exploit the behavior of ensembles of ^{87}Rb atoms (which are composite bosons) and ^{40}K atoms (composite fermions). In Fig. 1.1 I show schematically some of the fields of research that can benefit from the type of work we are doing. Particular applications of Bose-Fermi mixtures are discussed in the next section, but these mixtures were originally conceived as a tool for producing degenerate Fermi gases, and this is how they have been most commonly used to date. Atomic Fermi gases may be used to understand such wildly different fermionic systems as normal metals, neutron and white dwarf stars, heavy nuclei, superfluid ^{3}He, and metallic hydrogen. There is much to be learned about high-T_c superconductivity, for example, from the study of ultracold gases. And if we make a quantum computer in the process, then who's going to complain?

In qualified defense of our friend the fermion, I would like to argue against the notion that fermions are less "sociable" than bosons [1]. The renowned Pauli exclusion principle only describes a fermion's reluctance to share a quantum state with an *identical* fermion. A fermion will happily make room for a *distinguishable* fermion, or even a boson. In this sense I would argue that fermions are more open and sociable than the narcissistic bosons — the bosons, who would all crowd into their ground state with others just like themselves, and never ask what lies above.

For better or worse, Pauli taught us that identical fermions will not share a quantum state. It is this very behavior that leads to the well known statistical distribution of fermions at zero temperature, with a single fermion in each available quantum state, starting at lowest energy and moving up one state at a time until we run out of particles. The very last fermion occupies a special place in this

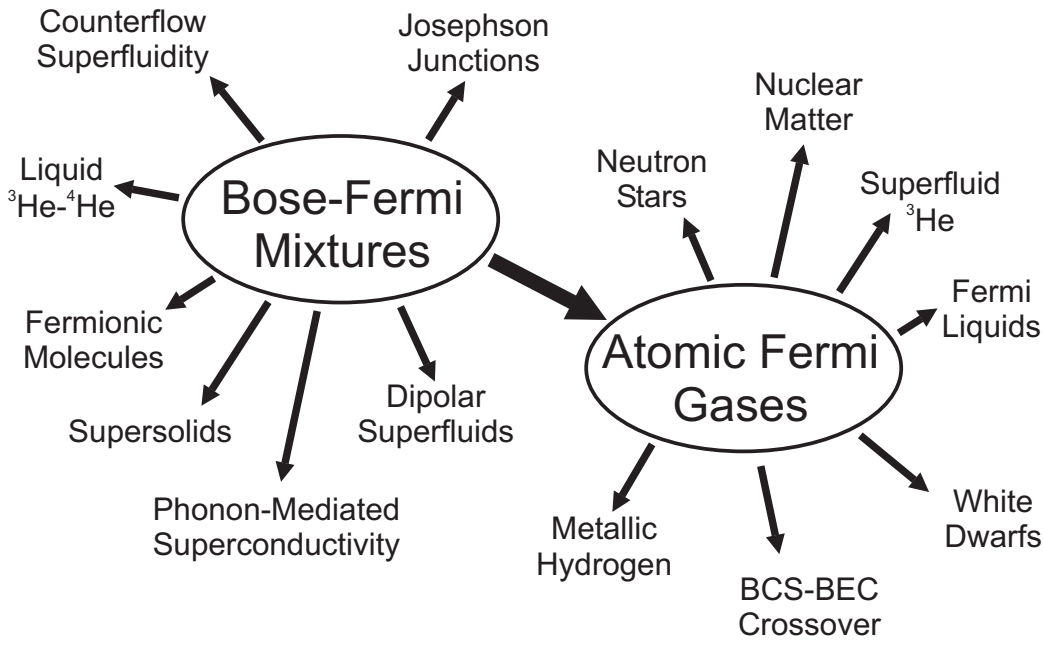

Figure 1.1: Applications of work with atomic Fermi gases and Bose-Fermi mixtures.

distribution, which defines the Fermi energy E_F of the system. Only particles in states near the Fermi energy can partake in the joys of perturbative excitation [2]. States far above E_F are not occupied, and particles below E_F are pinned by the presence of the fermions around them, with no unoccupied state to scatter into. The Fermi temperature, defined by $T_F = E_F/k_B$ with k_B Boltzmann's constant, defines the characteristic temperature that the system must approach before quantum statistical effects may begin to appear.

The Fermi temperature is directly related to the density of a system, in the sense that high densities lead to high T_F, and low to low. One reason that dilute atomic gases are so useful to study is our ability to understand their behavior with relatively simple theories. This in turn is due to the fact that our systems are dominated by short-range interactions, and have such low densities that we rarely have to go to more than a two-body picture to get some understanding of what is happening. As seen in Fig. 1.2, where I outline some typical values of T_F for various quantum degenerate fermion systems, this means we must get our atoms extremely cold in order to access their quantum statistical properties. This incredible technical achievement has only been possible in the last decade, and is at the heart of the work I'll describe here.

1.2 Fermions And Bosons Unite!

When we began designing the experiment described in this thesis there was still only one successful Fermi gas experiment [3], using simultaneous evaporative cooling of two spin states of ^{40}K. The presence of a second spin state helps bypass the reluctance of fermions to collide during the cooling. The common wisdom at the time was that a simpler approach might be to sympathetically cool a gas of fermions in the presence of bosons. Although we can debate the premise that this is "simpler," I know of ten quantum degenerate Fermi gas experiments in the

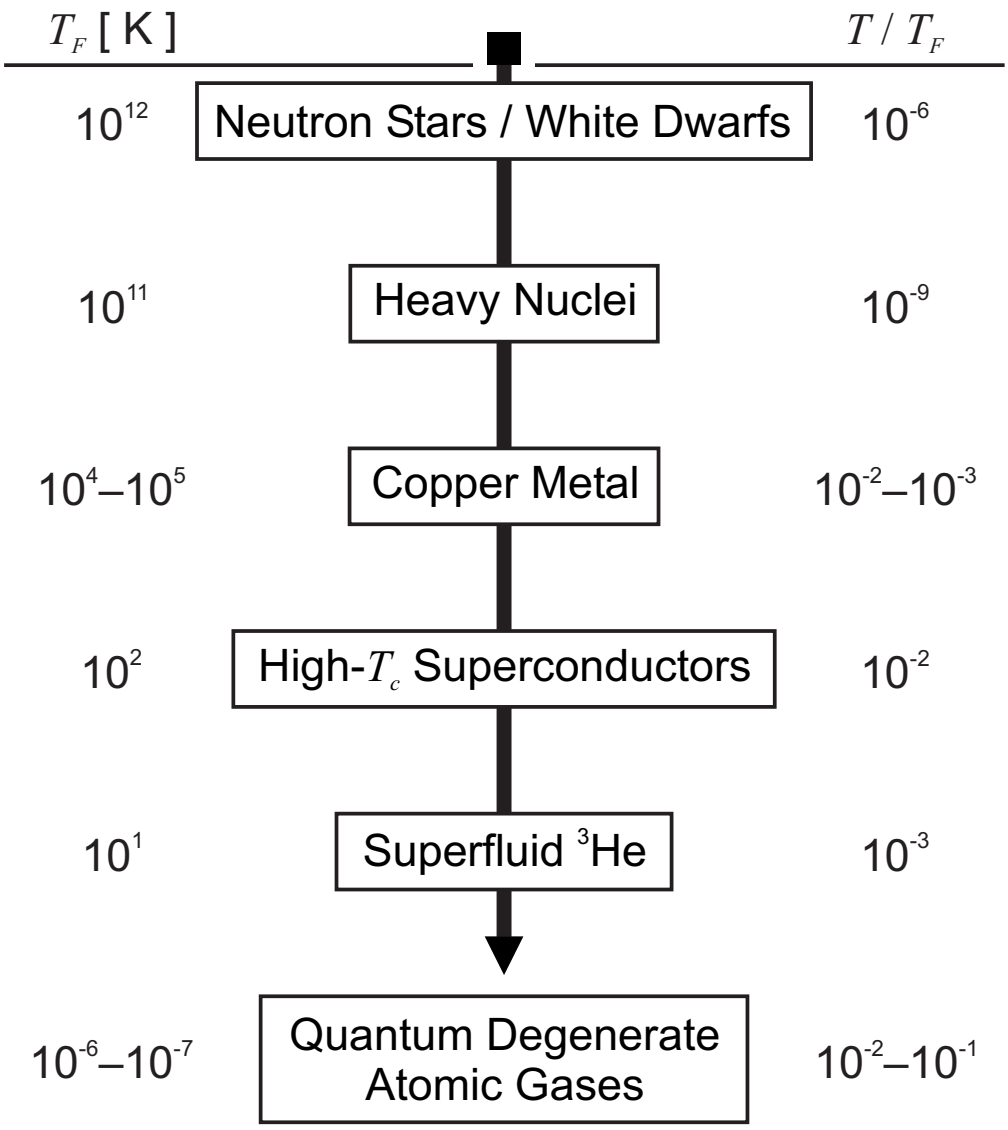

Figure 1.2: Characteristic Fermi temperatures and operating temperatures of some quantum degenerate fermion systems.

world, and only two of them use different spin states of a single isotopic species. The rest are produced by sympathetic cooling. There are at least seven more sympathetic cooling experiments being built.

It is my belief that the quantum degenerate Bose-Fermi mixture will ultimately be seen as more than just a way to produce degenerate Fermi gases. For example, although fermions in optical lattice potentials already provide a great system for simulating Fermi gases in metals [4], the optical lattice cannot play all the roles of the condensed matter lattice it pretends to be. Specifically, optical lattices do not exhibit excitations such as phonons, which are crucial to our understanding of superconductivity in the BCS regime. I think the most exciting prospect for Bose-Fermi mixtures is the prediction of a boson-mediated pairing of the fermions [5, 6, 7], where phonons in the condensate give rise to the effective attractive interactions between fermions needed for Cooper pairing and Fermi superfluidity. Other applications of Bose-Fermi mixtures include the formation of ultracold fermionic molecules [8], which can only be produced from a combination of bosons and fermions, and the creation of a supersolid phase [9] or a host of other exotic phases [10] in optical lattices.

1.3 Overview of this Thesis

As stated at the beginning of this chapter, this thesis describes some of the first experiments probing and manipulating the cross-species interactions in Bose-Fermi mixtures. Although many of the theoretical descriptions and experimental techniques presented here are extensions of work already established in the field, the Bose-Fermi mixture is more than the sum of its parts and deserves to be considered a unique and rich system on its own. In this thesis I hope to lay out a very specific and detailed account of the tools needed to produce such a system, as well as a more general treatment of the kind of physics one may encounter by

studying it. In this final introductory section, I would like to lay out the basic structure of this thesis, in order to guide the interested reader.

In chapter 2 I give a very detailed technical description of the apparatus we have built for producing a quantum degenerate ^{87}Rb -^{40}K mixture. This chapter is intended mainly for the benefit of people in our lab, and for others working with or developing new ultracold gas experiments. I describe the design and assembly of the vacuum system, the various elements of computer control, the magnetic trapping coils and their control circuits, and the many lasers and optics used in the experiment.

Chapter 3 describes the cooling and trapping techniques needed to achieve simultaneous quantum degeneracy of bosons and fermions. The process begins with the capture and cooling of atoms in a two-species magneto-optical trap; the atoms are subsequently transferred in a three-step process to a Ioffe-Pritchard type magnetic trap for the final stages of evaporative and sympathetic cooling. The experimental procedure is described, and the characterization of quantum degeneracy is outlined in some detail for bosons and fermions. Some possible limits to the temperature we can achieve with sympathetic cooling are discussed, along with implications for future experiments. This "incredible journey" the atoms take from room temperature to a few tens of billionths of a degree above absolute zero is outlined schematically in Fig. 1.3.

Chapter 4 details the main experimental results we have achieved with the machine. I first discuss some ways to probe the collisional interactions between species. The discussion focuses on our extension of cross-dimensional rethermalization techniques to the (non-degenerate) Bose-Fermi mixture. I will describe why the knowledge gleaned from these measurements, namely the magnitude of the cross-species scattering length, is so important in understanding a variety of properties of the mixture. I will then present some measurements of collective ex-

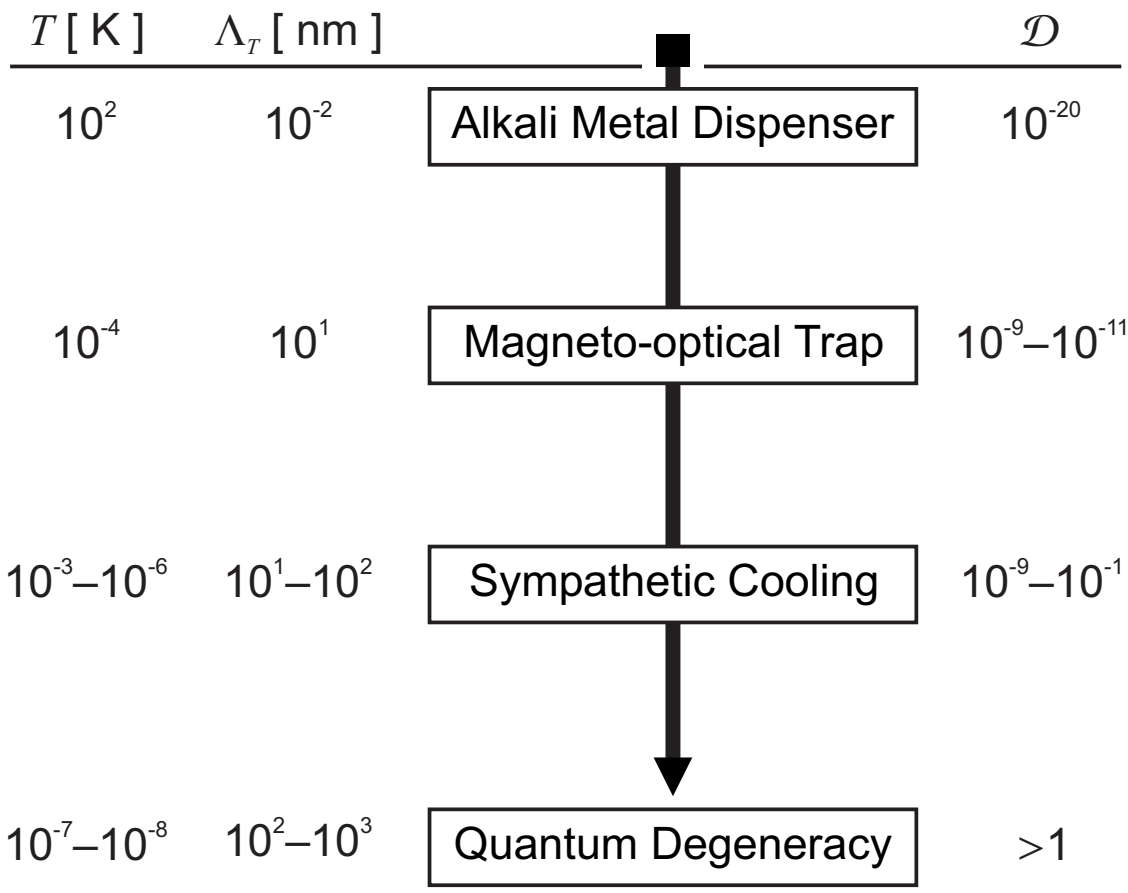

Figure 1.3: The incredible journey from room temperature to quantum degeneracy. The quantities Λ_T and $\mathcal{D}$ are the thermal de Broglie wavelength and peak phase-space density, respectively. Both are discussed in detail in Sect. 3.4.

citations of the mixture, and describe a variety of related measurement techniques, with an eye towards future experiments.

Also in chapter 4 I describe our search for, and discovery of, several heteronuclear Feshbach resonances in the ^{87}Rb -^{40}K system. These resonances represent, in my view, the crowning achievement of the work described here, due to the large number of significant and exciting experiments that resonant control of the interactions renders accessible to us. I describe our use of a far off-resonant optical trap and discuss the preparation and detection of resonant states of the mixture. Implications for the theoretical understanding of the ^{87}Rb -^{40}K system are laid out, based on detailed coupled-channel calculations of the collision processes performed by Chris Ticknor and John Bohn. The comparison between theory and experiment allows us to refine the parameters characterizing the collisions between ^{87}Rb and ^{40}K atoms.

Finally in Chapter 5 I conclude with a summary of the work presented in this thesis, and describe what I think are the natural next steps for the experiment. I will additionally describe some proposals for some of the more exciting future experiments that could be performed with our system, including the coveted boson-mediated mechanism for the high-T_c pairing of fermions.

Chapter 2

The Machine

In this chapter I'll describe the details of the design, construction, and operation of our experimental apparatus. I will focus on aspects of the experiment that are unique and include some more detailed discussions of the installation or optimization procedures we use for some of the components. This chapter is intended to be most useful for people still working in the lab, or others hoping to build a similar experiment of their own.

The chapter is organized as follows. I begin in Section 2.1 with a description of the vacuum system we have built, and in Section 2.2 I describe the computer control elements that we use. In Section 2.3 I present the moving magnetic coil assembly used in our experiment, and describe how it is used for the MOT, for the mechanical transport to an ultrahigh vacuum (UHV) cell, and for production of uniform magnetic fields for accessing inter-species Feshbach resonances. In Section 2.4 I describe the Ioffe-Pritchard trap we have built for evaporative cooling; this trap is extremely compact, and operates at relatively low power. Finally Sect. 2.5 details the various lasers used for cooling, trapping, pumping, and probing the atoms. This section also includes a description of a far-off-resonance optical dipole trap, which we used to access the Feshbach resonances described in Chapter 4.

2.1 Vacuum System

In this section I will describe our vacuum system in some detail. The vacuum assembly is shown schematically in Fig. 2.1. The system consists of two Pyrex cells separated by a stainless steel tube that allows for differential pumping between cells. The first cell, which we call the "collection cell," was made at JILA and is home to the two-species magneto-optical trap (MOT). The $2'' \times 2'' \times 6''$ cell contains two arms — one with four Rb dispensers, and one with four K dispensers. The Rb dispensers are purchased from SAES Getters [11], and the enriched K dispensers are produced at JILA, as described in Ref. [12]. Enriched K dispensers are necessary due to the extremely low natural abundance of ^{40}K (0.0117%) [13].

The collection cell is connected with a "T" to a 20 L/s ion pump and a long, narrow tube, which we call the "transfer tube." The purpose of the tube is to allow differential pumping between the collection cell (at relatively high pressure, in order to collect a lot of atoms), and the second glass cell, or "science cell," which is maintained at higher vacuum in order to provide long trapping lifetimes and efficient evaporation of the ^{87}Rb atoms. For example our $1/e$ lifetime in the magnetic trap in the collection cell is about 2 to 4 seconds. In contrast our lifetimes in the science cell exceed 100 seconds for ^{87}Rb atoms, and 400 seconds for ^{40}K. Our evaporative cooling sequence lasts about 30 seconds.

The pressure gradient from end-to-end across the transfer tube is inversely proportional to the conductance of the tube. At the low pressures used in these experiments, the vacuum is in the so-called "molecular flow" regime. This means that the conductance is independent of pressure [14]. In this case the conductance of air through the tube is given by $C = 12\, d^3/l$ [L/s], where d is the diameter of the aperture, and l is the length of the component, and both are measured in cm. Note that conductances add (in series and parallel) like capacitors in an electronic

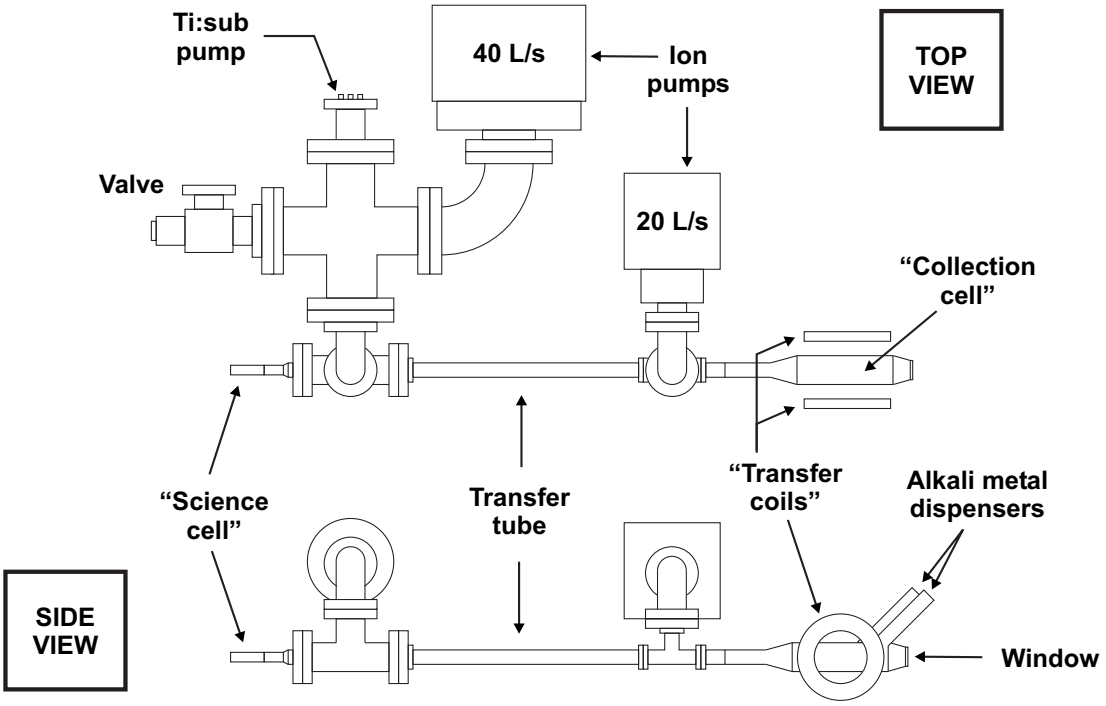

Figure 2.1: Schematic of the vacuum assembly. The top view is shown above and the side view below. The "collection" and "science" cells are glass, and the rest of the components are stainless steel connected by ConFlat components with copper gaskets. For clarity we have omitted the alkali metal dispensers from the top view. Additionally a bellows to the left of the "transfer tube," which corrects for imperfections in the straightness of some commercial vacuum parts, has been incorporated into the tube itself in the drawing. The valve was used to rough out the system before the bake-out. The window on the front of the collection cell transmits light for optical pumping and imaging of the atoms in either cell. The total distance between cell centers is ~ 81 cm, and the smallest inner diameters are 1 cm. The "transfer coils" are free to move between cells by means of a linear translation stage, described in Section 2.3.

circuit. As an example, our transfer tube is ~ 1 cm in diameter, and 9.5 inches (~ 24 cm), giving a conductance of only $C_{\rm tube} = 0.5$ L/s.[1] If for simplicity we consider just the transfer tube and the 20 L/s pump, then the pressure at the output end of the transfer tube is related to pressure at the input end by [14]

$$\begin{aligned} \frac{P_{\rm out}}{P_{\rm in}} &= \frac{C_{\rm tube}/S_{\rm pump}}{1 + C_{\rm tube}/S_{\rm pump}} \\ &\simeq 2\% \quad , \end{aligned} \tag{2.1}$$

where $S_{\rm pump} = 20$ L/s is just the pumping speed of the ion pump.

The room-temperature vapor pressure of Potassium is much lower than that of Rubidium, so that some amount of heating of the collection cell is required to keep ^{40}K atoms from adsorbing onto the glass. The vapor pressure constants A and B are shown in Table 2.1. The constants A and B give the vapor pressure as a function of temperature T (in Kelvin) according to $P_{\rm vap}[\text{Torr}] = 760 \times 10^A 10^{B/T}$ [15], as shown in Fig.2.2 for temperatures around 300 K. The Rubidium pressure is roughly 20 times higher at 300 K; Potassium must be brought to 328 K to obtain a pressure equal to the Rubidium pressure at 300 K. In order to maintain a workable ^{40}K pressure in the collection cell, we have built a set of heaters, shown in Figure 2.3. Parts of the cell not covered by these heaters are wrapped with Minco flexible foil heaters, allowing us to keep the entire cell above 50° C.

The science cell is made from a commercial fluorometer cell from Starna cells, and is a 1 cm square cylinder of 4 cm length. The cell was smoothly matched to a glass-to-metal seal welded onto a standard conflat vacuum flange. The science cell is pumped by a Titanium sublimation (Ti:sub) pump and a 40 L/s ion pump. The Ti:sub pump is attached to a homemade nipple that places the pump filaments in the center of a large ($4\,\frac{1}{2}''$) four-way cross. The large area provides an excellent

[1] Note that the total conductance is even lower if we take into account the rest of the distance between the two cells. The remainder of this distance is comprised mostly of two "T" components, leading to each of the two ion pumps, and a $3''$ long bellows (not shown in Fig. 2.1), with an inner diameter of ~ 1 cm.

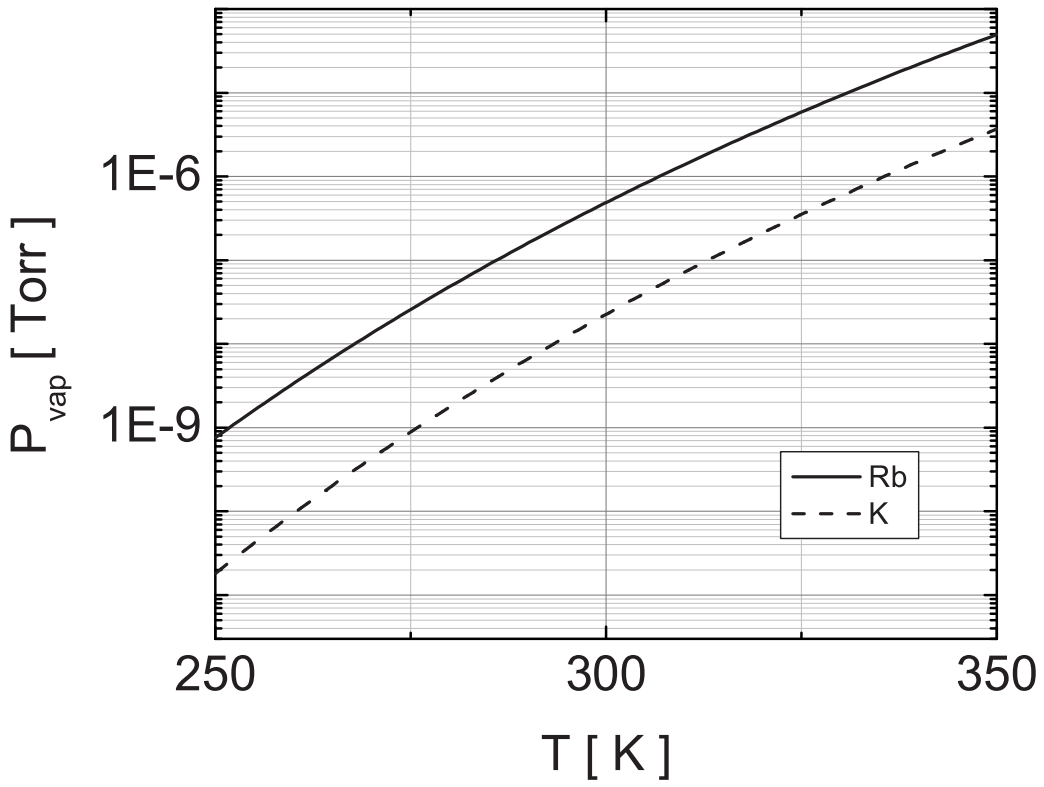

Figure 2.2: Vapor pressures P_{vap} of Rubidium (solid curve) and Potassium (dashed) as a function of temperature T in the vicinity of 300 K.

	A	B	P_{vap} @ 300 K
Rb	4.857	-4215	5×10^{-7} Torr
K	4.961	-4646	2×10^{-8}

Table 2.1: Vapor pressures for Rubidium and Potassium. The constants A and B are used to calculate the vapor pressure P_{vap} according to the formula $P_{\text{vap}}[\text{Torr}] = 760 \times 10^{A} 10^{B/T}$, with T the temperature in Kelvin. Values for A and B were taken from Ref. [15].

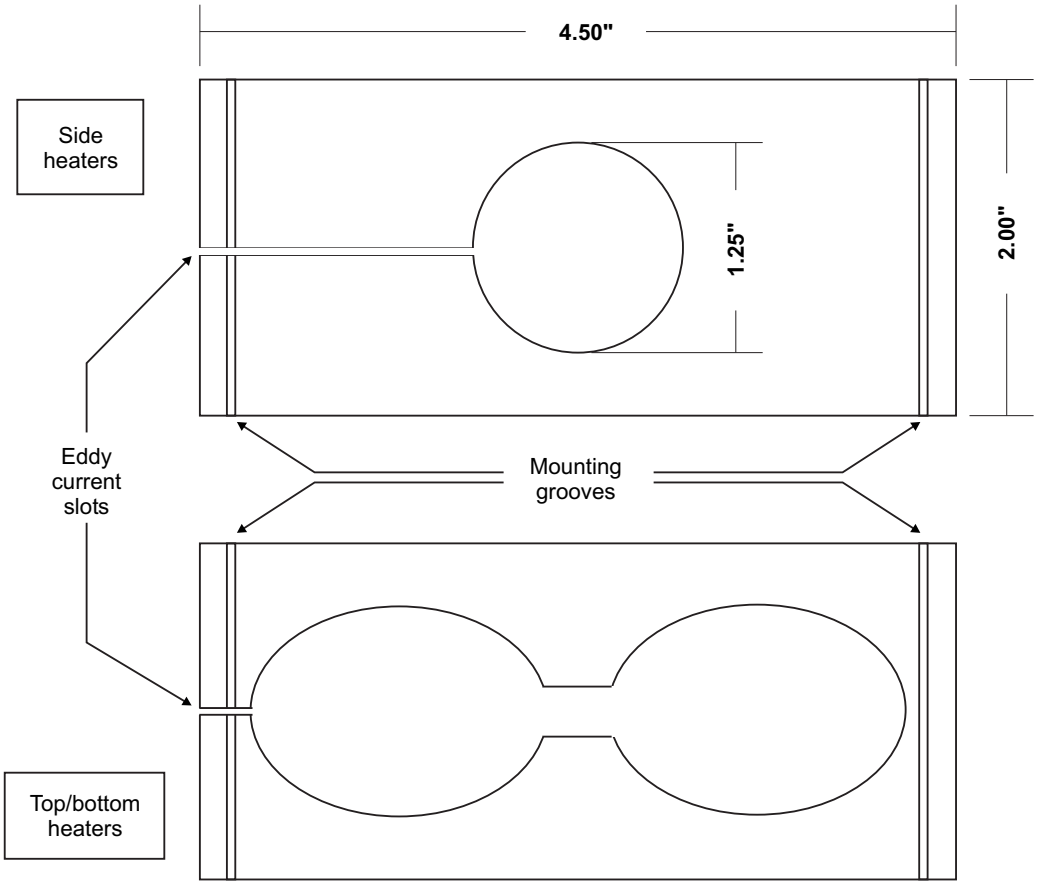

Figure 2.3: Heaters for the collection cell. All parts are 1/8-inch thick black anodized aluminum. Slots are cut to inhibit large-wavelength eddy currents in the bodies of the Al plates. The large holes allow the MOT beams to enter and exit the cell, and show the beam geometry in the experiment. (Note that the holes are slightly larger than shown here, and actually allow a 1.25″ beam to pass through.) The mounting grooves allow the plates to be bound to the collection cell with insulated wire and a thin layer of thermal grease. Not shown are several tapped holes for mounting low-profile 1 Ω resistors, driven at constant current to provide ohmic heating to temperatures $> 50°$ C.

surface for the evaporated Titanium, which was crucial in achieving high vacuum early in the experiment.

2.2 Computer Control

Computer controls for the experiment can be broken down into three categories: (i) control over 64 TTL (logic) bits, used for driving various pieces of electronic equipment; (ii) GPIB control of frequency synthesizers and abitrary waveform generators; and (iii) control of digital-to-analog converters (DACs), used in a variety of ramp controls throughout the experiment. I will briefly describe each type of control. An overview of the computer control for the experiment is shown schematically in Fig. 2.4. For completeness I have included communication with the linear positioning table that moves the transport coils (see Sect. 2.3), and the CCD camera used for imaging the clouds.

2.2.1 Logic Control

To control the TTL's necessary for the experiment, we use a single fast timing board, the DIO-128, from Viewpoint Systems. This is the same timing board used in the experiment described in Ref. [16]. Because of the importance of this board in the experiment, I'll discuss its operation in some detail. The DIO-128 board is capable of handling 64 digital lines of input and 64 digital outputs; as we have only used the outputs, I will limit the discussion here to the board's output capabilities. The outputs are organized into four "ports," consisting of 16 TTL lines each. The maximum output frequency (defined as half the update rate, since a high/low sequence is necessary for a square-wave cycle) is spec'd at $\sim$ 1100 kHz for a single port, and 500 kHz when operating all four ports. In other words, one can achieve μs switching with all lines running. Note that the board can be daisy-chained with additional DIO-128 boards in the event that more lines are

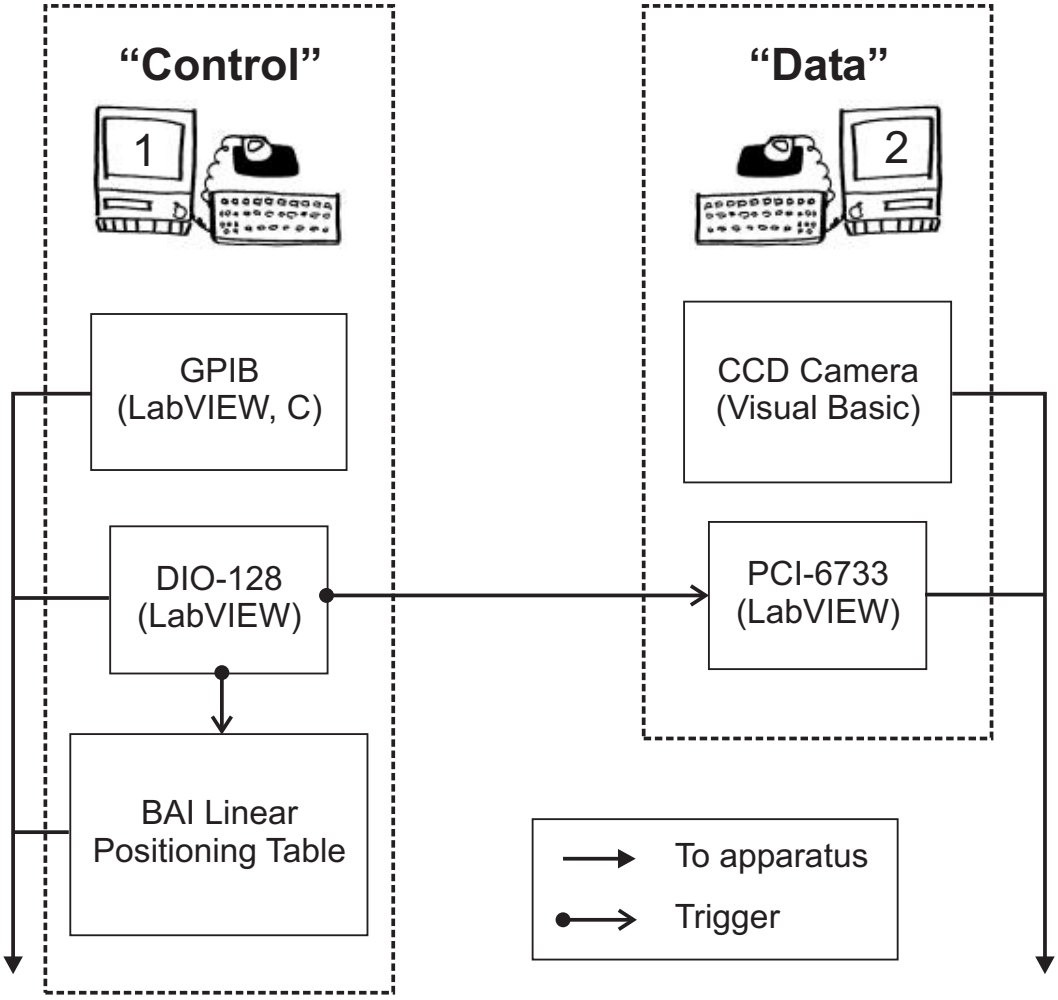

Figure 2.4: Schematic of computer controls for the experiment. The "Control" computer (1) sends digital outputs, and GPIB commands, and can communicate with the linear positioning table used for transporting the magnetic trap, as described in Section 2.3. The "Data" computer (2) controls the CCD camera used to acquire images of the clouds, and houses the DAC board, which produces analog voltages upon being triggered by computer (1).

needed. In addition to providing more TTL lines, this could allow the production of home-made digital-to-analog converters.

The maximum current sourced by the board is specified at only 15 mA per line, meaning any instrument accepting a TTL should have greater than 333 Ω input impedance. Since this is not the case for all of our instruments, and in order to isolate electrical noise in the computer from the instruments, we optically isolate and buffer the outputs. The isolation circuit is shown in Fig.2.5.

The data describing a single experimental time-line are downloaded to the DIO-128 first-in-first-out (FIFO) buffer. Upon receiving a software trigger (in our case provided by LabVIEW code), the board begins outputting the experimental sequence. The board can perform two concurrent types of task — the higher priority task controls the digital outputs, and the lower priority task communicates with the computer. Because of this prioritization, communication with the control computer does not affect the performance of the experiment.

The data loaded to the FIFO buffer consist of six 16-bit words for each time stamp — two words giving the time-stamp itself, and four words each describing the state of one port at that time. That is, the state of all 16 lines comprising a given port are encoded in a single 16-bit number. Only times when a bit is switched are included in the buffer, so that holding a set of TTLs for an indefinitely long time has no effect on the length of the buffer. The 32-bit time-stamp allows times as large as $(2^{32} - 1) = 4294967295$ in units of the resolution, or more than 72 minutes of μs timing.

2.2.2 GPIB Control

The GPIB control for the experiment has been limited to (i) real-time GPIB control of the radio-frequency (rf)-synthesizer used for evaporation, and (ii) downloading of arbitrary waveforms to function generators for a variety of ramps and

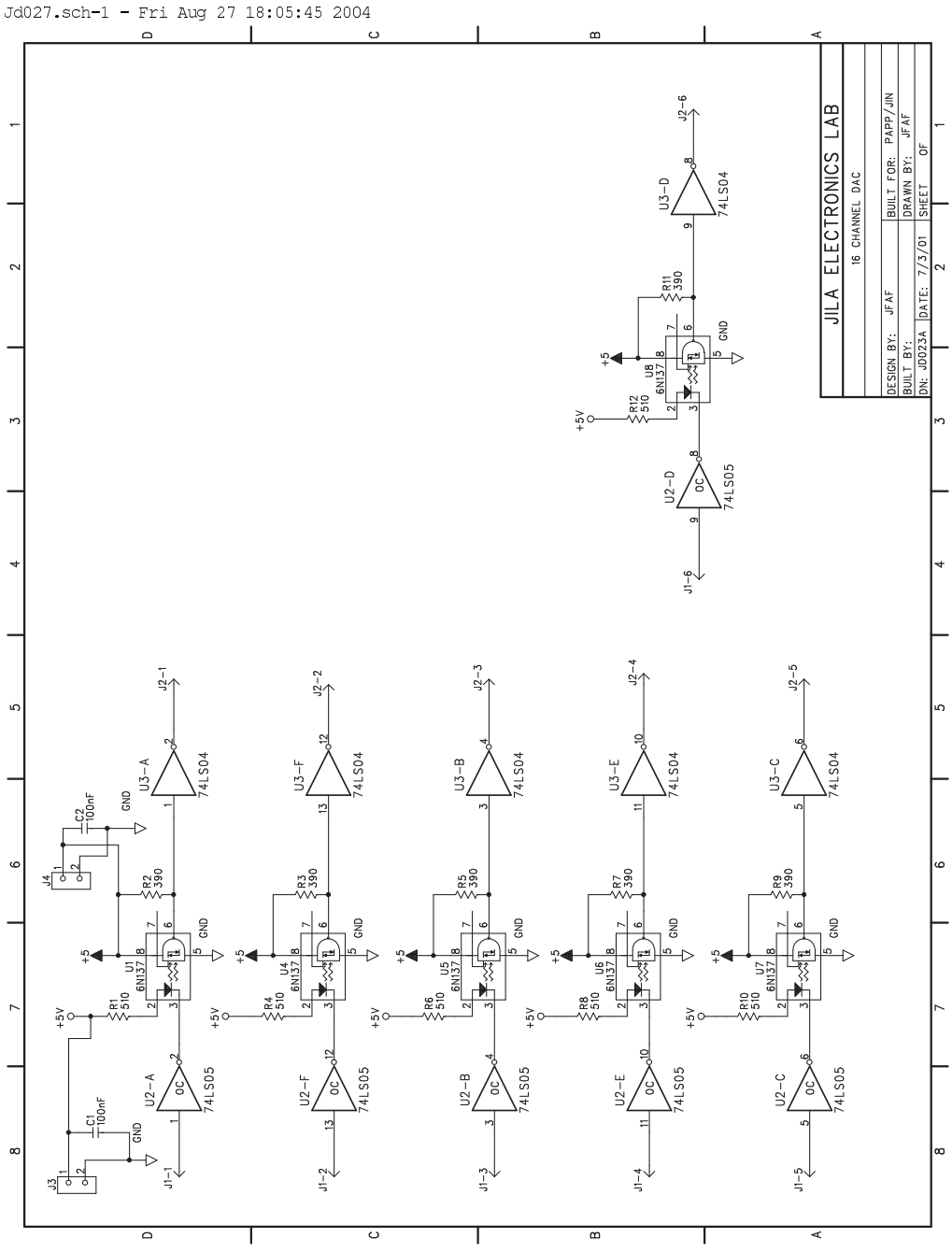

Figure 2.5: Buffer circuit for digital TTL lines. Each line is optically isolated and buffered between the computer output and the experimental apparatus.

modulations.

The evaporation is controlled by a dynamic link library (DLL) written in the C language, and controlled by the same LabVIEW software that controls the DIO-128 timing board. The evaporation "trajectory" consists of a set of times, powers, frequencies, exponential decay time constants, and offsets (or "asymptotes") used to build a series of exponential frequency sweeps, as described in Ref. [16]. The DLL waits 50 ms before updating the synthesizer. At 50 ms, the system clock is polled and the time is used to calculate the correct frequency, and the frequency and power (if the power is to be switched) commands are sent to the synthesizer. We originally used the DLL to control the evaporation because the shot-to-shot variation in timing with LabVIEW was as large as a few hundred milliseconds. The downside of the DLL in its current form is that it completely takes over the computer operating system while it runs. Although this doesn't affect the TTL timing, as described above, it does prevent real-time control of other GPIB devices and makes it necessary to wait until completion of a running experiment before modifying the next experimental timeline. We are currently working on eliminating the timing problem from the LabVIEW control, which does not appear to affect other experiments at JILA.

The remaining GPIB control is limited to downloading arbitrary waveforms to Stanford Research Systems (SRS) DS-345 function generators. These devices are capable of 16,300-point arbitrary waves, as well as a variety of built-in sweeps and modulations with frequencies up to 30 MHz. We used these with GPIB programming primarily for various ramp-and-hold applications before we acquired a digital-to-analog converter (DAC) board. Since installation of the DAC board, described in the next section, the DS-345s are used mostly for pulsed modulations, for example to modulate the trapping potentials in the magnetic or optical traps, or for the rf- and μ-wave sweeps (by frequency-mixing with the synthesizers) used

to transfer atoms into the appropriate magnetic sub-states for experiments with Feshbach resonances.

2.2.3 Digital-to-Analog Converters

For arbitrary analog voltages, we use the PCI-6733 DAC board from National Instruments. The PCI-6733 allows control of eight 16-bit analog voltages, with up to 1 MS/s update rates for four channels. (As with the DIO-128 board, there are inputs available that we don't use, and will therefore be ignored here.) The default voltage range is ± 10 V, corresponding to a minimum voltage step of $\sim 300\mu$V. If finer resolution is desired, an external reference voltage V_{ref} can be used to give selected channels a range of $\pm V_{\text{ref}}$ corresponding to a voltage step size of $2^{-15} \times V_{\text{ref}}$. There are an additional eight digital I/O lines that can be either added to the DIO-128 board or processed as homemade DACs, depending on the needs of the experiment.

The data describing the desired DAC voltages as a function of time are downloaded to the PCI-6733 buffer, and the board waits for a TTL trigger from the DIO-128 board. One drawback to the DAC board is that a uniform time-step is assumed, rather than using individual time-stamps like the DIO-128. This means that fast timing required in one part of the buffer will enforce fast timing everywhere, leading to very large buffer sizes. Since the buffer length is limited to $2^{14} = 16384$ samples, this limits the total on-board signal length to less than 2 seconds for a 100 μs time step.[2] To help overcome this problem we use several separate buffers that are triggered serially. One could also use a simple multiplexing circuit to use fast DAC buffers to generate ramps (for example) and then switch over to constant voltages for long holds.

[2] Actually the board can also be used for much longer waveforms by utilizing the computer memory. We have so far not seen a degradation in performance when running the board this way.

2.3 Transport Coils

In this section I will describe the moving transport coils at the heart of our experiment. This versatile coil set (i) provides the magnetic gradient potential used in the MOT, (ii) provides the stronger quadrupole trap used during the transport, and (iii) produces the nearly uniform B-field used to access magnetic-field-tunable Feshbach resonances.

First I will describe the coil design and the circuits that control the coils. These circuits provide stable currents from a few Amps all the way to the power-supply limited value of 440 A.

I then discuss the actual motion of the coil set between cells. This type of transfer was introduced at JILA in the lab next door to ours (see Ref. [16]) during the design stage of our experiment. We adopted this technology in our experiment in order to obviate the need for a capture MOT in the science cell. The system is simple to setup and essentially never requires readjustment, realignment, re-optimization, or other forms of re-tweaking. We did, however, encounter a potentially catastrophic flaw with the proprietary control software that will be described.

2.3.1 Coil Design and Control Circuitry

The transport coils consist of a simple pair of identical solenoids, each three layers deep axially, and five deep radially, wrapped from insulated hollow square copper tubing. The 1/8-inch inner diameter of the tubing allows sufficient water flow to cool the coils when running up to our highest currents ($\sim$ 400 A, for a few seconds). The inner diameter of the smallest turns is 7.4 cm, and the inner distance between coils is 7.6 cm. The coils are mounted on a large anodized aluminum "cart," with slots cut through all mounting parts to inhibit large-scale

eddy currents.

The coil set operates as a quadrupole trap in anti-Helmholtz configuration and produces a nearly uniform field in Helmholtz configuration.[3] The magnetic field component along the z-axis produced by a single coil of radius a at $z = 0$ is given by [17]

$$B_z(z) \;=\; \frac{\mu_0\, I}{2}\,\frac{a^2}{(a^2+z^2)^{3/2}} \quad , \tag{2.2}$$

where I is the current, and $\mu_0 = 4\pi \times 10^{-7}\,\mathrm{H/m} = 1.257\,\mathrm{G\cdot cm/A}$ is the permeability of free space. In Helmholtz configuration the field is therefore flat to first order in z. From the requirement $\nabla \cdot \vec{B} = 0$ in free space, and using the x-y symmetry of the system, we get a radial gradient in anti-Helmholtz configuration that is half the strength of the axial gradient and opposite in sign. In other words, the magnitude of the field near the center of the coils takes the form

$$|\,\vec{B}\,| \;\simeq\; \begin{cases} B_0 & , \ \text{Helmholtz} \\ \beta\,\sqrt{\rho^2 + 4\,z^2} & , \ \text{anti-Helmholtz} \end{cases} \quad , \tag{2.3}$$

where $\rho = (x^2+y^2)^{1/2}$ is the radial distance, and z is measured from the center of the coils. It is the field magnitude $|\,\vec{B}\,|$ which is proportional to the potential acting on the atoms.

The axial magnetic field measured with a Gauss meter is shown for Helmholtz (anti-Hemholtz) configuration in Fig. 2.6 (Fig. 2.7). The points are the measured fields, and the solid lines are fits to a model assuming two sets of ideal coils (thirty coils total). Since the coils are wound from hollow tubing, there is some ambiguity in the location of the current in the idealized coils. To accommodate this I

[3] Throughout this thesis I will use "Helmholtz" ("Anti-Helmholtz") configuration as a shorthand to refer to the case where the fields from the two coils add (subtract) at the center point. This does not imply the B-field along the axial direction has a zero second derivative in "Helmholtz" configuration. This condition would require that the radius of the coils be equal to the distance between coils, which is not true for either magnetic trap in our system.

measured the inner and out radii $a_i^{(\pm)}$ and coil positions $z_j^{(\pm)}$, and included fitting parameters $\Delta_{a,z}$ that place the idealized coils within the real coils according to

$$\begin{aligned} a_i^{\text{ideal}} &= a_i^{(-)} + \Delta_a \left[a_i^{(+)} - a_i^{(-)} \right] \quad , \quad i = 1,2,3,4,5 \\ z_j^{\text{ideal}} &= z_j^{(-)} + \Delta_z \left[z_j^{(+)} - z_j^{(-)} \right] \quad , \quad j = 1,2,3 \quad , \end{aligned} \tag{2.4}$$

with the constraints $0 \leq \Delta_{a,z} \leq 1$ for the fits. The best fit to the Helmholtz data gave $\Delta_{a,z} \simeq 0.5$, and the Anti-Helmholtz data gave $\Delta_a \simeq 0.3$ and $\Delta_z \simeq 0.4$. The systematic uncertainty due to the inexact placement and angle of the flexible Gauss meter probe was estimated to be an additional 2%, which is much larger than the fit uncertainties. This gives a final B-field calibration of

$$\begin{aligned} B_0 &= 1.50 \pm 0.03 \text{ G/A} \qquad \text{(Helmholtz)} \\ 2\,\beta &= 0.490 \pm 0.010 \text{ G/cm/A} \quad \text{(Anti-Helmholtz)} \end{aligned} \quad . \tag{2.5}$$

We will see later, when we discuss our observation of Feshbach resonances, that this bias field calibration is in reasonable agreement with calibrations from microwave and rf-sweeps of the atoms at different fields.

The control circuit for the transport coils is shown schematically in Fig. 2.8. An H-type configuration of four MOSFETs is used to switch the current direction of one of the coils (coil "B" in the figure), and another MOSFET acts as the master switch for the circuit.[4] The FETs are mounted onto liquid heat-exchanging plates for cooling, and copper bus bars are used for connections between FETs, and to connect to the 4/0 welding cable delivering the current from the power supply. The power supply is an Agilent 6690A, capable of delivering 15 V and 440 A, with an interlock set to trip when the flow of cooling water through the coils or FETs becomes too low. The power supply voltage is controlled by the DAC board described in Section 2.2.

[4] Physically, each FET in the schematic consists of a set of three APT10M07JVR (Advanced Power Technologies) FETs in parallel. This improves the field stability by reducing the power dissipated by each FET.

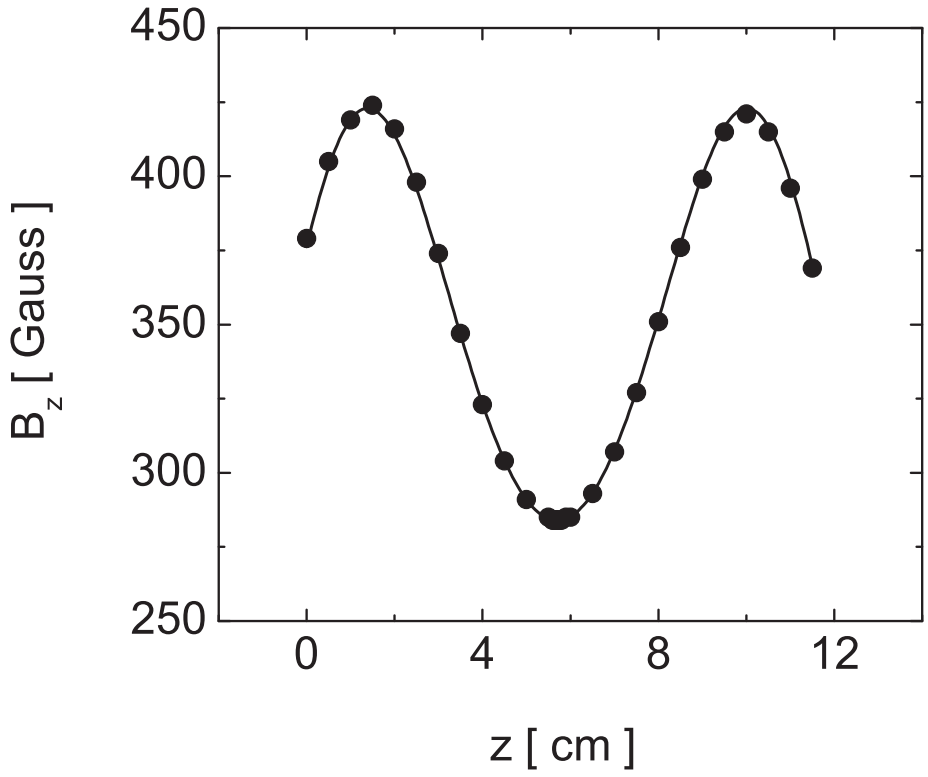

Figure 2.6: Measured axial field of the transport coils, running 200 A in Helmholtz configuration. The points were measured with a Gauss meter, and the line is a fit to a model described in the text.

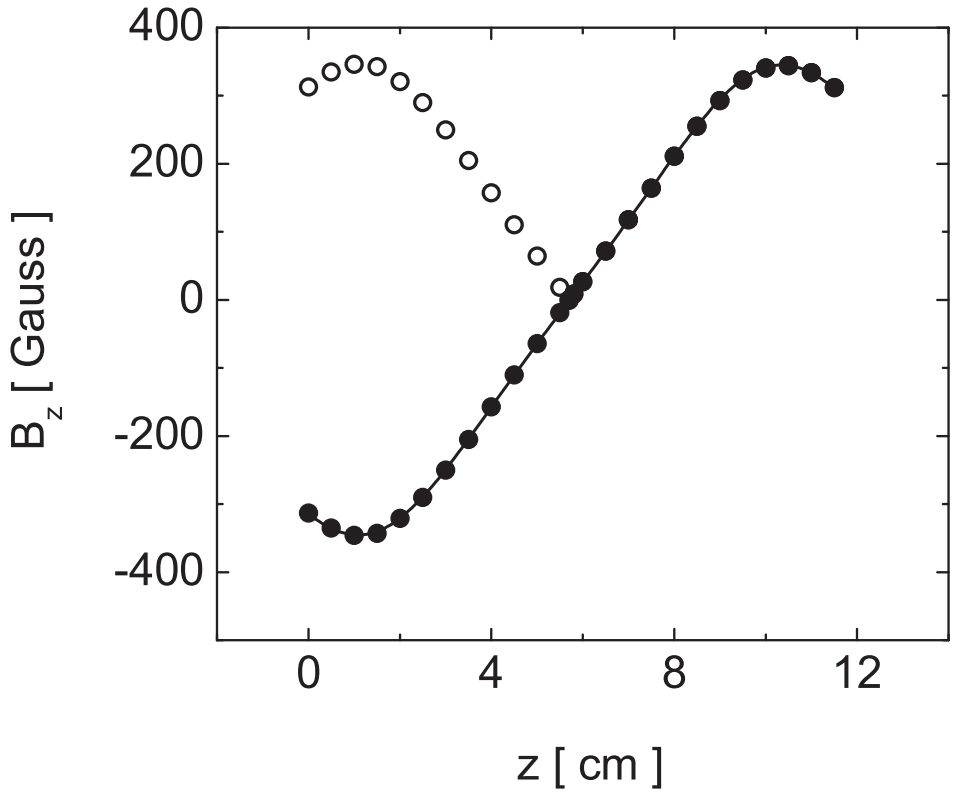

Figure 2.7: Measured axial field of the transport coils running 200 A in anti-Helmholtz configuration. The solid points were measured with a Gauss meter, and the open points give the absolute value of the field, which is proportional to the potential experienced by trapped atoms.

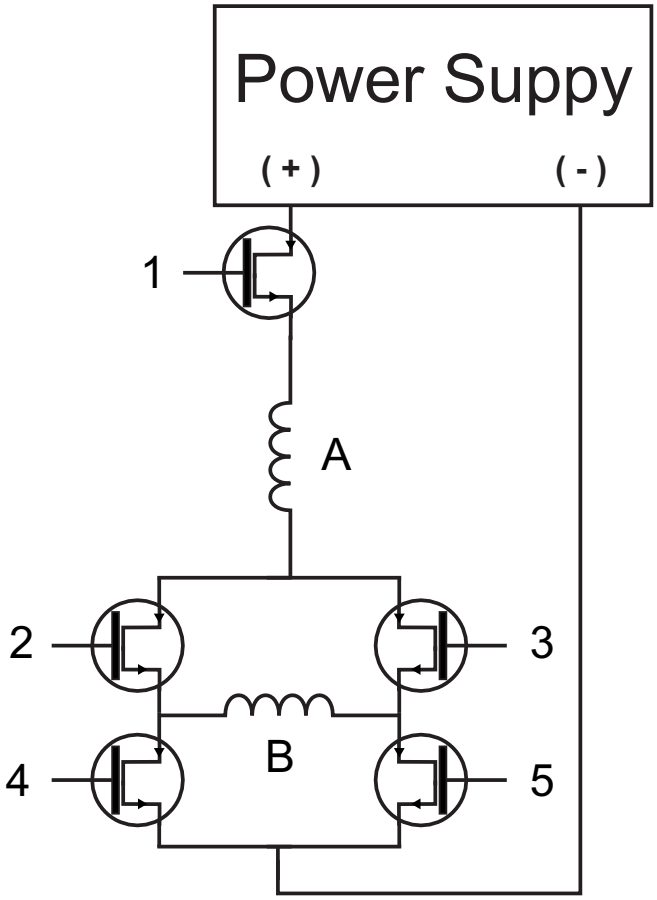

Figure 2.8: Schematic of the control circuit for the transport coils. Every FET drawn in the circuit consists of three APT10M07JVR FETs (Advanced Power Technology) in parallel. The solenoids A and B are the coils and FET 1 is the master switch. In Helmholtz configuration, FET 2 conducts with FETs 3 and 4 open, and FET 5 controls the current; in anti-Helmholtz configuration, FET 3 conducts, FETs 2 and 5 are open, and FET 4 controls the current. The servo (Fig. 2.9) compares a control voltage from the multiplexing circuit (Fig. 2.10) with the output from a Hall effect current sensor (not shown), and the FET switches are controlled by the switching circuit (Fig. 2.11). The power supply is an Agilent 6690A with the negative terminal at ground (not shown).

Active stabilization of the B-field is provided by the servo circuit shown in Fig. 2.9. The current is monitored using an F. W. Bell CLN-500 Hall effect current sensor. The multiplexing circuit in Fig. 2.10 allows us to switch the servo control voltage between various (constant) set points, or a DAC control voltage for ramps and modulations. The switching between Helmholtz and anti-Helmholtz current configurations is achieved with the circuit shown in Fig. 2.11.

2.3.2 Cart Motion

The coil set described in the previous section is used to mechanically transport atoms from a relatively high-pressure cell where the atomic sources reside to a low-pressure cell with long lifetimes for evaporation and experiments [16]. The total distance traveled by the coils is ~ 81 cm, in a time of about 6 seconds. This time is limited by the need to stop and move slowly across an anomalous magnetic feature in our vacuum system near the science cell. We refer to this feature as the magnetic "speed bump," and find that we must move slowly across it in order to avoid a severe loss of atoms.

We use a Parker-Daedal 406900XR series linear positioning table[5] with an Aerotech BM/BMS series brushless motor. The track is 900 mm long, with a 25 mm lead ballscrew, and is specified to have ± 5.0 μm repeatability and to be capable of traveling the whole stroke in 1.5 seconds. With the Aerotech motor, the measured step size was 6.32 ± 0.08 μm. When testing the repeatability of the positioning without re-zeroing the device between commands, I could observe no variation in the final cart position using a dial indicator with 0.005 inch (12.7 μm) markings. When re-zeroing between motion commands I observed better than 1/2 tick-mark (~ 6 μm) repeatability, moving the cart at speeds of ~ 6 to 60 cm/s.

[5] Full part number: 406900XR-MS-D5H3L3C9M4E1B1R1P1, from which various features and specifications may be divined.

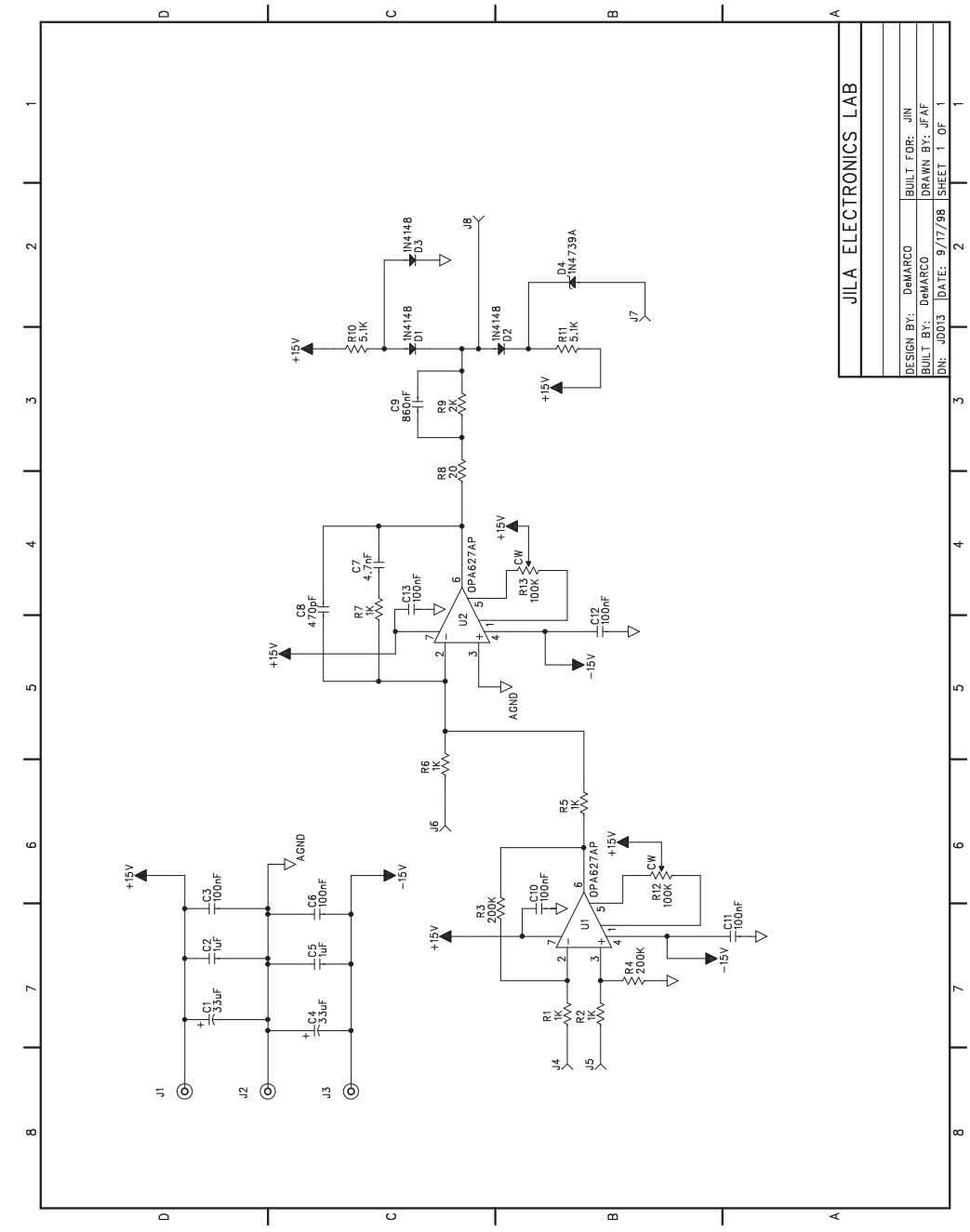

Figure 2.9: Servo circuit for B-field stabilization. The signal from a Hall effect field probe is compared to a voltage set-point from the multiplex circuit in Fig. 2.10.

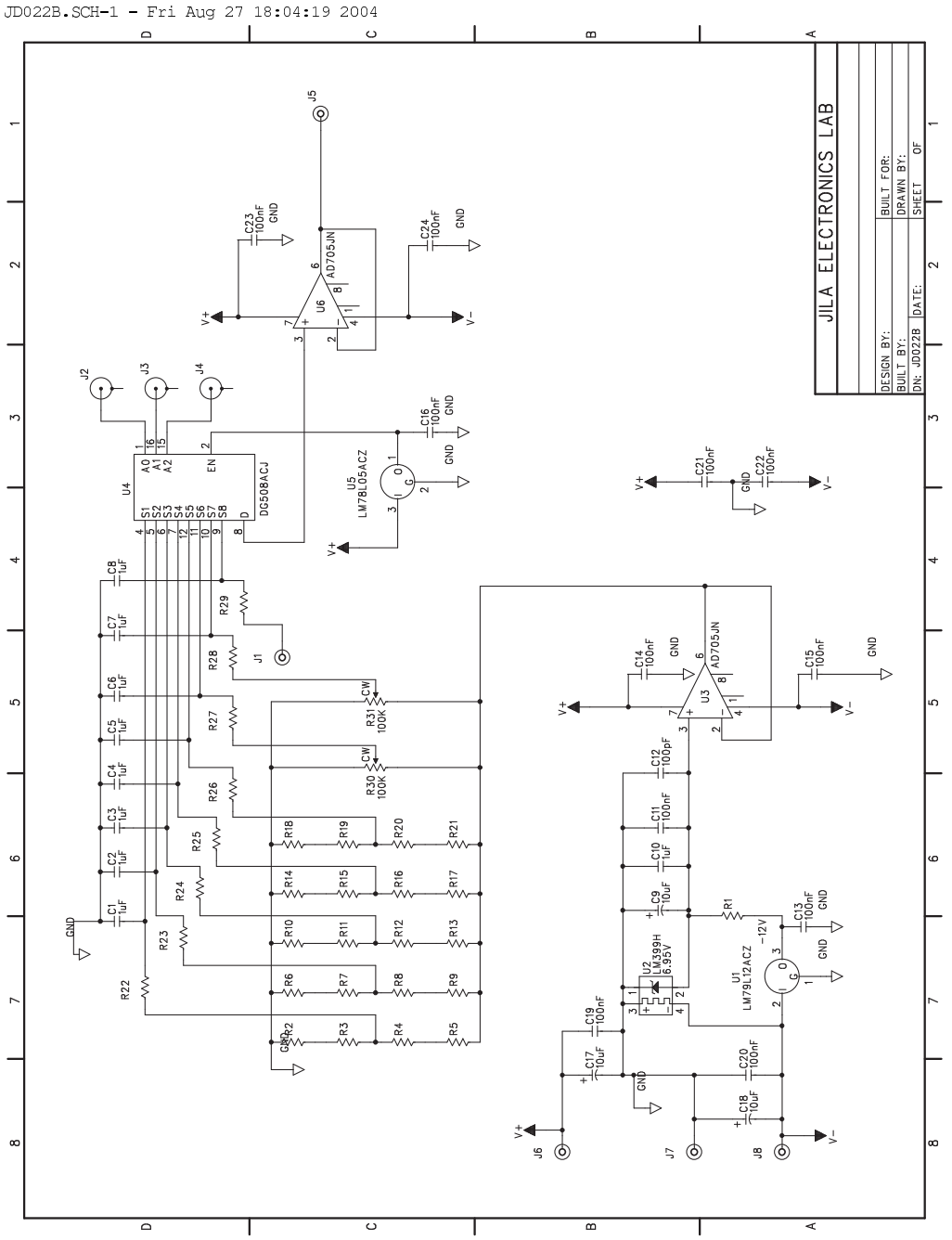

Figure 2.10: Multiplexing circuit. The circuit uses a three-bit digital input to switch between eight possible control voltages for the servo circuit in Fig. 2.9. The input at J_1 allows a variable voltage input, which is provided by the DAC board described in Section 2.2.3.

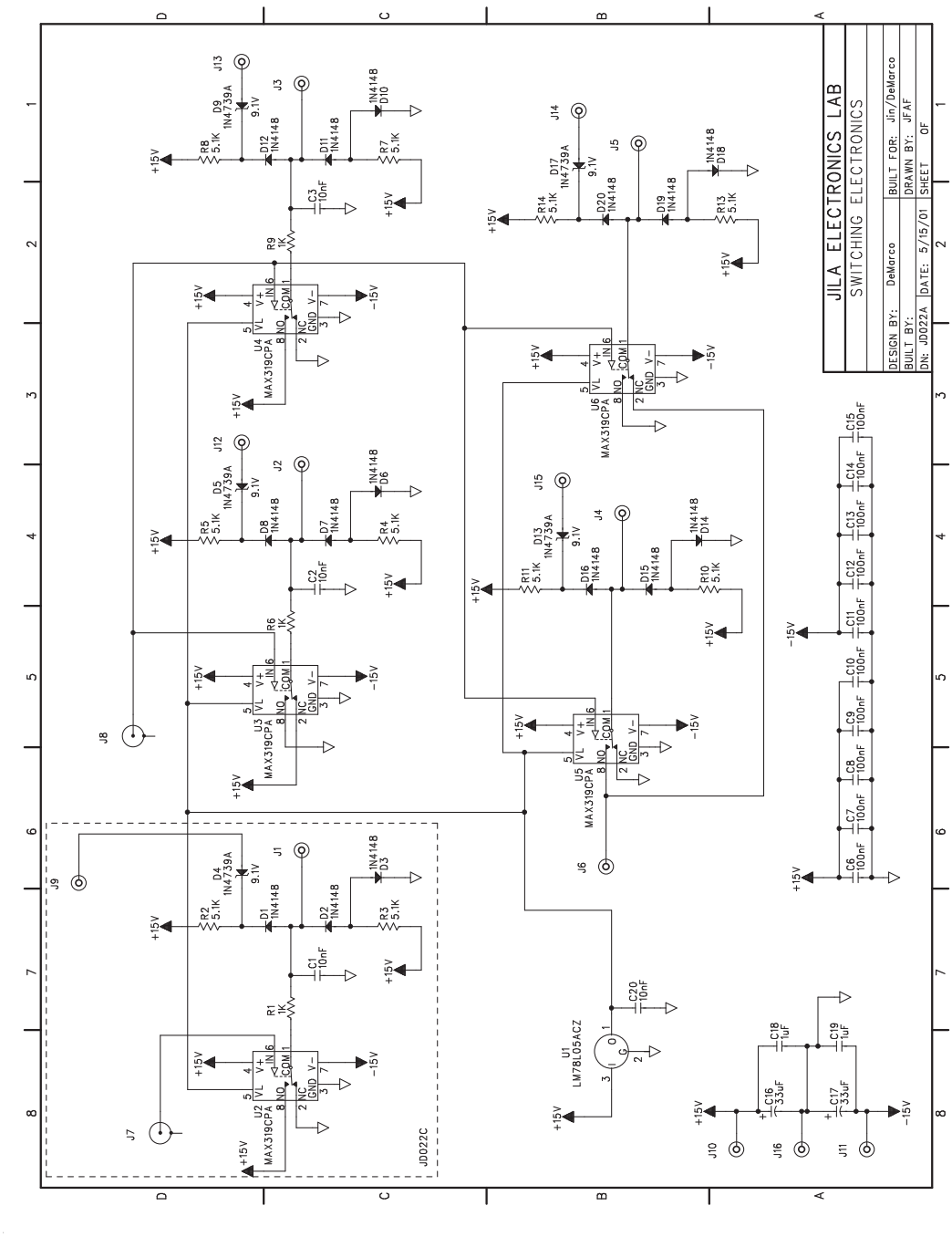

Figure 2.11: Switching circuit for the transport coils. The switching circuit feeds all of the FETs shown in the schematic in Fig. 2.8. This includes the master switch, the directional switches (Helmholtz to anti-Helmholtz), and the control FETs.

We do not typically re-zero the cart unless there has been some failure (such as a power outage) that leads us to doubt the accuracy of the current position.

The control for the cart motion is provided by a text-based series of commands that are downloaded to the cart controller. The controller then waits for a TTL input to trigger the motion (the controller allows three bits each of input and output TTLs). An example of the velocity of the cart as a function of position is shown in Fig. 2.12. When the cart is not in motion, the motor applies a stall torque in order to maintain the position. We find that this creates electrical noise which gets written onto the diode lasers. This is eliminated by "disabling" the cart when not in motion, which turns off the stall torque. Since the motion of the cart creates a lot of table vibration and acoustic noise, we further use a sample-and-hold feature in our laser frequency stabilization servos to temporarily disable the servo while the cart is in motion.[6] Finally to protect against electro-magnetic fields produced by the motor, we have the track oriented with the motor nearest the collection cell, where we are much less sensitive to stray fields and radiated rf than in the science cell.

Before leaving the discussion of the cart, I want to mention a potentially catastrophic bug we uncovered in the proprietary software. The track has software limit switches (the code will not let you send a motion command that would surpass the limit) as well as hardware limit switches (a small magnet attached to the cart passes over a sensor fixed onto the track). We found that if we tell the cart to move to the exact location of the software limit, the cart will execute the motion to the software limit, and then continue **at full speed** into the physical end of the track. This represents a serious threat to anything in the path of the cart.

[6] Actually the Rb master laser can hold its lock during the cart motion, but we temporarily unlock it anyway.

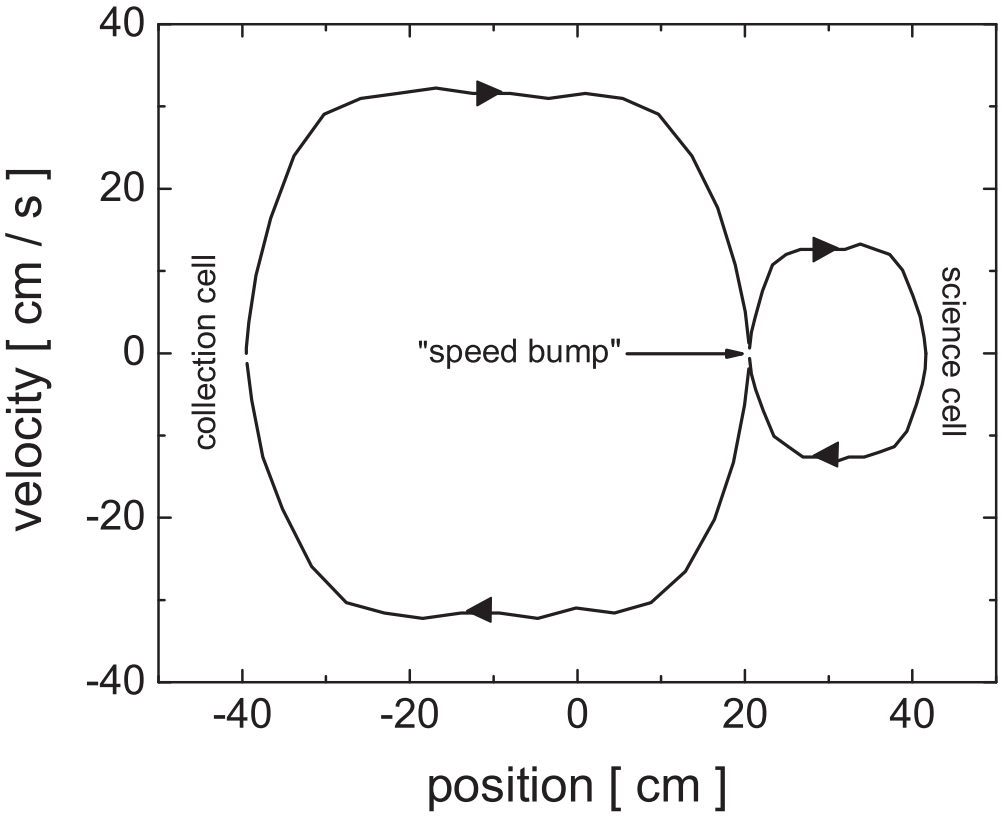

Figure 2.12: Example cart motion during the experiment. Data were obtained by polling the cart controller for the position and velocity during the motion, and arrows indicate the time-order of the travel. The motion here is symmetric between cells, although it need not be in the experiment. The trajectory we currently use reaches three times the top speed of the data shown here.

2.4 Ioffe-Pritchard Trap

A well known limitation of the type of quadrupole magnetic trap described above is that the magnetic field goes to zero at the center of the trap. This gives the opportunity for an atom moving through the center to experience a so-called Majorana spin flip (see, for example [18]), which may result in the atom being lost from the trap. One solution to this problem is to transfer to a trap with a non-zero bias field. Although the elegant TOP trap was the first home to an atomic BEC [19], the celebrated Ioffe-Pritchard trap has been the workhorse of the majority of BEC experiments throughout the last decade.

Since the magnetic transport allows us to forego the production of a second two-species MOT in the science cell, we are able to use a very small (1 cm $\times$ 1 cm) cell, and correspondingly small Ioffe-Pritchard trap. The ability to place our trapping coils so close to the atoms allows us to run with a current of only 27 A. In this section I'll describe the design and construction of the trap, the magnetic field it produces, and the corresponding trapping frequencies for ^{87}Rb and ^{40}K atoms.

2.4.1 Trap Design

Our basic Ioffe-Pritchard trap design is shown schematically in Fig. 2.13. The radial gradient field is produced by four identical coils, oriented with axes along the x- and y-directions of the trap. The direction of flow of the current is arranged so that the axial (z) component of the fields generated by each pair cancel, leaving a pure radial gradient field. The axial confinement is produced by a pair of "pinch" coils that produce the strong field curvature, and a larger pair of "bias" coils which provide near-cancellation of the offset field at the center of trap. As we'll see below, smaller offset fields result in stronger radial confinement.

All coil forms are made from copper with internal channels for cooling wa-

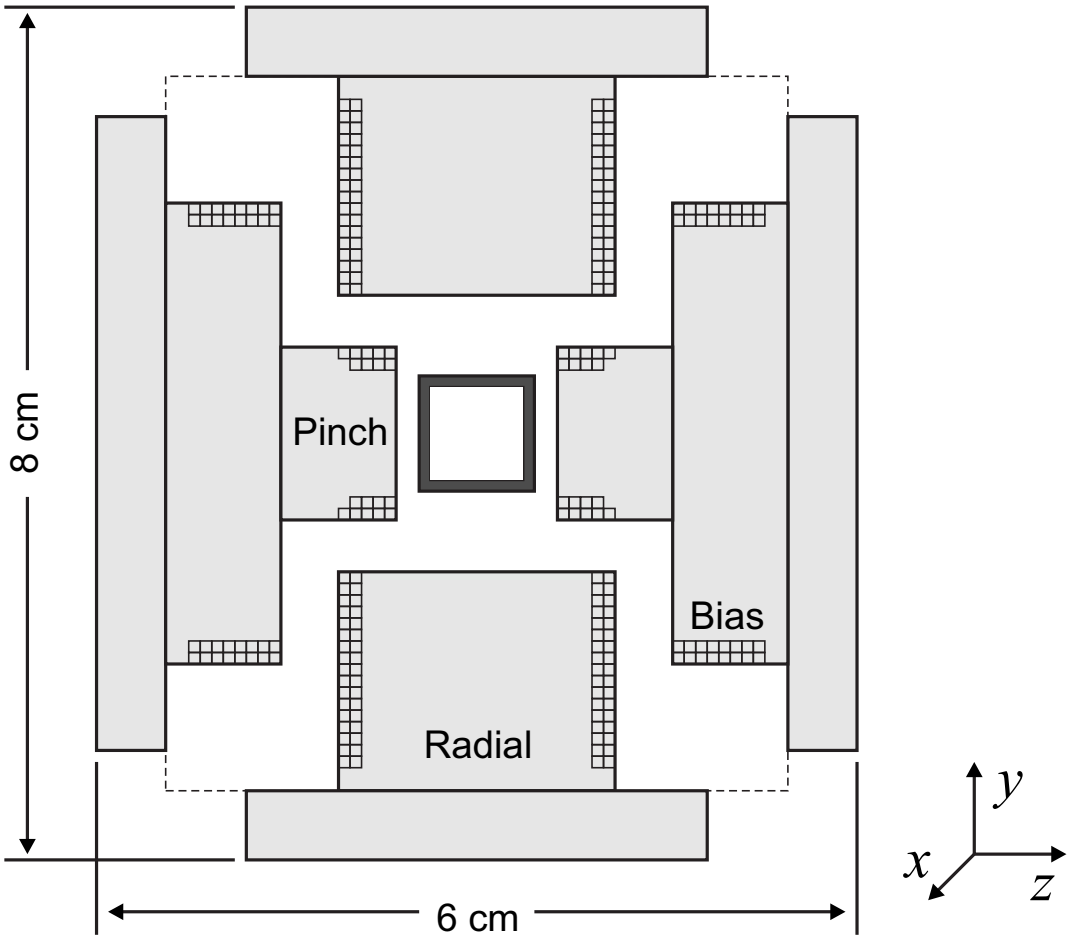

Figure 2.13: Schematic of the Ioffe-Pritchard trap. Not shown is an additional pair of radial coils which slide over the glass cell (dark grey, center), perpendicular to the page. Coils are wrapped on water-cooled copper forms (light grey). All forms are mounted on a phenolic cube (dashed lines). There are $4 + 5$ turns on each pinch coil, 2×8 turns for each bias coil, and 2×17 turns for each radial coil.

ter, slits to prevent eddy currents, and holes on axis for optical access. Coils are wrapped from 19 AWG square magnet wire with Kapton insulation. Thermal grease and vacuum-impregnated epoxy help maintain thermal conductance between the two coil layers, and a thin copper shim is wrapped around the outer layer and connected to the form to help cool the outer layer. All forms are mounted on a phenolic cube. There are $4 + 5$ turns on each pinch coil, 2×8 turns for each bias coil, and 2×17 turns for each radial coil.

The current through the coils is actively stabilized with the same basic servo circuit shown in Fig. 2.9. We additionally provide a "bleed" circuit that includes a servo to shunt current away from the bias coils. This allows us to raise the offset field at the center of the trap, which decompresses the trap in the radial directions.

2.4.2 Trap Frequencies

As described above, a Ioffe-Pritchard trap is generically composed of a radial gradient field superposed on an axial curvature field. A positive offset, or bias, field at the center of the trap prevents atom losses from Majorana spin-flips. Here we will focus on the properties of the magnetic field near the center of the trap, where the atoms in cold gases typically reside. The interested reader may consult Pritchard's original paper [19] or the nice overview in Ref. [20] for more detailed descriptions of the field.

Near the center of the trap the field is characterized by the bias field B_0, the radial gradient $\beta = \partial_x B_x = -\partial_y B_y$, and the axial curvature $\gamma = \partial_z^2 B_z / 2$.[7] The field magnitude is given by [21]

$$\left| \vec{B} \right| = \sqrt{\left[B_0 + \gamma\, z^2 - \frac{1}{2}\gamma\,(x^2 + y^2) \right]^2 + (\beta - \gamma\, z)^2\, x^2 + (\beta + \gamma\, z)^2\, y^2} \quad .$$

[7] Note that there is no consensus in the literature over whether "curvature" should denote the second derivative of the field, or half as much.

The axial field is, to a good approximation, harmonic everywhere. The radial field is harmonic near the center, and linear farther away. That is,

$$|\,\vec{B}\,| \simeq \begin{cases} B_0 + \frac{1}{2}\left(\frac{\beta^2}{B_0} - \gamma\right)\rho^2 + \gamma\, z^2 & , \quad \rho \ll R_0 \\ \beta\,\rho + \gamma\, z^2 & , \quad \rho \gg R_0 \end{cases} , \tag{2.6}$$

where $\rho = (x^2 + y^2)^{1/2}$ is the radial distance from the axis, and $R_0 = 2\,B_0^2/(\,\beta^2 - \gamma\,B_0)$ sets the length scale for the change.

At low fields the potential $U_{\rm IP}$ an atom feels is given by $\mu|\,\vec{B}\,|$, where $\mu = g_F m_F \mu_B$ is the magnetic moment of an atom whose z-component of total spin $\vec{F}$ is m_F (g_F is the Landé g-factor and μ_B the Bohr magneton). All of the magnetic trapping discussed in this work involves alkali-metal atoms in their so-called "stretched" states, which have magnetic moments equal to the Bohr magneton. In other words $U_{\rm IP}$ will be the same for ^{87}Rb and ^{40}K atoms in their stretched states. We can then rewrite Eq.(2.6) in terms of the energy,

$$U_{\rm IP} \simeq \begin{cases} \mu\,B_0 + \frac{1}{2}\,m\,\left(\omega_\rho^2\rho^2 + \omega_z^2 z^2\right) & , \quad k_B T \ll \mu\,B_0 \\ \mu\,\beta\,\rho + \frac{1}{2}\,m\,\omega_z^2 & , \quad k_B T \gg \mu\,B_0 \end{cases} , \tag{2.7}$$

where the harmonic trapping frequencies for an atom of mass m are given by

$$\begin{aligned} \omega_\rho^2 &= \frac{\mu}{m}\left(\frac{\beta^2}{B_0} - \gamma\right) \\ \omega_z^2 &= 2\,\frac{\mu}{m}\,\gamma \quad . \end{aligned} \tag{2.8}$$

Note that (i) the axial frequency ω_z is determined solely by the curvature γ, (ii) changing B_0 offers a simple way to independently adjust ω_r, and (iii) the product $\kappa = m\,\omega^2$ is the same for each species if μ is the same. This last fact, together with the properties of Boltzmann gases in harmonic potentials, allowed us to replace R_0 with $k_B T$ when we went from Eq.(2.6) to Eq.(2.7).

To measure the trap frequencies, we induce a small-amplitude center-of-mass "sloshing" motion to very cold ^{87}Rb clouds. The cloud then oscillates at

exactly the trap frequency. As an example, the calibration we performed during our rethermalization measurements gave

$$\begin{aligned} \omega_\rho &= 2\,\pi \times 156.6 \pm 0.4 \text{ Hz} \\ \omega_z &= 2\,\pi \times 25.01 \pm 0.11 \text{ Hz} \quad , \end{aligned} \tag{2.9}$$

at an operating current of 27 A. Note that due to the mass difference between species, the trapping frequencies for ^{40}K are $(87/40)^{1/2} \simeq 1.5$ times higher. Assuming a bias field of 1.4 Gauss (from measurements of the trap bottom using rf sweeps), this implies $B_0 = 52$ mG/A, $\beta = 5.6$ G/cm/A, and $2\,\gamma = 14$ G/cm^2/A.

Finally, note that when trapping two species with very different masses it becomes necessary to provide strong radial trapping in order to preserve overlap between the two species. If we add gravity (in the y-direction) to Eq.(2.7) we find the equilibrium vertical position $y_0 = -g/\omega_r^2$ (measured from the center of the IP trap). Since $\omega_r^2 \propto m$, the different species experience a different vertical trap center. As the clouds are cooled they become smaller and the spatial overlap between clouds is reduced. This in turn inhibits the rethermalizing collisions needed to drive the process of sympathetic cooling of the fermions. This point is elaborated on in Sect. 3.3.2.

2.5 Laser Systems

2.5.1 Lasers, Lasers, and More Lasers

We use a total of three external-cavity diode lasers (ECDLs), three injected ("slave") lasers, and one semiconductor tapered-amplifier (TA) to produce all of the laser light for the experiment, with the notable exception of the optical dipole trap described in Sect. 2.5.3. The hyperfine frequency shift for a state with nuclear

Element	I	F_g ($J_g = 1/2$)	A_g [MHz]	F_e ($J_e = 3/2$)	A_e [MHz]	B_e [MHz]
^{87}Rb	3/2	1, 2	3417.341	0–3	84.845	12.52
^{39}K	3/2	1, 2	230.859	0–3	6.06	2.83
^{40}K	4	7/2, 9/2	−285.731	5/2–11/2	−7.59	−3.5
^{41}K	3/2	1, 2	127.007	0–3	3.40	3.34

Table 2.2: Hyperfine constants for ^{87}Rb and the stable isotopes of K, after Ref. [22]. Subscripts g and e refer to the $S_{1/2}$ ground and $P_{3/2}$ excited states, respectively. Note the negative values of A and B for ^{40}K, reflecting the inversion of its hyperfine structure, as shown in Fig. 2.14.

spin I and total electron spin J, is given by [22][8]

$$\Delta\nu_{\rm hf} = \frac{1}{2}\,K A_{\rm hf} + \frac{1}{8}\,\frac{3\,K(K+1) - 4\,I(I+1)\,J(J+1)}{I(2I-1)\,J(2J-1)}\,B_{\rm hf} \quad , \tag{2.10}$$

where $K \equiv F(F+1) - I(I+1) - J(J+1)$, and the constants $A_{\rm hf}$ and $B_{\rm hf}$ are determined empirically [23]. Values of $A_{\rm hf}$ and $B_{\rm hf}$ for ^{87}Rb and the stable isotopes of K are shown in Table 2.2. Energy level schematics calculated from Eq.(2.10) are shown for ^{87}Rb and ^{40}K in Fig. 2.14. The saturated absorption spectra used for locking the Rb and K lasers are shown in Figs. 2.16 and 2.17, respectively.

Each species requires two frequencies of light for the MOT, one on a closed cycling transition ("trap" light) which performs the bulk of the trapping and cooling,[9] and one for "repumping" atoms out of the lower-F ground state (*i.e.*, the ground state with lower F, not lower energy). Atoms can spontaneously decay into the lower-F ground state after off-resonant excitation to other excited states by the trap light. This is especially a problem in ^{40}K MOTs, due to the small excited state hyperfine splittings. We use the $F = 2 \rightarrow F' = 3$ $(9/2 \rightarrow 11/2)$ transition for

[8] Note that the corresponding equation (4.2) in Ref. [22] has a typographical error, so that the $(2J-1)$ term in the denominator reads $(J-1)$.

[9] Actually, as discussed in Ref. [13], a ^{40}K MOT can experience a non-negligible trapping force from the repump light.

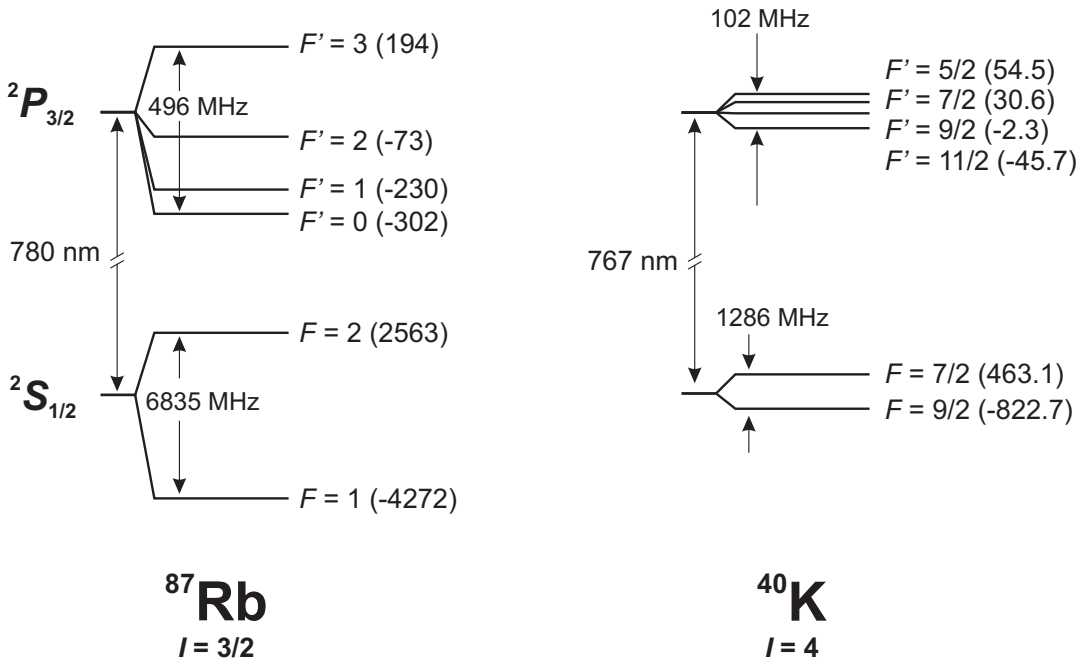

Figure 2.14: Energy level schematics for ^{87}Rb and ^{40}K. Numbers in parentheses are the hyperfine frequency shifts in MHz. Here I is the nuclear spin, which is relatively large in ^{40}K, and aligned anti-parallel to the nuclear magnetic moment, giving rise to the inverted hyperfine structure [13]; F is the total spin. For comparison the natural atomic linewidth of the D_2 ($S_{1/2} \rightarrow P_{3/2}$) transition $\Gamma_{\rm at}$ is $2\pi \times 5.98$ MHz for Rb and $2\pi \times 6.09$ MHz for K.

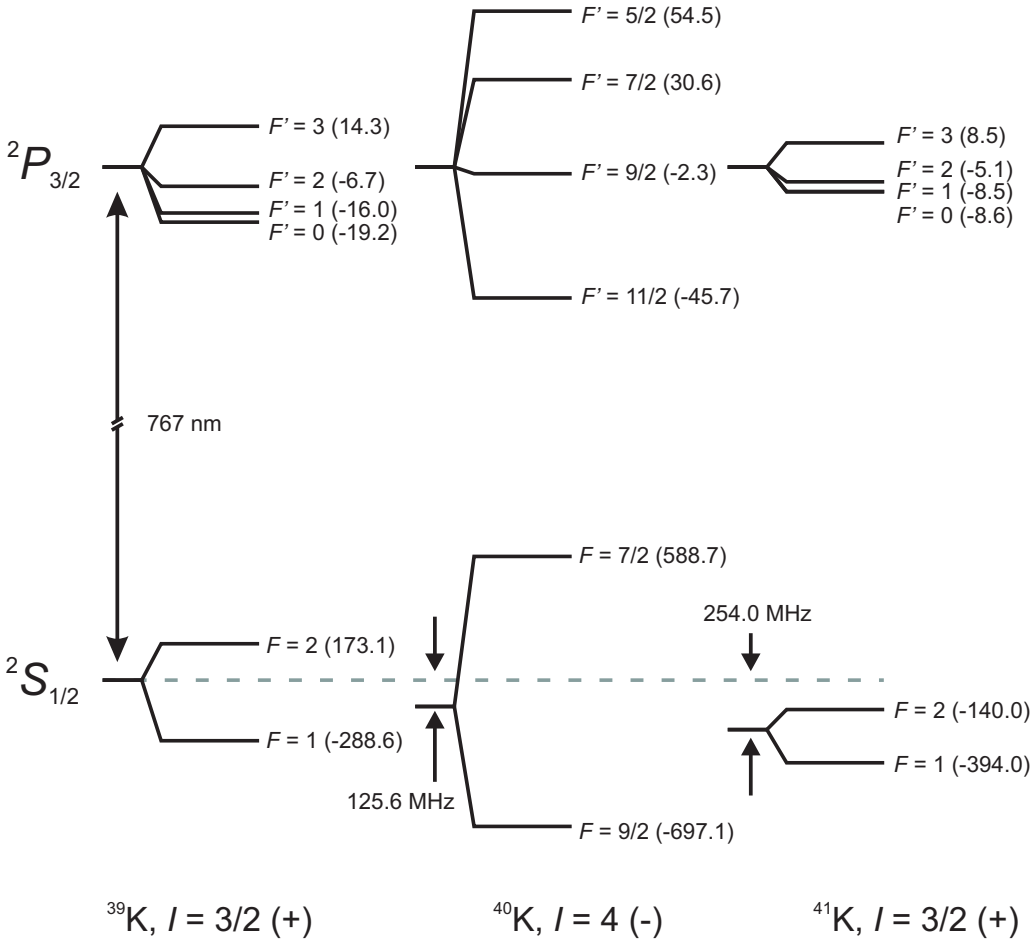

Figure 2.15: Energy level schematics for the stable K isotopes, after Ref. [24]. Numbers in parentheses are the frequency shifts in MHz. The + (−) after I denotes a nuclear spin parallel (anti-parallel) to the nuclear magnetic moment. The ground-state frequencies are referenced to ^{39}K.

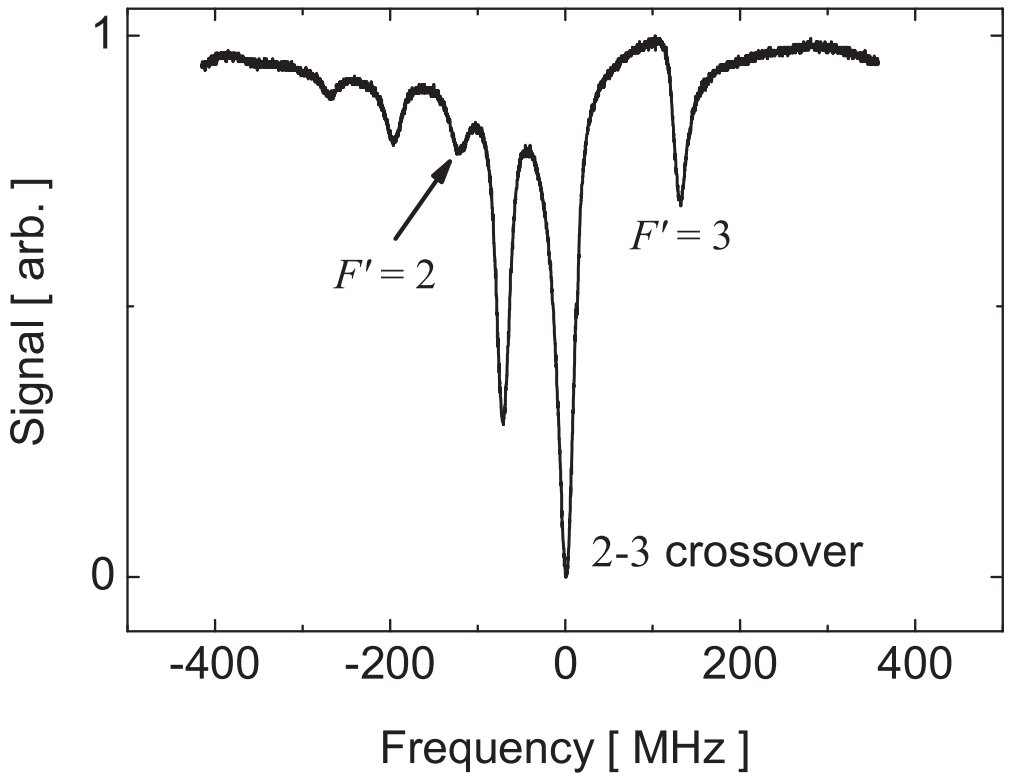

Figure 2.16: ^{87}Rb saturated absorption spectroscopy. Only the $F = 2 \rightarrow F'$ manifold is shown. The laser is locked to the peak of the $F' = 2, 3$ crossover.

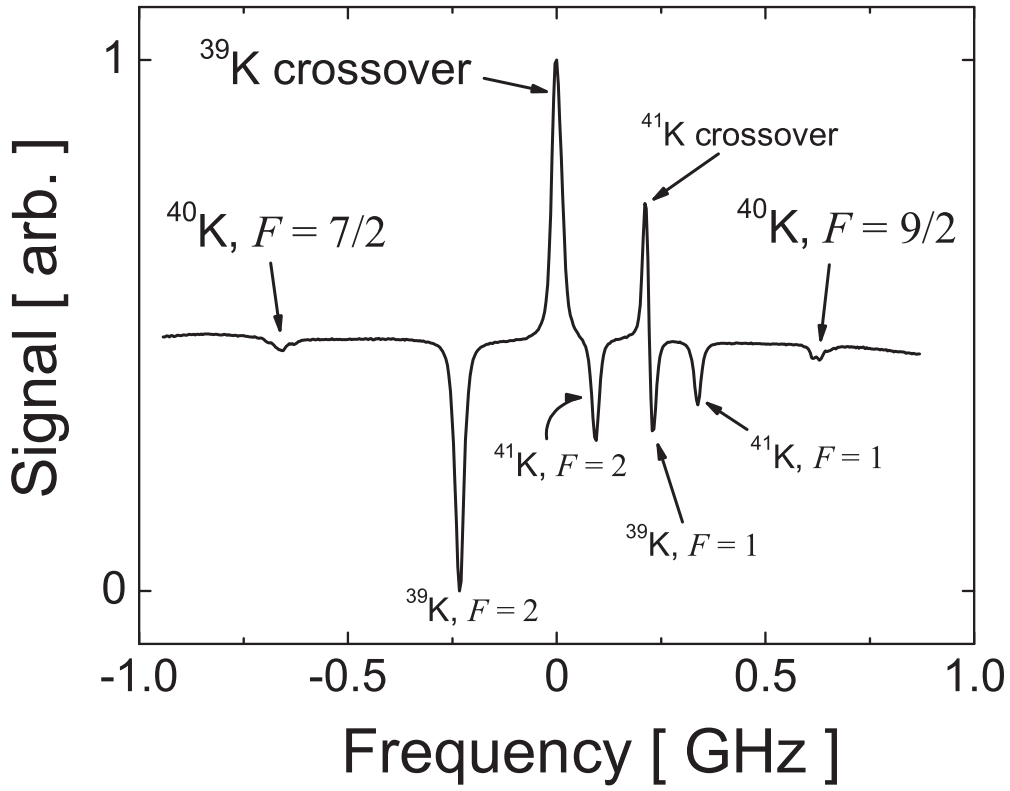

Figure 2.17: K saturated absorption spectroscopy, with enriched ^{40}K. The narrow spacing of the excited states is not resolved (see Fig. 2.15), so that only one absorption line is observed per F ground state. Note that the crossovers lead to reduced absorption, and the ^{41}K crossover overlaps with the ^{39}K, $F = 1 \rightarrow F'$ line. The laser is locked to the peak of the ^{39}K $F = 1, 2$ crossover.

Species	$\lambda_{\rm at}$ [nm]	$\Gamma_{\rm at}/2\pi$ [MHz]	$I_{\rm sat}$ [W/cm^2]
Rb	780.24	5.98	1.64
K	766.70	6.09	1.77

Table 2.3: Transition wavelengths, linewidths, and saturation intensities for Rb and K, taken from Ref. [22].

the ^{87}Rb (^{40}K) trap, and $F = 1 \rightarrow F' = 2$ ($7/2 \rightarrow 9/2$) for the repump.[10]

For a given detuning Δ and laser intensity I, the photon scattering rate (per atom) $\Gamma_{\rm sc}$ is related to the atomic linewidth $\Gamma_{\rm at}$ according to [22]

$$\Gamma_{\rm sc} = \frac{\Gamma_{\rm at}}{2} \frac{I/I_{\rm sat}}{1 + (I/I_{\rm sat}) + (2\Delta/\Gamma_{\rm at})^2} \quad , \tag{2.11}$$

where $I_{\rm sat}$ is the saturation intensity. For simplicity we assume a transition with unity oscillator strength.[11] The value of $I_{\rm sat}$ taken in this sense is a function only of transition wavelength $\lambda_{\rm at}$ and lifetime $\Gamma_{\rm at}^{-1}$, which are both similar for Rb and K. Values of $\lambda_{\rm at}$, $\Gamma_{\rm at}$, and $I_{\rm sat}$ are shown in Table 2.3. Equation (2.11) can be used in various contexts to estimate the amount of light intensity and duration of pulses one may need.

Diode lasers are commonly available with wavelengths in the range of 780–785 nm, meaning lasers for Rb can be purchased without much trouble at all, and lasers for K can be made with some fortuitously low-wavelength diodes and/or aggressive cooling of the lasers. Our homemade ^{87}Rb trap external cavity diode laser (ECDL), which uses a 50 mW Hitachi diode, is based on the design of T. W. Hänsch [27], which was itself based on the original JILA design [28, 29]. The ^{40}K laser uses a 20 mW, 777 nm diode from Sharp and follows the basic JILA design, with some modifications to allow cooling down to $\sim -7^\circ$ C. Modifications

[10] Note that since our work in Ref. [25] we have added a separate repump laser for ^{87}Rb and eliminated the optical sideband generated by current modulation of the ^{87}Rb trap slave. This resulted in improved day-to-day stability.

[11] For a heroic discussion of $I_{\rm sat}$ for optical molasses, see Ref. [26]

include enclosure in a sealed aluminum box to inhibit moisture build-up, the use of smaller aluminum parts for lower thermal mass, a DC fan which flows air over the fins on the heat sink, and vacuum-style feed-throughs which allow manipulation of the collimation lens and grating without opening the laser. The ^{87}Rb repump ECDL is a Vortex laser from New Focus, which uses an anti-reflection (AR)-coated diode and the Littman-Metcalf cavity design [30].

We additionally use three injection-locked ("slave") diode lasers to provide "pre-amplification" before injecting the tapered amplifier (TA), described below. The ^{87}Rb trap slave again uses a 50 mW Hitachi diode, as does the ^{40}K trap slave, which is cooled to $-40°$ C with a combination of two thermo-electric coolers (TECs) and a copper liquid heat exchange plate from Melcor. The housing for the ^{40}K trap slave is again hermetically sealed to inhibit condensation on the laser and collimating lens. The ^{40}K repump slave uses a special diode from a batch of five diodes purchased from Semiconductor Laser International. The diode operates (at room temperature) at 768 nm, allowing us to avoid extravagant cooling.

All lasers are driven by JILA current drivers, and the current to each diode passes through a diode protection circuit connected as close as possible to each diode [13]. This circuit protects the diodes from reverse voltages and transient spikes. For completeness some AOM configurations used in the experiment are shown in Fig. 2.18, and a circuit to drive the voltage-controlled oscillators (VCOs) and mixers for the AOMs is shown in Fig. 2.19.

2.5.2 Tapered Amplifier

One advantage of the ^{87}Rb-^{40}K system, which we pointed out in Ref. [25], is the ability to use a single semiconductor tapered amplifier (TA) for all four colors of light used in the two-species MOT. These devices easily achieve the 13 nm (7 THz) optical bandwidth required, allowing us to produce a single beam with

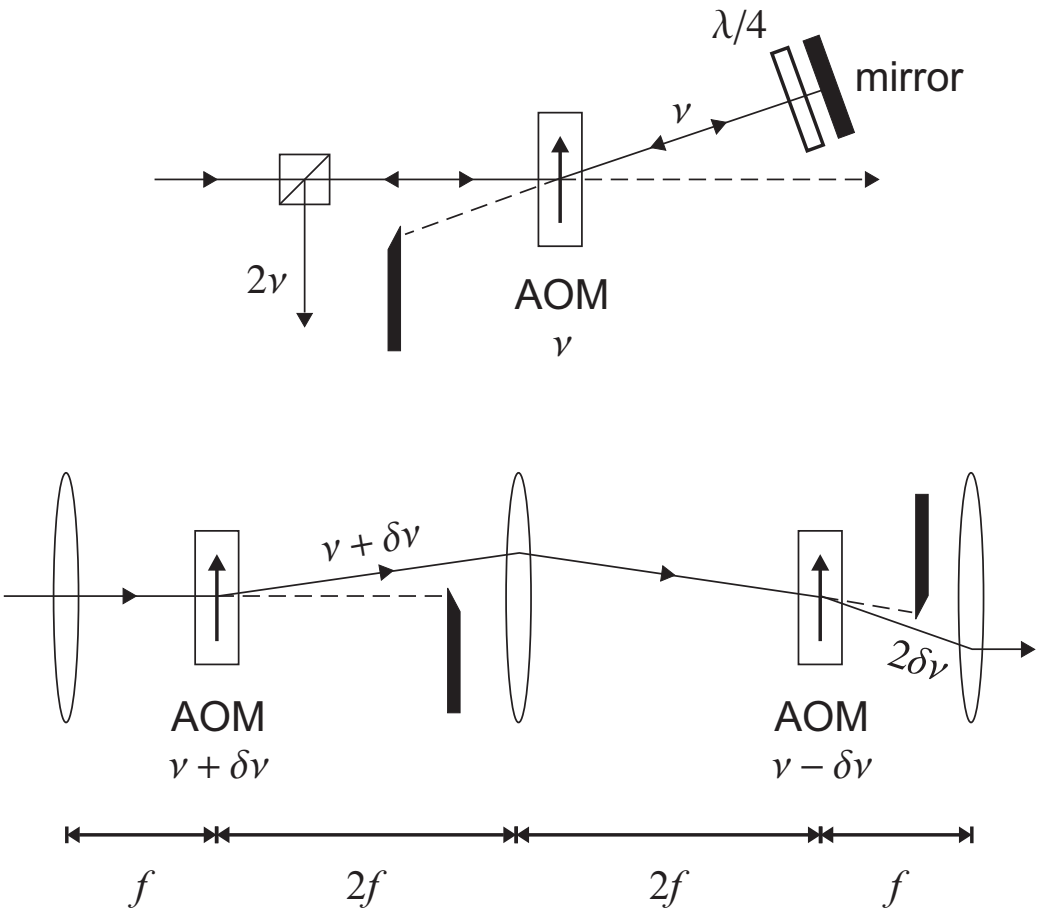

Figure 2.18: Some AOM configurations used in the experiment. The direction of the AOM arrow reflects the direction of beam deflection for a positive frequency shift. In the top "double-passed" configuration, which is the most common in the experiment, a single AOM shifts the beam by a frequency ν in the first pass. The beam is retroreflected and shifted again, for a total frequency shift of 2ν. Although this configuration typically produces less power at the desired frequency than a single AOM, the output beam exhibits no steering as ν is tuned. In the lower configuration, which is used only by the ^{87}Rb repump ECDL, two AOMs running at $\nu + \delta\nu$ and $\nu - \delta\nu$ are combined using a system of three lenses of focal length f in a way that gives a total shift of $2\delta\nu$. This configuration allows us to quickly control the output power of the laser with only a small frequency shift from the lock point at the peak of the $F = 1 \rightarrow F' = 2$ transition.

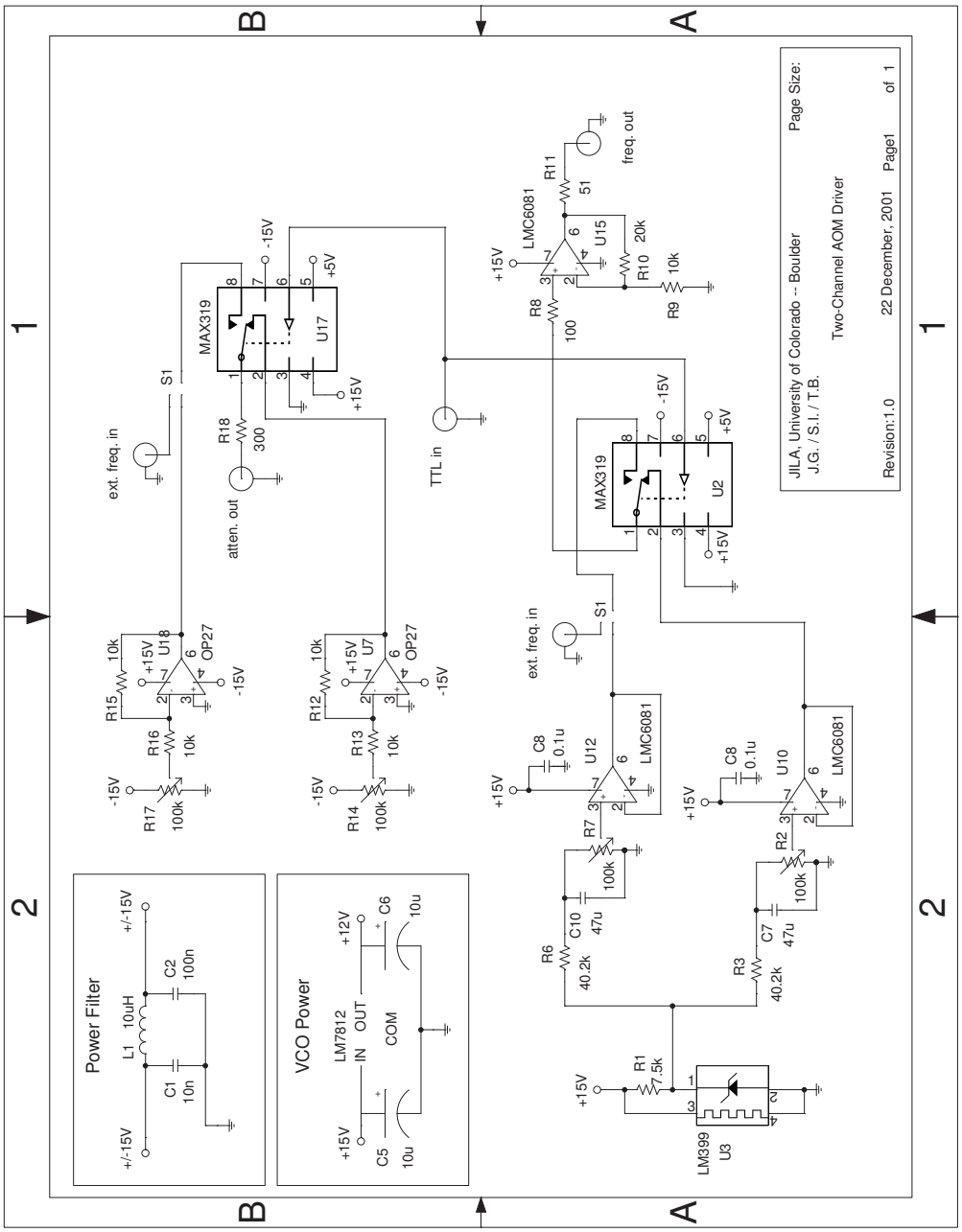

Figure 2.19: Circuit used for driving VCOs and mixers for AOMs. An analog switch (MAX319) selects between two settings for power ("atten.") and frequency. One pair of settings can further be manually switched between a potentiometer on the front panel and an input control voltage. The ±15 V power is filtered to block rf reflections from getting back onto the power supply. Not shown are 0.1 μF capacitors connected to ground on the power to all the devices (see, for example, the +15 V power on U_{10} and U_{12}).

all of the light needed for the MOT. The spectrum of the injected TA is shown in Fig.2.20. A detailed description of the use of such a device for multi-color injection (up to 12 GHz) is given in Ref. [31]. The TA chip is purchased as a stand-alone product from Toptica Photonics, and is installed in a homemade housing [13] and driven by a homemade current driver. The device produces optical power up to 500 mW.[12]

The light injecting the TA must have a particular linear polarization for amplification [13]. To combine 780 and 767 nm light, we use a combination of polarizing beam-splitting (PBS) cubes and custom waveplates. The waveplates, produced by Lens Optics, provide $27\,\frac{1}{2}\,\lambda$ retardation at 780 nm, and $28\,\lambda$ (*i.e.*, none) at 767 nm. This allows us to combine 780 and 767 nm light with the same polarization without losing power. To do this we combine the two colors using orthogonal (linear) polarizations on a PBS cube. Then a waveplate after the cube rotates the polarization of the 780 nm light in order to be the same as the 767 nm light.

With a single beam output from the TA containing all the necessary frequencies, we build a three-beam (retro-reflected) $\sigma \perp \sigma$ MOT, where the two species are simultaneously trapped and cooled. Typical values for the detunings of the trap light and the intensities of the trap and repump light are shown in Table 2.4. The beam geometry has one horizontal pair entering the cell transverse to the axis of the transfer tube, and two pairs each at 45° to the table surface, in a vertical plane through the axis (recall the collection cell heaters shown in Fig 2.3). We typically trap a few 10^9 ^{87}Rb atoms with 1 to 2×10^7 ^{40}K atoms. The MOTs are overlapped in space, although the physically smaller ^{40}K MOT is not perfectly centered on the ^{87}Rb MOT.

[12] New devices from Eagleyard Photonics appear to perform similarly, but are cheaper, and have output powers greater than 1.5 W at 767 nm.

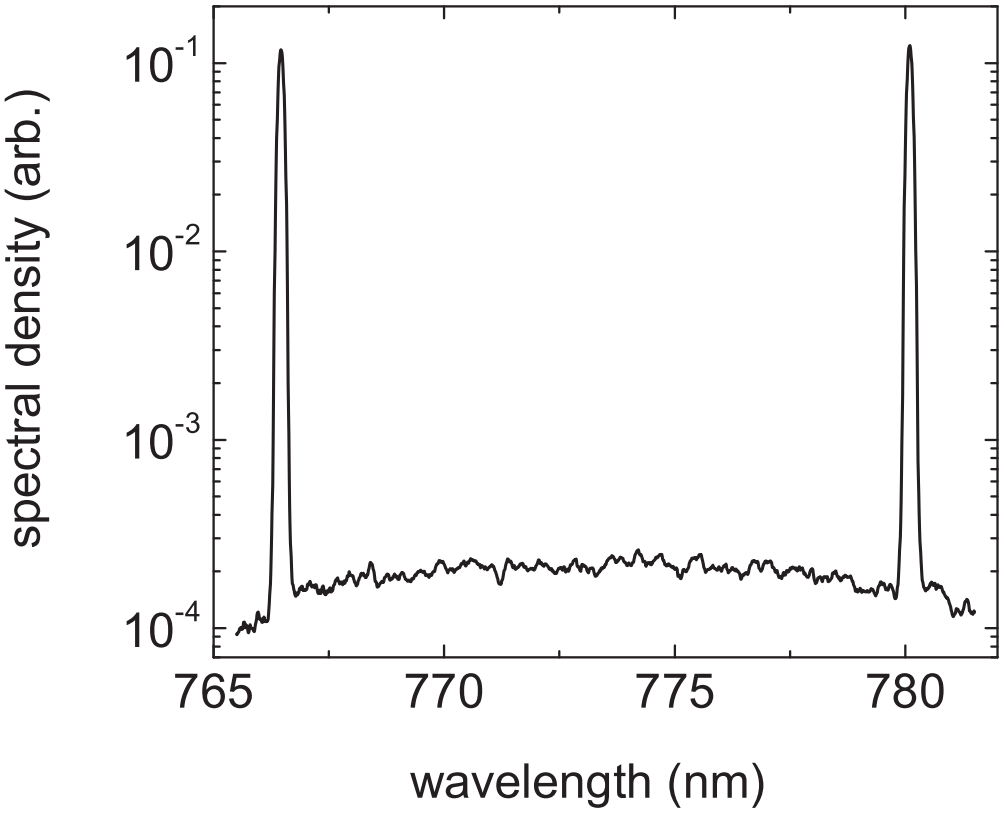

Figure 2.20: Spectral output of the injected tapered amplifier. These data were taken on an Ando spectrum analyzer, with a resolution of 0.1 nm. The Rb and K peaks at 780 and 767 nm, respectively, are clearly visible, although the separate trap and repump frequencies are not resolved. The amplified spontaneous emission is suppressed by almost three orders of magnitude compared to the peaks.

	^{87}Rb	^{40}K
$-\Delta_{\text{trap}}$ [MHz]	22	19
I_{trap} [mW/cm^2]	50	26
I_{rep} [mW/cm^2]	2	6

Table 2.4: MOT light detunings and total peak intensities. Peak intensities do not account for losses on the collection cell and nearest optics, or the competition between different frequencies in the TA when all colors are injecting it simultaneously. The intensity at the atoms is estimated to be lower by no more than half. Using these numbers gives a lower limit on the number of atoms in the MOTs calculated from fluorescence of the atoms.

Before leaving the discussion of the TA chips, I should say something about their lifetimes. Our first device, which had much higher amplification (100 to 200× gain) than its successors, lasted about 21 months from installation to death. We believe the chip died with burn damage on the front facet. Evidence for this included a comb-like structure in the spectral output, which we interpreted as showing cavity modes arising from the increased reflection of the front facet due to the burn. Also, the power in the amplified spontaneous emission (ASE) had increased greatly, and when we imaged the facet with our CCD camera we could see a shadow in the center of the output light. The next device survived only four months after installation. This device worked fine until we went to lunch one day. When we returned, the output power had dropped considerably and was too low to make a MOT. Neighboring labs had experienced no electrical disturbances during our time away from the lab, and Toptica was unable to determine what happened after studying the device. The replacement device, which is currently in use, has been running for 16 months. We always keep a backup device in the lab.

2.5.3 Far Off-Resonance Optical Trap

Last, but not least, is the laser we use to form the far off-resonance optical trap (FORT). We use a VersaDisk Yb:YAG laser from Elektronik Laser System, capable of producing as much as 5.7 W of single-frequency light at 1030 nm. Although we observe mode-hops due to temperature drifts of the laser cavity, the output power remains stable. Since we do not actually require single-frequency operation for our trap, we have not upgraded the cavity to a more stable design.

The laser itself resides in a closed box on its own breadboard beneath the main optics table. The breadboard sits on a homemade steel I-beam table, with large compressible hemispheres from Berg between the breadboard and table for

vibration isolation. The intensity of the YAG light is controlled with an 80 MHz AOM, using the servo circuit shown in Fig. 2.21. The unshifted light is sent to a power meter and Fabry-Perot spectrum analyzer for monitoring. The shifted light is coupled into an optical fiber, using a fiber coupler from Oz Optics. We typically run the system at powers of 1 W at the atoms (2 W out of the laser) without any problems.

The fiber delivers the light for the optical trapping beam to the main experimental table. The optics which generate the trap reside on a small aluminum breadboard that can be removed from the experiment for setup and testing purposes. The optical setup is shown schematically in Fig. 2.22.

The installation of the FORT was performed as follows. On a breadboard in a separate lab we set up and tested the optics with 1030 nm light, optimizing the alignment and tilt of the lenses to minimize any astigmatism or other aberrations in the beam profile. Measurements of the spot size as a function of position were made with a CCD beam profiler, as shown in Fig. 2.23. The focal position (x, y, and z) was then compared to that for resonant (767 or 780 nm) light, and the difference was recorded. The FORT optics were then installed into the experiment and aligned by eye onto the Ioffe-Pritchard trap. This alignment was good enough to observe loss of magnetically trapped atoms when sending resonant laser light into the science cell. Using resonant light, the optical alignment was then adjusted for the strongest "kill" of the trapped atoms (using the translating lens and finely adjustable mirror L_3 and M_2 in Fig. 2.22). After switching back to the far-detuned YAG light, and making the previously determined adjustments to the lens and mirror, we were able to load cold atoms into the FORT. Finally the lens and mirror were tweaked again to optimize the number and temperature of the atoms trapped in the FORT.

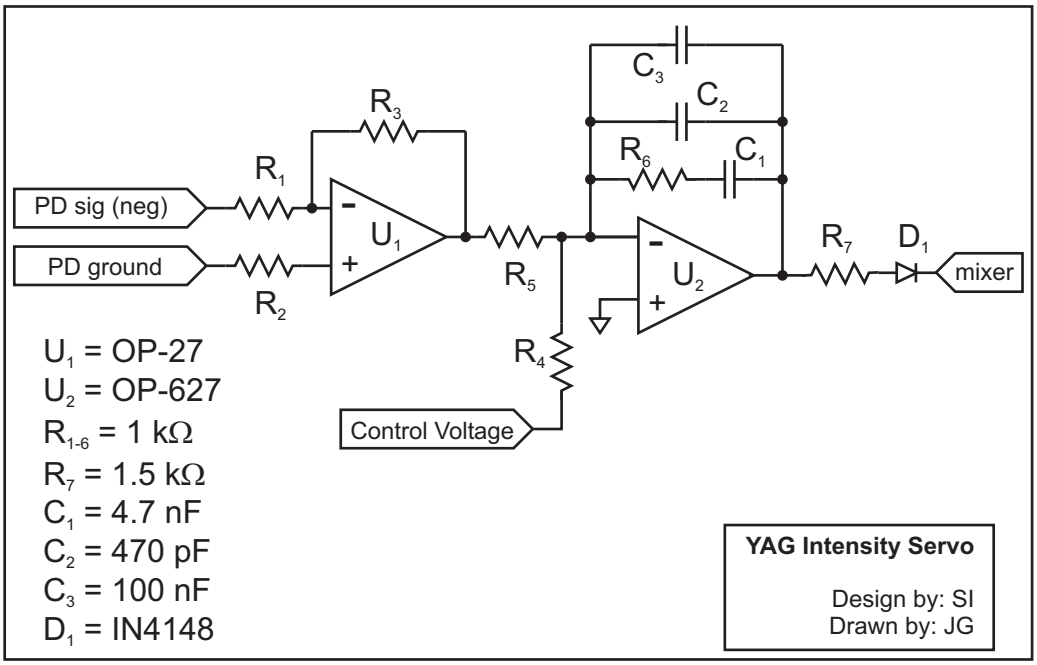

Figure 2.21: YAG intensity servo. The laser power is observed on a photodiode (PD) after the atoms and stabilized with a mixer and AOM placed before the fiber. The circuit allows the control voltage to be derived from a knob on the front panel or an external input, for example a DAC signal (not shown). Also not shown is a MAX319 analog switch before R_7 for switching between control voltages. The diode D_1 ensures the output is always positive. Since the mixer responds only to the magnitude of the current, fluctuations around zero when controlling low powers could otherwise lead to a 180° phase-shift in the servo loop.

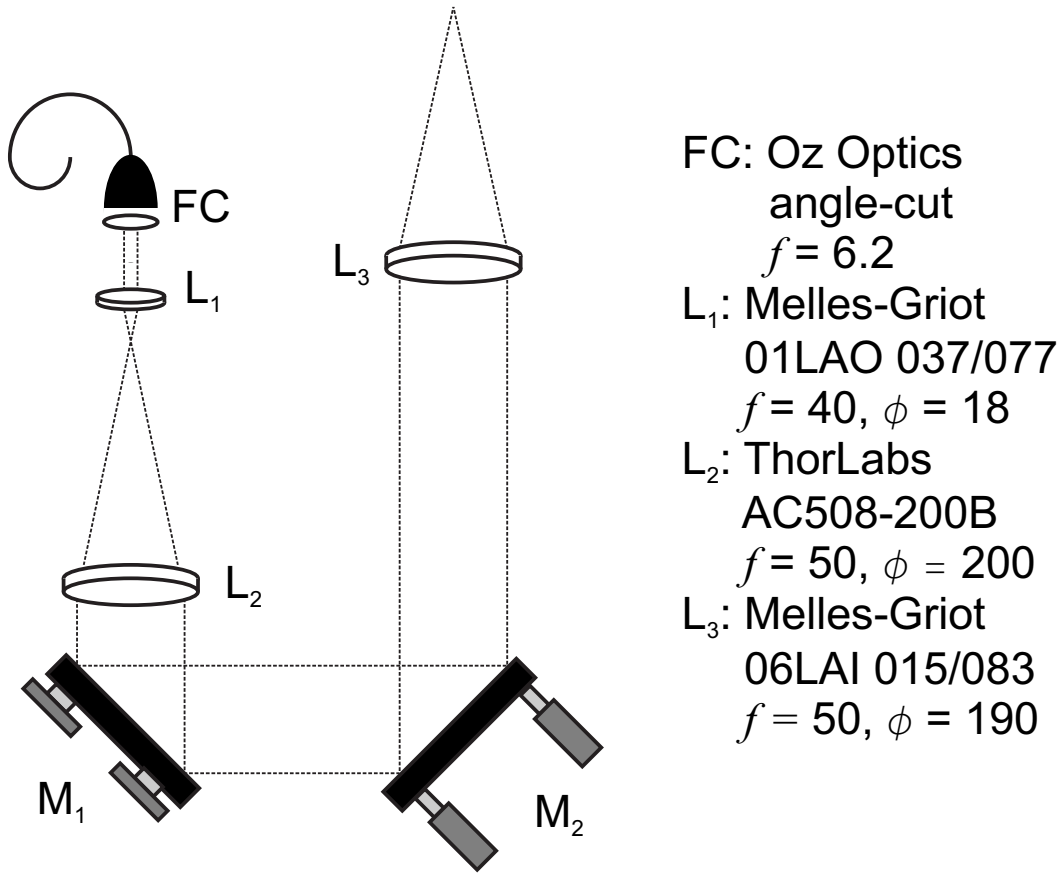

Figure 2.22: FORT optics schematic. The light from the YAG is coupled into the experiment using an angle-cut fiber (FC). The angle-cut prevents intensity fluctuations from etalon effects. The lenses L_1 and L_2 form a simple telescope to expand the beam, and L_3 focuses the beam onto the position of the atoms. The position of L_3 along the propagation direction is adjusted with a translation stage not shown. The mirrors M_1 and M_2 use New Focus Ultima mirror mounts, and M_2 has micrometer knobs for repeatable optimization and adjustment. All focal lengths f and lens diameters ϕ are given in mm.

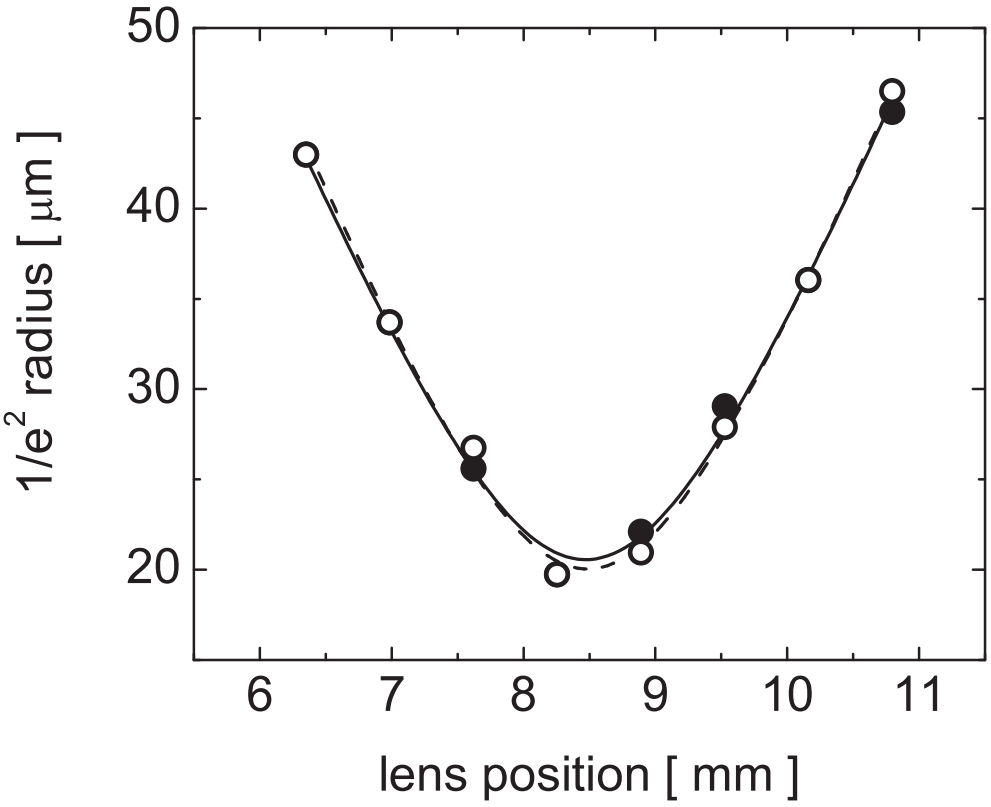

Figure 2.23: FORT beam characterization. Shown is the measured $1/e^2$ radius of the focused YAG beam as a function of position along the beam path. Measurements were made with a CCD beam profiler, and the longitudinal (z) position is referenced to the translation stage holding the lens L_3 (see Fig. 2.22). The solid points (•) correspond to the x-direction (horizontal), and the open points (◦) to the y-direction (vertical). The solid (dashed) curve is a fit to Eq. (2.14) for the horizontal (vertical) data, giving minimum beam waists of $w_{0x} = 20.6\pm0.5$ μm and $w_{0y} = 20.0\pm0.5$ μm, and focal positions $z_{0x} = 8.47\pm0.02$ mm and $z_{0y} = 8.49\pm0.02$ mm. Both fits give $M^2 = 1.07 \pm 0.02$ for the Gaussian beam parameter.

The FORT potential is related to the light intensity $I(\vec{x})$ by [32]

$$\begin{aligned} U_{\mathrm{FORT}}(\vec{x}) &= -\frac{3\,\pi\,c^2}{2\,\omega_{\mathrm{at}}^3}\,\Gamma_{\mathrm{at}}\left(\frac{1}{\omega_{\mathrm{at}}-\omega}+\frac{1}{\omega_{\mathrm{at}}+\omega}\right)I(\vec{x}) \\ &\simeq \frac{3\,\pi\,c^2}{2\,\omega_{\mathrm{at}}^3}\,\frac{\Gamma_{\mathrm{at}}}{\Delta}\,I(\vec{x}) \quad , \end{aligned} \tag{2.12}$$

where c is the speed of light in vacuum, $\omega_{\mathrm{at}} = 2\pi\,c/\lambda_{\mathrm{at}}$ is the atomic resonance frequency, and $\omega = 2\pi\,c/1030$ nm is the FORT laser frequency. The second equation holds for $|\Delta| \ll \omega$, where $\Delta = \omega - \omega_{\mathrm{at}}$ is the detuning of the FORT laser from the atomic resonance. Note that in our experiment $\Delta < 0$, so that the potential is attractive.

Our FORT potential is derived from a single focused beam with a nearly pure TEM_{00} mode (see Figs. 2.22 and 2.23). The intensity distribution for such a beam is given by

$$I(\vec{x}) = \frac{P}{\pi\,w^2(z)}\,\exp\left[-2\frac{\rho^2}{w^2(z)}\right] \quad , \tag{2.13}$$

where P is the total power in the beam, $\rho = (x^2+y^2)^{1/2}$ is the radial distance from the optical axis, and z is the distance along direction of propagation of the beam. The $1/e^2$ beam radius varies along the beam path according to

$$w(z) = w_0\,\sqrt{1+M^2\left(\frac{z}{z_R}\right)^2} \quad , \tag{2.14}$$

where M^2 is the Gaussian beam parameter ($M^2 = 1$ for an ideal Gaussian beam), and $z_R = \pi\,w_0^2/\lambda_{\mathrm{FORT}}$ is the Rayleigh range for $\lambda_{\mathrm{FORT}} = 1030$ nm. The measured beam radius as a function of position was shown in Fig. 2.23, along with a fit to Eq.(2.14) giving $M^2 = 1.07 \pm 0.02$, verifying the nearly ideal nature of the spatial mode of the beam. The measurements in Fig. 2.23 suggest a waist $w_0 \sim 20\ \mu$m, which was the design goal for the optical system in Fig. 2.22.

Although the intensity distribution described by Eq.(2.13) is anharmonic, we can Taylor expand around the beam focus for sufficiently small (that is, cold)

clouds to get

$$\begin{aligned} U_{\rm FORT} &\simeq -U_0 \left[1 - 2\left(\frac{r}{w_0}\right)^2 - \left(\frac{z}{z_R}\right)^2\right]^2 \\ &= -U_0 + \frac{1}{2}\, m\, \left(\omega_\rho^2\, \rho^2 + \omega_z^2\, z^2\right) \quad , \end{aligned} \tag{2.15}$$

where $U_0 = |U_{\rm FORT}(0)|$ and the trapping frequencies are given by

$$\begin{aligned} \omega_\rho^2 &= \frac{4\, U_0}{m\, w_0^2} \\ \omega_z^2 &= \frac{2\, U_0}{m\, z_R^2} \quad . \end{aligned} \tag{2.16}$$

We measured the trap frequencies in two sets of measurements, both taken at an optical power of 1 W (measured after exiting the science cell). In the first set we parametrically excited trapped ^{87}Rb atoms and watched the subsequent center-of-mass sloshing and oscillation of the cloud aspect ratio in time of flight. The second method, which was most useful for determining the axial frequency (which is much lower), was to monitor the size of the cloud in time-of-flight, and compare to the prediction for harmonically trapped atoms. The resulting trap frequencies were

$$\begin{aligned} \omega_\rho &= 2\pi \times\, 2.3 \pm 0.3 \text{ kHz} \\ \omega_z &= 2\pi \times\, 22 \pm 3 \text{ Hz} \quad , \end{aligned} \tag{2.17}$$

where the uncertainties are dominated by an estimated 10% systematic uncertainty due to the anharmonic nature of the FORT potential for the relatively hot ($14\,\mu$K) clouds we used. The corresponding ^{40}K trap frequencies are again $(87/40)^{1/2} \simeq 1.5$ times higher.

Chapter 3

Cooling to Quantum Degeneracy

In this chapter I will describe the various stages of trapping and cooling that lead from a room temperature vapor of various Rb and K isotopes to a quantum degenerate ^{87}Rb -^{40}K mixture at only a few tens of nanokelvin (recall Fig. 1.3).

The first stage of collection and cooling is provided by the two-species magneto-optical trap (MOT). The MOT gets us all the way down to $\sim 150\ \mu$K, which still amazes me, considering the relative simplicity of it all. I'll describe various elements of the main challenge we have experienced with the MOT, namely that our enriched ^{40}K sources do not appear to provide independent control of the K vapor pressure. Through the work of Kurt Miller and extensions by Josh Zirbel here at JILA, I'll describe a simple model of the expected source behavior, and how to diagnose bad sources.

The MOT also gives rise to the first interactions between ^{87}Rb and ^{40}K in our experiment. Light-assisted inelastic collisions lead to a depletion of roughly half of our trapped ^{40}K atoms when ^{87}Rb atoms are introduced into the MOT. I'll present our observation of these losses and compare to a previous measurement performed in another lab using ^{85}Rb and ^{39}K.

From the MOT we transfer the atoms into a purely magnetic quadrupole potential, which moves on a translation stage to a higher vacuum cell. I will briefly describe the preparation of atoms before their transfer to the quadrupole

trap (compression, cooling, and optical pumping).

Atoms are finally loaded from the quadrupole trap into the Ioffe-Pritchard trap for the final stage of cooling. I'll describe how we can directly cool ^{87}Rb atoms via forced rf evaporation without evaporating the ^{40}K atoms. This allows us to efficiently cool the ^{40}K atoms sympathetically by virtue of their thermal contact with the ^{87}Rb gas. In addition to discussing the efficiency of the evaporation, and our characterization of the quantum degeneracy of the bosons and fermions, I'll discuss the temperature dependence of the ^{87}Rb -^{40}K elastic collision cross-section and some possible limits to the sympathetic cooling process.

3.1 Two-Species Magneto-Optical Trap

In this section I will describe the construction and operation of the two-species magneto-optical trap (MOT) used in the initial trapping and cooling stage of the experiment. The MOT is perhaps the only part of a sympathetic cooling experiment that is any more complex than a comparable single-species experiment. Specifically, the need for lasers and optics is essentially doubled, which has led in our lab to an optical table so dense with components that many visitors express some shock at the apparent complexity of it all. This is in fact why we have adopted the magnetic transport design developed in Ref. [16], which eliminates the need for a second MOT and the near-doubling of the numbers of optics and lasers that would imply.

3.1.1 Atomic Sources and Vapor Pressures

I would like to first discuss the use of alkali metal dispensers for the two-species MOT. In particular I will address the competition between the ^{87}Rb and ^{40}K vapor pressures and the consequences for the numbers of atoms that are loaded into the MOT. The discussion here is derived (to my knowledge) from a

conceptual picture developed by Kurt Miller [33], and adapted to the two-species case by Josh Zirbel. Because of the problems we have had in our experiment, I consider this discussion important to those wishing to build similar apparatuses.

We first consider the behavior of a single-species ^{87}Rb MOT. For simplicity we ignore the effects of density-dependent losses. In this case loading of atoms into the MOT obeys [34]

$$\frac{d}{dt}\,N(t) = L - \Gamma\,N(t) \quad , \tag{3.1}$$

where N is the number of trapped atoms, L is the loading rate of atoms into the MOT, and Γ is the loss rate of atoms from the MOT. The MOT loading rate is proportional to the pressure P_{Rb} of ^{87}Rb atoms. The MOT loss rate Γ is given by [35]

$$\Gamma = \Gamma_{\mathrm{Rb}} + \Gamma_{\mathrm{bg}} \quad , \tag{3.2}$$

where Γ_{Rb} is the loss rate due to collisions with ^{87}Rb atoms, and Γ_{bg} is due to collisions with "background" atoms (*i.e.*, everything else). It is important to note that, like L, Γ_{Rb} is proportional to P_{Rb}. Likewise Γ_{bg} is proportional to the background pressure P_{bg}.

It is useful to make the dependence on pressures explicit. To that end we define the reduced quantities $l = L/P_{\mathrm{Rb}}$, $\gamma_{\mathrm{Rb}} = \Gamma_{\mathrm{Rb}}/P_{\mathrm{Rb}}$, and $\gamma_{\mathrm{bg}} = \Gamma_{\mathrm{bg}}/P_{\mathrm{bg}}$. Then Eq.(3.1) becomes

$$\frac{d}{dt}\,N = l\,P_{\mathrm{Rb}} - (\gamma_{\mathrm{Rb}}\,P_{\mathrm{Rb}} + \gamma_{\mathrm{bg}}\,P_{\mathrm{bg}})\;N \quad , \tag{3.3}$$

which yields the solution

$$N(t) = N_0\,\left(1 - e^{-\Gamma\,t}\right) \quad , \tag{3.4}$$

where the MOT loss rate Γ is written in reduced form

$$\Gamma = \gamma_{\mathrm{Rb}}\,P_{\mathrm{Rb}} + \gamma_{\mathrm{bg}}\,P_{\mathrm{bg}} \quad , \tag{3.5}$$

and the equilibrium MOT number N_0 is given by

$$N_0 = \frac{L}{\Gamma_{\rm Rb} + \Gamma_{\rm bg}} = \frac{l\, P_{\rm Rb}}{\gamma_{\rm Rb}\, P_{\rm Rb} + \gamma_{\rm bg}\, P_{\rm bg}} \quad . \tag{3.6}$$

In the limit $P_{\rm Rb} \gg P_{\rm bg}$, the steady-state MOT number is independent of the ^{87}Rb vapor pressure. This number represents the maximum number of atoms that could conceivably be trapped in the MOT, given by

$$N_{\rm max} = \frac{l}{\gamma_{\rm Rb}} \quad . \tag{3.7}$$

The limit $N_{\rm max}$ is generally a function of parameters like beam size and intensity, detunings, and the B-field gradient, as well as the ^{87}Rb-^{87}Rb scattering cross-section and the natural abundance of ^{87}Rb. According to Eq.(3.6), N_0 is equal to half of $N_{\rm max}$ when $P_{\rm Rb} = (\gamma_{\rm bg}/\gamma_{\rm Rb})\, P_{\rm bg}$. This condition represents the boundary between background- and ^{87}Rb-dominated operation of the MOT.

Kurt's main contribution to our understanding of the MOT behavior begins with considering a plot of $N_0\,\Gamma$ as a function of Γ. Such a plot is shown schematically in Fig. 3.1. The values of N_0 and Γ are determined experimentally from fitting the time-dependence of the MOT fluorescence to Eq.(3.4) during a filling sequence. At first it may seem that a plot of $N_0\,\Gamma$ versus Γ just yields a line through zero with slope N_0, but it is important to remember that we are varying Γ here only by increasing $P_{\rm Rb}$ and keeping $P_{\rm bg}$ fixed. Because there is still some background pressure in the absence of Rb, the MOT number N_0 extrapolates to zero where $\Gamma = \Gamma_{\rm bg} \neq 0$. The y-intercept can therefore be used to determine the point $P_{\rm Rb} = P_{\rm bg}$ where the ^{87}Rb vapor pressure is exactly equal to the background pressure. Similarly the slope of the curve is given by

$$\begin{aligned} \frac{d}{d\,\Gamma}\,(N_0\,\Gamma) &= \left(\frac{d\,\Gamma}{d\,P_{\rm Rb}}\right)^{-1} \frac{d}{d\,P_{\rm Rb}}\,(N_0\,\Gamma) \\ &= \frac{l}{\gamma_{\rm Rb}} \quad . \end{aligned} \tag{3.8}$$

The slope therefore gives the maximum number of atoms that could be trapped by the MOT $N_{\max}$, given by Eq.(3.7). This simple plot contains some important information on the vacuum system and MOT performance.

We now extend our discussion to the two-species case. The goal is to know how many ^{87}Rb or ^{40}K atoms could be trapped in a single-species MOT with both species present in the vacuum system. When considering the behavior of one MOT, the other species can be considered a part of the background gas P_{bg}. For concreteness let's consider the loading rate and equilibrium number of atoms for a ^{40}K MOT with ^{87}Rb also present in the vacuum chamber. If there is independent control of the ^{40}K pressure P_{K}, then changing P_{K} just reproduces the results for the single-species MOT in Fig. 3.1. However if we increase P_{Rb} (keeping P_{K} constant), we expect to move out horizontally from the y-axis. The expected behavior is shown schematically in Fig. 3.2.

We now turn to some data from our experiment. In Fig. 3.3, we see the response of the single-species MOTs to the Rb dispenser. The parameters Γ and N_0 are obtained from fitting a series of MOT fills to Eq.(3.4). The ^{87}Rb data give $N_{\max}^{\mathrm{Rb}} = 5.08 \pm 0.11 \times 10^9$, where the uncertainty is from the fit only. Referring back to Fig. 3.2, we see that the positive slope for the ^{40}K data reflects the lack of independent control of P_{Rb} and P_{K} in our system. To be exact, the data here give $N_{\max}^{\mathrm{K}} = 1.44 \pm 0.03 \times 10^7$, while only firing the Rb dispenser! Although this is ~ 300 times smaller than $N_{\max}^{\mathrm{Rb}}$, it corresponds roughly to the number of ^{40}K atoms we actually do capture in the MOT. We interpret this as being due to the presence of ^{40}K atoms adsorbed onto the Rb dispenser or the nearby glass. Firing the dispenser heats the area, releasing ^{40}K back into the system.

In Fig. 3.4, we perform a similar series of measurements, this time firing the K dispenser. The first thing to note is that the value obtained for $N_{\max}^{\mathrm{K}}$ is about the same as in Fig. 3.3. This again suggests that our K dispensers are malfunctioning,

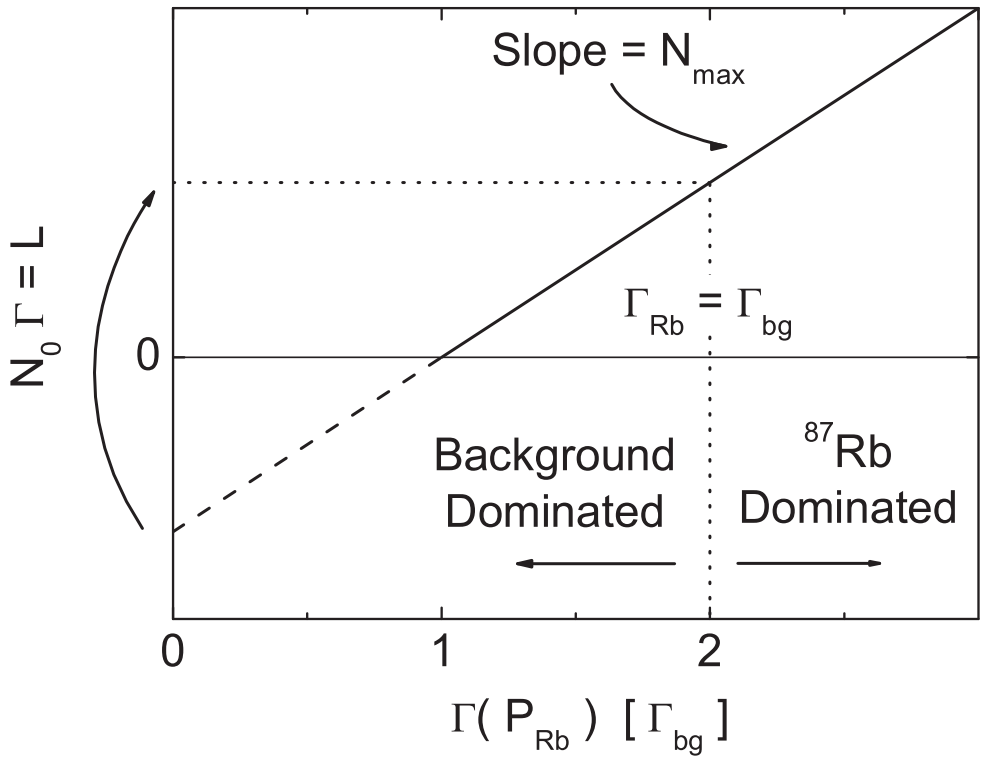

Figure 3.1: Schematic of MOT loading rate with increasing alkali-metal vapor pressure for a single-species ^{87}Rb MOT, after Ref. [33]. The solid line shows the expected behavior of $N_0\Gamma$ as a function of Γ as the ^{87}Rb vapor pressure is increased. The line extrapolates to $N_0\Gamma = 0$ when the ^{87}Rb pressure goes to zero, leaving only the vacuum background pressure $P_{\rm bg}$. The slope of the line gives the maximum number that could be trapped in the MOT $N_{\rm max}$, defined in Eq.(3.7). The boundary between background pressure dominated operation and vapor pressure dominated is defined by the condition $\Gamma_{\rm Rb} = \Gamma_{\rm bg}$, and can be determined from the y-intercept.

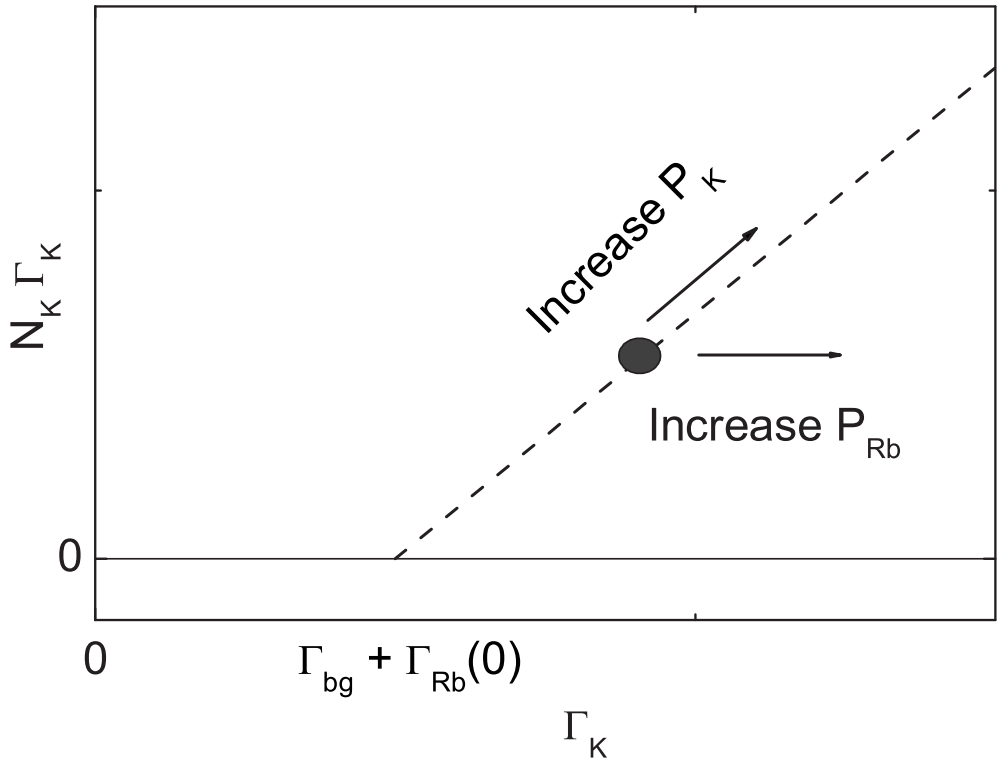

Figure 3.2: MOT loading rate with increasing ^{40}K vapor pressure for a single-species ^{40}K MOT in the presence of ^{87}Rb. The solid grey dot represents the initial condition, at time $t = 0$. If only the ^{40}K pressure P_{K} is increased, then the behavior from Fig. 3.1 is reproduced. If on the other hand P_{K} is kept fixed and P_{Rb} is increased, then the system moves horizontally on this plot. A lack of independent control over the pressures results in a line with reduced slope. This can be identified in the experiment if the y-intercept becomes positive.

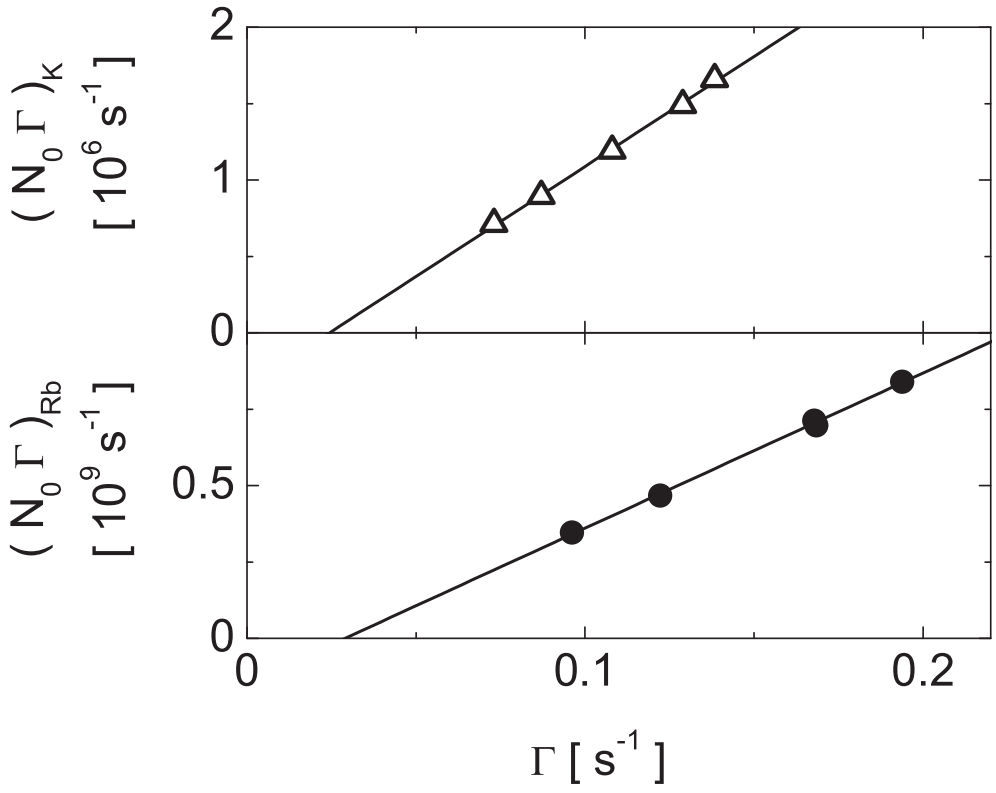

Figure 3.3: Response of ^{87}Rb and ^{40}K MOTs to the Rb alkali metal dispenser. Solid points (•) correspond to the ^{87}Rb MOT, and open triangles (△) are for ^{40}K. The lines are linear fits to the data, giving $N_{\rm max}^{\rm Rb} = 5.08 \pm 0.11 \times 10^9$ and $N_{\rm max}^{\rm K} = 1.44 \pm 0.03 \times 10^7$. The x-intercepts agree within the fit uncertainties, giving a background-limited lifetime of 39 ± 2 seconds.

since they provide no more trapped ^{40}K than the Rb dispenser. Furthermore, the value of $N_{\max}^{\mathrm{Rb}}$ obtained here is almost 80% of the previous, suggesting that the K dispenser is releasing significant amounts of ^{87}Rb into the system. Since performing the experiments described in this thesis, we have opened the vacuum system and replaced the alkali sources. Future work will include characterizing the new sources as described here and developing some workable level of independent control over the ^{87}Rb and ^{40}K vapor pressures.

3.1.2 Light-Assisted Collisions and Losses

In the previous section we considered the behavior of the single-species MOTs with respect to the atomic sources we use. In this section I would like to briefly turn our attention to the operation of the two-species MOT. In particular I will discuss our observation of light-assisted loss processes that reduce the number of atoms that can be trapped. This loss represents the first instance of cross-species interactions in our experiment, and is intimately related to the variety of ^{87}Rb -^{40}K molecular states that can contribute to cold collisions between species.

The effects of inelastic collisions between species are shown in Fig. 3.5. The number of ^{40}K atoms as a function of time is determined through fluorescence imaging in the collection cell, using a narrow-band interference filter from CVI. This filter has a transmission of ~ 0.5 at 767 nm, with an optical depth of 4 (*i.e.*, transmission of e^{-4}) outside of its 3 nm bandwidth. We take a sequence of images by strobing the camera during the MOT fill, beginning with a single-species ^{40}K MOT, and then introducing ^{87}Rb. As the ^{87}Rb MOT fills, there is a corresponding depletion of the ^{40}K MOT number to about 55% of the single-species value, due to light-assisted collisions. For these data, the single-species ^{40}K loading rate $N_0\,\Gamma = 4 \times 10^6\,\mathrm{sec}^{-1}$, and the depletion rate is about half as

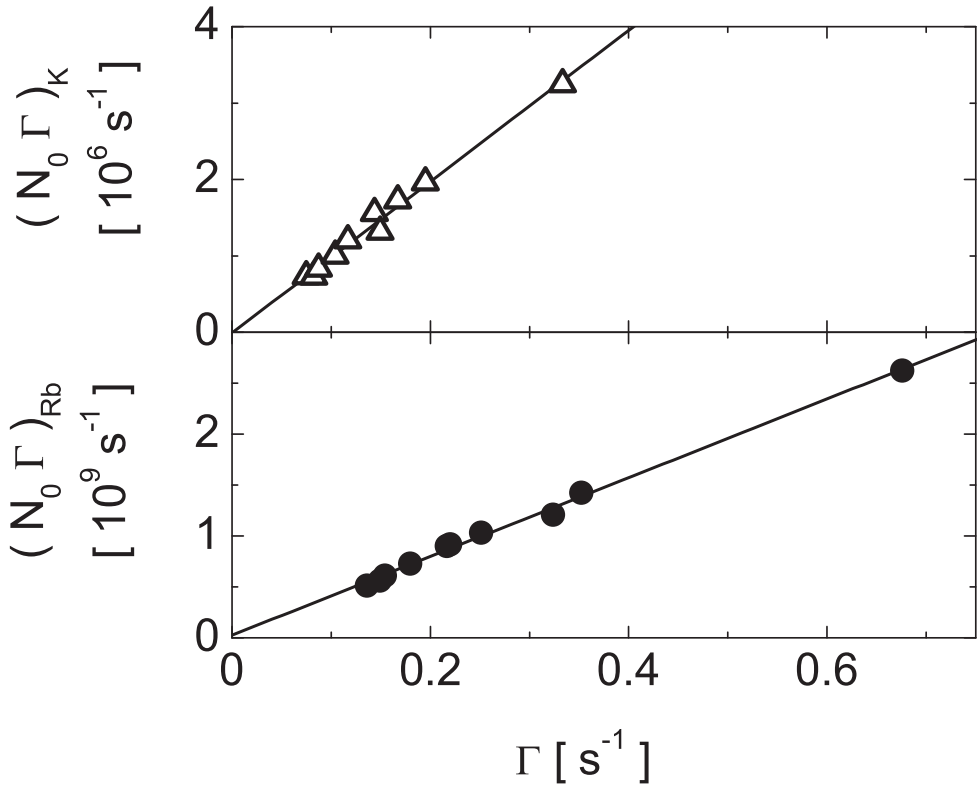

Figure 3.4: Response of ^{87}Rb and ^{40}K MOTs to the K alkali metal dispenser. Solid points (•) again correspond to the ^{87}Rb MOT, and open triangles (△) are for ^{40}K. The lines are linear fits to the data, giving $N_{\max}^{\mathrm{Rb}} = 3.87 \pm 0.09 \times 10^9$ and $N_{\max}^{\mathrm{K}} = 0.99 \pm 0.04 \times 10^7$. Both x-intercepts are consistent with zero. Rather than being evidence of zero background pressure in the chamber, this suggests that the dispenser is releasing contaminants into the system. This leads to shallower curves, giving the appearance of a reduced background pressure.

much.

Gallagher and Pritchard [36] first realized that the low temperatures obtained in MOTs made it necessary to consider slow, long-range collisions, in the sense that hyperfine interactions and spontaneous decay from excited molecular states can occur during the time the atoms interact. Although their original work considered a single-species MOT, the same basic physical principles apply for heteronuclear collisions. In fact a whole literature of two-species experimental results has been obtained by the group of V. S. Bagnato in São Paulo, Brazil, in addition to work at the Universities of Connecticut and Wisconsin. An excellent summary of both the theoretical and experimental work on this subject is given in Ref. [37].

Returning to our discussion in the previous section, we should modify Eq.(3.1) to include such loss processes in our expression for the MOT fill. Since our number of trapped ^{40}K atoms is relatively small, we can neglect ^{40}K-^{40}K losses and focus on the loss induced by ^{87}Rb atoms. Following the Brazilian group's work with a ^{85}Rb -^{39}K MOT [38], we write

$$\frac{d}{dt} N_{\rm K} \;=\; L - \Gamma\, N_{\rm K} - \beta' \int d^3x\, n_{\rm K}(\vec{x})\, n_{\rm Rb}(\vec{x}) \quad , \tag{3.9}$$

where L and Γ should be interpreted as the loading and loss rates for a single-species ^{40}K MOT, $n(\vec{x})$ is the density of each species, and β' is the loss-rate coefficient. The data in Fig. 3.5 suggest a loss-rate coefficient of

$$\beta' = 6 \pm 3 \times 10^{-11}\,{\rm cm}^3/{\rm s} \quad , \tag{3.10}$$

where the uncertainty is dominated by the uncertainty in the atom numbers. This value is similar to the ^{85}Rb -^{39}K value reported in Ref. [38] for similar beam intensities. In principle the relative importance of various competing loss mechanisms can be determined by varying the laser intensities and detunings. We decided early in the experiment, however, that the loss of half of our ^{40}K atoms from the

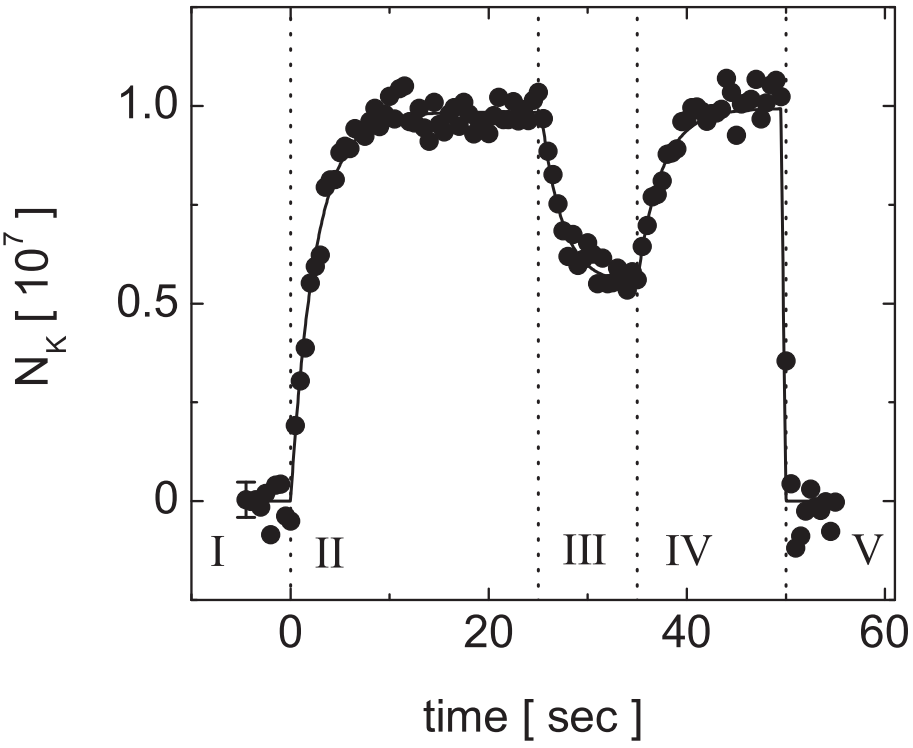

Figure 3.5: Observation of light-assisted losses of ^{40}K in the two-species MOT, as presented in Ref. [25]. The MOT number is determined from fluorescence images of the cloud, with a narrow-band filter providing an optical depth of ~ 4 for Rb light. Each point is the average of nine consecutive runs of the experiment, and the error bar is the standard error. The solid line is a fit to exponential fill or decay in each region (II-IV). In region I ($t \leq 0$) the ^{87}Rb light is locked off-resonance, and the B-field is turned off, in order to allow a calibration of the light levels for the fluorescence; in region II ($0 \leq t < 25$ sec) the ^{87}Rb light remains off-resonance and the B-field is turned on, allowing a fill of the single-species ^{40}K MOT; in region III ($25 \leq t < 35$ sec) the ^{87}Rb MOT is allowed to fill, and the subsequent collisional losses deplete the number of ^{40}K atoms; region IV ($35 \leq t < 50$ sec) sees a return to the single-species MOT, and in region V ($t \geq 50$ sec) the B-field is off and the ^{87}Rb light is again off-resonance.

two-species MOT is acceptable. As we will see later in this chapter, sympathetic cooling places less stringent requirements on the number of ^{40}K atoms we load into the magnetic trap than if the atoms were being evaporated directly.

3.2 Compressing, Cooling, Pumping, and Loading

After collection and cooling in the two-species MOT, atoms are loaded into a strong quadrupole magnetic trap, generated by a coil pair mounted on a moving translation stage, as described in Section 2.3. In this section I'll describe the transfer into the quadrupole trap, which involves compressing the ^{87}Rb cloud, cooling the ^{40}K cloud, and optically pumping both clouds. With atoms loaded into the quadrupole transfer trap we will then be in a position to begin sympathetically cooling our fermions towards quantum degeneracy.

The first challenge in the transfer sequence is to load a spatially large ^{87}Rb MOT into the quadrupole transport trap ("QT trap"). If the cloud is too large the atoms will pick up excess potential energy in the tightly confining QT trap, and that energy will result in an increased temperature after rethermalization. The ^{87}Rb MOT is large due to the strong radiation trapping [39]. Ways to address this problem include transiently increasing the magnetic field gradient, adjusting the intensity and detuning of the trapping and repumping light, or any combination of the above [40]. Another solution is the so-called dark-spot MOT [41], where the repumping light is blocked from the center of the cloud so that atoms trapped there stop absorbing and emitting photons. In our case we use what may be the simplest possible compression scheme — we reduce the repumping light intensity for 50 ms before releasing from the MOT. The time scale, to which the compression is not very sensitive, is long enough to let the atoms go "dark" to the trap light and short enough to avoid any significant losses from the MOT. We refer to this compressed MOT stage as the CMOT, and I stress that

we perform the CMOT only for the ^{87}Rb atoms, by reducing the power of the ^{87}Rb repump light injecting the tapered amplifier.

The ^{40}K MOT, which has $\sim$ 100 times fewer atoms, is already roughly the size of the ^{87}Rb CMOT. We can still try to reduce the temperature of the ^{40}K cloud in the QT trap by optically cooling the atoms before loading. If we quickly jump the ^{40}K trap light frequency towards resonance before releasing from the MOT, we observe a pronounced ($\sim 3\times$) increase in the number of ^{40}K atoms. We show in Fig. 3.6 an example of the dependence of the ^{40}K number at the end of the sympathetic cooling cycle on the detuning of the cooling light.[1] Since the MOT number is roughly unchanged by the jump (and the steady-state MOT number is *reduced* at the jump frequency), we attribute this increase in number to begin due to improved Doppler cooling of the ^{40}K atoms. This reduces losses associated with adsorption of atoms onto the walls of the transfer tube and science cell. As with the CMOT, the cooling is not very sensitive to the duration of the cooling stage as long as it's greater than $\sim$ 10 ms (we use 50 ms, as with the CMOT).

With our ^{87}Rb atoms compressed, and our ^{40}K atoms cooled, there is still some optical pumping to be done before loading into the QT trap. Our goal is to load the ^{87}Rb $|\, F = 2, m_F = 2 \,\rangle$ and ^{40}K $|\, 9/2, 9/2 \,\rangle$ states into the Ioffe-Pritchard trap for evaporative cooling. These states have the strongest confinement in the magnetic trap, and their combination is immune to spin-exchange collisions. The CMOT, by design, puts ^{87}Rb atoms into some uncontrolled mixture of the $F = 1$ ground states; it is not known what states the ^{40}K atoms populate after the cooling stage. To optically pump the atoms, we release them from the CMOT/cooling stage and apply a few-Gauss bias field to provide a quantization axis. We then

[1] Due to the relatively low atom numbers, our ^{40}K clouds are too dilute to image with absorption imaging until nearly the end of the evaporation sequence.

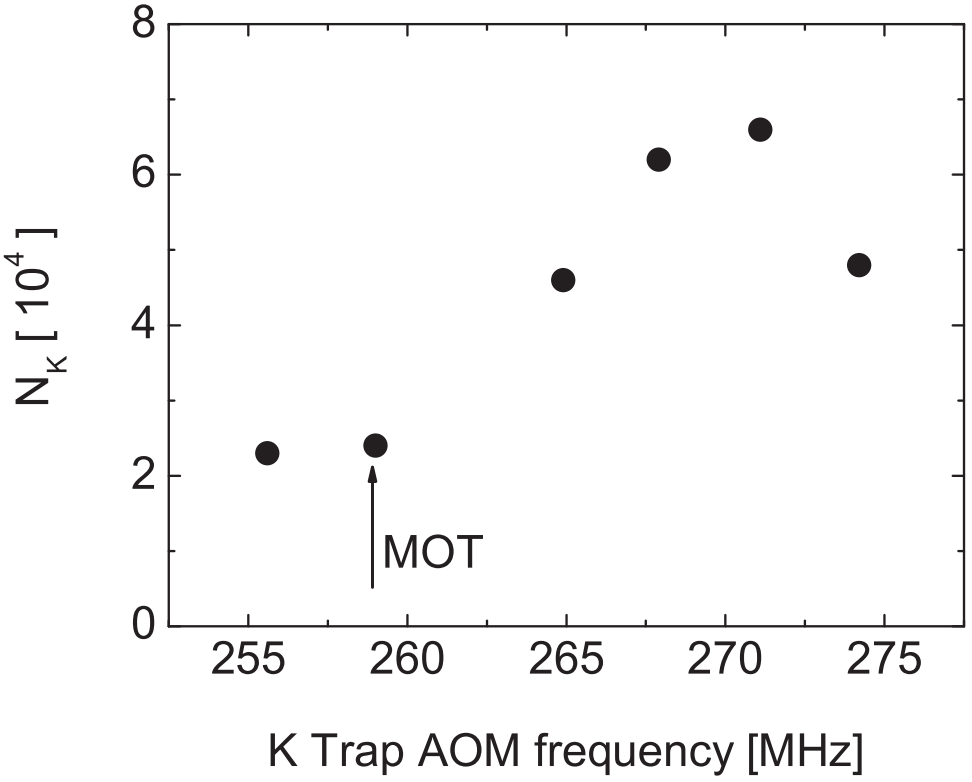

Figure 3.6: Effect of Doppler cooling of ^{40}K atoms before loading the QT trap. The number of ^{40}K atoms at the end of the evaporation sequence is shown as a function of the trap AOM frequency during the cooling stage. The AOM shifts the frequency towards the blue in a single pass. The arrow at 259 MHz indicates the MOT detuning. The resonance frequency (at zero field) corresponds to 278 MHz.

apply, within 1 ms, σ^+-polarized light resonant on the $F = 2 \rightarrow F' = 2$ ($9/2 \rightarrow 9/2$) ^{87}Rb (^{40}K) transition, which we call Zeemann pumping (ZP) light. Repump (RP) light is applied during the ZP pulse to prevent population of the other states.

Monte Carlo simulations of optical pumping under ideal conditions show that ^{87}Rb atoms in any state could on average be transferred to the $|\,2,2\,\rangle$ state with less than 3 ZP and 4 RP photons. Similar simulations for ^{40}K show that 6 photons of each type would be sufficient. For our 1 ms pumping duration, Eq.(2.11) tells us that seven photons per atom of either species can be scattered with an intensity of only $\sim 4\times10^{-4} I_{\rm sat} < 1\ \mu$W/cm^2. For comparison we typically use a roughly 1 cm^2 beam with a few tens of μW (~ 1 mW) of ZP (RP) power. This suggests that our $\sim 80\%$ transfer of atoms from the MOT to the QT trap is limited by the size of the optical pumping beams (relative to the cloud sizes), the large optical depths of the clouds, and imperfections in the quantization field and light polarization.

3.3 Sympathetic Cooling

In this Section I will discuss the final stage in the production of a quantum degenerate ^{87}Rb -^{40}K mixture by means of forced rf evaporation of ^{87}Rb atoms. I'll begin with how we actually perform the cooling in the experiment, and why we are able to use fairly standard techniques even in the presence of trapped ^{40}K atoms. I'll then give a summary of some of the thermodynamics of atoms in the Ioffe-Pritchard trap. This discussion will cover some results for particles in the Maxwell–Boltzmann regime which we will use throughout this thesis. Finally, I'll point out an important fact which has not, to the best of my knowledge, been discussed in the literature. We'll see that one consequence of the negative inter-species scattering length that we now know exists between ^{87}Rb and ^{40}K is the deep suppression of elastic scattering at energies relevant to the initial stages

of our evaporation. This may have important ramifications for the design and construction of new ^{87}Rb -^{40}K experiments.

3.3.1 Experiment: Evaporation "Trajectories"

To evaporatively cool the ^{87}Rb gas, we selectively remove high-energy atoms from the cloud, thereby lowering the mean energy per particle. Subsequent collisions rethermalize the gas to a lower temperature, and in the presence of ^{87}Rb -^{40}K collisions the ^{40}K atoms are cooled as well. The term "selectively" must be taken here to mean (i) selecting specifically high-energy atoms, as well as (ii) evaporating only ^{87}Rb atoms, and leaving high-energy ^{40}K atoms alone.

The criterion (i) is satisfied by exploiting resonant spin-flipping transitions to anti-trapped states in the spatially-dependent magnetic field of the Ioffe-Pritchard (IP) trap. Atoms with higher energies are more likely to reach locations of higher potential (proportional to $|\vec{B}_{\rm IP}(\vec{x})|$), and can be selectively removed with resonant spin-flips at the higher field.

Due to the relatively large nuclear spin for ^{40}K ($I = 4$) there are more total spin states than for ^{87}Rb ($I = 3/2$). This is shown schematically in Fig. 3.7 for the experimentally relevant $F = 2$ states of ^{87}Rb and $F = 9/2$ states of ^{40}K. We can now see a way to satisfy criterion (ii) during the cooling. Since the energy splittings are different for ^{87}Rb and ^{40}K (the ^{40}K splittings are 4/9 the size of the ^{87}Rb splittings), the ^{87}Rb $|\, F = 2, m_F = 2 \,\rangle$ and ^{40}K $|\, 9/2, 9/2 \,\rangle$ states will satisfy the resonance condition for spin-flips at very different fields. Equivalently, for a given spin-flip frequency a ^{40}K atom must have 9/4 the energy of a ^{87}Rb atom in order to be transferred out of the trap.

Our primary diagnostic in evaluating the performance of the evaporation is

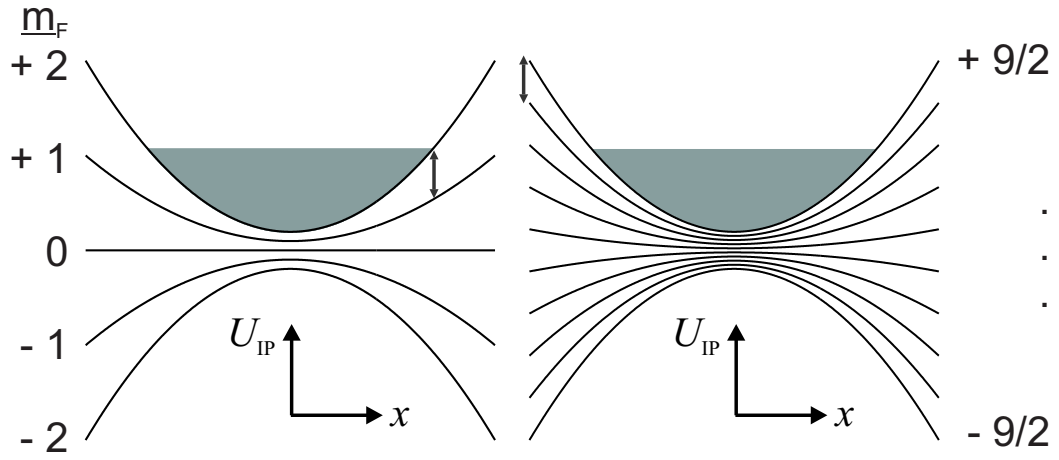

Figure 3.7: Zeemann sublevels of ^{87}Rb (left) and ^{40}K (right) in a harmonic magnetic potential. Clouds in the stretched states ($|F = 2, m_F = 2\rangle$ for ^{87}Rb and $|9/2, 9/2\rangle$ for ^{40}K) are shown schematically as the dark solid regions, which have the same energies for Boltzmann distributions in thermal equilibrium. The arrows ($\updownarrow$) designate the rf photon, which drives a Zeemann transition in ^{87}Rb, and leaves the ^{40}K cloud unaffected.

the evaporation efficiency parameter α defined by [42]

$$\alpha_{\rm ev} = \frac{d\,\ln T}{d\,\ln N} \quad , \tag{3.11}$$

where N is the number of ^{87}Rb atoms, T is the temperature of the gas in Kelvin, and we assume the distribution is never far from equilibrium. An example of the dependence of N on T is shown for ^{87}Rb evaporation in the absence of ^{40}K atoms in Fig. 3.8.

The goal in the experiment is to achieve runaway evaporation, where the mean rate of rethermalizing elastic collisions rapidly increases as the temperature decreases. In other words,

$$\frac{d\,\ln \Gamma_{\rm coll}}{d\,\ln T} < 0 \quad , \tag{3.12}$$

where $\Gamma_{\rm coll}$ is the mean rate of elastic collisions in Hz. We will see later that $\Gamma_{\rm coll}$ is proportional to N/T in a harmonic trap. Then using $T \propto N^{\alpha_{\rm ev}}$ we have the critical value of $\alpha_{\rm evap}$ for runaway evaporation

$$\alpha_{\rm crit} = 1 \quad . \tag{3.13}$$

Note that we have neglected losses due to collisions with background atoms and inelastic density-dependent losses, which make $\alpha_{\rm crit}$ slightly greater than 1 in the experiment. Our good evaporation conditions correspond to $\alpha_{\rm ev} \sim 1.2$ to 1.4.

A full diagnostic of the two-species evaporation is not available to us due to the low optical density of ^{40}K atoms during the early stages of evaporation. The highest temperature ^{40}K cloud we have imaged out of the IP trap is only $\sim 10\ \mu$K, which is well over an order of magnitude colder than our initial ^{87}Rb load. Looking at the ^{87}Rb cloud over the whole range of evaporation we can see no significant change in the evaporation with ^{40}K atoms present until at or near the Bose-Einstein condensate phase transition. This is consistent with the sympathetic

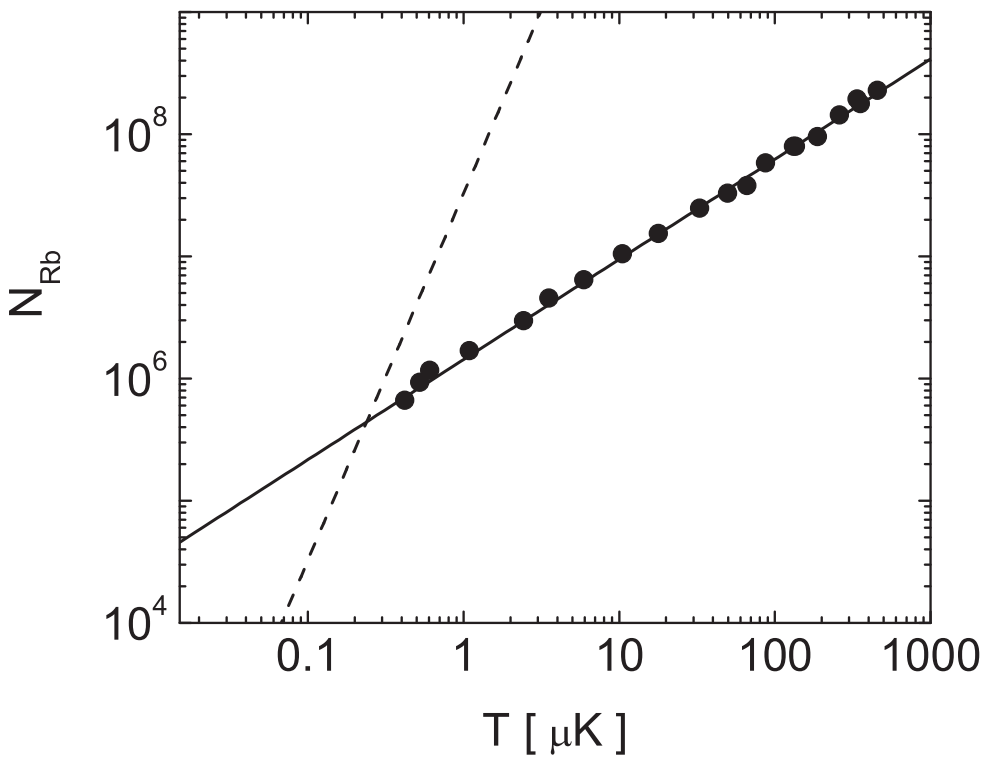

Figure 3.8: Single-species ^{87}Rb evaporation trajectory. The solid points show the number of atoms at each temperature during the evaporation, and the solid line is a fit to Eq.(3.11), giving $\alpha_{\rm ev} = 1.218 \pm 0.013$ (more recent results give an improved $\alpha_{\rm ev} = 1.35 \pm 0.06$). The dashed line is the expected BEC transition temperature for an ideal gas (data with BEC are not shown). The ^{87}Rb trapping frequencies were $\omega_\rho = 2\pi \times 112$ Hz and $\omega_z = 2\pi \times 27$ Hz.

cooling model in Ref. [43], considering our relatively low ^{40}K number. Near the BEC transition there is some enhanced loss of both species, probably due to ordinary 2- and 3-body inelastic losses accompanying the sharp increase in ^{87}Rb density. An example of the ^{87}Rb and ^{40}K numbers during the last stage of evaporation is shown in Fig. 3.9. The apparent delay between the onset of the ^{40}K loss and the formation of the condensate is believed to be due to the 100-200 ms hold before the image, allowing a small condensate to form at relatively high density and then "melt" before imaging. This would be consistent with the calculated BEC transition temperature for 3×10^6 atoms of $T_c \simeq 500$ nK, as shown in the figure. By assuming either purely 2- or 3-body losses we can estimate upper limits for the corresponding inelastic rate constants. Using the $1/e$ decay time for ^{40}K of 2.4 ± 0.5 s from the data we obtain $K_{\mathrm{RbK}} = 4 \times 10^{-15}\,\mathrm{cm}^3/\mathrm{s}$ and $K_{\mathrm{RbRbK}} = 3 \times 10^{-29}\,\mathrm{cm}^6/\mathrm{s}$. These numbers are in rough agreement with other measurements we have performed of ^{40}K loss rates.[2]

3.3.2 Thermodynamics Intermezzo — IP Trap

In this subsection I will summarize some basic thermodynamic results for non-degenerate atoms in the Ioffe-Pritchard (IP) trap. I will focus on the collision rate, which is important to our rethermalization measurements described in the next chapter. We will also consider the phase-space-density, which characterizes the importance of quantum statistical effects on the thermodynamics of the gases.

For Maxwell-Boltzmann (MB) statistics, the statistical distribution function $f_{\mathrm{MB}}(\vec{x}, \vec{p})$ is proportional to $\exp[-(U_{\mathrm{IP}} + p^2/2m)/k_B T]$, where m is the mass and p the momentum. For simplicity we will work in the harmonic approximation for the potential $U_{\mathrm{IP}}(\vec{x})$. Recall that this approximation becomes better as the

[2] During two separate measurements of ^{40}K losses in the presence of condensates, we obtained upper limits of $K_{\mathrm{RbK}} = 2$ and $3 \times 10^{-15}\,\mathrm{cm}^3/\mathrm{s}$ and $K_{\mathrm{RbRbK}} = 1 \times 10^{-29}\,\mathrm{cm}^6/\mathrm{s}$.

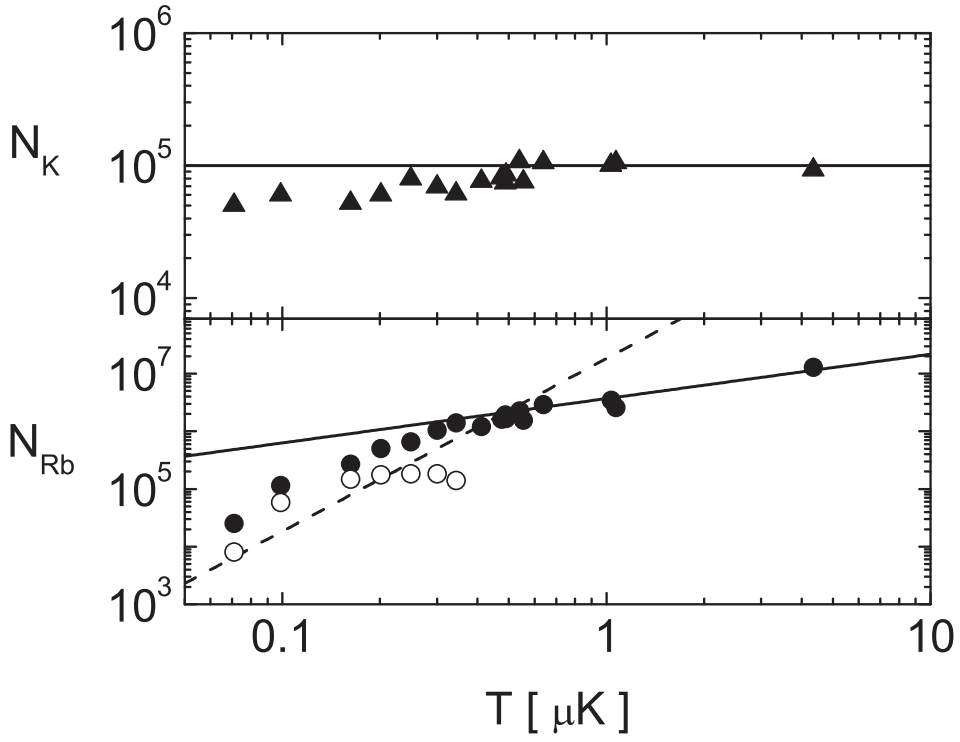

Figure 3.9: Inelastic losses at the end of evaporation. The number of ^{40}K atoms is shown above, and the number of ^{87}Rb atoms below, as a function of temperature. A pair of ^{87}Rb and ^{40}K images were taken in each experimental run using the kinetics mode of the CCD camera. For the ^{87}Rb data the closed points give the total number of atoms, and the open points give the number of atoms in the condensate. The solid line above corresponds to 10^5 atoms and below to $\alpha_{\rm ev} = 1.3$, to provide a sense of scale. The ^{87}Rb trapping frequencies were $\omega_\rho = 2\pi \times 155$ Hz and $\omega_z = 2\pi \times 25$ Hz. The dashed curve shows the expected BEC phase transition. Viewed as a function of time, the ^{40}K loss at the end has a $1/e$ time constant of 2.4 ± 0.5 sec.

clouds become colder. The peak density is fixed by the normalization condition $\int d^3x\, n(\vec{x}) = N$ giving

$$n(\vec{x}) = N \left(\frac{\kappa}{2\pi\, k_B T}\right)^{3/2} \exp\left(-\frac{\kappa_\rho^2\, \rho^2 + \kappa_z^2\, z^2}{2\, k_B T}\right) \quad , \tag{3.14}$$

where $\kappa_\rho = m\,\omega_\rho^2$ and $\kappa_z = m\,\omega_z^2$ are the radial and axial trap spring constants (which are the same for ^{87}Rb and ^{40}K atoms in the stretched states), $\kappa = (\kappa_\rho^2\,\kappa_z)^{1/3}$ is the geometric mean spring constant, and $\rho = (x^2 + y^2)^{1/2}$ as before. Using the thermal de Broglie wavelength $\Lambda_T = (2\pi\hbar^2/m\,k_B T)^{1/2}$, this immediately gives the peak phase-space density

$$\begin{aligned} \mathcal{D} &= n(0)\,\Lambda_T \\ &= N \left(\frac{\hbar\,\omega}{k_B T}\right)^3 \quad , \end{aligned} \tag{3.15}$$

where $\omega = (\omega_\rho^2\,\omega_z)^{1/3}$ is the geometric mean trap frequency. The phase-space density (PSD) relates the spatial extent of a quantum mechanical wave-packet in the gas to the distance between atoms. The onset of quantum degeneracy occurs when $\mathcal{D} \sim 1$.

One important quantity for both evaporative and sympathetic cooling is the mean rate of elastic collisions per particle. To calculate collision rates, we need to consider two systems of particles, labeled i and j; we can take $i = j$ to calculate single-species averages (for example, the mean rate of ^{87}Rb-^{87}Rb collisions). The mean rate per 1-type atom of collisions with 2-type atoms is defined by

$$\begin{aligned} \Gamma_{12} &= \langle\, n_2\, \sigma_{12}\, v_{12}\,\rangle_1 \\ &= \langle\, n_2\,\rangle_1\, \sigma_{12}\, \langle\, v_{12}\,\rangle_1 \quad , \end{aligned} \tag{3.16}$$

where n_2 is the density of type-2 atoms, σ_{12} is the elastic collision cross section,[3] and $v_{12} = |\vec{v}_1 - \vec{v}_2|$ is the relative collision speed. The subscript on the brackets

[3] Note that for distinguishable particles the s-wave cross section is related to the scattering length a by $\sigma = 4\pi\, a^2$, and for identical bosons we have $\sigma = 8\pi\, a^2$. The cross section between identical fermions is zero according to the Pauli exclusion principle.

reflects the fact that we are averaging n_2 and v_{12} over the distribution of 1-type atoms. To separate σ_{12} and the averages $\langle\, n_2 \,\rangle_1$ and $\langle\, v_{12} \,\rangle_1$ we have assumed isotropic, energy-independent collisions, appropriate in the limit of s-wave scattering. We will return to the question of how good an assumption this is for the ^{87}Rb -^{40}K system in the next section.

The density overlap $\langle\, n_2 \,\rangle_1$ is defined by

$$\langle\, n_2 \,\rangle_1 \;=\; \frac{1}{N_1} \int d^3x_1\, n_1(\vec{x}_1)\, n_2(\vec{x}_1) \quad .$$

According to Eq. (3.14), the densities $n_1(\vec{x})$ and $n_2(\vec{x})$ differ only by the factor of $N_{i,j}$ out front. Then for Gaussian density profiles we get

$$\langle\, n_2 \,\rangle_1 = N_2 \left(\frac{\kappa}{4\pi\, k_B T} \right)^{3/2} \quad . \tag{3.17}$$

To get $\langle\, v_{12} \,\rangle$ we transform to center-of-mass (CM) and relative coordinates

$$\begin{aligned} \vec{V}_{\rm CM} &= \frac{m_1\, \vec{v}_1 + m_2\, \vec{v}_2}{m_1 + m_2} \\ \vec{v}_{\rm rel} &= \vec{v}_1 - \vec{v}_2 \quad . \end{aligned} \tag{3.18}$$

This allows us to rewrite the total kinetic energy

$$\frac{p_1^2}{2\, m_1} + \frac{p_2^2}{2\, m_2} \;=\; \frac{P_{\rm CM}^2}{2\, M} + \frac{p_{\rm rel}^2}{2\, \mu} \quad ,$$

where $P_{\rm CM} = M\, V_{\rm CM}$, $p_{\rm rel} = \mu\, v_{\rm rel}$, and $M = m_1 + m_2$ is the total mass, and $\mu = m_1\, m_2/(m_1 + m_2)$ the reduced mass, of the colliding atoms. Now v_{12} is just another name for $v_{\rm rel}$. Then the average collision speed between 1- and 2-type particles is

$$\begin{aligned} \langle\, v_{12} \,\rangle &= \left(\frac{\mu}{2\pi\, k_B T} \right)^{3/2} \int_0^\infty 4\pi\, v_{\rm rel}^2\, dv_{\rm rel}\, \exp\left(-\frac{1}{2}\, \frac{\mu\, v_{\rm rel}^2}{k_B T} \right)\, v_{\rm rel} \\ &= \sqrt{\frac{8\, k_B T}{\pi\, \mu}} \quad . \end{aligned} \tag{3.19}$$

Combining Eqs.(3.16),(3.17), and (3.19), we finally have

$$\Gamma_{12} \;=\; \frac{\sigma_{12}}{2^{3/2}\pi^2}\,\frac{\kappa^{3/2}}{\sqrt{\mu}}\,\frac{N_2}{k_B T} \quad . \tag{3.20}$$

There are two things I'd like to point out about this result. First note that the collision rate goes like N/T. This fact was used in our previous discussion of the evaporation efficiency. In contrast a uniform (*i.e.*, untrapped) sample has a collision rate proportional $T^{1/2}$, so that runaway evaporation can not occur.

Second let me discuss the effect of gravity, which we have so far neglected. We used $n_1(\vec{x})/N_1 = n_2(\vec{x})/N_2$ in our derivation of the collision rate, which is not exactly true under the influence of gravity. Although to lowest order the shapes and sizes of the clouds are not affected, the equilibrium vertical position becomes $y_0 = -g/\omega_\rho^2$ (measured from the trap center), where g is the gravitational acceleration. This leads to different y_0 for ^{87}Rb and ^{40}K atoms in the trap. For Gaussian density profiles this results in a reduction in overlap between species given by

$$\langle\, n_2 \,\rangle_1 \;=\; f_{\rm sag}\,\langle\, n_2 \,\rangle_2 \quad , \tag{3.21}$$

where

$$f_{\rm sag} \;=\; \exp\left[-\frac{1}{4}\,(m_1 - m_2)^2\,\frac{g^2}{\kappa_\rho\, k_B T}\right] \quad . \tag{3.22}$$

For a ^{87}Rb -^{40}K mixture with a ^{87}Rb radial trap frequency of $\omega_\rho = 2\pi \times 160$ Hz, $f_{\rm sag} = 1/e$ at a temperature of 73 nK. For comparison if the trap frequency is reduced by half, then $f_{\rm sag} = 1/e$ at 290 nK. The effect of gravity on the collision rate at 1 μK for varying trap frequency is shown in Fig. 3.10. The differential sag in the trap sets an additional design constraint for two-species experiments.

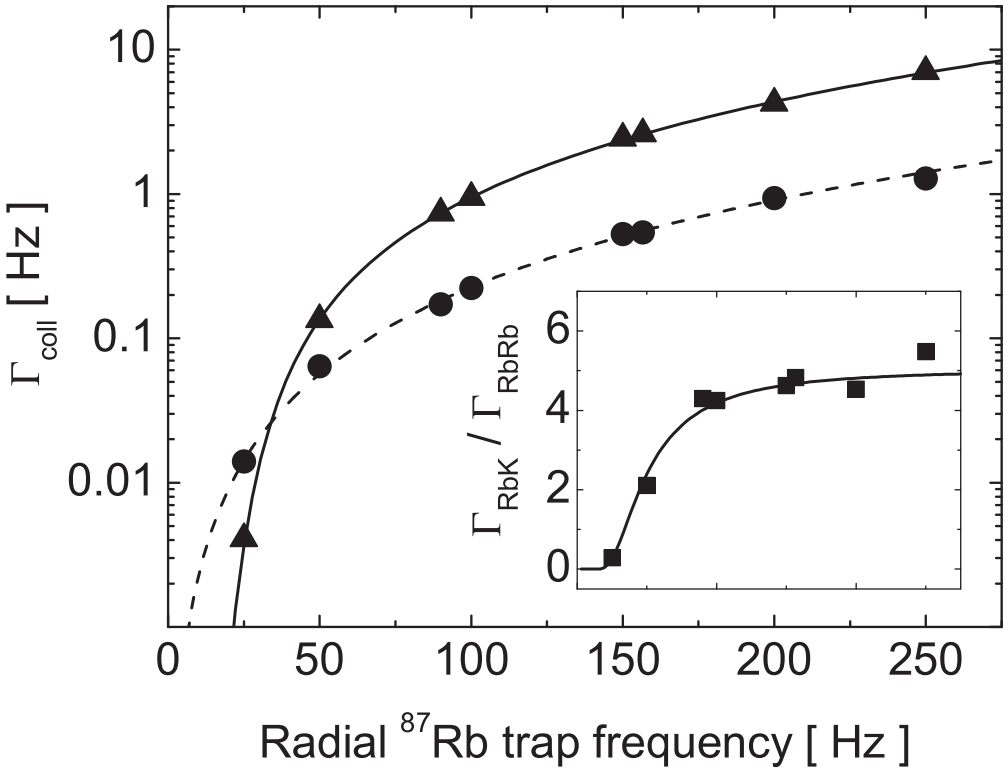

Figure 3.10: Effect of gravity on the collision rate. Shown is the mean collision rate per particle, with triangles (▲) corresponding to ^{87}Rb-^{40}K collisions, and circles (●) to ^{87}Rb-^{87}Rb collisions. Points are the results of Monte Carlo simulations, and the solid and dashed curves are the behavior described by Eqs.(3.20) and (3.22). The inset shows the ratio of collision rates. Simulations assumed 10^4 atoms of each species at $1\,\mu$K, with a ratio of cross sections $(\sigma_{\mathrm{RbK}}/\sigma_{\mathrm{RbRb}}) = 4$, and a ^{87}Rb axial trap frequency $\omega_z = 2\pi \times 25$ Hz. Note that in our experiments we typically have 10^6 ^{87}Rb atoms at $1\,\mu$K, so that the corresponding experimental collision rates are 100 times higher.

3.3.3 Theory: Energy-Dependent Collision Cross-Section

In the last section we calculated the collision rate, assuming an s-wave cross-section with no energy dependence. Here I would like to examine the real energy-dependence of the ^{87}Rb -^{40}K collision cross-section, and in the process we'll see something I haven't seen discussed in the literature — namely that the ^{87}Rb -^{40}K s-wave cross-section has a zero at a collision energy of $\sim 630\,\mu$K. Chris Ticknor and John Bohn have calculated the ^{87}Rb -^{40}K s- and p-wave cross-sections for varying energy using scattering potentials derived from our analysis of the Feshbach resonances described in Ref. [44]. The results of their calculations are shown in Fig. 3.11. The fact that the total collision cross-section between species does not reach its full zero-temperature value until $T \lesssim 10\,\mu$K could have important consequences for the design of new ^{87}Rb -^{40}K experiments.

There are two important features of the collision cross-sections apparent in Fig. 3.11. First is the appearance of the zero in the s-wave cross-section mentioned above. The suppression of s-wave collisions at relatively low energies is a general property of systems with large, negative scattering lengths. The physical origins underlying this effect, known as the Ramsauer-Townsend effect [1], are discussed in the context of ^{85}Rb -^{85}Rb collisions in Ref. [47]. We additionally see in the figure that the total cross-section is supported in the vicinity of the s-wave zero by the presence of p-wave collisions. This is a fortunate property of the ^{87}Rb -^{40}K system that is not at all guaranteed. At low enough temperatures, the p-wave threshold falls off like T^2, which can be understood semiclassically as a consequence of the colliding atoms not having enough energy to overcome the centrifugal barrier in the scattering potential.[4] The ^{87}Rb -^{40}K mixture benefits from having the p-wave threshold at lower energies than the zero in the s-wave cross section.

[4] This behavior, known as the Wigner threshold law, was observed experimentally for ^{40}K-^{40}K collisions in Ref. [46]. The p-wave threshold for ^{40}K-^{40}K collisions occurs at $T \simeq 190\,\mu$K.

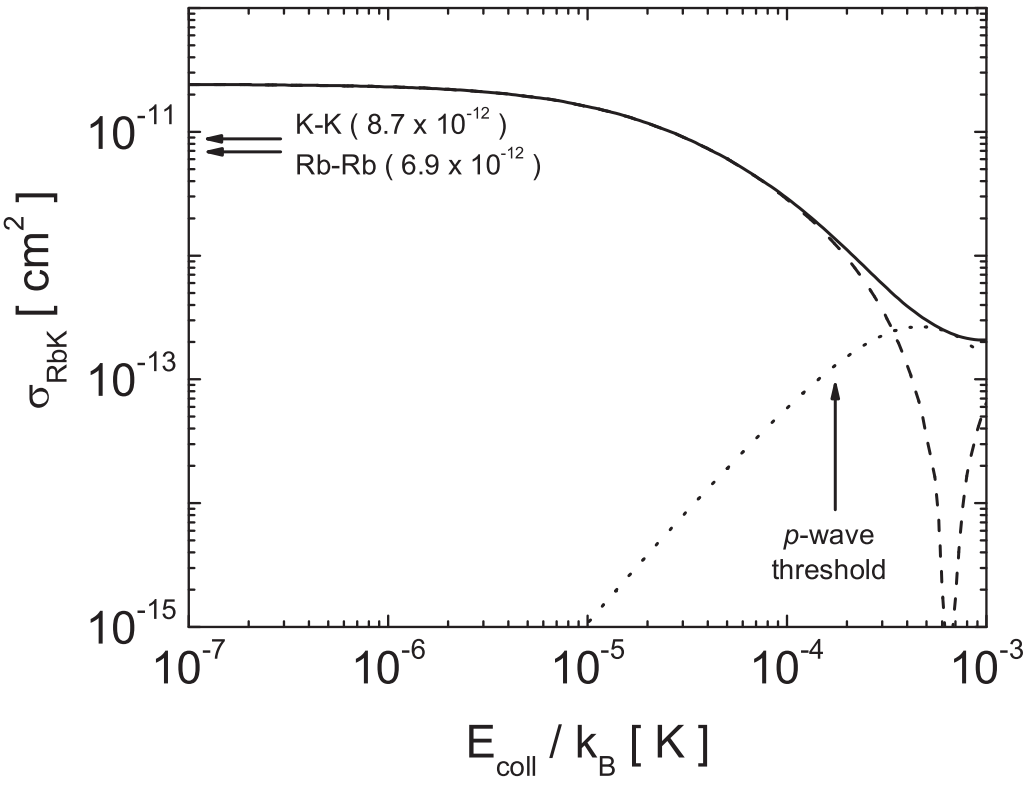

Figure 3.11: Theoretical energy dependence of the ^{87}Rb -^{40}K elastic collision cross-section. The dashed (dotted) curve is the s-wave (p-wave) cross-section as a function of collision energy (but *not* thermally averaged), and the solid curve is the total cross-section. Calculations were performed by Chris Ticknor and John Bohn and assume a triplet scattering length $|a_{\mathrm{RbK}}| = 280\ a_0$ [44]. For reference we have marked the $T = 0$ limits for $|\, F = 2, m_F = 2 \,\rangle_{\mathrm{Rb}} \otimes |\, 2, 2 \,\rangle_{\mathrm{Rb}}$ and $|\, 9/2, 9/2 \,\rangle_{\mathrm{K}} \otimes |\, 9/2, 7/2 \,\rangle_{\mathrm{K}}$ collisions, from Refs. [45] and [46], respectively. (The symbol $\otimes$ here denotes the direct or Cartesian product [1]).

To estimate the ^{87}Rb -^{40}K p-wave threshold we consider the long-range form of the collision potential,

$$U_{\mathrm{RbK}}(R) \simeq \frac{\hbar^2\, l(l+1)}{2\,\mu\, R^2} - \frac{C_6}{R^6} \quad , \tag{3.23}$$

where R is the internuclear separation, $l = 1$ is the angular momentum quantum number for p-wave collisions, $\mu = m_{\mathrm{Rb}}\, m_{\mathrm{K}}/(m_{\mathrm{Rb}} + m_{\mathrm{K}})$ is the reduced mass, and $C_6 = 4274\,\mathrm{a.u.}$ is the van der Waals coefficient [48]. Setting the collision energy E_{coll} equal to the maximum of U_{RbK}, and using $E_{\mathrm{coll}} = 3k_BT/2$ gives a p-wave threshold of $\sim 110\ \mu$K (or 170 μK collision energy). This energy is marked in Fig. 3.11, and is in good agreement with the behavior described by the full coupled-channel calculation. The fact that the p-wave threshold is at lower energy than the s-wave zero means that collisions between species are never fully suppressed. Note, however, that the cross-section in the vicinity of the s-wave zero is only about 1% of the zero temperature value.

Finally we note that the T^2 dependence of the p-wave cross-section at low temperatures is just a specific example of a more general threshold behavior. Specifically the cross-section corresponding to the l^{th} partial wave obeys $\sigma_l \propto T^{2\,l}$ at low energies [1]. For example the calculated threshold temperature for ^{87}Rb -^{40}K d-wave collisions is $577\,\mu$K, and below this temperature the d-wave cross-section will fall off like T^4. This means that the total cross-section in the vicinity of the s-wave zero may be larger than what is shown in Fig. 3.11.

3.4 Onset of Quantum Degeneracy

We now turn our attention to the onset of quantum degeneracy in the experiment. The quantum statistics of bosons and fermions will each be considered in turn. We will see how quantum degeneracy is manifest in the experiment, and set the ground work for our discussions of interactions between species in the next

chapter. More detailed derivations of these results can be found in Refs. [49, 21] for the bosons and Refs. [50, 13] for the fermions.

3.4.1 Bosons

For Bose-Einstein distributions the density profile corresponding to Eq.(3.14) is modified by quantum statistics to give

$$n_{\rm BE}(\vec{x}) \;=\; g_{3/2}(\exp[(\mu - U_{\rm IP})/k_B T])\,\Lambda_T^{-3} \quad , \tag{3.24}$$

where $g_\nu(\alpha) = \sum_{i=1}^{\infty} \alpha^i/i^\nu$ is the Bose function (sometimes called the polylogarithm and denoted $\mathrm{Li}_\nu(\alpha)$), $\Lambda_T = (2\pi\hbar^2/m\,k_B T)^{1/2}$ is the thermal de Broglie wavelength, and we have suppressed the spatial dependence of $U_{\rm IP}(\vec{x})$ for simplicity. Note that for $\alpha \ll 1$ the Bose function obeys $g_{3/2}(\alpha) \simeq \alpha$, so that a Gaussian distribution is recovered in the classical limit, or in the "wings" of the gas, where higher-energy atoms are more likely to be found. In contrast the profile of the cloud is more sharply peaked at the center than the classical Gaussian profile. This reflects the proclivity of bosons in a single spin-state to aggregate into the lower-energy states of the trapping potential.

In the thermodynamic limit an ideal gas of harmonically trapped bosons undergoes a phase transition to BEC at a critical temperature

$$k_B T_c^{(0)} \;=\; \hbar\,\omega \left[\frac{N}{\zeta(3)}\right]^{1/3} \quad , \tag{3.25}$$

where $\zeta(3) = 1.20206...$ is the Riemann zeta function. At this point a macroscopic number of atoms N_0 begins to occupy the ground state of the system. For fitting images of expanded clouds, we consider the total density of bosons to be the sum of a "thermal" component and a condensed component [21].

The number of atoms in the condensate is related to the total number of

atoms $N_{\rm tot}$ by

$$\frac{N_0}{N_{\rm tot}} \;=\; 1 - \left[\frac{T}{T_c^{(0)}}\right]^3 \quad , \tag{3.26}$$

showing a steep initial population of the condensate after cooling below $T_c^{(0)}$. Results from the experiment are shown in Fig. 3.12.

Corrections to the calculated condensate fraction due to the finite number of atoms and repulsive boson-boson interactions are discussed in Refs. [49, 51]. The main result of these corrections is a softening of the transition and a shift towards lower transition temperature, as seen in the data. When including these effects the agreement between theory and experiment is excellent. Although these data were taken in the presence of $\sim 10^4$ ^{40}K atoms, the fermions are expected to have a negligible effect on the bosons here. As we'll discuss in more detail later, this is due to the fact that the density of 10^4 fermions under these conditions is much less than the condensate density.

The ground-state condensate wave-function, or order parameter Ψ_0, obeys the time-independent Gross-Pitaevskii (GP) equation [49]

$$\left[-\frac{\hbar^2}{2\,m}\nabla^2 + U_{\rm IP}(\vec{x}) + g\,N_0\,|\Psi_0(\vec{x})|^2\right]\,\Psi_0(\vec{x}) \;=\; \mu\,\Psi_0(\vec{x}) \quad , \tag{3.27}$$

where $g = 4\pi\hbar^2 a/m$ is the coupling constant for bosons with scattering length a, and N_0 is the number of atoms in the condensate.[5] With our choice of normalization $\int d^3x\,|\Psi_0|^2 = 1$, the density of condensed atoms is related to the condensate wave function by $n_c = N_0\,|\Psi_0|^2$. Note that the chemical potential μ is typically on the order ~ 1.5 kHz (75 nK) in our experiments.

In the limit of small gN_0, the solution to Eq.(3.27) is just $n_c = N_0|\psi_0|^2$, with ψ_0 the single-particle Gaussian oscillator ground state. For sufficiently large and positive gN_0, the mean-field term in Eq.(3.27) dominates and the kinetic energy

[5] As pointed out in Ref. [52], we replace N_0 by $N_0 - 1$ if the particle number is fixed.

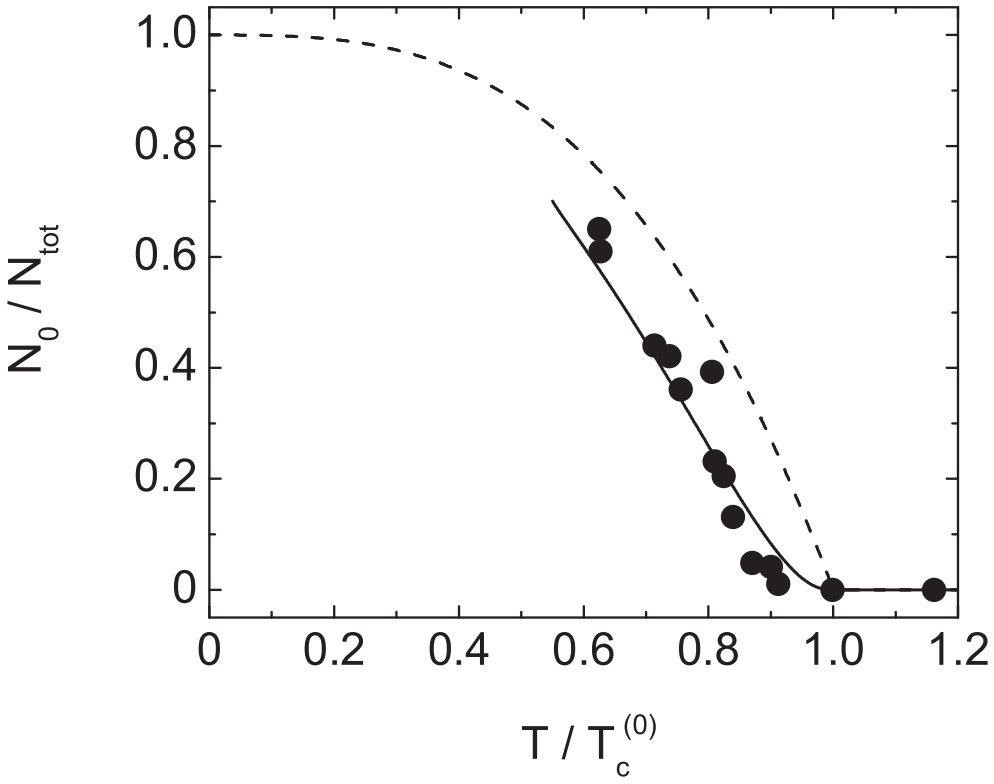

Figure 3.12: Observation of the BEC phase transition. Points are from surface fits to images of expanded clouds using the sum of a Thomas-Fermi parabola and a thermal distribution, with $T_c^{(0)}$ given by Eq.(3.25). The dashed line corresponds to the ideal gas prediction (3.26), and the solid line includes the effects of finite $N_{\rm tot}$ and boson-boson interactions according to the theory in Ref. [51]. The data were taken with $\sim 10^4$ ^{40}K atoms, which are expected to contribute a negligible mean-field energy for the ^{87}Rb atoms.

can be neglected. This yields an algebraic equation for the Thomas-Fermi (TF) density profile of the condensate

$$n_c(\vec{x}) \quad \xrightarrow{\text{TF}} \quad \frac{1}{g}\,[\,\mu_{\text{TF}} - U_{\text{IP}}(\vec{x})\,]\,\Theta[\,\mu_{\text{TF}} - U_{\text{IP}}(\vec{x})\,] \quad , \tag{3.28}$$

where $\Theta(\cdot)$ is the unit step function. The condensate density is therefore zero outside the TF radius in the i^{th} direction, given by $m\,\omega_i^2\,X_{\text{TF}i}^2/2 = \mu_{\text{TF}}$. The chemical potential is determined by the normalization condition on n_c, yielding

$$\mu_{\text{TF}} \quad = \quad \frac{\hbar\,\omega}{2}\left(15N_0\,\frac{a}{a_{\text{HO}}}\right)^{2/5} \quad , \tag{3.29}$$

where $a_{\text{HO}} = (\hbar\,/m\,\omega)^{1/2}$ is the geometric mean oscillator length for the bosons, which is typically ~ 1 μm for our experiments, compared to $a \simeq 5$ nm [45].

To determine when the TF approximation is valid, I solved the GP equation for the peak condensate density $n_c(0)$ as a function of N_0. The results are shown in Fig. 3.13 and compared to the weakly- and strongly-interacting limits. The calculations assumed ^{87}Rb atoms in a $2\pi \times 100$ Hz spherical trap. For these parameters there is a clear transition from non-interacting behavior to the TF approximation at $N_0 \sim 100$. Since we are not even able to measure so few atoms with our imaging system, we feel free to use the TF approximation for fitting our images.

3.4.2 Fermions

Things are somewhat more subtle for fermions, since there is no phase transition in our system.[6] Thermodynamic properties of the Fermi gas can be attained through the chemical potential, but practically speaking we focus on the fugacity $\mathfrak{Z} = \exp(\mu/k_BT)$, which can be obtained by solution to the equation [13]

$$-g_3(-\mathfrak{Z}) \quad = \quad \frac{1}{6}\left(\frac{T}{T_F}\right)^{-3} \quad , \tag{3.30}$$

[6] Note that we love them all the same, however.

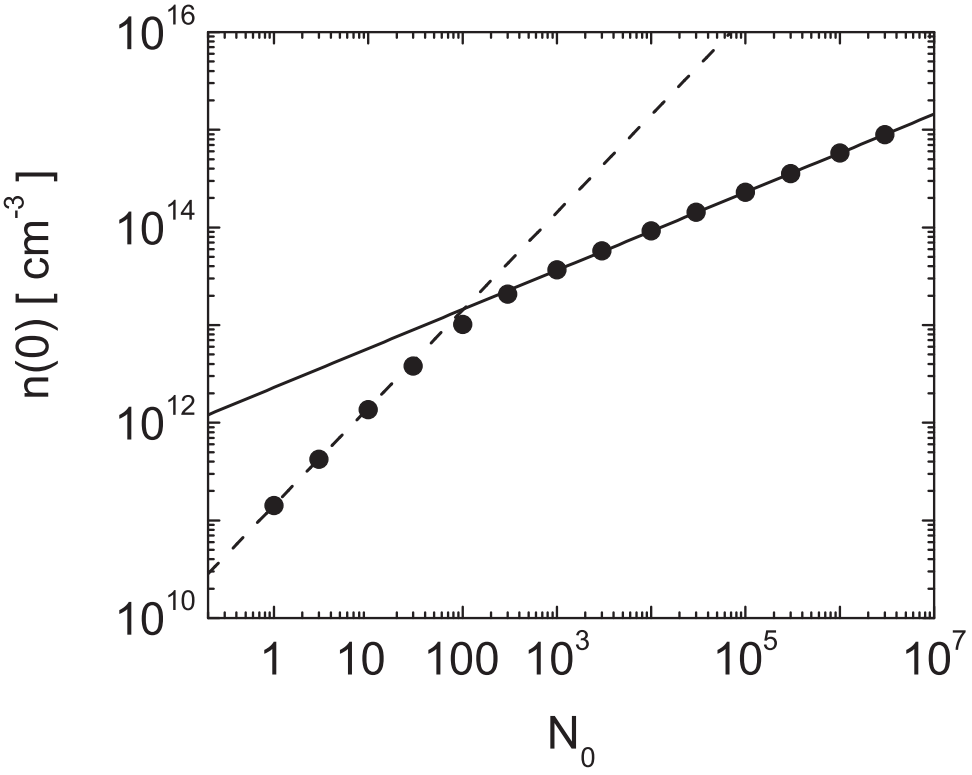

Figure 3.13: Calculated peak BEC density as a function of number. The solid points are results from the full solution of Eq.(3.27), with $N_0 \to N_0 - 1$, for ^{87}Rb atoms in a $2\pi \times 100$ Hz spherical trap. The dashed line is just N_0 times the square of the single-particle oscillator ground state, and the solid line is the TF approximation.

where T_F is the Fermi temperature, given by [50]

$$k_B T_F \;=\; \hbar\,\omega\,(6\,N)^{1/3} \quad . \tag{3.31}$$

The fugacity determined from fits to expanded ^{40}K clouds near the end of the evaporation is shown in Fig. 3.14.[7] The data appear to be shifted horizontally in the plot, probably due to a calibration error of $\sim 40\%$ in the ratio T/T_F. We attribute this to a 10% systematic uncertainty in T, combined with a $\sim 2\times$ underestimation of our ^{40}K number due to imperfections in our absorption imaging [53]. The data were taken under various ^{87}Rb conditions (with a ^{87}Rb thermal cloud, BEC, or no ^{87}Rb atoms) and show no obvious effects resulting from interactions between species.

Butts and Rokhsar [50] worked out low- and high-temperature approximations to the chemical potential to get

$$\mu \;\simeq\; \begin{cases} k_B T_F \left[1 - \dfrac{\pi^2}{3}\left(\dfrac{T}{T_F}\right)^2\right] & , \quad T \ll T_F \\ \\ -k_B T \,\ln\left[6\left(\dfrac{T}{T_F}\right)^3\right] & , \quad T \gg T_F \end{cases} \quad . \tag{3.32}$$

These two approximations are equal at $T \simeq 0.6\,T_F$, which we can take in the absence of a phase transition to mark the emergence of quantum statistical effects. In comparison the data in Fig. 3.14 suggest the fermions in our experiment reach temperatures $T \simeq 0.24\,T_F$.[8]

As Brian DeMarco pointed in his thesis [13], all formulas describing the ideal Fermi gas can be obtained by the corresponding formulas for Bose distributions using the functional transformations

$$f_{\mathrm{Fermi}}[\,g_\nu(\alpha);\mathfrak{Z}\,] \;=\; f_{\mathrm{Bose}}[\,-g_\nu(\alpha);-\mathfrak{Z}\,] \quad . \tag{3.33}$$

[7] The details of determining $\mathfrak{Z}$, T, and T_F from these fits are described in Ref. [13].

[8] This value for T/T_F uses the measured N and T; using the fugacity $\mathfrak{Z}$ suggests $T = 0.17\,T_F$. We always use the more conservative value.

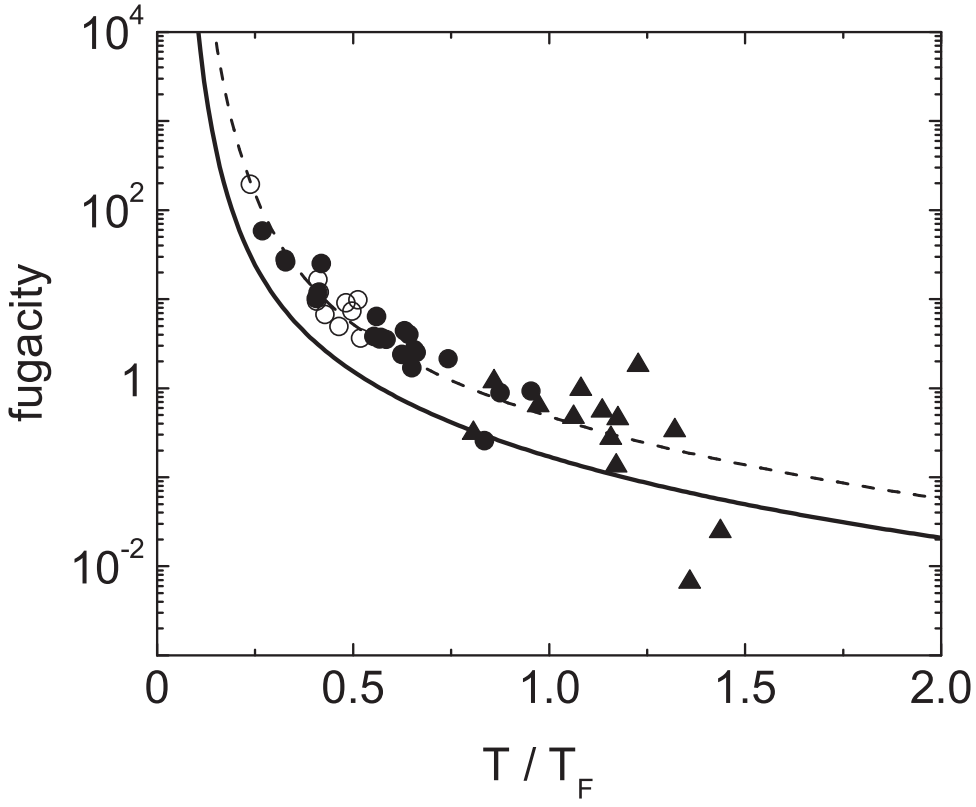

Figure 3.14: Observation of Fermi degeneracy. The points show the fugacity as a function of T/T_F, determined from surface fits as described in Ref. [13]. The triangles (▲) are in the presence of thermal ^{87}Rb atoms, solid circles (●) are in the presence of BEC, and open circles (○) have had ^{87}Rb atoms removed by evaporating through the trap bottom. The solid line is the ideal gas prediction from Eq.(3.30), and the dashed line is the same prediction with a 1.4× correction to T/T_F.

The density profile of the fermions corresponding to Eq.(3.24) is now more rounded than the classical Gaussian profile at the center of the cloud. This reflects the effect of the Pauli pressure for the fermions.

In the limit $T \to 0$ there is a Thomas-Fermi (TF) approximation for the density of the fermions. The chemical potential $\mu = k_B T_F \equiv E_F$ in this limit, and the density distribution becomes

$$n_{\rm FD}(\vec{x}) \quad \stackrel{\rm TF}{\longrightarrow} \quad \frac{\sqrt{2}}{3\,\pi^2}\,\frac{m_f}{\hbar^3}^{2/3}\,[\,E_F - U_{\rm IP}(\vec{x})\,]^{3/2}\,\Theta[\,E_F - U_{\rm IP}(\vec{x})\,] \quad . \qquad (3.34)$$

Note that the TF approximation here yields a profile with no atoms outside a distance determined by $\mu = U_{\rm IP}(\vec{x})$, as with the condensate in the previous section. Due to the Pauli pressure, however, $\mu_{\rm TF}$ is typically much larger for the fermions than for the bosons. For example consider 10^5 atoms of either species in a spherical trap with ^{87}Rb frequency $2\pi \times 100$ Hz. Under these conditions the Fermi energy $E_F \simeq 500$ nK, whereas the BEC chemical potential is only $\simeq 80$ nK. In other words, the Pauli pressure results in a fermi gas roughly 3 times larger than the condensate and about 13 times larger than the single-particle Guassian ground state for ^{40}K.

3.5 Limits to Sympathetic Cooling

One important question deserving our attention here is what limits the lowest T/T_F we can achieve by sympathetic cooling? Here I will just summarize some mechanisms that have been proposed, and what they each predict for the ^{87}Rb -^{40}K system. At this point more experimental work is needed to understand what technical issues, if any, may be limiting the lowest T/T_F in the experiments. We can, however, see in Table 3.1 that the four existing ^{87}Rb -^{40}K experiments have all reported similar results.[9]

[9] Note that all of the experiments have similar trapping potentials except the ETH experiment, which has a weaker radial confinement leading to a geometric mean trapping frequency

Expt.	T/T_F	N_{K}	Ref.
LENS	0.2	5×10^4	[54]
JILA	0.2	1×10^5	[53]
ETH	0.3	6×10^5	[4]
Hamburg	0.2	1×10^6	[55]

Table 3.1: Lowest values of T/T_F reported in ^{87}Rb -^{40}K experiments.

The first sympathetically cooled degenerate Fermi gas was produced by the Rice group using ^{6}Li and ^{7}Li [56]. To the best of my knowledge, that work represents the introduction of the assertion that the sympathetic cooling "bottoms out" when the heat capacity C_f of the fermions exceeds the heat capacity C_b of the bosons. This occurs because the total number of bosons N_b is decreasing while the number of fermions N_f is held roughly constant, and because the heat capacity of the bosons drops precipitously after crossing the BEC transition. The heat capacities for ideal Bose and Fermi gases are shown as a function of T in Fig. 3.15, assuming equal numbers of ^{87}Rb and ^{40}K atoms in their respective stretched states. Note that due to the different masses, Eqs.(3.25) and (3.31) show that under these conditions Bose-Einstein condensation occurs at a temperature $0.35\,T_F$. Since the BEC phase transition is accompanied by a discontinuous jump in C_b, and the low-temperature behaviors obey $C_f \propto T$ and $C_b \propto T^3$, this suggests the existence of a point where $C_b = C_f$. This point is given by $0.18\,T_F$ in this example, which is actually quite close to what we observe in the experiment. This agreement is almost certainly fortuitous, however, since we have so far neglected the important effects of gravitational sag (which is minimal in the ^{6}Li-^{7}Li experiment), and the finite heating rates in the experiments.

of $\omega_{\mathrm{Rb}} = 2\pi \times 70$ Hz, compared to $\omega_{\mathrm{Rb}} \sim 2\pi \times 90$ Hz for the other experiments. Note also that in the ETH experiment, the ^{87}Rb atoms are removed after sympathetic cooling, and a two-component ^{40}K mixture is evaporatively cooled to $0.2\,T_F$ with 5×10^4 atoms in each spin state.

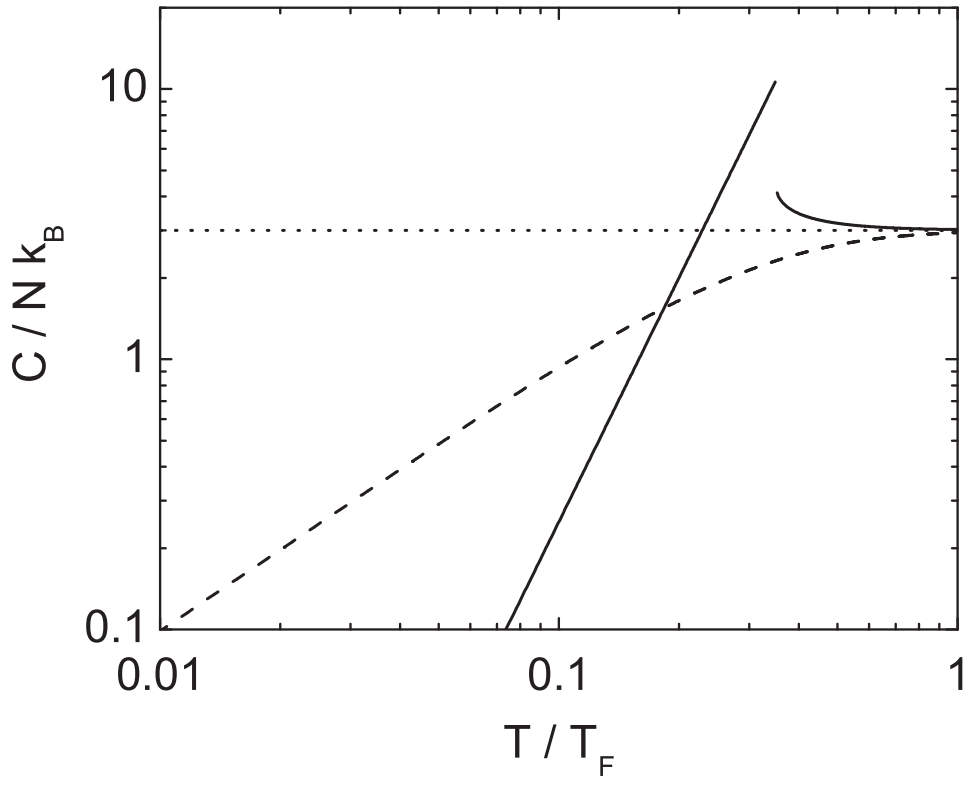

Figure 3.15: Specific heats of ideal Bose and Fermi gases. The heat capacity per particle is given in units of k_B as a function of T/T_F for equal numbers of non-interacting ^{87}Rb and ^{40}K atoms in the thermodynamic limit. The solid line is for the bosons, showing the transition to BEC at $\sim 0.35\,T_F$, and the dashed line is for the fermions. The dotted line shows the Maxwell-Boltzmann behavior, $C = 3Nk_B$.

Recently, Brown-Hayes and Onofrio [57] have elaborated on the simple heat capacity model. They consider Bose and Fermi gases in their respective TF regimes, and assume that the sympathetic cooling actually continues until $C_b/C_f \simeq 0.1$. Using low temperature approximations for C_b and C_f, they predict a minimum achievable temperature of $0.06\,T_F$ for equal numbers of atoms in a ^{87}Rb -^{40}K mixture. Although this is significantly lower than what we observe, they go on to include the effects of gravitational sag and mean-field interactions. As we saw in Sect. 3.3.2 gravity reduces the spatial overlap of the clouds, but we will see later that the attractive ^{87}Rb -^{40}K interactions act to recover some of the overlap. The result is a net increase in minimum temperature (proportional to the square of the reduction in overlap) of about 8 times to $0.5\,T_F$, which is incompatible with our results. Although their model seems insufficient to quantitatively predict the minimum temperature, I have pointed it out here because the authors additionally suggest some ways to improve sympathetic cooling by optimizing the choice of species (for masses and magnetic confinement) and trap frequencies, including the application of bichromatic optical dipole traps to selectively change the confinement of each species.

The heat capacity model of the limit to sympathetic cooling is based on an intuitive model of the cooling process where two gases initially at different temperatures are brought into thermal contact. The idea is that both species are initially in thermal equilibrium, and some evaporation of the bosons leads to a lower-energy Bose gas. The fermions are then cooled as both gases reach an intermediate temperature, and a new evaporation step proceeds. Carr and Castin have shown [58] that in some sense it is ideal to have $C_f \gg C_b$, in order to minimize the number of bosons one must evaporate in order to reach zero temperature. Although their work casts some important doubts on the simple heat capacity argument for the limit of the cooling process, their model always achieves $T = 0$

fermions, and is therefore not useful in our search here to understand what actually does limit the process in experiments.

Another possible limit that Carr and Castin examined (in conjunction with Bourdel [59]) is based on a heating mechanism originally suggested by Timmermans [60], where particle losses in the Fermi sea lead to an increase in T/T_F. They predict minimum attainable temperatures below $0.1\,T_F$ for a ratio of loss rate to collision rate of 10^{-2}. Without performing detailed calculations for our masses, atom numbers, and heating and collision rates, it is hard to make a better quantitative prediction. Note also that their theory neglects the gravitational sag, and boson-boson and boson-fermion interactions. The interesting thing about their work is rather the suggestion that even in the absence of other limits to the cooling, the hole-heating will ultimately limit experiments to the $\sim 0.01\,T_F$ level, which is not significantly lower than the best degenerate Fermi gas experiments to date (which include some direct evaporation of the fermions). This mechanism additionally effects any degenerate Fermi gas, regardless of whether sympathetic cooling is employed.

The last mechanism I'd like to consider was proposed by Timmermans and Côté in Ref. [61]. They pointed out that the superfluidity of the BEC will inhibit collisions with fermions traveling slower than the Landau critical velocity in the gas. This velocity c is given by the Bogoliubov speed of sound

$$m_b\, c^2 \;=\; \mu_b \quad ,$$

where m_b and μ_b are the boson mass and chemical potential, respectively. Using the local density approximation (LDA) this gives a spatially dependent critical speed

$$c(\vec{x}) \;=\; \sqrt{\frac{g}{m_b}\, n_c(\vec{x})} \quad , \tag{3.35}$$

where $g = 4\pi\hbar^2 a/m_b$ is the coupling constant for bosons with scattering length a and n_c is the condensate density. The authors used the quantum Boltzmann equation to show that a homogenous Maxwell-Boltzmann distribution originally with a thermal speed $v_T = 3\,c$ would cool to a distribution with peak speed slightly lower than c. To translate this to our harmonically trapped samples we take the average speed of sound $\langle\, c\,\rangle = N_0^{-1} \int d^3x\, n_c(\vec{x})\, c(\vec{x})$. For our typical conditions we then get $\langle\, c\,\rangle = 1.9$ mm/s. Setting $v_T = \langle\, c\,\rangle$ and using $m_f\, v_T^2/2 = 3\, k_B T/2$ with m_f the mass of a ^{40}K atom, we get a limiting temperature of $\simeq 6$ nK, or $T/T_F \simeq 0.01$, which is again much better than what we achieve in the experiment. This, together with the fact that the real fermion distribution is weighted towards higher speeds than a Maxwell-Boltzmann distribution, suggests that superfluidity is not yet limiting the cooling process in our experiment.[10] As with the hole-heating, however, we see what may be a fundamental limit to the cooling of our fermions to about 1% of the Fermi temperature.

[10] With the caveat that we have ignored the fact that fermions will always be able to scatter off of the low-density edge of the condensate. A more detailed calculation is needed to address this effect.

Chapter 4

Cross-Species Interactions

In this chapter I will present our main experimental results investigating ways to probe and manipulate the cross-species interactions characterized by the s-wave scattering length a_{bf}. The parameter a_{bf} is crucial in understanding a variety of the static and dynamic properties of quantum degenerate Bose-Fermi mixtures.

I'll begin in Sect. 4.1 with a discussion of how we can make relatively precise measurements of the magnitude of a_{bf} by measuring rethermalization rates in non-degenerate clouds. This type of measurement was originally developed at JILA for a single-species Bose gas in Ref. [62]. Subsequent studies have extended the technique to Fermi-Fermi mixtures [46], single-species resonant collisions [63], and Bose-Bose mixtures [64]. The quantum statistical suppression of fermion-fermion collisions makes this type of measurement especially robust for Bose-Fermi mixtures.

In Sect. 4.2 I will elaborate on the importance of the Bose-Bose and Bose-Fermi scattering lengths with respect to the equilibrium state of the mixture. We will discuss some possible mechanical instabilities and how they relate to the size and sign of the scattering lengths, and the numbers of atoms of each species in the mixture.

In Sect. 4.3 I'll describe some measurements of the excitations of the mixture.

We first examine the quadrupole "breathe" mode for non-degenerate fermions in the presence of bosons. The damping rate gives us the magnitude of the scattering length and the excitation frequency, in principle, gives information on the importance of hydrodynamic effects. This will lead to our observation of somewhat higher-lying excitations of a ^{87}Rb BEC in the presence of a thermal cloud of ^{87}Rb atoms. Besides being, to my knowledge, the first verification of some longstanding theoretical calculations of the excitation spectra of BECs in elongated traps, this measurement serves as an example of how parametric excitation of the atoms can be extremely useful for systems with many available excitation modes. Finally, as one possible excitation for future study, I will discuss the theoretical proposal for a Boson-induced pairing of the fermions. This calculation suggests the observation of pairing may be within reach of current experiments using Feshbach resonances between species.

Finally, in Sect. 4.4 I will describe our hunt for, and observation of, heteronuclear Feshbach resonances in the collisions between ^{87}Rb and ^{40}K atoms. The discovery of these resonances represents the "crown jewel" of the work described in this thesis. It is these resonances that in principle grant the experimenter real-time control over a_{bf} in the mixture. In addition to providing access to phenomena such as phase-separation and mechanical collapse, this control may allow production for the first time of quantum degenerate fermionic molecules, as well as observation of boson-mediated pairing of the fermions. Finally we use the observations of the resonance locations to refine our knowledge of the non-resonant scattering properties we measured in Sects. 4.1 and 4.3.1. The knowledge gleaned from the locations of the resonances gives us the first insight in our experiment into the singlet scattering properties between ^{87}Rb and ^{40}K atoms. This knowledge could in turn be used to refine the predictions of various ^{87}Rb -^{40}K Feshbach resonances presented in Ref. [65].

4.1 Cross-Dimensional Rethermalization

In this section I will describe our cross-dimensional rethermalization (CDR) measurements on non-degenerate ^{87}Rb -^{40}K mixtures. These measurements provide a relatively simple and robust way to determine the value of $|a_{bf}|$ in the system, which is crucial to characterizing a variety of equilibrium and dynamic properties of the mixture. Our CDR measurements were reported in Ref. [53] and our theoretical work was presented in Ref. [66].

The essence of cross-dimensional rethermalization is as follows. If one prepares a gas with different mean energies in the different Cartesian directions, the gas will subsequently relax into thermal equilibrium. An example from the experiment is shown in Fig. 4.1. In a purely harmonic trap the only way for the gas to spatially redistribute its energy is through collisions between atoms, since the potential energy is perfectly separable in the three directions. In an elastic s-wave collision, where the total energy and momenta are conserved, the relative motion of colliding particles is completely randomized. That is, the isotropic nature of the scattering amplitude leads to a uniform redistribution of kinetic energy between directions. The potential energy in each direction can be thought of as being on average equal to the corresponding kinetic energy immediately following the collision. This assumption is valid in the so-called "collisionless" regime, where the collision rate is small compared to the trapping frequencies. This is the regime where we perform the measurements described in this section.

A detailed analysis of single-species CDR reveals that the relaxation has the form of an exponential decay, with a $1/e$ time-constant proportional to the mean time between collisions in the gas [67]. The Bose-Fermi case is more difficult to handle analytically, but we make the following important observation. The fermions in our mixture are spin-polarized, so that if they are well below the p-

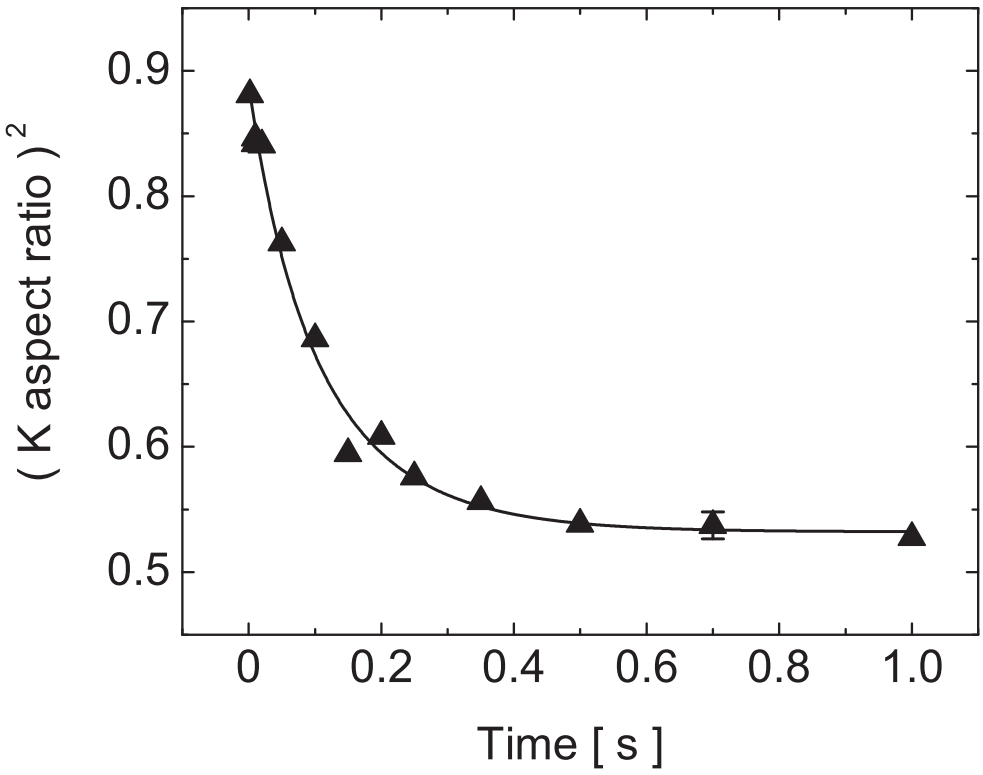

Figure 4.1: Cross-dimensional rethermalization of ^{40}K in the presence of ^{87}Rb. Shown is the square of the cloud aspect ratio (radial/axial) in time-of-flight, as a function of hold time after introducing an energy anisotropy between the radial and axial directions. The square of the aspect ratio is proportional to the ratio of energies in the radial and axial directions. The ^{40}K atoms rethermalize by means of collisions with the ^{87}Rb atoms. The solid line is a fit to the ratio of exponentially decaying curves. The error bar shows the typical statistical uncertainty.

wave threshold (~ 190 μK for ^{40}K [46]) fermion-fermion collisions are suppressed; s-wave collisions between identical fermions are forbidden by the Pauli exclusion principle. The fermions therefore collide only with the bosons. Then the discussion above regarding the spatial redistribution of kinetic energy holds for the fermions. We again expect their rethermalization to look like exponential decay with a time constant proportional to the mean time per fermion between collisions.

In the experiment the non-equilibrium state of the mixture is prepared in the following way. We first produce a mixture of 1×10^5 ^{40}K and 4×10^5 ^{87}Rb atoms at $\sim$ 1 μK as described in the previous chapter. The radial trap strength is reduced for the entire cooling stage by applying an extra ~ 3 G bias field to the IP trap. The ^{87}Rb radial trap frequency is $\omega_\rho = 2\pi \times 95$ Hz in the decompressed trap (the axial frequency is always $2\pi \times 25$ Hz). We then optionally apply a sequence of 1 ms rf sweeps to reduce the ^{87}Rb number by as much as a factor of 4 using spin-flips in the magnetic trap. The ^{87}Rb radial trapping frequency is then ramped to $2\pi \times 160$ Hz over a time scale that is slow compared to the radial trap period and fast with respect to the rethermalization rates in the gas. Immediately after the compression there is therefore an excess of energy in the radial directions. Neglecting any rethermalization that may occur during the compression, the mean energies (kinetic plus potential) in the radial and axial directions are related by $(E_{x,y}/E_z) = (160/95)$ for either species of atoms.[1] The fact that both species begin at the same temperature, experience the same initial energy anisotropy, and then equilibrate together means that there is never any net transfer of energy from one gas to the other during the rethermalization. This is instrumental in removing effects due to the systematic uncertainty in determining atom numbers.

[1] Note that in Ref. [53] we state that the trap frequency ($\nu_\rho = \omega_\rho/2\pi$) goes from 90 to 160 Hz during the compression. I think the 90 Hz is a typo. During the CDR measurements we measured $\nu_\rho = 95.23 \pm 0.13$ Hz before the compression and 156.6 ± 0.4 Hz after, using ^{87}Rb dipole oscillations. This calibration was used for the data analysis as well as the Monte Carlo simulations, so that our results remain unchanged.

With an excess of energy in the x and y directions, we simply vary the hold time in the compressed trap, and then measure the rms Gaussian sizes ($\sigma_{\rho,z}$) of the clouds after time-of-flight expansion. The aspect ratio (σ_z/σ_ρ) is used for the analysis instead of the radial and axial sizes in order to reduce the effects of shot-to-shot variations in the starting temperature of the mixture. The square of the aspect ratio, which is proportional to $E_z/E_{x,y}$, is fit to the ratio of exponentially decaying curves, whose $1/e$ time constant determines the relaxation time constant τ. Such a fit is shown as the solid curve in Fig. 4.1.

We measured $\tau_{\rm K}$ over a variety of different ^{87}Rb densities. The results are shown in Fig. 4.2, where we plot the relaxation rate versus the product of ^{87}Rb density and $T^{1/2}$ (proportional to the mean collision speed). We also show a set of "control" experiments where we measure $\tau_{\rm Rb}$ in the absence of ^{40}K atoms. Note that both relaxation rates vary linearly with the product $\langle\, n_{\rm Rb}\,\rangle\, T^{1/2}$. We'll see below that the slopes of linear fits through the origin are proportional to the collision cross-sections, and therefore the square of the scattering lengths. This linear behavior additionally demonstrates that we remain in the collisionless regime for these measurements. Hydrodynamic behavior leads to a nonlinear density dependence, since energy is "stored" in the potential energy of particles pinned in place by collisions. For examples of this kind of behavior, see the experiment in Ref. [68] and the discussion in Appendix A.

For these measurements we extract the magnitude of the ^{87}Rb -^{40}K scattering length as follows. The linear behavior in Fig. 4.2 allows us to write the relaxation rates [62, 53]

$$\begin{aligned} \Gamma_{\rm K} \equiv \tau_{\rm K}^{-1} &= \frac{1}{\beta}\,\langle\,\Gamma_{\rm RbRb}\,\rangle \\ \Gamma_{\rm Rb} \equiv \tau_{\rm Rb}^{-1} &= \frac{1}{\alpha}\,\langle\,\Gamma_{\rm RbK}\,\rangle \quad , \end{aligned} \tag{4.1}$$

where $\Gamma_{\rm RbRb}$ ($\Gamma_{\rm RbK}$) is the Rb-Rb (Rb-K) collision rate, and the average $\langle\,\Gamma_{\rm RbK}\,\rangle$

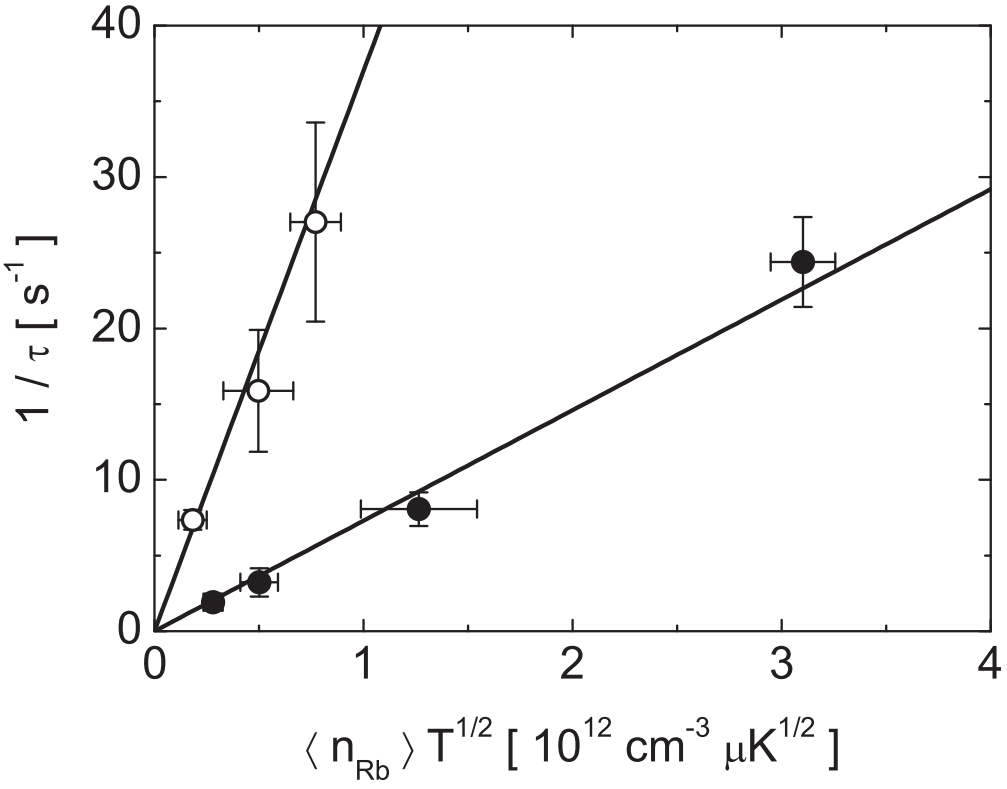

Figure 4.2: Cross-dimensional relaxation over varying ^{87}Rb density. Open points ($\circ$) are for ^{40}K relaxation in the presence of ^{87}Rb, and solid points ($\bullet$) are for the single-species ^{87}Rb control experiment. Lines are fits through the origin; the slopes are proportional to the corresponding collision cross-sections. Vertical error bars are from the fit uncertainties, and horizontal error bars include shot-to-shot fluctuations in ^{87}Rb number and temperature, and a 10% systematic uncertainty in T [53]; the systematic uncertainty in ^{87}Rb number is removed in the analysis by taking the ratio of the two slopes and using Eq.(4.2).

is taken over the distribution of ^{40}K atoms (see Eqs.(3.20) and (3.22)). The constants of proportionality α and β reflect the mean number of collisions per particle needed for rethermalization.

If we compare the observed single-species ^{87}Rb relaxation rate to the relaxation rate of ^{40}K atoms in the presence of ^{87}Rb, we find

$$\frac{\tau_{\mathrm{Rb}}}{\tau_{\mathrm{K}}} = \frac{1}{2^{3/2}} \frac{\alpha}{\beta} \sqrt{1 + \frac{m_{\mathrm{Rb}}}{m_{\mathrm{K}}}} \left(\frac{a_{\mathrm{RbK}}}{a_{\mathrm{RbRb}}} \right)^2 \quad , \tag{4.2}$$

where we have suppressed the appearance of $f_{\mathrm{sag}}(T)$ in the ^{87}Rb -^{40}K collision rate for simplicity.[2] This important relation is at the heart of why the CDR technique is so robust for Bose-Fermi mixtures. The ^{87}Rb density has fallen out of the analysis, taking with it the large systematic uncertainty that typically accompanies it and limits the precision of such measurements. In conjunction with the facts that (i) there is no energy transferred between gases (which would give rise to an additional number dependence) and (ii) the ^{87}Rb-^{87}Rb scattering length $a_{\mathrm{RbRb}} = 98.98 \pm 0.04\, a_0$ is extremely well known from a variety of high-precision experiments with ^{85}Rb and ^{87}Rb [45, 69], Eq.(4.2) allows a relatively precise determination of $|a_{\mathrm{RbK}}|$ with a simple collisional measurement.

The constants α and β were determined for our experimental conditions using classical Monte Carlo simulations, as described in Refs. [53, 66]. The result is

$$\begin{aligned} \alpha &= 2.67 \pm 0.13 \\ \beta &= 2.1 \pm 0.2 \quad . \end{aligned} \tag{4.3}$$

Note that a number of analytic and numerical studies have found α to lie between 2.5 and 2.7 [62, 70, 71, 46, 72, 67], in good agreement with our results. I am not aware of any previous theoretical results for β in the literature.

[2] For the experiments considered here, f_{sag} represents a 3–5% correction to the density, and is included in the analysis.

With these values of α and β, our measurements of relaxation rates in Fig. 4.2, and the accepted value of a_{RbRb}, we obtain a value for $|a_{\mathrm{RbK}}|$ of

$$|a_{\mathrm{RbK}}| \;=\; 250 \pm 30\, a_0 \quad , \tag{4.4}$$

where we have used $\sigma_{\mathrm{RbRb}} = 8\pi\, a_{\mathrm{RbRb}}^2$ and $\sigma_{\mathrm{RbK}} = 4\pi\, a_{\mathrm{RbK}}^2$. For comparison I have compiled in Table 4.1 values of $|a_{\mathrm{RbK}}|$ from a variety of different works.[3] I have additionally included the result of measurements we have performed using quadrupole "breathe" oscillations. These experiments are described in detail in Sect. 4.3.1 below.

Finally, we compare in Fig. 4.3 our experimental measurements of the collision cross-section with the results of detailed coupled-channel calculations performed by Chris Ticknor and John Bohn. The calculations assume the value of a_{RbK} determined we obtained in Ref. [44] from our observation of inter-species Feshbach resonances (described in Sect. 4.4 below). The agreement between experiment and theory is excellent.

4.2 Mean-Field Intermezzo — Equilibrium Properties

So far our theoretical descriptions of the degenerate Bose and Fermi gases have neglected the interactions between species. In this section I'll detail some of the more important aspects of the zero-temperature mean-field theory of Bose-Fermi mixtures, using the Thomas-Fermi (TF) approximations for each species. This model was introduced in the seminal paper by Mølmer [77], and has been expanded on in numerous works since.[4]

Here I'll focus on the mean-field energies for each species in the mixture, as well as the equilibrium density profiles for different signs and strengths of the

[3] I feel obliged to point out here a pre-print I have recently discovered, wherein the scattering lengths for various isotopic Rb-K mixtures are calculated. Öztürk and Özçelik obtain $-200\ a_0$ for the ^{87}Rb -^{40}K mixture. See `arXiv:physics/0403073`.

[4] The interested reader is urged to look up papers citing Ref. [77].

$\lvert a_{\mathrm{RbK}}\rvert$	Ref.	Method
95^{+98}_{-33}	[73]	Heat-transfer*
261^{+159}_{-170}	[74]	Heat-transfer + dipole oscillation*
330^{+160}_{-100}	[75]	Heat-transfer
410^{+90}_{-80}	[76]	Dipole oscillation
395 ± 15	[54]	Mean-field theory + experiment
250 ± 30	[53]	CDR
$260 \pm 50 \pm 70$	§ 4.3.1	Quadrupole oscillation
281 ± 15	[44]	Feshbach resonances
275^{+7}_{-8}	§ 4.4.3	Feshbach resonances

Table 4.1: Compendium of reported values for the ^{87}Rb -^{40}K triplet scattering length. All values are in units of a_0, the Bohr radius. An asterisk (*) denotes a result employing a mass-scaling to ^{87}Rb -^{40}K from a measurement on a ^{87}Rb-^{41}K mixture. Heat-transfer experiments selectively heat the Rb atoms, and then monitor the transfer of energy to K atoms. Results below the double bar are from our experiment. The uncertainty on our quadrupole oscillation measurement is stated in the form ± statistical ± systematic, where the systematic uncertainty arises from the systematic uncertainty in atom numbers.

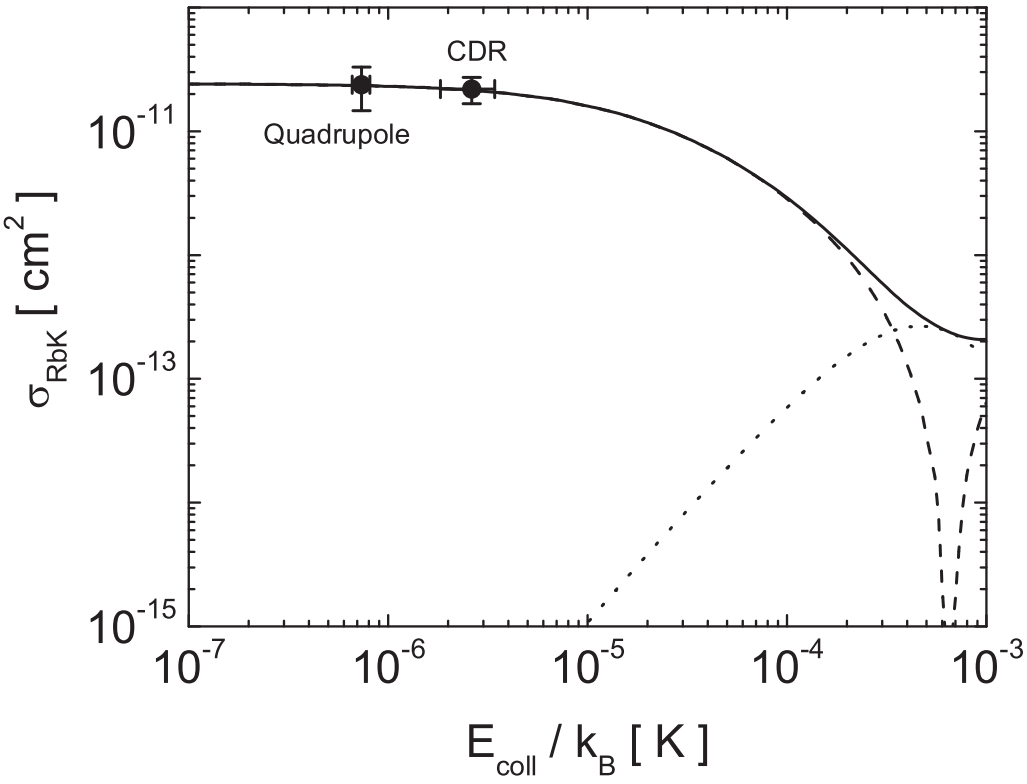

Figure 4.3: Comparison of experiments and theory for the ^{87}Rb -^{40}K cross-section. The solid curve is the calculated total cross-section, and the dashed (dotted) curve is just the s-wave (p-wave) contribution. Theory curves were calculated by Chris Ticknor and John Bohn, using the triplet scattering length determined from the best match to our experimental observations of the ^{87}Rb -^{40}K Feshbach resonances in Ref. [44]. Points are from our CDR and quadrupole excitation (§ 4.3.1) measurements, using $E_{\rm coll} = 3k_BT/2$. The error-bar on x for the CDR measurement reflects the range of temperatures used for the measurement. The error bar on y for the quadrupole mode measurement neglects a $\pm 70\, a_0$ uncertainty on $|a_{\rm RbK}|$ arising from the systematic uncertainty in atom numbers.

coupling parameter (proportional to the interspecies scattering length). In addition I'll discuss some null results from our experiment which appear to contradict some observations from the LENS group. Resolution of this conflict is important for understanding the equilibrium properties of ^{87}Rb -^{40}K mixtures with different numbers of atoms and in different confining potentials.

4.2.1 Theory: Phase Separation, Fermions in a Box, and Collapse

Our description of Bose-Fermi mixtures is centered on the concept of mean-field potentials, proportional for one species to the density of atoms of the other species. Specifically we write the total boson and fermion potential energies

$$\begin{aligned} U_b(\vec{x}) &= U_{\rm ext}(\vec{x}) + g_{bf}\, n_f(\vec{x}) \\ U_f(\vec{x}) &= U_{\rm ext}(\vec{x}) + g_{bf}\, n_b(\vec{x}) \quad , \end{aligned} \tag{4.5}$$

where $U_{\rm ext}$ is the external trapping potential, n_σ is the density of species $\sigma = (b, f)$, and the coupling constant $g_{bf} = 2\pi\hbar^2 a_{bf}/\mu_{bf}$, with a_{bf} the scattering length between bosons and fermions, and μ_{bf} the reduced mass between bosons of mass m_b and fermions of mass m_f. We assume that $U_{\rm ext}$ is a spherically symmetric harmonic potential with trapping frequencies ω_b and $\omega_f = (m_b/m_f)^{1/2}\omega_b$ for the bosons and fermions, respectively.

Roth and Feldmeier gave the energy density functional for the system [78, 79]

$$\varepsilon(\vec{x}) = \frac{2\pi\hbar^2 a_{bb}}{m_b}\, n_b^2 + \frac{3\,(6\pi^2)^{2/3}\hbar^2}{10 m_f}\, n_f^{5/3} + \frac{4\pi\hbar^2 a_{bf}}{m_{bf}}\, n_b\, n_f + U_{\rm ext}\,(n_b + n_f) \quad , \tag{4.6}$$

where a_{bb} is the boson-boson scattering length, and we have suppressed the spatial dependence for simplicity. The chemical potentials μ_σ are obtained from the relations $\mu_\sigma = \partial\varepsilon/\partial n_\sigma$, giving

$$\begin{aligned} \mu_b &= U_b(\vec{x}) + g_{bb}\, n_b(\vec{x}) \\ \mu_f &= U_f(\vec{x}) + \frac{\hbar^2\,[6\pi^2 n_f(\vec{x})]^{2/3}}{2m_f} \quad , \end{aligned} \tag{4.7}$$

where $g_{bb} = 4\pi\hbar^2 a_{bb}/m_b$ is the coupling constant between bosons. Note that since we are working at zero temperature, we can further identify $\mu_f = E_F$, the Fermi energy.[5] Eqs.(4.5) and (4.7) immediately yield coupled equations for the density profiles

$$\begin{aligned} n_b(\vec{x}) &= \frac{1}{g_{bb}} \left[\mu_b - U_b(\vec{x})\right] \Theta[\mu_b - U_b(\vec{x})] \\ n_f(\vec{x}) &= \frac{(2m_f)^{3/2}}{6\pi^2\hbar^3} \left[\mu_f - U_f(\vec{x})\right]^{3/2} \Theta[\mu_f - U_f(\vec{x})] \quad , \end{aligned} \tag{4.8}$$

where $\Theta(\cdot)$ is the unit step function. The chemical potentials are fixed by the normalization condition that the integral over the density gives the total number of atoms for each species.

In practice the full self-consistent solution to Eq.(4.8) is determined numerically, as described in detail in Ref. [79]. There is a simple approximation, however, that will give us some physical insight into the behavior of the system. Let $n_b^{(0)}$ be the condensate density profile for the non-interacting case, $g_{bf} = 0$. Because the fermions are typically less dense than the condensate, we expect the fermion mean-field to contribute very little to U_b. We therefore consider $n_b = n_b^{(0)}$ to be "frozen" for the moment. As a first approximation to U_f we then define

$$U_f^{(1)} = U_{\rm ext} + g_{bf}\, n_b^{(0)} \quad . \tag{4.9}$$

Using Eq.(4.8), we can write

$$U_f^{(1)} = \begin{cases} (1-\gamma)\, U_{\rm ext} & , \quad r < R_b \\ -\gamma\, \mu_b^{(0)} + U_{\rm ext} & , \quad r \geq R_b \end{cases} \quad , \tag{4.10}$$

where we have introduced $\gamma = g_{bf}/g_{bb}$, $R_b = (2\mu_b/m_b\,\omega_b^2)^{1/2}$, and have added a constant to the potential in order to keep $U_f^{(1)}(0) = 0$. The potential $U_f^{(1)}$ is

[5] Note also, however, that E_F is modified from the expression in Eq.(3.31) due to the Bose-Fermi interactions. This point will be elaborated on below.

shown schematically in Fig. 4.4 for various values of γ (neglecting the shift of $\gamma\,\mu_b^{(0)}$ for clarity). Our analysis of the positions of the ^{87}Rb -^{40}K Feshbach resonances in Ref. [44] suggests a value of $\gamma = -4.5 \pm 0.2$ for a mixture in the state $|\,F = 2, m_F = 2\,\rangle_{\rm Rb} \otimes |\,9/2, 9/2\,\rangle_{\rm K}$, which is the mixture we magnetically trap and sympathetically cool. This sets a sense of scale for γ. Note also that the resonances themselves give us access in principle to any value of γ desired. For this reason we will consider all values of γ in our discussion.

Equation (4.10) and Fig. 4.4 show that fermions within the condensate radius R_b experience a harmonic potential with an effective trapping frequency $\omega_f' = \omega_f\,(1-\gamma)^{1/2}$ for $\gamma < 1$. For the "magic" value $\gamma = 1$, the condensate mean-field cancels the external potential for the fermions, giving rise to a uniform sample of fermions at the trap center, or "fermions in a box." Fermions in a box are predicted to occur for $a_{bf} = 2\,a_{bb}\,m_f/(m_b + m_f) \simeq 62\,a_0$ for the ^{87}Rb -^{40}K system.[6] For $\gamma > 1$, the fermions feel a repulsive bump in the center of the trap, and for sufficiently strong interactions, the fermions will be expelled from the trap center. This phenomenon is referred to as phase separation. In this limit the fermions are expected to form a dilute shell around the BEC core.[7] In the limit of strong attractive interactions between species (large, negative γ), the presence of the bosons gives rise to a region of exceedingly strong confinement for the fermions at the center of the trap. For strong enough attractive interactions, the peak fermion density can become large enough to appreciably modify U_b in such a way that the boson density then begins to increase. The positive feedback between n_b and n_f can lead to a runaway "collapse" of the system, where the

[6] Production of BEC in a box has just been observed in the group of Mark Raizen at the University of Texas, using specially tailored optical potentials. See `arXiv:cond-mat/0503590`.

[7] In our discussion of phase separation, we are assuming a moderate boson-boson repulsion, and that there are not more fermions than bosons, as in the experiments. Under different conditions it is also possible to have a condensate shell around a Fermi gas core. For a detailed discussion of this, along with the only description I've seen of spontaneous symmetry-breaking for Bose-Fermi mixtures in elongated traps, see Ref. [80].

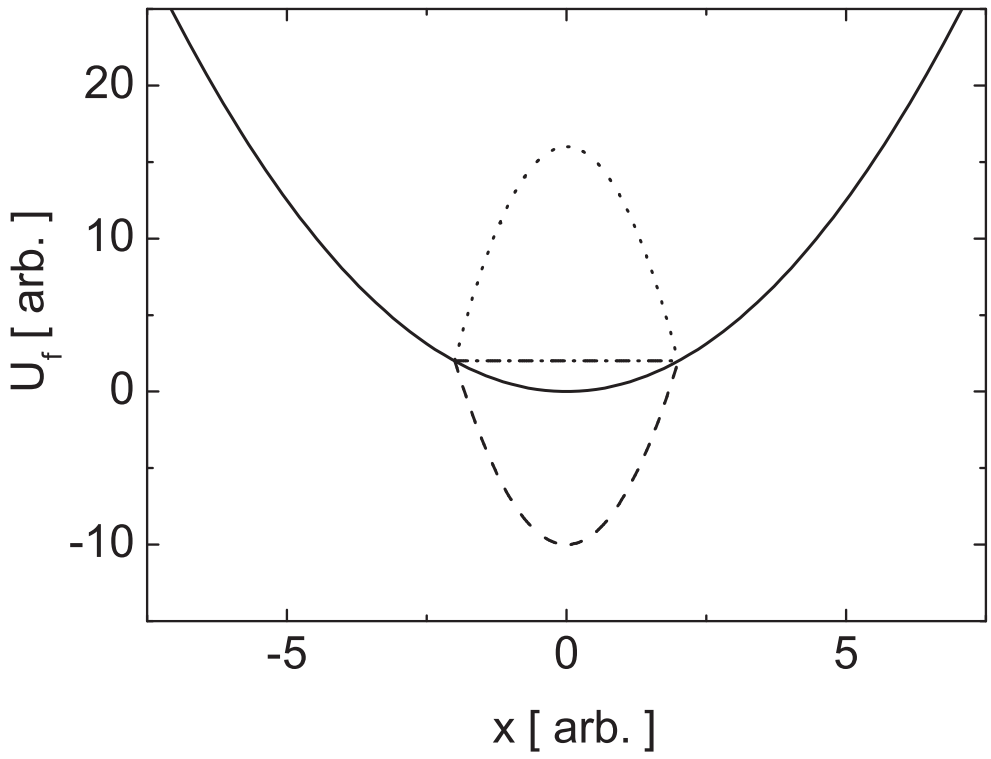

Figure 4.4: Mean-field effect of a condensate on the fermions. The approximate potential $U_f^{(1)}$ from Eq.(4.10) is shown for a variety of parameters $\gamma = g_{bf}/g_{bb}$. The solid line is the external potential $U_{\rm ext}$, corresponding to $\gamma = 0$, and the dashed, dash-dotted, and dotted curves use $\gamma = -5$, $+1$, and $+8$, respectively. The shift $\gamma\,\mu_b^{(0)}$ appearing in Eq.(4.10) has been removed for clarity.

densities become essentially singular at the trap center. We will have more to say about this scenario later. Self-consistent equilibrium density profiles calculated from Eq.(4.8) are shown in Fig. 4.5 for various values of the interaction strength.

In analogy with the discussion leading to Eq.(4.10) we can estimate the fermion chemical potential by

$$\mu_f^{(1)} \;=\; \mu_f^{(0)} - \gamma\,\mu_b^{(0)} \quad . \tag{4.11}$$

This in turn leads us to some approximations for the central density of the mixture. For positive γ, we get an estimate for the critical parameter for phase separation $\gamma_{\rm sep}$ by simply defining

$$n_f^{(1)}(0) \;=\; \frac{(2\,m_f)^{3/2}}{6\,\pi^2\hbar^3}\left[\,\mu_f^{(0)} - \gamma\,\mu_b^{(0)}\,\right]^{3/2} \quad . \tag{4.12}$$

The phase separation is then expected when $n_f^{(1)}(0) = 0$ in Eq.(4.12), so that we predict $\gamma_{\rm sep}^{(1)} = \mu_f^{(0)}/\mu_b^{(0)}$.

For sufficiently strong attractive interactions our method of approximation is expected to fail, as we have assumed $n_b^{(1)} \simeq n_b^{(0)}$, which will no longer be accurate as the collapse is approached. We may, however, write Eq.(4.7) in matrix form $\mathbf{G}\cdot\vec{n} = \vec{\mu}$, with $\vec{n} = (n_b(0), n_f(0))^T$ and $\vec{\mu} = (\mu_b, \mu_f)^T$ (superscript T's denote a transpose), and coupling matrix

$$\mathbf{G} \;=\; \begin{bmatrix} g_{bb} & g_{bf} \\ g_{bf} & 3\,\pi^2\,\hbar^2/m_f\,k_F \end{bmatrix} \quad , \tag{4.13}$$

with $k_F = [6\,\pi^2 n_f(0)]^{1/3} = (2\,m_f\mu_f)^{1/2}/\hbar$ the Fermi wavenumber. The condition that $\mathbf{G}\cdot\vec{n} = \vec{\mu}$ has a non-trivial solution for the densities is then equivalent to setting the determinant of $\mathbf{G}$ equal to zero. Solution of the resulting equation gives a critical value of γ for collapse of

$$\gamma_{\rm col} \;=\; \sqrt{\frac{3\,\pi^2\hbar^2}{m_f\,k_F\,g_{bb}}} \quad . \tag{4.14}$$

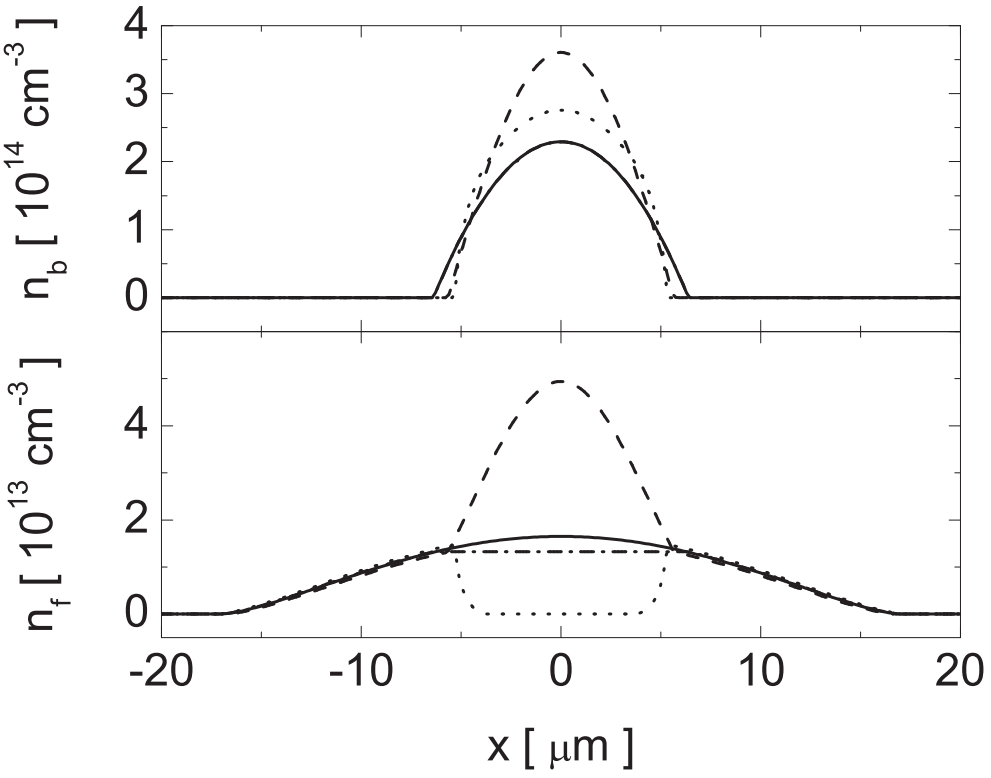

Figure 4.5: Theoretical equilibrium profiles in the TF approximation. The calculations assumed 10^5 atoms each of ^{87}Rb and ^{40}K, in a spherical trap with $\omega_{\rm Rb} = 2\pi \times 100$ Hz. The values of γ are the same as in Fig. 4.4.

Similar results have been derived in a number of ways [81, 82, 83]. Although this expression may seem to have limited value, since the appearance of k_F on the right-hand side assumes prior knowledge of the real equilibrium density profiles, we can make the approximation

$$\gamma_{\rm col}^{(1)} = \sqrt{\frac{3\,\pi^2\hbar^2}{m_f\,k_F^{(1)}\,g_{bb}}} \quad , \tag{4.15}$$

with the approximate wavenumber

$$k_F^{(1)} = \frac{\sqrt{2\,m_f\,\mu_f^{(1)}}}{\hbar} \quad . \tag{4.16}$$

In Fig. 4.6 we compare our simple approximation $\mu_F^{(1)}$ to μ_f over the whole range of γ from phase separation to collapse. Surprisingly the approximation remains accurate even for $\gamma > 1$, and only fails very close to the collapse instability.

In Fig. 4.7 we plot the central densities $n_\sigma(0)$ from the full solution to Eq.(4.8) as a function of γ, and compare to the prediction from Eq.(4.12). The simple prediction again performs well over a large range of γ, failing only near the collapse point. For example our prediction for the onset of phase-separation gives $\gamma_{\rm sep}^{(1)} = 7.1$ compared to a value of 6.1 obtained from the full self-consistent calculation. In contrast the prediction for the onset of collapse is $\gamma_{\rm col}^{(1)} = -11.5$, compared to the value -5.9 obtained from the full calculation. This shows that the assumption of a frozen boson density profile is not robust enough to quantitatively describe strongly attractive systems.

4.2.2 Experiment: No Collapse Instability Observed at JILA

We have seen that for sufficiently strong attractive interactions between species a collapse instability may occur in the mixture. Specifically the mean-field theory predicts a divergence in the peak densities of both species if the atom numbers become large enough. From our observations of ^{87}Rb -^{40}K Feshbach

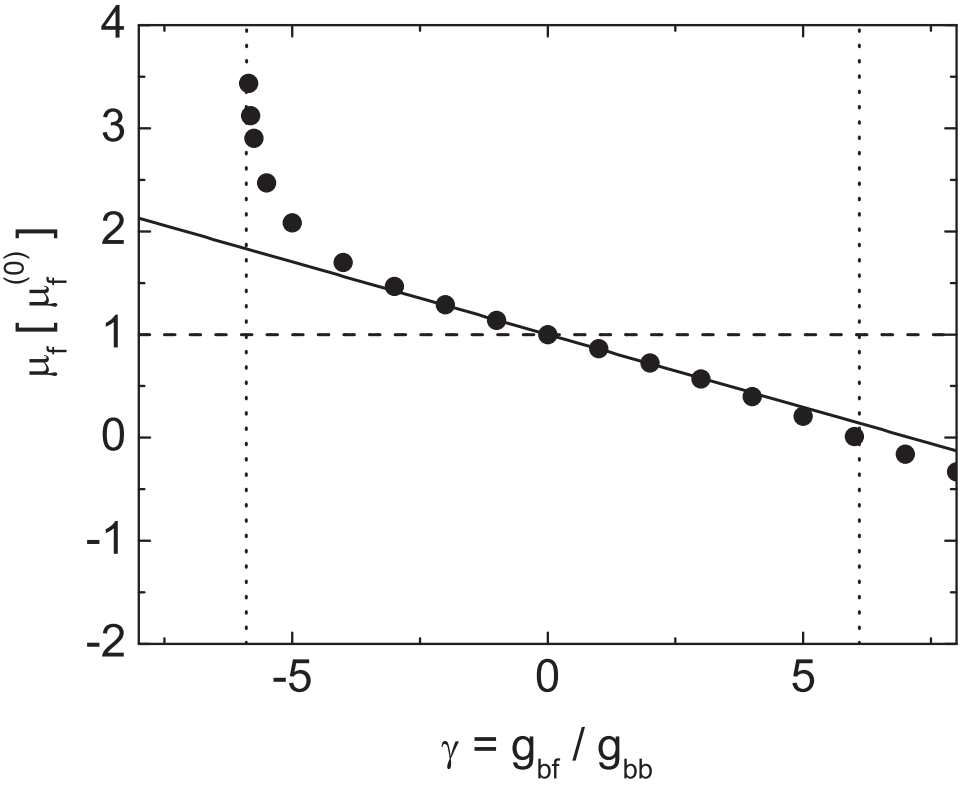

Figure 4.6: Fermion chemical potential with interactions. The points are the calculated chemical potential for a ^{87}Rb -^{40}K mixture with 10^5 atoms of each species in a spherical trap with $\omega_{\rm Rb} = 2\pi \times 100$ Hz. The solid line shows the prediction of a slope $-\gamma\,\mu_b^{(0)}$ through the non-interacting value (dashed line). The vertical dotted lines show the locations of the collapse (left) and phase separation (right), as shown in Fig. 4.7.

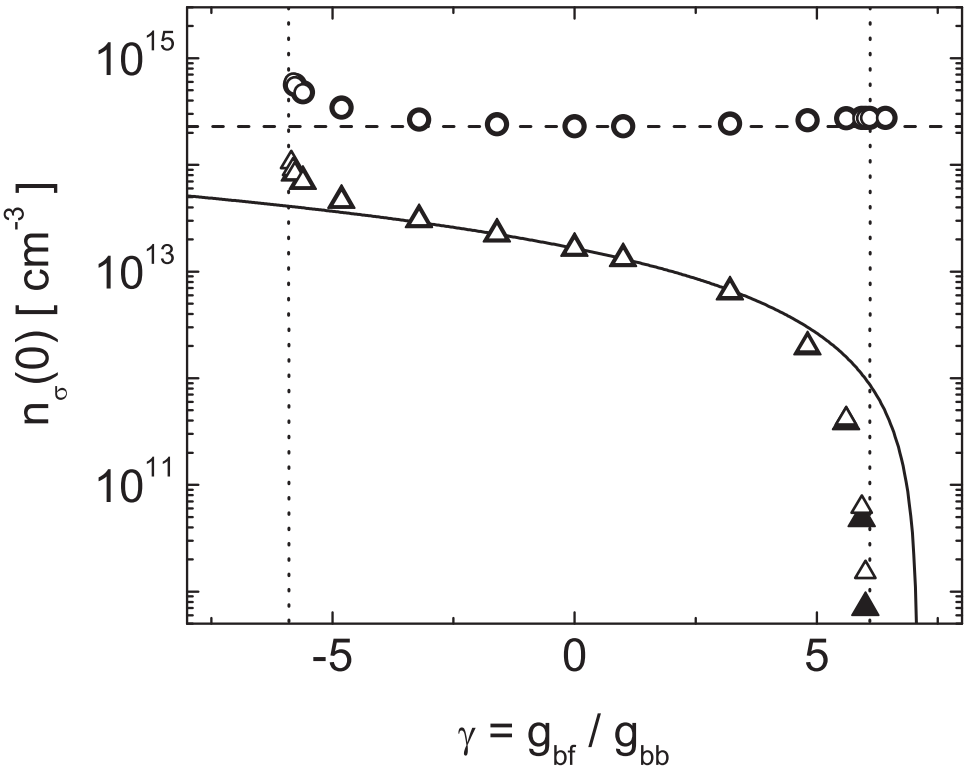

Figure 4.7: Theoretical dependence of the central densities on mean-field coupling strength. Circles give the condensate density, and triangles correspond to the fermions, for the same conditions as in Fig. 4.6. In each case the open points use the TF approximation for the bosons, and the filled points use the GP equation. The solid curve is the prediction from Eq.(4.12), and the dashed line is the noninteracting value for the bosons. The vertical dotted lines mark the collapse (left) and phase-separation (right) instabilities.

resonances, we have determined $a_{\mathrm{RbK}} = -281 \pm 15\, a_0$ [44]. We can then ask whether this attraction is strong enough to allow us to observe the mean-field collapse in the lab. This question occurs in response to a previous claim by our friends in the LENS group that they have observed the collapse in their experiment [84]. By analyzing their experimental observations in the context of the mean-field theory, they determined $a_{\mathrm{RbK}} = -395 \pm 15\, a_0$ [54], which is almost eight standard deviations from our value.

In the LENS experiment the number of atoms in each species was monitored as a function of time during the last stage of the ^{87}Rb evaporation. When the number of atoms in the condensate reached a critical value, they observed a sudden loss of $56 \pm 7\,\%$ of the ^{40}K atoms. The interpretation that this is evidence of the mean-field collapse was based on the following observations: (i) when the number of atoms in either species was halved and the experiment repeated, the loss was not observed, and (ii) the time scale for the loss ($\tau_{\mathrm{loss}} < 50$ ms) was too short to be explained by other loss processes they had observed. With respect to (i) we note that when the number of ^{40}K atoms was reduced (Fig. 2 in Ref. [84]) they still observed a loss of $50 \pm 20\,\%$, which is actually in agreement with the results for higher N_{K}. Unfortunately it is impossible to address point (ii) without knowing exactly how small τ_{loss} is, and without seeing the behavior of N_{K} measured over smaller time steps.[8]

We have tried numerous times, and under various conditions, to reproduce the results from the LENS experiment. We have never observed a sudden loss of ^{40}K atoms. An example of data from our experiment taken with our highest numbers of atoms is shown in Fig. 4.8. We observe only a slow decay of ^{40}K atoms

[8] For example, using the 3-body (Rb-Rb-K) inelastic rate constant from Ref. [84], a value of $\tau_{\mathrm{loss}} = 50$ ms would be consistent with a ^{87}Rb density of 1 to $2 \times 10^{14}\,\mathrm{cm}^{-3}$; using the 2-body rate constant from Ref. [65], the observed loss would be consistent with a density of ^{87}Rb atoms in the $|\, F = 2, m_F = 1 \,\rangle$ state of only 0.4 to $1 \times 10^{13}\,\mathrm{cm}^{-3}$.

when the ^{87}Rb condensate is formed. Additional measurements using faster evaporation rates, as in the LENS experiment, showed similar results.

In Fig. 4.9 we show the theoretical stability diagram for the ^{87}Rb -^{40}K mixture for attractive interactions of varying strengths. All calculations assume a spherical trap with $\omega_{\rm Rb} = 2\pi \times 90$ Hz, which is similar to the geometric mean trap strengths of both our experiment and the LENS experiment. The theoretical calculations are compared to the experimental observations, and we have included a recent result from a new ^{87}Rb -^{40}K experiment in the group of Klaus Sengstock at the University of Hamburg.[9] The results of the LENS experiment are clearly incompatible with the other experiments and the value $a_{\rm RbK} = -281 \pm 15\, a_0$. Since our calculations have neglected the stabilizing effects of finite temperature [85, 86, 87], gravitational sag,[10] and a repulsive second-order contribution to the interaction [88],[11] the discrepancy is actually worse than what we have shown here.

Finally in Table 4.2 we show the upper limits on $|a_{\rm RbK}|$ imposed by the mean-field theory as a result of the various experimental findings. Note that the gravitational sag is neglected in these calculations, which leads to a value of $|a_{\rm RbK}|$ that is 3% lower than what was given in Ref. [54]. From our work we must conclude that there is either some aspect of the mean-field theory which has been neglected or violated, or the sudden loss of fermions reported in Ref. [84] must find a new interpretation, for example enhanced inelastic losses due to the presence

[9] Christian Ospelkaus, in a seminar presented at JILA [55], has reported a stable mixture with 1.5×10^6 ^{87}Rb atoms and 7.0×10^5 ^{40}K atoms in a trap with $\omega_{\rm Rb} = 2\pi\times(255^2\cdot11.3)^{1/3}$ Hz.

[10] The LENS trap has stronger radial confinement than ours, which reduces their vertical sag and helps to preserve the density overlap. However, they have a weaker axial confinement and a significant tilt to their trap, resulting in a large axial displacement between equilibrium cloud positions [54]. In any event the reduction in overlap always suppresses the collapse instability to some degree. Note also that the Hamburg experiment has the tightest radial confinement of the three experiments.

[11] Quoted from the LENS group in Ref. [54]: "[T]he inclusion of [the second-order] term stabilizes the system in the range of atom numbers considered here for any value of the scattering length, thus forbidding the collapse, in contrast with the experimental findings."

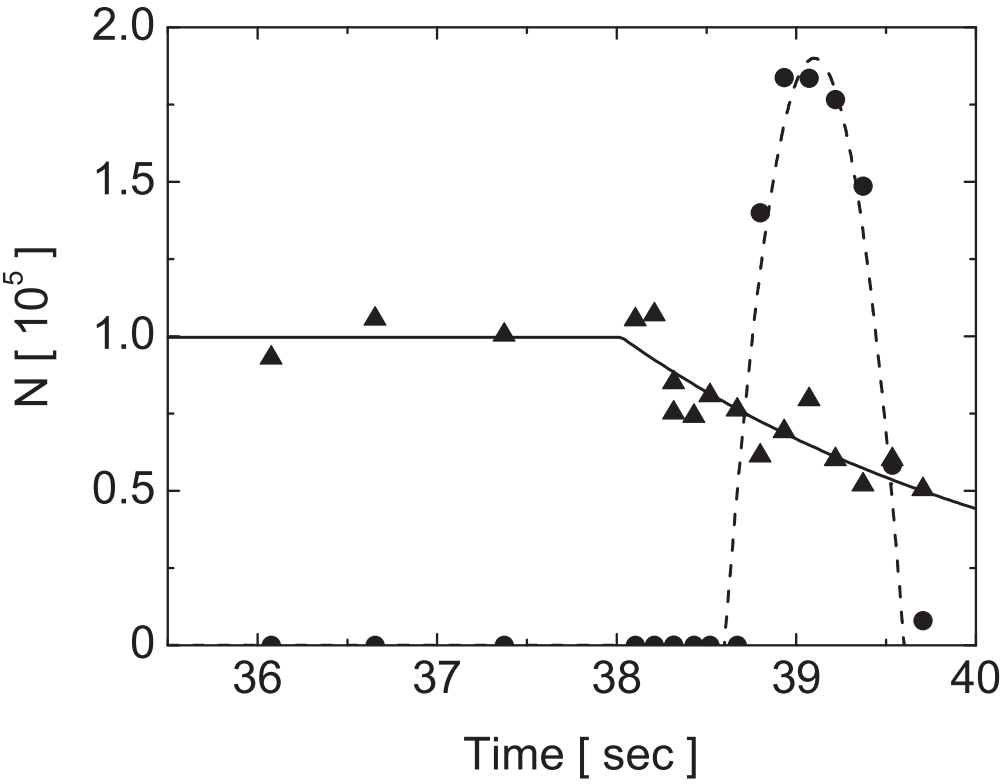

Figure 4.8: Slow decay of ^{40}K atoms with ^{87}Rb BEC. Circles give the number of atoms in the BEC and triangles give the number of ^{40}K atoms, as a function of time during the final stage of ^{87}Rb evaporation ($t = 0$ marks the start of the evaporation). The solid curve is a fit to a flat region followed by exponential decay, with a $1/e$ time constant of about 2 seconds. This curve and the dashed curve are intended as guides to the eye. These are the same data as in Fig. 3.9, where we discussed the fact that the apparent delay between the loss of ^{40}K atoms and the formation of the condensate is an artifact of a short hold time between the end of evaporation and the time-of-flight. Similar data taken without this delay (using an rf switch on the evaporation knife) also showed a slow decay of ^{40}K number, as did data taken with different evaporation rates. We have never observed evidence of the collapse instability in our experiment.

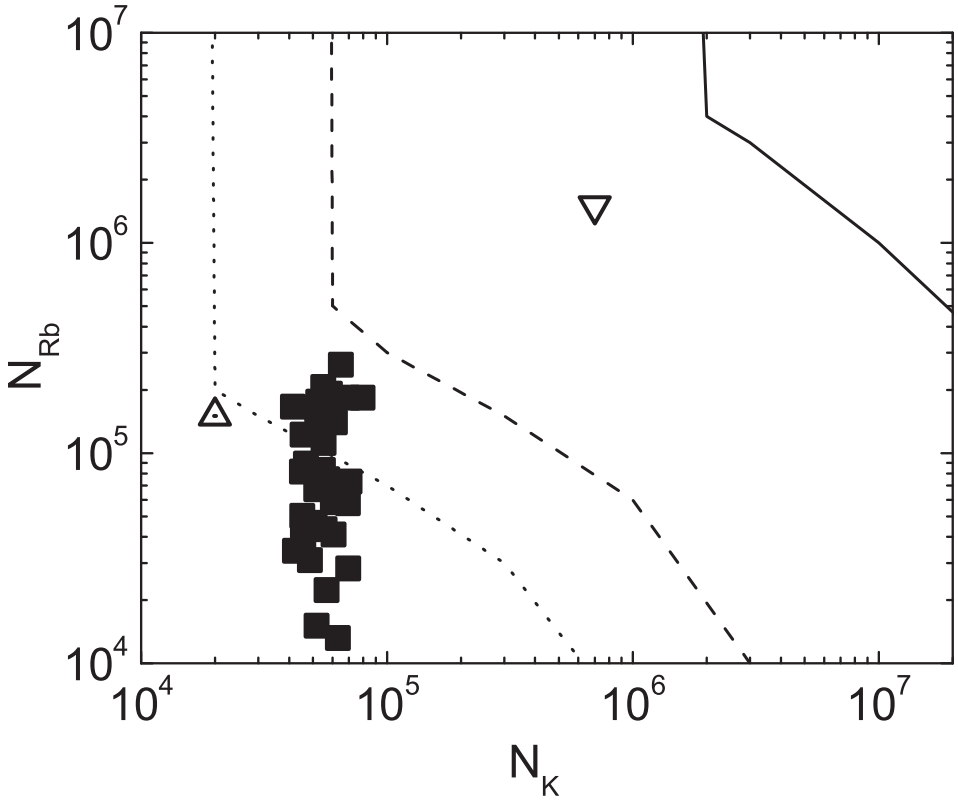

Figure 4.9: Stability diagram for attractive interactions, showing the critical number N_{Rb} for collapse as a function of N_{K}. The stability boundaries calculated from the mean-field theory correspond to cross-species scattering lengths of $a_{\mathrm{RbK}} = -281\,a_0$ (solid curve), $-350\,a_0$ (dashed curve) and $-380\,a_0$ (dotted curve); regions of stability are to the lower left of the curves. All calculations assume a zero-temperature ^{87}Rb -^{40}K mixture in a spherical trap with $\omega_{\mathrm{Rb}} = 2\pi \times 90$ Hz. Squares (■) correspond to stable mixtures in our experiment and the upward triangle (Δ) represents the onset of the observed loss of fermions from the LENS group in Ref. [84]. The downward triangle (∇) represents a stable mixture recently reported by the Hamburg group [55]. For a similar stability diagram assuming $a_{\mathrm{RbK}} = -260\,a_0$ and varying the trap strength, see Ref. [79].

Expt.	N_f	N_b	$\lvert a_{\mathrm{RbK}}\rvert_{\mathrm{max}}$
LENS [84, 54]	2.0×10^4	1.5×10^5	$384\, a_0$
JILA	6.5	2.6	366
Hamburg [55]	70	15	308

Table 4.2: Upper limits on $|a_{\mathrm{RbK}}|$. The maximum numbers of atoms observed in stable, quantum degenerate mixtures in each experiment are used to determine upper limits on $|a_{\mathrm{RbK}}|$ according to the mean-field theory.

of trapped atoms in undesired spin states. The ^{87}Rb -^{40}K Feshbach resonances which we observed in Ref. [44], and which are discussed in detail in Sects. 4.4.2 and 4.4.3, should allow us to study the collapse in a more controlled manner in the future.

4.3 Excitations

So far we have been concerned with the equilibrium properties of Bose-Fermi mixtures. In this section I will turn to some measurements of excitations in our system. The spectra of excitations are generally enriched by the coupling between purely bosonic and fermionic modes, and can reveal information about the interactions not easily obtained by other means. For example Capuzzi and co-workers showed in Ref. [89] that the modification to the frequencies of low-lying collective excitations can herald the onset of the collapse and phase-separation instabilities.

Here I'll begin with an experiment we have performed where we measured the damping rate of fermions undergoing a quadrupolar "breathe" mode after selective excitation in the presence of thermal bosons. The rate of damping of the excitation reveals information on the strength of the interactions through the magnitude of the scattering length $|a_{bf}|$. The measurement we have performed is in the collisionless regime, where the frequency of the excitation is just equal to

twice the bare trap frequency. As the bosons condense or the mean-field coupling between species increases, the frequencies of the modes are expected to change, and therefore reveal additional information, including even the sign of the scattering length [89].

I'll then discuss how we can map out the excitation spectra in the fourier domain by varying the frequency at which we parametrically excite the gas and measuring the response. This discussion will focus on a measurement we have performed with a partially condensed sample of ^{87}Rb in the absence of ^{40}K atoms. In this measurement we were able to use the coupling between thermal atoms and the condensate to observe higher-lying condensate excitations. The frequencies of these modes were mapped out by observing the "melting" of the condensate due to the dissipative coupling.

Finally I'll discuss the prospects for observing p-wave pairing of the fermions induced by interactions with the condensate [5, 6, 7]. I will show how the use of inter-species Feshbach resonances may make it feasible to observe the pairing in experiments without reaching the phase-separation or collapse instabilities.

4.3.1 Quadrupole "Breathe" Mode

Consider a single particle in a harmonic trapping potential with radial and axial frequencies ω_ρ and ω_z, respectively. If the radial trap frequency is modulated with strength ε at a frequency ω the total potential energy is given by

$$U(\vec{x},t) \;=\; \frac{1}{2}\,m\left[\,\omega_\rho^2\,(1+\varepsilon\,\sin\omega t)\,\rho^2+\omega_z^2\,z^2\,\right] \quad , \tag{4.17}$$

which leads to the Mathieu equation for the total energy. In a gas of atoms the presence of collisions generally leads to damping, so that the work done on the particles goes into heating the gas. This kind of parametric heating is considered in Refs. [90, 91]. If, however, the modulating drive is short compared to rether-

malization times, the heating can be initially avoided and a collective excitation can be generated. Data from the experiment showing the damping of this kind of excitation are shown in Fig. 4.10. This mode, which is often called the "breathe" mode, has quadrupolar symmetry with $m = 0$ and was studied theoretically for a single-species thermal gas in Refs. [71, 92], and experimentally across the BEC phase transition for a ^{87}Rb gas in [93]. In the collisionless regime, the energy oscillates between kinetic and potential energies at twice the trap frequency, until collisions convert the excess energy into heat and the gas relaxes into thermal equilibrium.

One interesting aspect of the breathe mode is that the constant of proportionality $\alpha = \tau_{\rm damp}/\tau_{\rm coll}$ which we discussed with respect to the ^{87}Rb-^{87}Rb CDR experiment is now quite different. We found for the CDR measurement that $\alpha_{\rm CDR} \simeq 2.5$ to 2.7, but the theoretical prediction for the quadrupole breathe mode is $\alpha_{\rm QB} = 15$, higher by a factor of six. Furthermore the non-interacting modes for ^{87}Rb and ^{40}K are well separated as a result of the different masses between species. This allows us to selectively excite a breathe mode in ^{40}K without affecting the ^{87}Rb atoms. We will see that the constant of proportionality $\beta_{\rm QB}$ for the ^{40}K atoms is much smaller than $\alpha_{\rm QB}$ under these conditions.

The constants $\alpha_{\rm QB}$ and $\beta_{\rm QB}$ are again determined from classical Monte Carlo simulations. To save computation time, we neglect the possibility of collisions during the trap modulation. This, together with the fact the simulation assumes a perfectly harmonic potential whose frequency is known exactly, means that the response of the simulated particles to the excitation is larger than in the experiments. We can, however, vary the amplitude of the drive in the simulations, and observe the behavior of $\alpha_{\rm QB}$ and $\beta_{\rm QB}$. The results are shown in Fig. 4.11. The ^{87}Rb single-species simulations show that $\alpha_{\rm QB} \to 14.7 \pm 0.4$ as $\varepsilon \to 0$, in agreement with the prediction $\alpha_{\rm QB} = 15$ from Refs. [71, 92]. To the best of my knowledge,

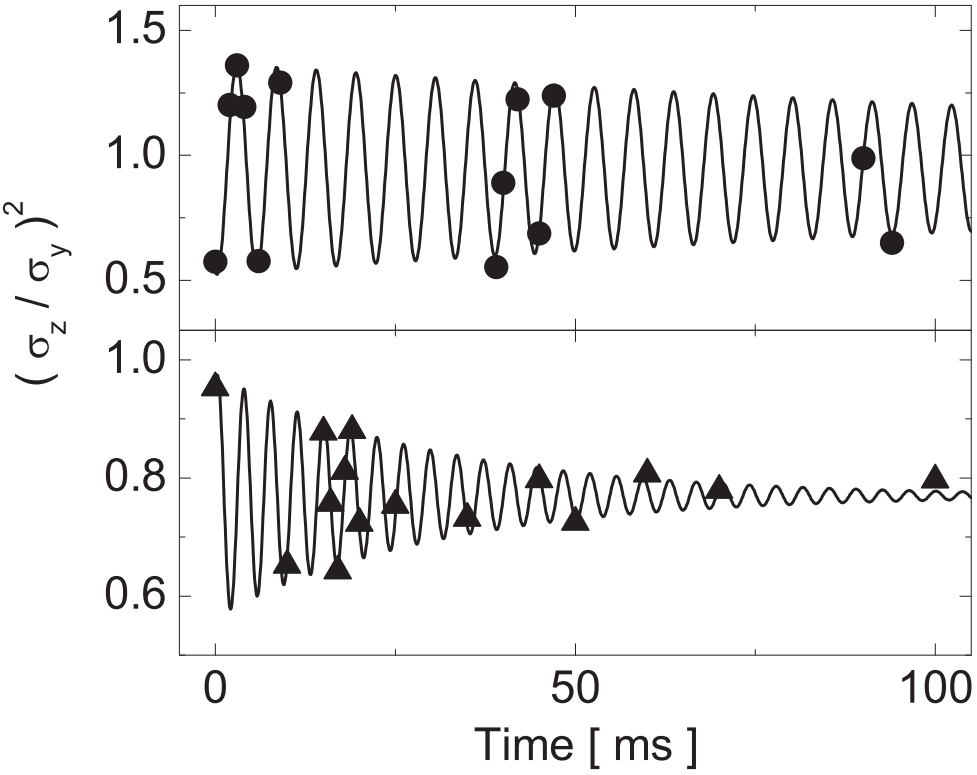

Figure 4.10: Measurement of the damping of breathe modes. Shown is the square of the aspect ratio in time-of-flight expansion as a function of evolution time in the trap after the initial excitation. Dots (•, above) and triangles (▲, below) are for ^{87}Rb atoms alone and ^{40}K atoms in the presence of ^{87}Rb, respectively. The curves are fits to damped oscillations, giving damping times of $\tau_{\mathrm{RbRb}} = 200 \pm 30$ ms and $\tau_{\mathrm{RbK}} = 31 \pm 4$ ms. Note that the ^{87}Rb data extend to 1000 ms. The ^{87}Rb trap frequencies were $\omega_\rho = 2\pi \times 91.0$ Hz and $\omega_z = 2\pi \times 25.6$ Hz. The relevant experimental parameters were $N_{\mathrm{Rb}} = 7.0 \pm 0.8 \times 10^5$, $T = 510 \pm 50$ nK for the upper data and $N_{\mathrm{K}} = 1.9 \pm 0.2 \times 10^5$, $N_{\mathrm{Rb}} = 3.5 \pm 0.2 \times 10^5$, and $T = 470 \pm 50$ nK below, where the uncertainties on number reflect statistical uncertainties only.

there is no previous theoretical prediction for $\beta_{\rm QB}$ for this kind of excitation. Our simulations suggest that $\beta_{\rm QB} \to 2.33 \pm 0.06$ for the ^{87}Rb -^{40}K mixture under the conditions of interest here.[12]

The appropriate values of $\alpha_{\rm QB}$ and $\beta_{\rm QB}$ are determined by comparing the observed amplitude of the oscillations (taking into account the time-of-flight expansions) and the amount of heating in the experiment to the results of the simulations. Using the fits from Fig. 4.11 and the data shown in Fig. 4.10, we estimate $\alpha_{\rm QB} = 10.4 \pm 0.2$ and $\beta_{\rm QB} = 2.12 \pm 0.13$. We additionally include the sag correction $f_{\rm sag}(T)$ since these data were taken at low temperature (~ 500 nK) in a weak trap (see Eq.(3.22)).

Using the observed damping times $\tau_{\rm RbRb} = 200 \pm 30$ ms and $\tau_{\rm RbK} = 31 \pm 4$ ms, and using the ^{87}Rb experiment for calibration as before,[13] we finally extract

$$|a_{\rm RbK}| \;=\; 260 \pm 50\; a_0 \quad , \tag{4.18}$$

in excellent agreement with our CDR results and the results from analyzing the positions of the Feshbach resonances discussed later. This value was given in Table 4.1 and appeared in Fig 4.3. Note that the error bar contains the fit uncertainties, uncertainties in α and β, all systematic and statistical uncertainties in T, and statistical uncertainties in number, but neglects the *systematic* uncertainty in number. This contributes an additional $\pm 70\, a_0$ uncertainty. This uncertainty arises because the equilibrium temperature after damping is a function of the ratio of atom numbers, so that the systematic number uncertainty cannot be completely eliminated as it was in the CDR measurement. Although this limits the precision of this measurement of $|a_{bf}|$, there is generally additional information

[12] I stress that the results shown here for $\beta_{\rm QB}$ should not be generalized to other mixtures or other conditions (atom numbers, temperatures, collision cross-sections, *et cetera*).

[13] The ^{87}Rb data give $|a_{\rm RbRb}| = 135 \pm 17\; a_0$, where the uncertainty neglects the systematic uncertainty due to the systematic uncertainty in atom numbers. This value for $|a_{\rm RbRb}|$ is 2σ higher than the accepted value.

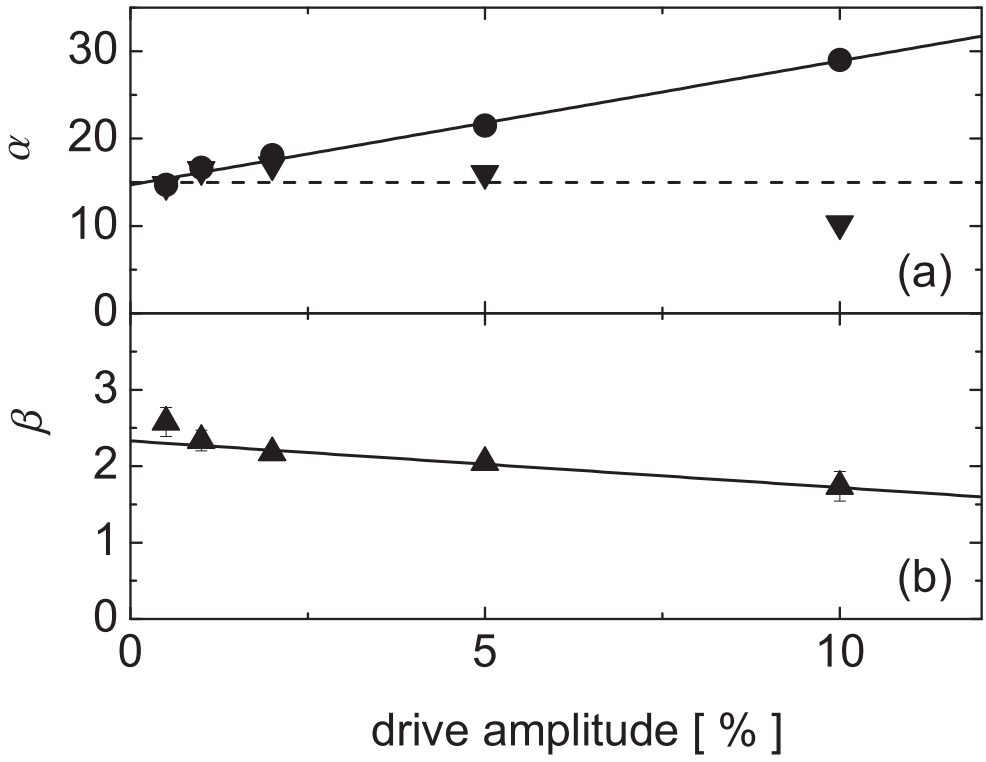

Figure 4.11: Dependence of breathe mode damping rates as a function of drive amplitude, from the Monte Carlo simulations. (a) Constant of proportionality $\alpha_{\rm QB}$, calculated using the collision rate before the drive (•) and after rethermalization (▲). The solid line is a fit to the data giving $\alpha_{\rm QB} = (14.7 \pm 0.4) + (142 \pm 8)\,\varepsilon$, and the dashed line is the theoretical prediction $\alpha_{\rm QB} = 15$. (b) Constant of proportionality $\beta_{\rm QB}$, calculated using the collision rate after rethermalization. The error bars are the statistical errors from repeated simulations. The solid line is a fit to the data giving $\beta_{\rm QB} = (2.33 \pm 0.06) - (6.1 \pm 1.9)\,\varepsilon$.

in the *frequency* of the mode. This could make this type of measurement preferable when the interactions between species become strong.

4.3.2 Frequency Domain and High-Order BEC Excitations

In Fig. 4.10 we observed the damped oscillation of $(\sigma_z/\sigma_\rho)^2$ as a function of time after the excitation. We could also have studied the breathe mode by varying the frequency of the drive, and measuring the response. For example, if we wait long enough after exciting the mode to let it completely damp out, then the excitation energy is converted into heat and the increased temperature of the gas reveals the underlying excitation. Data from this type of measurement are shown in Fig. 4.12, where we have driven an axial quadrupole mode in a single-species gas of thermal ^{87}Rb atoms. This type of collective excitation spectroscopy has a few important advantages when one is interested in the mode frequency.

One practical advantage of the frequency-domain method is that relatively few data points are needed to precisely determine the mode frequency. In Fig. 4.12 we took 10 data points and achieved a relative fit uncertainty of only 1.5×10^{-3} on the resonance frequency. Additionally, the width of the resonance is only 420 mHz, which is limited by the fourier width of the modulation pulse we applied to drive the excitation. This allowed us to observe that the frequency of the mode we excited did not equal $2\,\omega_z$, as we expected. We interpret this as evidence of beginning to approach the hydrodynamic regime. To verify this we compare this measurement to a similar measurement taken with lower atom number in Fig. 4.13. We have additionally included the theoretical prediction from Ref. [92], which interpolates between the value $2\,\omega_z$ in the collisionless regime to $(12/5)^{1/2}\,\omega_z \simeq 1.55\,\omega_z$ in the hydrodynamic regime.

Another potential advantage of the frequency-domain measurement becomes evident in systems where many modes exist at nearby frequencies. As an example

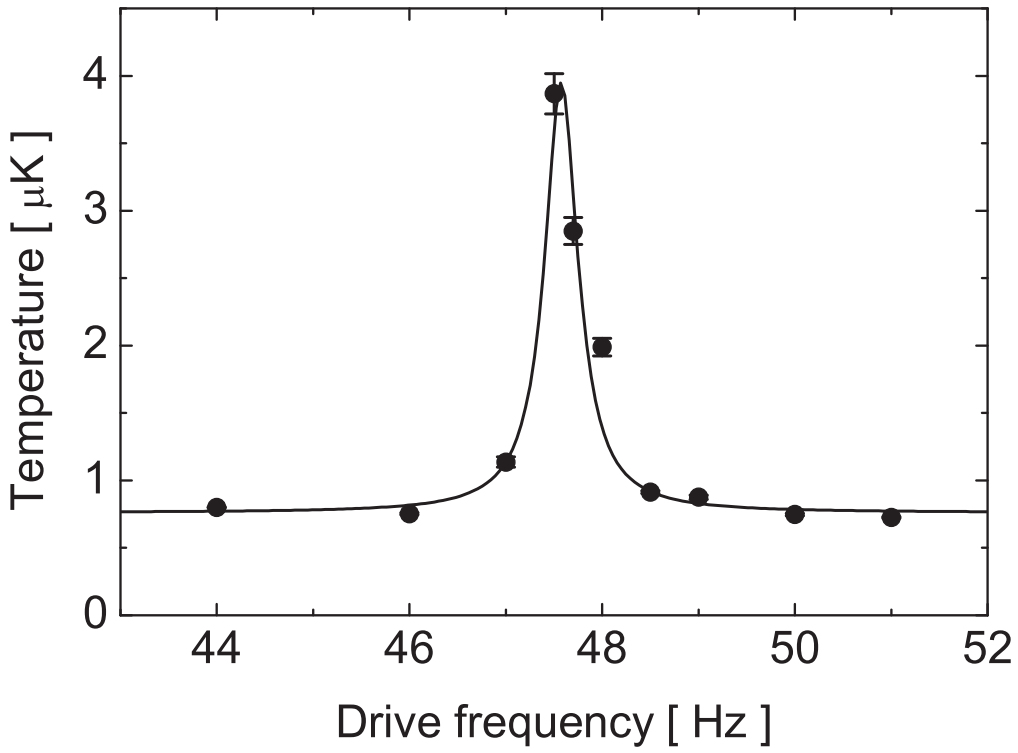

Figure 4.12: Example of excitation spectroscopy using parametric heating. Shown is the equilibrium temperature of the gas after excitation at various drive frequencies. The error bars reflect the difference between the temperatures obtained from the cloud sizes in the axial and radial directions. The curve is a fit to a Lorentzian with a FWHM of 420 ± 140 mHz and center frequency 47.58 ± 0.07 Hz.

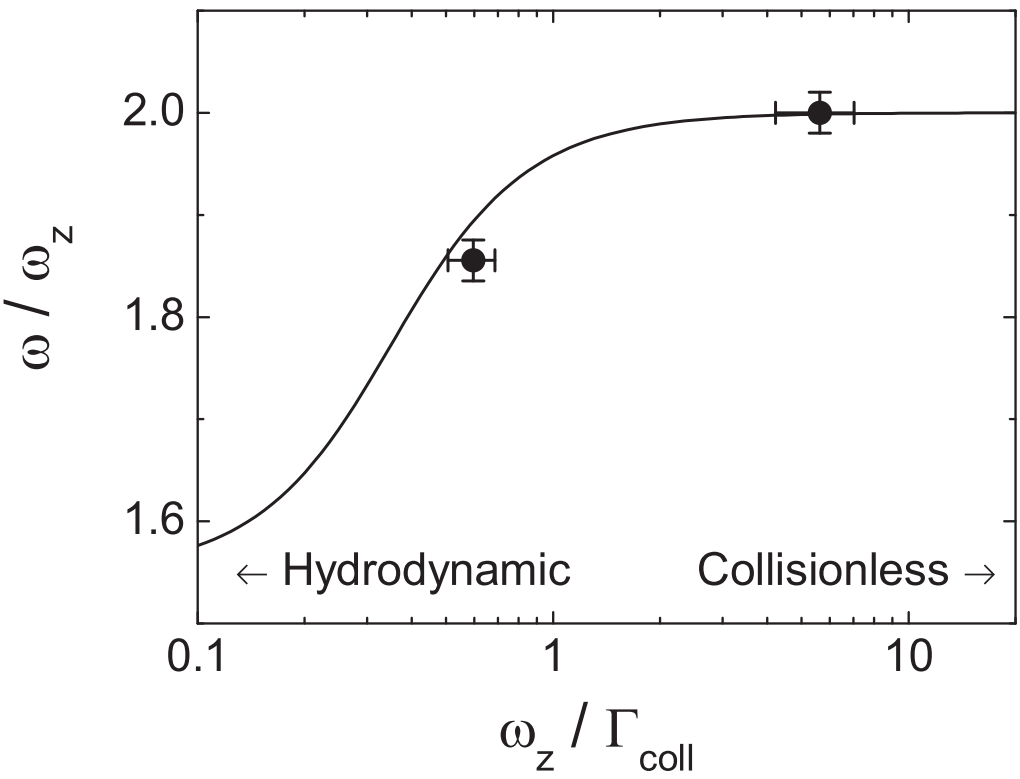

Figure 4.13: Density dependence of collective excitation frequency. Points show the axial quadrupole resonance frequency measured through parametric heating as a function of the ratio of trap frequency and collision rate. Error bars reflect statistical errors on N and T only. The curve is the interpolating formula Eq.(19) from Ref. [92] with no free parameters.

we show in Fig. 4.14 our observation of a series of nearly uniformly-spaced resonances of a ^{87}Rb condensate. The condensate is excited with a modulation of the axial trap strength, and the condensate fraction is monitored as a function of drive frequency. Dissipative interactions with thermal ^{87}Rb atoms lead to heating and subsequent melting of the condensate at the resonances. It is believed that the coupling between the BEC and thermal atoms, whose modes occur at different frequencies, also assists in the excitation process. Although these data were taken without ^{40}K atoms, I see no reason why ^{40}K atoms couldn't serve the purpose of the thermal ^{87}Rb atoms here in future experiments using interacting mixtures.

Stringari calculated the spectrum of azimuthally-symmetric axial excitations for elongated BECs and found [94]

$$\omega_l = \omega_z \sqrt{\frac{l\,(l+3)}{4}} \quad , \quad l = 1, 2, 3... \tag{4.19}$$

for mode number l. Note that the lowest mode ($l = 1$) is identified with the dipole or "slosh" mode and the $l = 2$ mode corresponds to the quadrupole mode, analogous to the breathe mode of thermal atoms we discussed in Sect. 4.3.1.

The mode frequencies are determined experimentally from Gaussian fits to the observed resonances. The positions of the peaks are then fit to Eq.(4.19) assuming consecutive modes, and letting ω_z vary. The best fit corresponds to $\omega_z = 2\pi \times 24.89 \pm 0.07$ Hz, compared to the value $2\pi \times 24.78 \pm 0.05$ Hz obtained from slosh measurements of ^{87}Rb clouds. In Table 4.3 we compare the predictions with the resonance positions observed in the experiment. These results suggest that the features in Fig. 4.14 correspond to modes $l = 12$ to 15.

Finally note that the calculation leading to Eq.(4.19) assumes $\omega_z \ll \omega_\rho$, compared to the experimental value here of $(\omega_z/\omega_\rho) = 0.16$. Corrections to the calculated spectrum due to the finite ratio of trap frequencies are dealt with in Refs. [94, 95], and beyond-mean-field corrections are discussed in Refs. [94, 96],

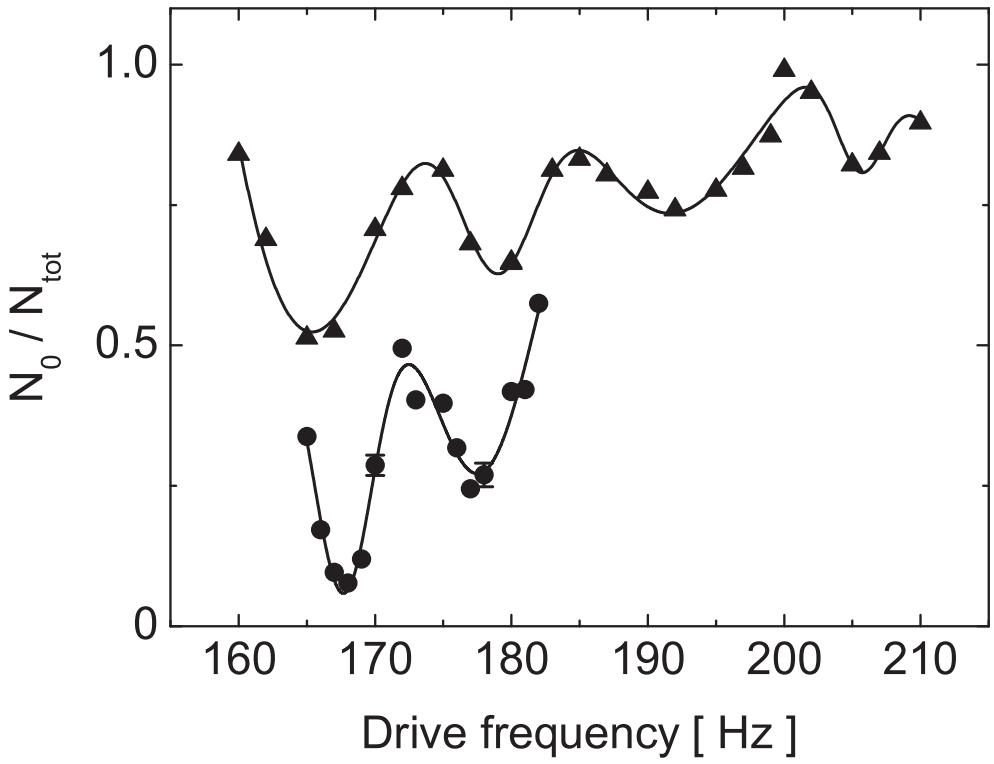

Figure 4.14: Observation of higher-lying BEC excitations. The condensate fraction $N_0/N_{\rm tot}$ is shown as a function of drive frequency from data sets taken on different days. The upper set of data have been shifted vertically by 0.5 for clarity. The error bars are the statistical errors from repeated experiments. The curves are fits to the sum of a linear background and multiple Gaussian peaks.

Experiment	Theory	l
167.7 ± 0.5 Hz	167.0 Hz	12
178.9 ± 0.3	179.5	13
189.4 ± 1.6	192.0	14
205.6 ± 0.5	204.5	15

Table 4.3: Identification of high-order BEC excitations. The fitted values are calculated from Eq.(4.19) with $\omega_z = 2\pi \times 24.89$ Hz. Experimental values are obtained from the two data sets in Fig. 4.14.

but are outside the scope of this work. A preliminary investigation suggests that corrections due to the trap anisotropy could move the values of l up by 1; I have not investigated condensate edge effects or other beyond-mean-field corrections.

4.3.3 Theory: Boson-Induced Pairing of Fermions

In this section I would like to analyze the prospects for inducing p-wave pairing among the fermions due to their interactions with density fluctuations in the condensate. This idea is considered in detail in Refs. [5, 6, 7], and is intimately related to the collective excitation spectra considered in Refs. [97, 89]. This connection will be elaborated on below.

We begin with the theoretical treatment of Efremov and Viverit [6]. They give the critical temperature for boson-mediated fermion pairing

$$k_B T_c^{(l)} \;=\; \tilde{\varepsilon}_F \, \exp\left[-\frac{1}{D(E_F) U_{fbf}^{(l)}(q)} \right] \quad . \tag{4.20}$$

Here $l = 1$ is the orbital spin for p-wave pairing, $\tilde{\varepsilon}_F$ is some energy parameter on the order of the Fermi energy, and $D(E_F) = m_f^2 \, v_F/(2\pi^2\hbar^3)$ is the density of states per volume at the Fermi surface. The quantity $U_{fbf}^{(l)}$ is the l^{th} partial-wave component of the induced interaction,

$$U_{fbf}(\vec{q}) \;=\; g_{bf}^2 \chi_b(\vec{q}, \omega = 0) \quad , \tag{4.21}$$

where we have introduced the boson density-density response function χ_b. The function $\chi_b(\vec{q},\omega)$ describes the response of the condensate density to perturbations with wave number $\vec{q}$ and frequency ω.

For simplicity, Efremov and Viverit neglected the effect of the fermions on the condensate response function. We note, however, that Yip has shown that the effect of the interactions between species is to modify χ_b according to [97]

$$\chi_b \quad \xrightarrow{g_{bf}} \quad \frac{\chi_b}{1 - g_{bf}^2\,\chi_b\,\chi_f} \quad . \tag{4.22}$$

The non-interacting response functions are given in the local density approximation by

$$\begin{aligned} \chi_b(\vec{q},\omega) &= -\frac{1}{g_{bb}}\left[\frac{c_b^2\,q^2}{\omega^2 - c_b^2\,q^2 - (q^2/2m_b)^2}\right] \\ \chi_f(\vec{q},\omega) &= D(E_F)\left[1 - \frac{\omega}{2\,v_F\,q}\,\ln\left(\frac{\omega + v_F\,q}{\omega - v_F\,q}\right)\right] \quad , \end{aligned} \tag{4.23}$$

where $c_b = (n_b/g_{bb}\,m_b)^{1/2}$ is the Bogoliubov sound speed for the condensate, and $v_F = (2E_F/m_f)^{1/2}$ is the Fermi speed. We have assumed $q \ll m_f\,v_F/\hbar$ in our expression for χ_f.[14]

Returning to Eq.(4.21) we can write

$$U_{fbf}(\vec{q}) \;=\; \frac{g_{bf}^2}{g_{bb}}\frac{1}{\Lambda_{bf} + (q/2m_b c_b)^2} \quad , \tag{4.24}$$

where we have introduced $\Lambda_{bf} = 1 - g_{bf}^2 D(E_F)/g_{bb}$ for simplicity. The $l^{\rm th}$ component of U_{fbf} is found by projecting onto the Legendre polynomial $P_l(\cos\theta)$, where $q = 2k_F\sin(\theta/2)$. This gives

$$U_{fbf}^{(1)}(\kappa_{bf}) \;=\; \frac{g_{bf}^2}{g_{bb}}\,\frac{2}{\kappa_{bf}^2}\left[\left(\frac{1}{2} + \frac{\Lambda_{bf}}{\kappa_{bf}^2}\right)\,\ln\left(1 + \frac{\kappa_{bf}^2}{\Lambda_{bf}}\right) - 1\right] \quad , \tag{4.25}$$

where $\kappa_{bf} = m_f\,v_F/m_b\,c_b$. Note that in the limit of weak interactions $\Lambda_{bf} \to 1$, and we recover the result from Ref. [6].

[14] Actually for fermion pairing we will be interested in q on the order of $m_f\,v_F$, but in the limit $\omega \to 0$. In this limit, the terms we are neglecting are equal to zero, so that our expression still holds.

Equations (4.20) and (4.25) can now be used to calculate the critical temperature for pairing. Without resonantly enhanced interactions the critical temperature for pairing under typical conditions in our magnetic trap is $\sim 10^{-11}\,T_F$, which is absurdly far outside the reach of current experiments. Assuming a ^{87}Rb -^{40}K Feshbach resonance is used to bring the system near the collapse or phase separation instabilities, however, the theory predicts $T_c^{(1)} \sim 0.17\,T_F$ for reasonable experimental conditions. It should be noted that once $U_{fbf}^{(1)}$ becomes sufficiently large, the assumptions underlying the theory begin to break down. In this case a more sophisticated calculation along the lines of that in Ref. [98] should be developed for Bose-Fermi mixtures. However the fact that we can approach this condition without hitting the collapse or phase separation instabilities is already a moral victory and extremely encouraging for future experiments.

4.4 Heteronuclear Feshbach Resonances

Throughout this thesis I have emphasized the importance of the inter-species s-wave scattering length a_{RbK} in characterizing the Bose-Fermi interactions in the mixture. From the need for large collision cross-sections during sympathetic cooling to the structure and stability of the equilibrium ground state of the mixture and its spectra of excitations, the parameter a_{RbK} is central to describing and understanding the properties of the system. In this section I will discuss our observation of ^{87}Rb -^{40}K Feshbach resonances. These resonances provide for the first time a means for experimentally varying a_{RbK} from $-\infty$ to $+\infty$ in a relatively straightforward way.

I'll begin this section with a brief description of the type of Feshbach resonances described in this thesis. We will cover a review of basic scattering theory, focusing more on results and applications than on detailed derivations. I will define what we mean by resonant scattering, and consider the example of scattering

from a spherical well potential. Although this simple example does not contain all of the ingredients of a real Feshbach resonance (which must have two or more coupled collision channels), the spherical well illustrates in a clear way the connection between bound states of a potential and the divergence of the scattering length.

I will then describe our experimental search for, and observation of, several magnetically-tunable Feshbach resonances between ^{87}Rb and ^{40}K atoms. First I'll explain how and why we load the atoms into a purely optical trapping potential and transfer the atoms to a particular set of states. Then I'll show how the strongly enhanced inelastic scattering at the position of the resonances allowed us to locate three resonances in an initial search covering a large range of magnetic fields. Subsequent comparison of the observed resonance positions with full coupled-channel calculations performed by Chris Ticknor and John Bohn suggested that one of these resonances could be p-wave in nature. This was verified experimentally through the observation of a predicted third s-wave resonance, which we had missed in the initial search. In the process of looking for the third s-wave resonance, we additionally observed a ^{87}Rb-^{87}Rb resonance, which I'll also discuss. Finally our observation of the third ^{87}Rb -^{40}K s-wave resonance is used to refine our values for the triplet and singlet scattering lengths between species.

4.4.1 Scattering Resonance Overview

4.4.1.1 Magnetically Tunable Feshbach Resonances

Scattering potentials between colliding alkali-metal atoms are shown schematically in Fig. 4.15. What the real ^{87}Rb -^{40}K potentials have in common with these cartoons is a long-range van der Waals attraction which gives way to a short-range

hard-core repulsion.[15] The net effect is an attractive potential well. Although the cartoons do not show it, these wells are typically on the order of 10^3 to 10^4 K deep, which is astronomically larger than any other energy scale in the problem. At very large inter-nuclear separations the potentials are flat, and we can think of the atoms as being independent. The asymptotic energies of the open (incoming and outgoing) and closed (excited state) channels are then separated by something like the hyperfine splitting, which may be 10 to 100 mK. This energy scale, although much smaller than the well depth, is still much higher than the temperature of the gas. The fact that exiting the collision in the excited state is energetically forbidden is the origin of the term "closed" for the upper state. However, because of the depth of the upper well it remains possible for a bound state of the well to be resonant with the low collision energy (typically 100 nK to 10 μK from the open channel threshold). If the two potentials enjoy some coupling γ, then a Feshbach resonance may arise. For example the hyperfine interaction between atoms can result in a temporary flip of one atom's spin. We'll see that virtual transitions of this type can have a dramatic effect on the collisions in the mixture.

In the experiments we exploit the fact that the different potentials generally have different magnetic moments. This allows us to tune the threshold energies of the open and closed channels relative to one another by means of the Zeeman effect. This is the nature of the Feshbach resonances described in this thesis.

4.4.1.2 Resonant Scattering and Bound States

I will now briefly review some basic results for quantum mechanical scattering. We will assume low-energy scattering, and focus primarily on the scattering length a. More detailed discussions of scattering and resonances can be found, for

[15] The real ^{87}Rb -^{40}K potentials are described in detail in Ref. [99].

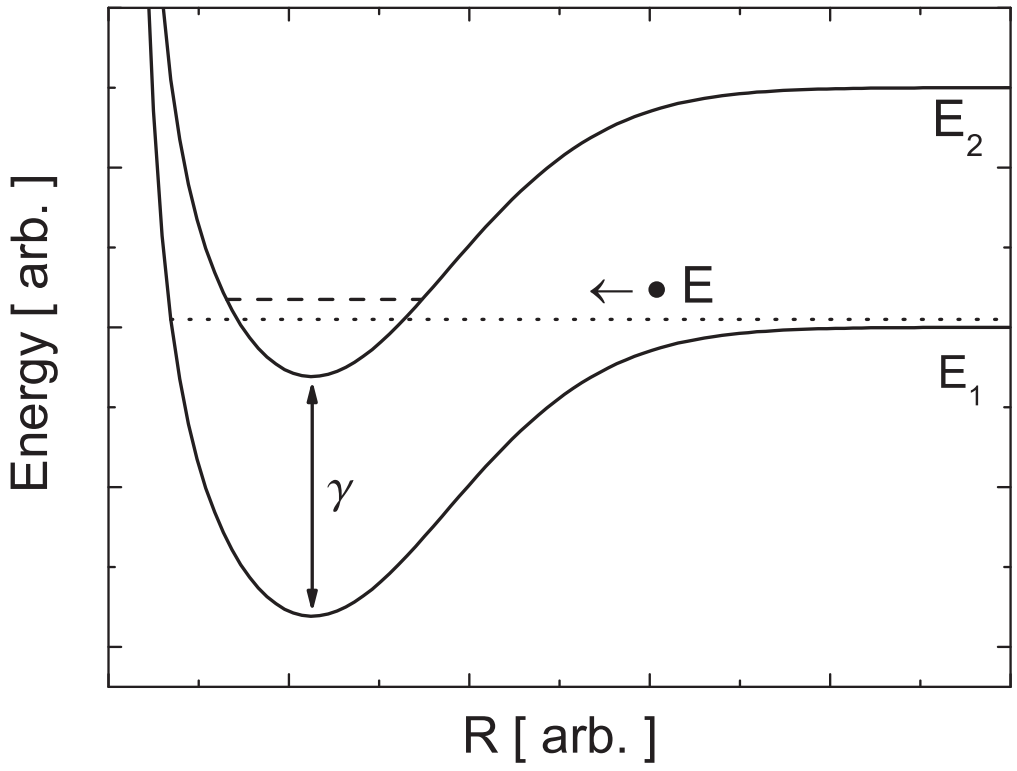

Figure 4.15: Feshbach resonance schematic. Ground and excited state molecular potentials are shown (fantastically out of scale) as a function of the distance between colliding atoms. The particles collide with total energy E (dotted line), which is just above the open channel threshold E_1 and nearly resonant with a bound state of the closed channel (dashed line). The energy difference between the open and closed channel thresholds ($E_2 - E_1$) is assumed to be much greater than the collision energy ($E - E_1$), so that exiting the collision in the closed channel is energetically forbidden. The open and closed channels are weakly coupled by some interaction γ which allows a virtual transition to the bound state before the atoms return to the open channel and exit the collision. Tuning of the energy of the bound state across the collision energy results in a divergence in the scattering length.

example, in Refs. [1, 100, 101].

The Schrödinger equation for two colliding atoms is given by

$$\left[-\frac{\hbar^2}{2\,\mu\,R}\nabla_R^2 + V(R)\right]\,\psi(R) \;=\; E\,\psi(R) \quad , \tag{4.26}$$

where μ is the reduced mass, $V(R)$ is the interaction potential, and R is the internuclear separation. In writing Eq.(4.26) we have neglected the center-of-mass (CM) degrees of freedom, which lead to a plane-wave solution if no potential acts on the CM position. For low-energy scattering it is convenient to rewrite Eq.(4.26) as

$$\left(\frac{d^2}{dR^2} + k^2\right)\,u_l(R) \;=\; \left[U(R) + \frac{l\,(l+1)}{R^2}\right]\,u_l(R) \quad , \tag{4.27}$$

where $k^2 = 2\mu E/\hbar^2$, $U(R) = 2\mu V(R)/\hbar^2$, and l is the angular momentum quantum number. The function $u_l(R)$ is the l^{th} partial-wave component of the reduced wave function. We will restrict our discussion to s-wave ($l = 0$) collisions, and drop the l labels for simplicity. As we have seen our gases are typically cold enough that atoms cannot (classically) overcome the centrifugal barrier for collisions with $l > 0$. Although this may not be true under resonant conditions, this assumption will simplify our discussion.

As in Fig. 4.15 the scattering potential $V(R)$ is assumed to be flat at exceedingly large separations. This is the region of interest to experimentally observable quantities. At large separations the solution to Eq.(4.27) therefore takes the form of a linear combination of $kR\,j_0(kR)$ and $kR\,n_0(kR)$ with j_0 and n_0 the spherical Bessel and Neumann functions of the first kinds, respectively. In the limit $R \to \infty$ this corresponds to the sum of $\sin kR$ and $\cos kR$. In other words, the only affect of the scattering potential on the outgoing wave function $\psi^{(+)}(R) = \exp(ikR)/R$

is encoded in a phase shift δ, defined by

$$\begin{aligned} \lim_{R\to\infty} \psi(R) &= \frac{e^{-ikR}}{R} - e^{2i\delta}\,\frac{e^{ikR}}{R} \\ &= \psi^{(-)}(R) - S\,\psi^{(+)}(R) \quad , \end{aligned} \tag{4.28}$$

where $\psi(R)$ is the total wave function, $\psi^{(-)}$ ($\psi^{(+)}$) is an incoming (outgoing) wave, and we have introduced the S- or scattering matrix, $S = \exp(2i\delta)$.[16]

The effect of the scattering potential has been reduced to the single parameter δ, but the phase-shift is not the most convenient quantity for describing experiments. On the other hand, I have stressed throughout this thesis that the scattering length a makes a wonderful choice. The connection between δ and a is given by

$$a = \lim_{k\to 0}\left(-\frac{\tan\delta}{k}\right) \quad . \tag{4.29}$$

We will see that the scattering potential can lead to a divergence in a under the right conditions. This is what is meant in this thesis by a scattering resonance.

Let's now consider a simple scattering calculation that will illustrate what a scattering resonance looks like, and how it relates to the presence of bound states of the scattering potential. For this discussion we will consider only a single open channel. As a crude model of the lower potential in Fig. 4.15 we introduce the absurdly-named spherical square well potential

$$V(R) = -V_0\,\Theta(R - R_0) \quad , \tag{4.30}$$

where $\Theta(\cdot)$ is the unit step function.

Since the potential $V(R)$ is piece-wise constant, the reduced wave function

[16] Despite its name, S will be a scalar throughout our discussion. Note also that since we are interested in elastic collisions, the phase shift δ is purely real.

$u(R)$ takes the form

$$u(R) \;=\; \begin{cases} \alpha \sin k'R & , \quad R \le R_0 \\ \exp(-ikR) - S\,\exp(ikR) & , \quad R > R_0 \end{cases} \quad , \tag{4.31}$$

where $\hbar\, k \;=\; (2\mu E)^{1/2}$, $\hbar\, k' \;=\; [2\mu(E + V_0)]^{1/2}$, and α is just a normalization constant.

To get α and S we match $u(R)$ and its derivative at $R = R_0$, giving

$$S \;=\; \exp(-2ikR_0)\left(\frac{k'R_0 \cot k'R_0 + ikR_0}{k'R_0 \cot k'R_0 - ikR_0}\right) \quad . \tag{4.32}$$

The S-matrix gives (i) the phase shift δ, and therefore the scattering length a, as well as (ii) the bound states of the potential $V(R)$ at the poles of S [1]. We begin with the scattering length.

Using Eq.(4.28), and taking the logarithm of Eq.(4.32) gives the phase shift

$$\delta = \tan^{-1}\left(\frac{k}{k'}\,\tan k'R_0\right) - kR_0 \quad , \tag{4.33}$$

and the scattering length is

$$a \;=\; R_0\left(1 - \frac{\tan k'R_0}{k'R_0}\right) \quad . \tag{4.34}$$

We can now identify the well radius R_0 with the off-resonant scattering length. Note that a diverges whenever $k'R_0$ equals an odd-integer multiple of $\pi/2$. This is an example of a potential that gives rise to multiple scattering resonances.

In Fig. 4.16 we show the scattering length and cross-section as a function of the well depth V_0 for zero-energy ($k = 0$) collisions. The cross-section $\sigma = 4\pi\, a^2$ for distinguishable scatterers. In the case of non-zero k, the collision cross-section is unitarity-limited according to [1]

$$\sigma \;=\; \frac{4\pi\, a^2}{1 + k^2 a^2} \quad . \tag{4.35}$$

For fixed k then, the resonant cross-section is limited to $\sigma_{\max} = 4\pi/k^2$. Alternatively for any given value of a, Eq.(4.35) allows us to determine the energy at which σ is reduced to $\sigma_{\max}/2$. As an example, for a ^{87}Rb -^{40}K mixture with $a_{\mathrm{RbK}} = -280\,a_0$ we have $k^2a^2 = 1$ for a collision energy $E_{\mathrm{coll}} \simeq 40\ \mu$K. This may be important for sympathetic cooling, which relies on large cross-sections for efficient rethermalization.[17]

Note that the scattering resonances in Fig. 4.16 occur whenever the scattering potential becomes deep enough to accommodate another bound state just below the open channel threshold. This connection between the appearance of a bound state and a scattering resonance is an example of Levinson's theorem [47].

4.4.2 Observation of Feshbach Resonances

Since the first observations of magnetically-tunable Feshbach resonances [102, 103, 104], control over the scattering length has led to a variety of important and exciting experiments in the field of ultracold atomic gases. Observations of Feshbach resonances have exploited the divergent nature of the elastic and inelastic scattering properties to perform very high-precision spectroscopy of the molecular potentials describing the collisions [105, 45, 69, 106, 107]. The ability to experimentally tune a has led to the production and controlled collapse of a ^{85}Rb Bose-Einstein condensate [108, 109], as well as the production of long-lived bright matter-wave solitons in ^{7}Li BECs [110, 111]. Ultracold molecules have been produced using time-dependent fields near Feshbach resonances [112, 113, 114, 115, 116, 117, 118, 119, 107]. BECs of molecules have been created from Bose gases [112, 120, 121], and the matter-wave coherence of the molecular BECs has been demonstrated [112, 121]. Molecular condensates have also been

[17] For more on the energy dependence of the ^{87}Rb -^{40}K elastic collision cross-section see the discussion in Sect. 3.3.3.

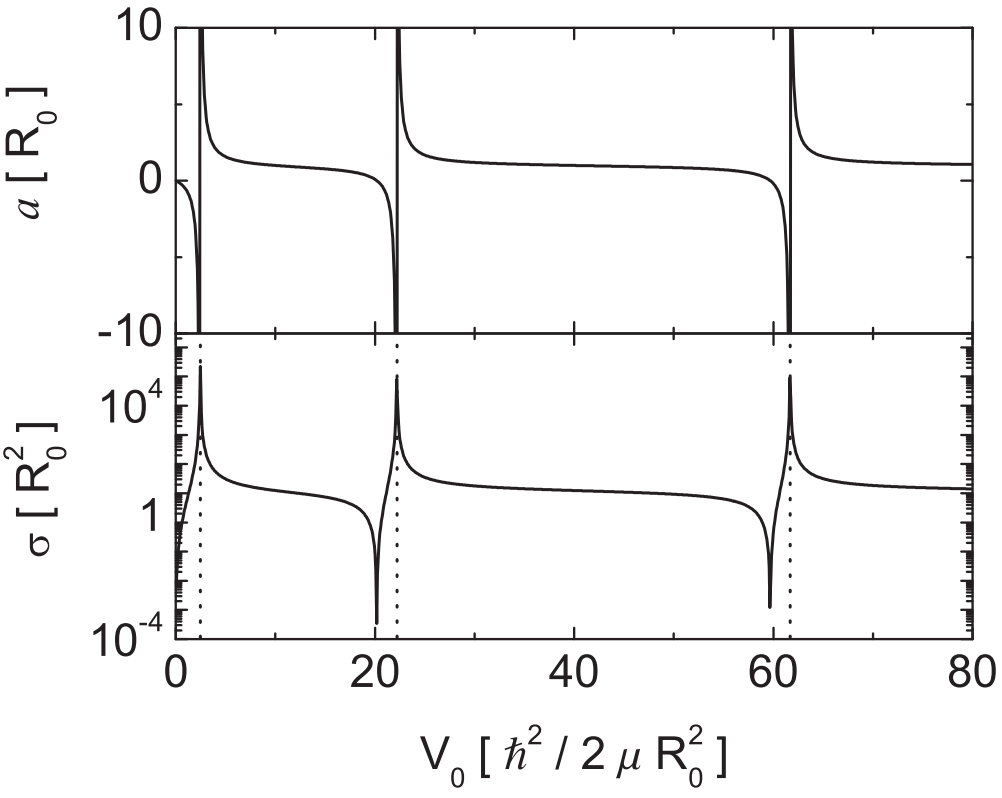

Figure 4.16: Spherical well scattering resonances. Shown is the scattering length a (above) and cross-section $\sigma = 4\pi\, a^2$ (below) as a function of V_0, with $k = 0$. The vertical dotted lines in the lower plot locate $[(2n+1)\pi/2]^2$ for integer $n \geq 0$, corresponding to the appearance of additional bound states of the potential.

produced from quantum degenerate Fermi gases [122, 123, 124], and more recent experiments with Fermi gases have accessed the BCS-BEC crossover regime [125, 126, 127, 128].

In this section I'll describe how we search for and induce Feshbach resonances in the collisions between atoms of chemically distinct species. For every one of the experiments described above, some analogous phenomenon has been predicted to occur in Bose-Fermi mixtures. These experiments are expected to greatly enrich our studies of Bose-Fermi mixtures in innumerable exciting ways.

4.4.2.1 Transfer to Resonant States

In our preceding discussion we noted that the Zeeman effect can be used to tune the separation between the threshold energies of molecular potentials with different magnetic moments. This in turn may lead to Feshbach resonances under favorable conditions. In Chapter 3 we said that our magnetic trapping is performed with the ^{87}Rb $|\,F=2, m_F=2\,\rangle$ and ^{40}K $|\,9/2, 9/2\,\rangle$ states (labeled by the low-field quantum numbers F and m_F). These states have the strongest magnetic confinement in the Ioffe-Pritchard trap and are immune to inelastic spin-changing collisions. However it is the nature of this combination of states that the molecular potentials corresponding to the cartoons in Fig. 4.15 both have the same magnetic moment. The relative energies of the open and closed channels are thus not tunable in a magnetic field. We must therefore transfer our atoms to other spin states to observe Feshbach resonances between species.

The ground-state energies of ^{87}Rb (^{40}K) atoms are shown as a function of magnetic field in Fig. 4.17 (4.18). Note the inverted hyperfine structure of ^{40}K, which has the larger-F manifold at lower energy. For the experiments described in this thesis we transfer the atoms to the lowest energy states, which are $|\,1, 1\,\rangle$ for ^{87}Rb and $|\,9/2, -9/2\,\rangle$ for ^{40}K. Mixtures of these states are stable against two-

body decay mechanisms such as dipolar loss, which can depend on magnetic field. Because these states are strong-field seeking, and because we will be applying external magnetic fields strong enough to overwhelm our Ioffe-Pritchard trap, we load the atoms into a far-off-resonance optical trap (FORT), formed at the focus of a Yb:YAG laser beam. This laser and the optical setup and drive electronics used to generate the trap were described in Sect. 2.5.3.

The energy of ground state $|\, J = 1/2; F, m_F \,\rangle$ as a function of magnetic field is determined by the Breit-Rabi formula [129],

$$\begin{aligned} E^F_{m_F}(B) &= -\frac{\Delta E_{\rm hf}}{2(2I+1)} + g_I\,\mu_B\,m_F\,B \\ &\quad \pm\frac{\Delta E_{\rm hf}}{2}\sqrt{1+\frac{4m_F}{2I+1}\,x+x^2} \quad , \end{aligned} \tag{4.36}$$

where the splitting $\Delta E_{\rm hf}$ is related to the hyperfine constant $A_{\rm hf}$ according to $\Delta E_{\rm hf} = A_{\rm hf}(I+1/2)$, and $x = (g_J - g_I)\,\mu_B\,B/\Delta E_{\rm hf}$ is a dimensionless variable related to the electronic and nuclear Landé g-factors. The $\pm$ in Eq.(4.36) corresponds to states with $m_F = m_I \pm 1/2$. Note that a sign ambiguity arises in evaluating Eq.(4.36) for states with $m_F = \pm(I+1/2)$. For these states it is convenient to use [26]

$$E^F_{m_F}(B) = \frac{I}{2I+1}\,\Delta E_{\rm hf} \pm \frac{1}{2}\,(g_J + 2I\,g_I)\,\mu_B\,B \quad . \tag{4.37}$$

The relevant constants and parameters for ^{87}Rb and ^{40}K are given in Table 4.4, and the Bohr magneton $\mu_B = h \times 1.399\,624\,624(56)$ MHz/G [130] with h Planck's constant.

The transfer to the resonant states is performed as follows. We halt the sympathetic cooling cycle just before the onset of quantum degeneracy, in order to limit density-dependent inelastic losses in the FORT. The optical trap is then ramped on linearly to 1 W in 500 ms, and the IP trap is shut off. During the IP trap shut-off a ~ 3 G bias field remains in order to maintain the spin-polarization

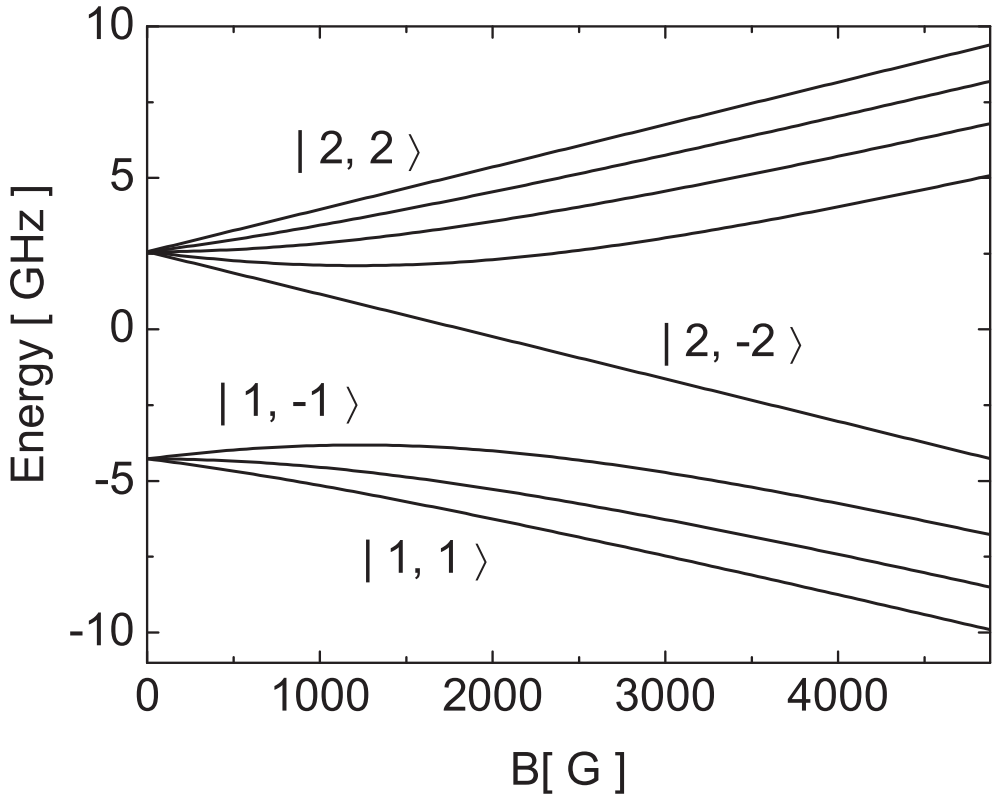

Figure 4.17: Breit-Rabi diagrams for ^{87}Rb. States are labeled according to the low-field quantum numbers $|\, F, m_F \,\rangle$. The state $|\, 2, 2 \,\rangle$ is used for magnetic trapping and evaporative cooling, and $|\, 1, 1 \,\rangle$ is used for accessing Feshbach resonances.

	^{87}Rb	^{40}K
I	3/2	4
A_{hf} [MHz]	3417.341 306 42(15)	−285.730 8(24)
g_I	−0.000 995 141 4(10)	0.000 176 490(34)
g_J	2.002 331 13(20)	2.002 294 21(24)

Table 4.4: Hyperfine parameters for the Breit-Rabi equation. All values are taken from Ref. [23].

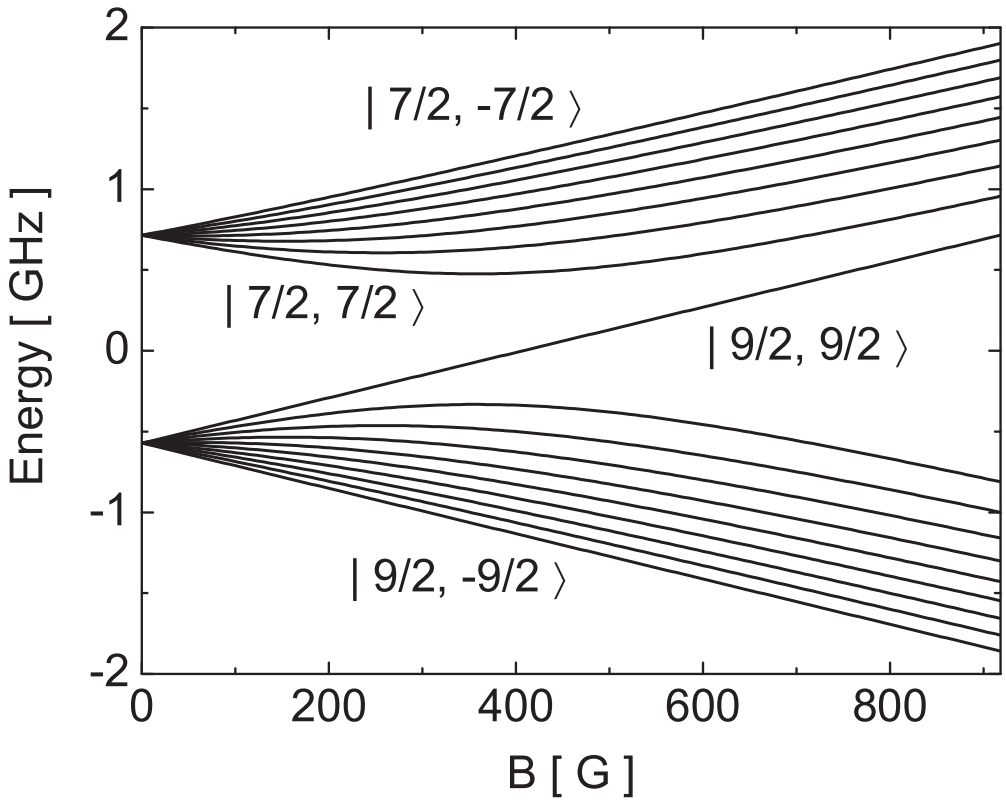

Figure 4.18: Breit-Rabi diagrams for ^{40}K. States are labeled according to the low-field quantum numbers $|\, F, m_F \,\rangle$. The state $|\, 9/2, 9/2 \,\rangle$ is used for magnetic trapping and sympathetic cooling, and $|\, 9/2, -9/2 \,\rangle$ is used for accessing Feshbach resonances.

of the atoms. At this point we have a non-degenerate $|\,2,2\,\rangle_{\rm Rb} \otimes |\,9/2,9/2\,\rangle_{\rm K}$ mixture at $\sim 14\ \mu$K. To transfer ^{87}Rb atoms from the $|\,2,2\,\rangle$ to the $|\,1,1\,\rangle$ state, we apply a frequency-swept μ-wave pulse at low field. The transfer efficiency is greater than 90%, and any atoms remaining in the $|\,2,2\,\rangle$ state are removed with a 5 ms resonant pulse of probe light. The B-field is then increased to ~ 17 G in 100 ms, and the ^{40}K atoms are transferred to the $|\,9/2,-9/2\,\rangle$ state via adiabatic rapid passage induced by an rf field that is frequency swept across all ten magnetic sublevels [131]. The ^{40}K transfer is reversible to within our number measurement fluctuations ($\sim 10\%$).

For imaging we transfer ^{87}Rb atoms back to the $|\,2,2\,\rangle$ state and image at low field. Imaging of ^{40}K atoms can either be performed using the $|\,9/2,-9/2\,\rangle$ state, by reversing the direction of the probe quantization field, or by returning the atoms to the $|\,9/2,9/2\,\rangle$ state. For our first measurements we imaged ^{40}K atoms in the optical trap, since the optical density was too low to image in time-of-flight expansion. Subsequent improvements to the experiment allowed us to increase our number of atoms and image ^{40}K in expansion and verify, among other things, that the temperature was the same for each species.

In order to calibrate the magnetic field we performed a variety of rf and μ-wave transfers of ^{87}Rb ($|\,2,2\,\rangle \rightarrow |\,2,-2\,\rangle$ and $|\,1,1\,\rangle$) and rf transfers of ^{40}K ($|\,9/2,9/2\,\rangle \rightarrow |\,9/2,-9/2\,\rangle$) with varying currents to the magnetic coils. The corresponding B-field values were determined using Eq.(4.36), yielding a calibration of

$$B \;=\; (2.5 \pm 0.3)\ \mathrm{G} + (145.11 \pm 0.10)\ \mathrm{G}/V_{\rm DAC} \quad , \tag{4.38}$$

where $V_{\rm DAC}$ is the DAC voltage used to control the magnetic coils, as described in Chapter 2. The 2.5 G offset is due to the field from the additional bias coil. The uncertainty here, which I'll refer to as the "calibration uncertainty," reflects only

the fit uncertainties in the calibration. Note that since the conversion from $V_{\rm DAC}$ to the current in the coils is given by 100 A/$V_{\rm DAC}$, the calibration in Eq.(4.38) is in reasonable agreement with the calibration in Eq.(2.5), which was obtained with a Gaussmeter over a large spatial range.

4.4.2.2 The Initial Search — "Happy Family"

We initially searched for ^{87}Rb -^{40}K Feshbach resonances over our entire range of B-fields (up to 640 G). This was because the predicted locations of the resonances in Ref. [65] had large uncertainties compared to the predicted widths, and because the predictions were based on values of the ^{87}Rb -^{40}K triplet scattering length which we believed to be inaccurate based upon our own measurements. In our search we exploited the technique used for the first observations of Feshbach resonances in ^{23}Na [102]. The MIT group's method involved sweeping the magnetic field over some relatively large range in order to locate positions of strong inelastic losses. A typical experimental timeline for the search is shown schematically in Fig. 4.19. Subsequent sweeps were narrowed until individual features could be discriminated.

Our initial search used 30 G, 1080 ms sweeps, and uncovered a broad region of loss at higher fields. By reducing the sweeps to 15 G we could see two clear features, and a third feature that was the subject of some initial controversy. We were also able to observe these features when we reversed the direction of the sweeps (sweeping from high to low fields). We subsequently held the mixture at fixed B for the full 1080 ms. The resulting loss features are shown in Fig. 4.20. For these measurements we had 3×10^5 ^{87}Rb atoms and only 3×10^4 ^{40}K atoms, so we could not observe loss of ^{87}Rb atoms at the resonances. We could however observe that no ^{40}K atoms were lost when ^{87}Rb atoms had been removed prior to loading the FORT. All of the known ^{87}Rb $|1,1\rangle \otimes |1,1\rangle$ resonances in this field

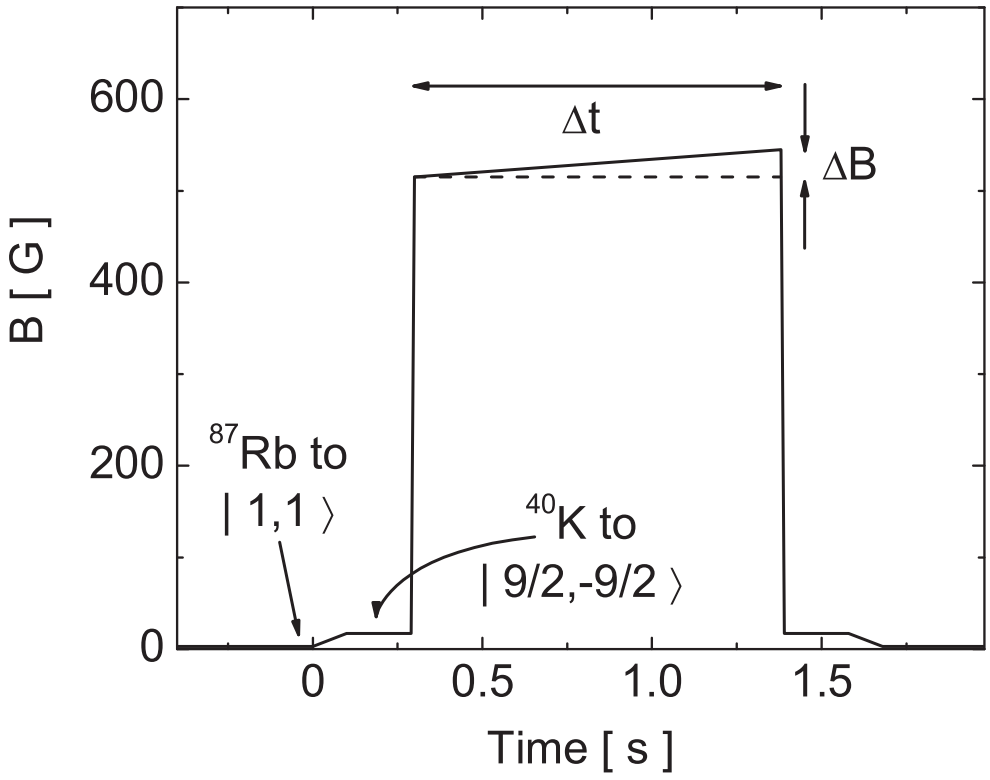

Figure 4.19: Schematic search for Feshbach resonances. Shown is the B-field as a function of time for a typical sweep in search of inelastic losses. After transferring atoms to the resonant states, the field is ramped to some high value over 10 ms. A slow sweep is then used to induce losses as the field crosses a resonance. The field is then quickly ramped down again, and the atoms are (optionally) transferred back to their original states for imaging, as described in the text. The first sweeps used $\Delta t = 1080$ ms and $\Delta B = 30$ G. To characterize the resonances in this section ΔB was reduced to zero and Δt was either 1080 or 180 ms.

range have been mapped out theoretically and experimentally by Marte *et al.* [69]. This allowed us to conclude that we had observed the first heteronuclear Feshbach resonances between ^{87}Rb and ^{40}K. A detail of the widest of the inelastic features (resonance "S") is shown in Fig. 4.21. Comparison with theoretical calculations suggests that this resonance also has the widest elastic feature, being about 10 G from peak to zero.

There is currently no theory directly connecting the elastic and inelastic scattering features for Bose-Fermi Feshbach resonances. We have used both Gaussian and Lorentzian fits to determine the center locations and widths of the observed inelastic features. These positions are compared to detailed coupled-channel calculations of ^{87}Rb -^{40}K scattering performed by Chris Ticknor and John Bohn [44]. For these calculations, the ^{87}Rb -^{40}K triplet and singlet scattering lengths a_s and a_t are tweaked by modifying the repulsive inner walls of the ^{87}Rb -^{40}K molecular potentials. For each pair of values of a_s and a_t, a calculation of $a(B)$ is performed, and the theoretical positions of the elastic Feshbach resonances can be compared to the experimentally observed loss features.

From the original predictions in Ref. [65], we expected a trio of resonances appearing somewhere roughly between 500 and 600 G. When we tried to make sense of the data in Fig. 4.20, however, we were unable to get reasonable agreement between theory and the experiment. Something was evidently still missing. We had an idea, but it seemed like a long shot.

4.4.2.3 The Missing Link

To reconcile the discrepancy between our observations and the theory, we proposed that the low-field ("M") resonance might be the p-wave resonance originally predicted to exist in Ref. [132]. When p-wave scattering was included in the calculations, we saw that it was possible that we had observed a p-wave resonance

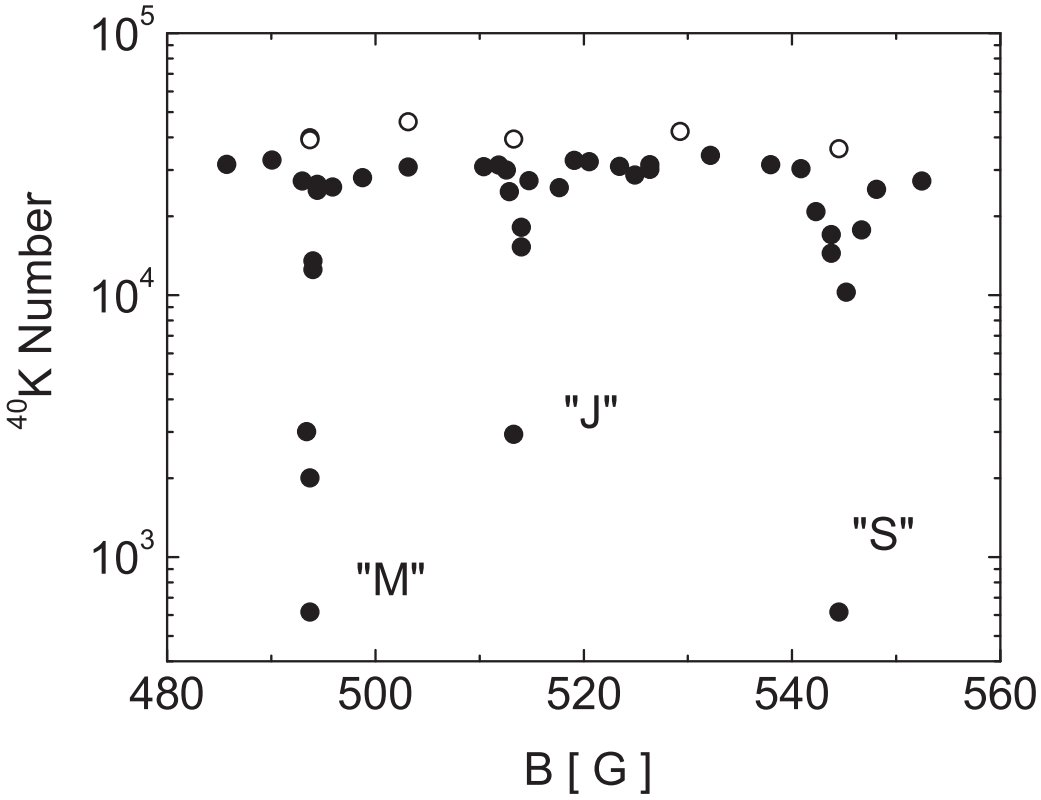

Figure 4.20: First observation of ^{87}Rb -^{40}K Feshbach resonances. The number of ^{40}K atoms is shown after holding at fixed B for 1080 ms. The solid points (•) are with ^{87}Rb atoms present, and the open points (∘) have had ^{87}Rb removed prior to loading the optical trap. For the two lowest points no ^{40}K atoms could be observed and we show our estimate for the smallest number we could measure, based on the noise level of the images. For the record the labels are not quantum numbers, but correspond to the names "Michele," "Jon," and "Shin," who each adopted one resonance. According to Gaussian fits to the loss features, and using the calibration from Eq.(4.38), the features occur at 493.6 ± 0.5, 513.5 ± 0.5, and 544.9 ± 0.6 G, where the uncertainty reflects only the fit and calibration uncertainties.

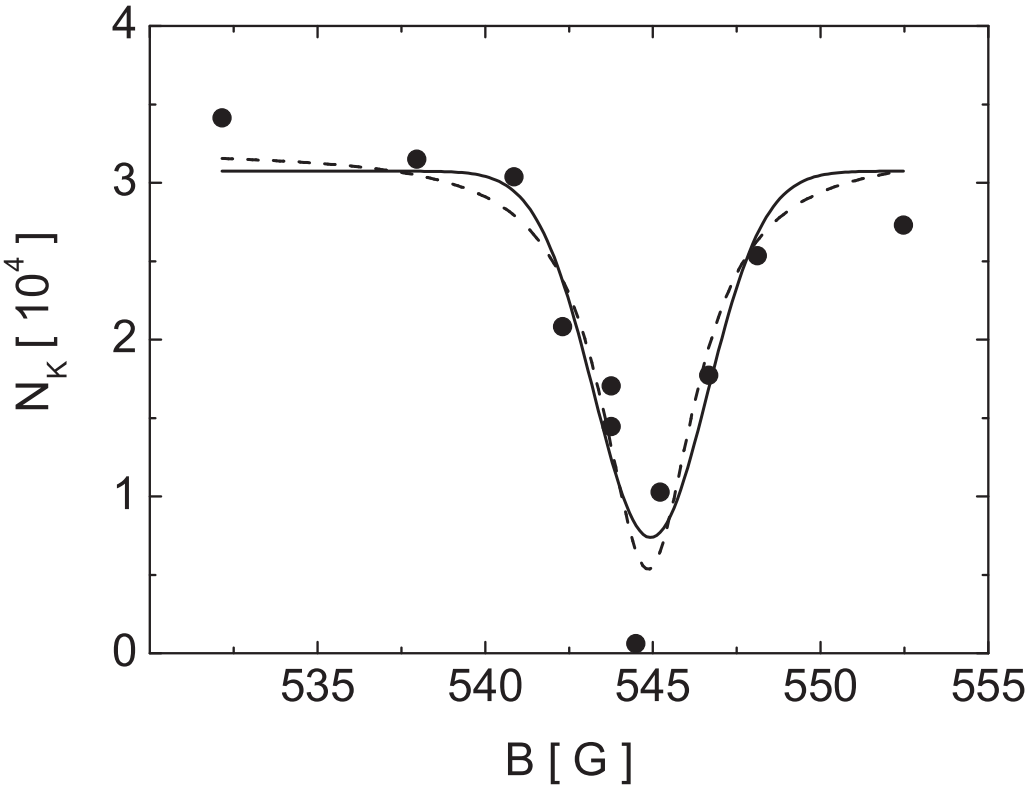

Figure 4.21: Detail of the widest inelastic feature. Solid points are the data for the "S" resonance from Fig. 4.20. The solid line is a fit to a Gaussian, and the dashed line to a Lorentzian, yielding center positions of 544.9 ± 0.3 G and 544.9 ± 0.2 G, respectively, where the uncertainty reflects only the fit and calibration uncertainties. The Gaussian $1/e^2$ width is 3.3 ± 0.7 G. Such fits are used to determine the center locations of the resonances, but do not represent a quantitative model of the loss features.

at 494 G and that we had missed a third s-wave resonance in our original search.[18] From analyzing the data in Fig. 4.20, Chris and John predicted the existence of another s-wave resonance at 444 ± 8 G.

We started scanning again at lower fields and worked our way back up. A feature was observed at 403.6 ± 0.4 G. Although we were initially pretty happy to find another resonance, the discrepancy between this field value and the prediction seemed to actually make things worse. The mystery deepened when we removed ^{40}K from the system and observed a strong loss of ^{87}Rb atoms, shifted by about 1 G from the ^{40}K feature. Both sets of data are shown in Fig. 4.22. This shift between the ^{40}K and ^{87}Rb loss features is well outside the repeatability of the machine. For example, two months after our first observation of the resonances in Fig. 4.20, we returned to the "M" resonance and found exactly the same center position. In contrast, the data in Fig. 4.22 were taken on consecutive days.

After consulting Ref. [69] we identified these features with a previously known $|\,1,1\,\rangle_{\rm Rb} \otimes |\,1,1\,\rangle_{\rm Rb}$ resonance. Specifically the narrow resonance predicted to lie at 403±2 G in Ref. [45], and observed by the Munich group at 406.23 ± 0.03 G in Ref. [69]. Without a better understanding of the nature of the inelastic processes involved in each case, I cannot say why we observe such a pronounced shift between the ^{40}K and ^{87}Rb loss features. I will note, however, that the observation of loss from one species near the other species' resonances was mentioned in passing by the MIT group in Ref. [133]. Regardless, we were hunting for a ^{87}Rb -^{40}K resonance, so we returned to the experiment.

As we moved up in field we encountered the resonance we had missed in the original search. The data are shown in Fig. 4.23, along with a Gaussian fit

[18] One interesting consequence of the p-wave nature of the "M" resonance is a predicted 290 mG splitting of the elastic feature [132]. Our narrowest data set for the corresponding inelastic feature has a $1/e^2$ width of 700 mG, so that such a splitting could not be observed in the experiment.

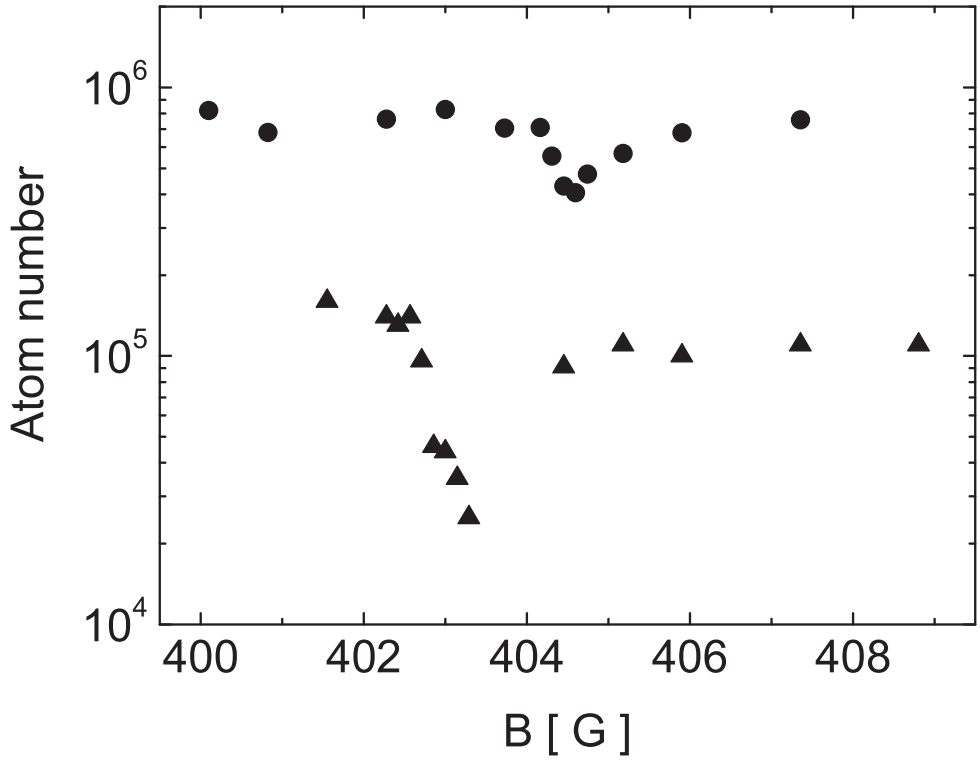

Figure 4.22: Observed ^{87}Rb-^{87}Rb resonance. The circles (•) show the ^{87}Rb number with no ^{40}K atoms present, and the triangles (▲) show the ^{40}K number in the presence of ^{87}Rb. Both measurements used 180 ms holds at each magnetic field value. The two features are separated by about 1 G, which is far outside the reproducibility of the experiment.

Resonance	B [G]	Δt [ms]
S	544.9 ± 0.6	1080
J	513.5 ± 0.5	1080
M	493.6 ± 0.5	1080
	493.8 ± 0.5	180
Jy	454.6 ± 0.5	180

Table 4.5: Summary of observed ^{87}Rb -^{40}K resonances. Shown are the center positions of the inelastic features obtained from Gaussian fits, and using the B-field calibration in Eq.(4.38). Error bars reflect only the fit and field calibration uncertainties. The hold time Δt is also shown in order to highlight a possible shift in the position of the "M" resonance.

with center position 454.6 ± 0.5 G, in good agreement with Chris' and John's prediction. These data used a 180 ms hold, and were measured in time-of-flight by imaging the ^{40}K atoms directly in the $|\,9/2, -9/2\,\rangle$ state with a reversed probe quantization field. Our search for and preliminary identification of the Feshbach resonances was now complete.

4.4.3 Analysis and Results

In this section we analyze our experimental observations and compare the results to the theoretical description of the resonances. We show in Table 4.5 the positions of the four ^{87}Rb -^{40}K resonances we have so far observed. I have included two measurements of the "M" resonance taken with different hold times (1080 and 180 ms). These data show a 170 ± 90 mG shift between centers. This may be a real effect related to the B-field stability over the longer hold time, or the shot-to-shot repeatability of the experiment. In the future the calibration uncertainty can be reduced by calibrating the field with single-species measurements at each resonance position [69]. This is superfluous for our purposes here, since we still lack a theory to connect the inelastic and elastic features.

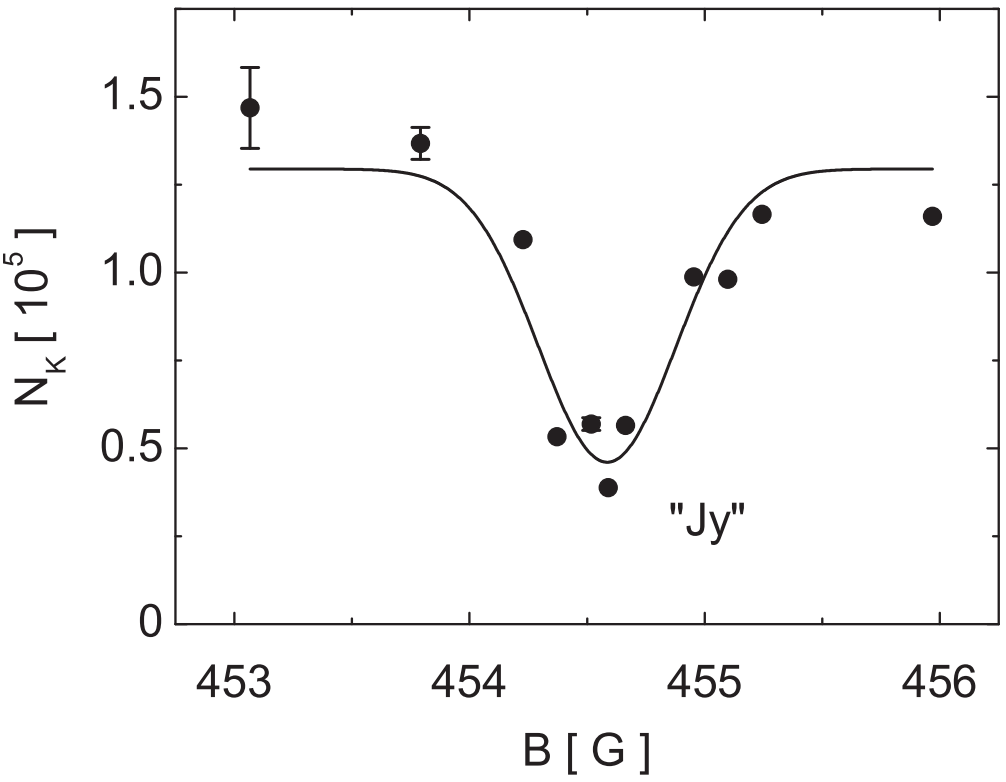

Figure 4.23: Most recently observed ^{87}Rb -^{40}K resonance. Points show the number of ^{40}K atoms remaining after 180 ms hold with ^{87}Rb at each field value. The error bars reflect the statistical error from repeated measurements. The curve is a Gaussian fit with center position 454.6 ± 0.5 G. This resonance is labeled "Jy" ("Jianying") throughout this thesis, in keeping with the labels in Fig. 4.20.

The Gaussian widths of the observed loss features and the estimated systematic uncertainty arising from imperfect B-field stability and field inhomogeneities are shown in Fig. 4.24. Although there is currently no theory available to relate the locations of the elastic scattering features to the inelastic features, we can say that the two types of feature should lie within the width of the narrower feature [69], assuming neither is narrower than the experimental resolution. The observed inelastic widths in Fig. 4.24 are all larger than the estimated experimental imperfections. We therefore use the inelastic widths to give the systematic uncertainties in the positions of the elastic features.

To fit the theory to the inelastic data, the triplet and singlet scattering lengths a_t and a_s are varied in the calculations until the peaks of the calculated elastic cross-sections coincide with the peaks of the observed inelastic features. Our original analysis of the three features in Fig. 4.20 yielded $a_s = -54 \pm 12\, a_0$ and $a_t = -281 \pm 15\, a_0$ [44]. However since our discovery of the third s-wave resonance ("Jy"), we can refine our best values for a_s and a_t. For simplicity we use only the three s-wave resonances for the analysis and vary only a_s and a_t in the calculations. This is because the locations of the s-wave resonances are generally less sensitive than the p-wave to the temperature and C_6 coefficient [132]. The reduced χ^2 contours are shown in Fig. 4.25. The best fit ($\chi^2 = 0.996$) corresponds to the scattering lengths

$$\begin{aligned} a_s &= -77^{+2}_{-4}\, a_0 \\ a_t &= -275^{+8}_{-7}\, a_0 \quad . \end{aligned} \tag{4.39}$$

This value of a_t is in excellent agreement with our result in Ref. [44], as well as the values obtained in the CDR and quadrupole oscillation experiments. The value of a_s in Eq.(4.39) is about 2σ larger in magnitude than the value we obtained from our original analysis. I believe the value here is more accurate. Since the

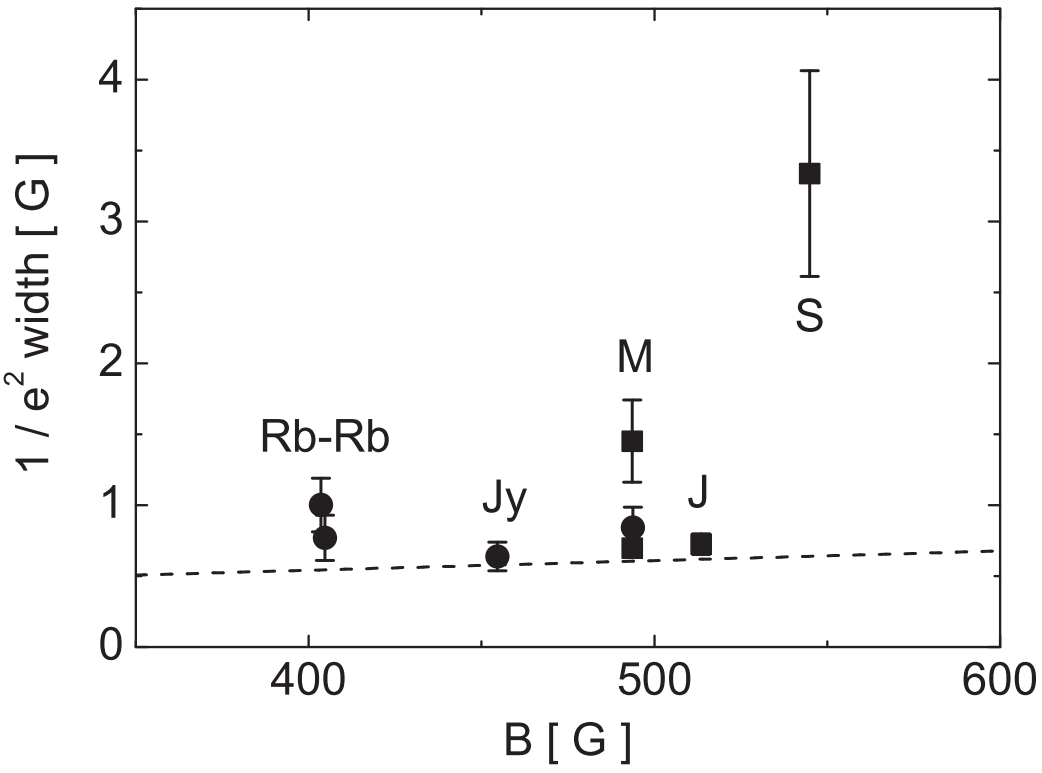

Figure 4.24: Measured widths of the inelastic features. Points show the $1/e^2$ widths of gaussian fits to the loss features. Squares (■) use 1080 ms hold times and circles (•) use 180 ms; error bars denote only the fit and calibration uncertainties. The dashed line is the total estimated width arising from systematic errors, scaled by $2\times$ to convert rms values to $1/e^2$ values.

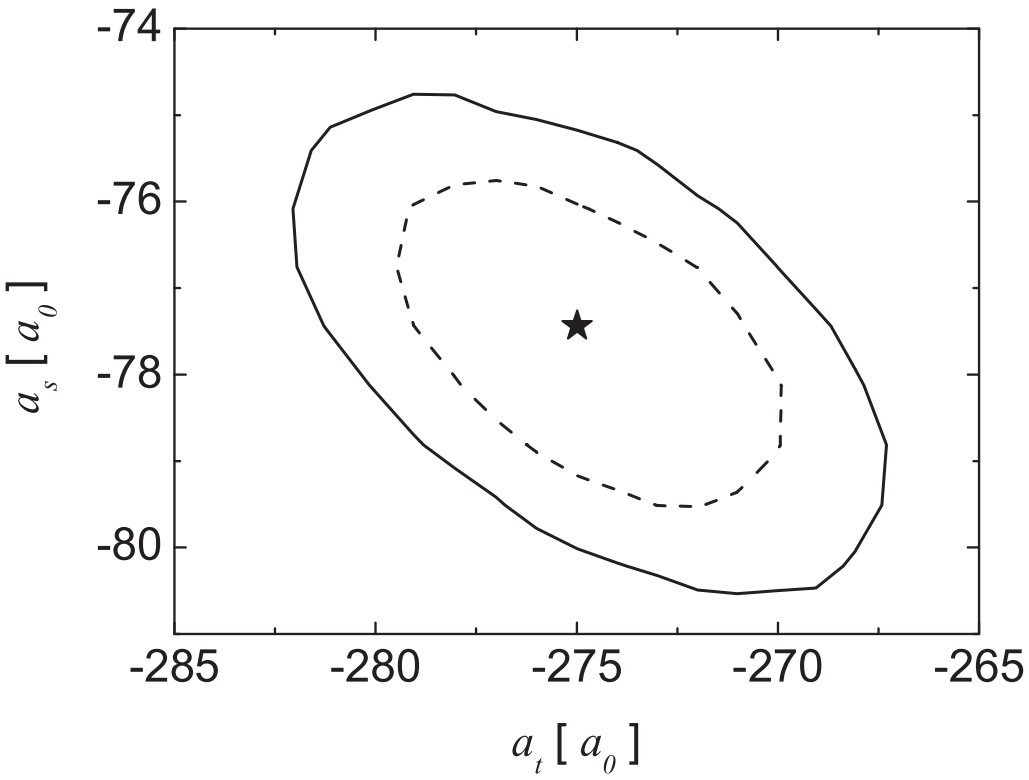

Figure 4.25: Scattering length determination from inelastic resonance features. Shown are reduced χ^2 contours in the singlet-triplet scattering length plane, from fits to the locations of the three s-wave resonances. The best fit gives $\chi^2 = 0.996$ for $(a_t = -275\,a_0, a_s = -77\,a_0)$, indicated by the star. The dashed contour shows where χ^2 has increased by 1, and the solid contour by 2.3 [134]. The solid contour determines the error bars shown in Eq.(4.39).

locations of the "S" and "J" resonances are predominantly sensitive to a_t, the original value of a_s was determined almost exclusively by the p-wave resonance. In contrast the position of the s-wave "Jy" resonance is more sensitive to a_s than to a_t, allowing us to obtain a more robust fit. We can re-analyze the p-wave resonance in the future after we have more detailed experimental and theoretical results. Newly acquired spectroscopic data [135, 136, 137] may help to fine-tune the calculations by improving the ^{87}Rb -^{40}K potentials.

Finally from the best fits we obtain a detailed picture of the predicted elastic scattering length as a function of magnetic field. In Fig. 4.26 we show the results of the coupled-channel calculation for the nominal singlet and triplet scattering lengths given in Eq.(4.39). By fitting the coupled-channel calculation to the formula

$$a(B) \;=\; a_{\rm bg}\left(1-\sum_{i=1}^{3}\frac{\Delta_i}{B-B_{0i}}\right) \quad , \tag{4.40}$$

we obtain the parameters characterizing the s-wave elastic resonance features. The results are shown in Table 4.6. According to the calculation the background scattering length $a_{\rm bg} = -225\,a_0$ for $|\,1,1\,\rangle_{\rm Rb} \otimes |\,9/2,-9/2\,\rangle_{\rm K}$ collisions. The predicted 10 G width of the "S" resonance makes it suitable for a variety experiments we would like to perform.

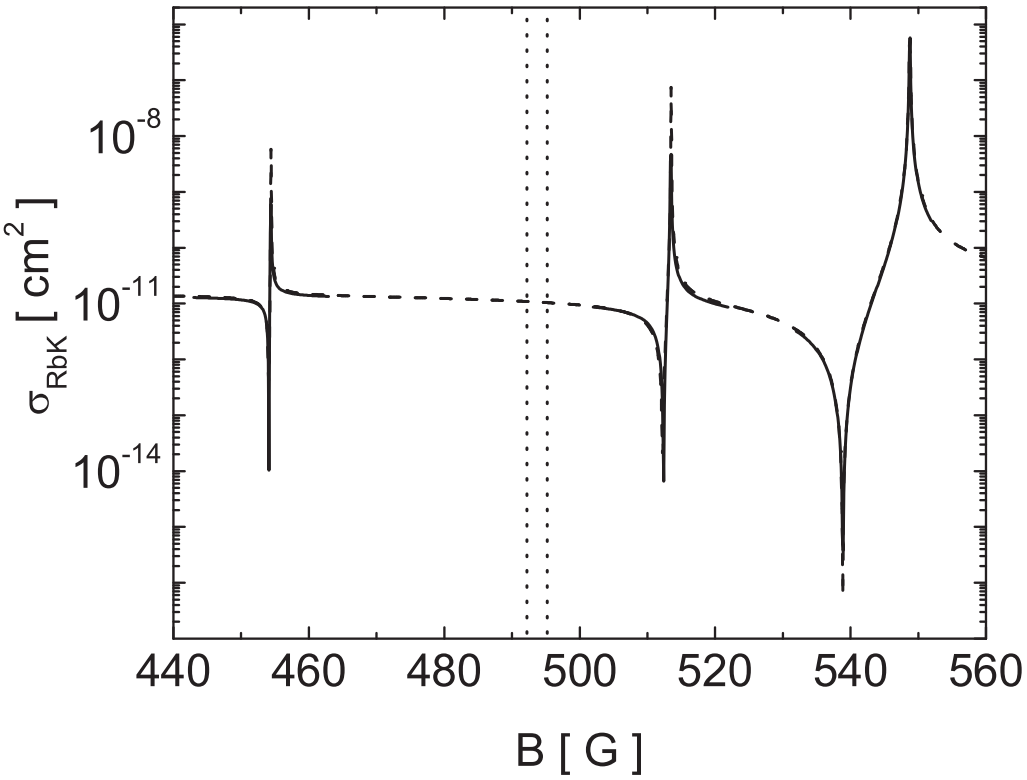

Figure 4.26: Theoretical elastic resonance features. Shown is the s-wave scattering cross-section as a function of field for $|\,1,1\,\rangle_{\rm Rb} \otimes |\,9/2,-9/2\,\rangle_{\rm K}$ collisions. The solid curve is the full coupled-channel calculation, performed by Chris Ticknor and John Bohn, and the dashed curve is a fit to Eq.(4.40). For reference the vertical dotted lines show the expected location of the elastic p-wave "M" resonance.

Resonance	$B_{\rm exp}$ [G]	B_0 [G]	Δ [G]
S	$544.9 \pm 0.6 \pm 3.4$	548.8	-10.3
J	$513.5 \pm 0.5 \pm 0.7$	513.5	-0.9
Jy	$454.6 \pm 0.5 \pm 0.6$	454.4	-0.3

Table 4.6: Summary of calculated elastic s-wave features. The experimental positions $B_{\rm exp}$ are reproduced from Table 4.5, and the second uncertainty gives the width of the inelastic feature. Also shown are the parameters describing the three ^{87}Rb -^{40}K s-wave resonances according to Eq.(4.40), as determined from the best fit in Fig. 4.25. The calculated background scattering length for $|\,1,1\,\rangle_{\rm Rb} \otimes |\,9/2,-9/2\,\rangle_{\rm K}$ collisions is $a_{\rm bg} = -225\,a_0$.

Chapter 5

Summary and Outlook

I have described in this thesis the design, construction, and operation of an experimental apparatus we have built for producing and studying quantum degenerate ^{87}Rb -^{40}K Bose-Fermi mixtures. By evaporatively cooling the bosons and sympathetically cooling the fermions, we can produce a nearly pure Bose-Einstein condensate of ^{87}Rb atoms coexisting with a Fermi gas of ^{40}K atoms at about 0.2 times the Fermi temperature. The appearance of quantum degeneracy in the experiments has been characterized for each species and compared to theoretical predictions.

I have additionally presented measurements of the magnitude of the s-wave scattering length $|a_{\mathrm{RbK}}|$ between species. The scattering length is important in characterizing a variety of the equilibrium and dynamic properties of the mixture. I have discussed techniques for studying some elementary excitations of the system, and have analyzed the prospect for exploiting interactions with phonons in the condensate to create fermion pairs. It has been shown that current theory places this prospect within reach of current experiments.

Finally I have discussed our observation of Feshbach resonances between ^{87}Rb and ^{40}K atoms in non-degenerate mixtures. These important experiments open up the possibility of tuning a_{RbK} to any desired value in the experiment. Our experimental observations have been compared to theoretical calculations

and used to refine parameters describing the collisions between species.

The future of this experiment lies in exploiting these resonances in a variety of useful and exciting ways. After first measuring the elastic properties of the resonances, we can begin to utilize the resonant control of the interactions between species in a number of experiments. Possible studies include the controlled collapse of the mixture, the production of polar fermionic molecules, the generation of a boson-induced sound mode among spin-polarized fermions, generation of bright Bose-Fermi matter wave solitons, and the boson-induced pairing of fermions.

Relevant Publications

- J. Goldwin, S. B. Papp, B. DeMarco, and D. S. Jin, *Two-species magneto-optical trap with ^{40}K and ^{87}Rb*, Phys. Rev. A **65** 021402 (2002)

- J. Goldwin, S. Inouye, M. L. Olsen, B. Newman, B. D. DePaola, and D. S. Jin, *Measurement of the interaction strength in a Bose-Fermi mixture with ^{87}Rb and ^{40}K*, Phys. Rev. A **70**, 021601 (2004)

- S. Inouye, J. Goldwin, M. L. Olsen, C. Ticknor, J. L. Bohn, and D. S. Jin, *Observation of Heteronuclear Feshbach Resonances in a Mixture of Bosons and Fermions*, Phys. Rev. Lett. **93**, 183201 (2004)

- J. Goldwin, S. Inouye, M. L. Olsen, and D. S. Jin, *Cross-dimensional relaxation in Bose-Fermi mixtures*, Phys. Rev. A **71**, 043408 (2005)

Appendix A

Monte Carlo Simulation Details

These appendices refer to the Monte Carlo simulations and analytic theory which we presented in detail in Ref. [66]. Familiarity with that reference is assumed throughout this discussion.

In this first Appendix, let me describe some aspects of the Monte Carlo (MC) simulations that lurk behind the scenes, and are not often presented in the light of day. These notes are intended for people wishing to develop MC simulations of their own, or even hoping to debunk our hard-earned and rigorously established results.

A.1 Choice of Parameters and Failure Modes

The Monte Carlo (MC) simulations are extremely useful for simulating various experiments, but they can also be very dangerous if the user puts his/her blind faith in their results. We have found that the best approach to the simulations is to treat them like the experiments themselves, and to subject them to intense scrutiny and modeling in order to understand (and, only then, believe) the results. Here I will talk about some failure modes of the simulations that we have studied.

In Ref. [66] we described the simulation in some detail. In that discussion we talked about the probability for two particles, labeled k and l to collide. This

probability was said to be given by

$$\tilde{p}_{\rm coll} \;=\; \frac{\sigma_{kl}\,|\vec{v}_k - \vec{v}_l|\,\Delta\,t}{\mathcal{V}_c} \quad . \tag{A.1}$$

Although we said it, and you believed it, this is only true assuming $\tilde{p}_{\rm coll}$ is very small. To see why, note that the equilibrium distribution of relative speeds is Gaussian. This means that for any fixed values of cross-section, time-step, and collision volume $\mathcal{V}_c$, there is still some finite probability that the relative collision speed will be large enough to make $\tilde{p}_{\rm coll}$ greater than one. We conclude that $\tilde{p}_{\rm coll}$ does not represent a probability in the conventional sense. The real distribution of times between collisions is given by a Poisson distribution [138], so that the collision probability is

$$\begin{aligned} P_{\rm coll} \;&=\; 1 - \exp(-\tilde{p}_{\rm coll}) \\ &\simeq\; \tilde{p}_{\rm coll} \quad . \end{aligned} \tag{A.2}$$

This is the basis for our statement that $\langle\, \tilde{p}_{\rm coll} \,\rangle$ should be kept well below $\sim 10\%$ for accurate results. Note that Eq.(A.2) is still only approximate, as it ignores any possibility for 3-body collisions, or multiple 2-body collisions within a single time-step, but we will see that it is still very good until exceedingly bad choices of the parameters Δt and r_c are made.

In Fig. A.1 we show the number of collisions per calculated collision time $\tau_{\rm coll} = \langle\, \Gamma_{\rm coll} \,\rangle^{-1}$ as a function of $\langle\, \tilde{p}_{\rm coll} \,\rangle$ for a single-species simulation of particles in equilibrium. When $\langle\, \tilde{p}_{\rm coll} \,\rangle$ becomes too large, we observe too *few* collisions, since we look for them only once per time-step. The results in Fig. A.1 suggest that the approximation in Eq.(A.2) is still good for $\langle\, \tilde{p}_{\rm coll} \,\rangle \sim 1$. Our simulations, which typically use $\langle\, \tilde{p}_{\rm coll} \,\rangle$ in the range of 10^{-3} to 10^{-2}, are therefore expected to be accurate in this respect.

The other input parameter we use is the critical distance r_c between atoms. Particles in the simulation must come within r_c of each other for a collision to be

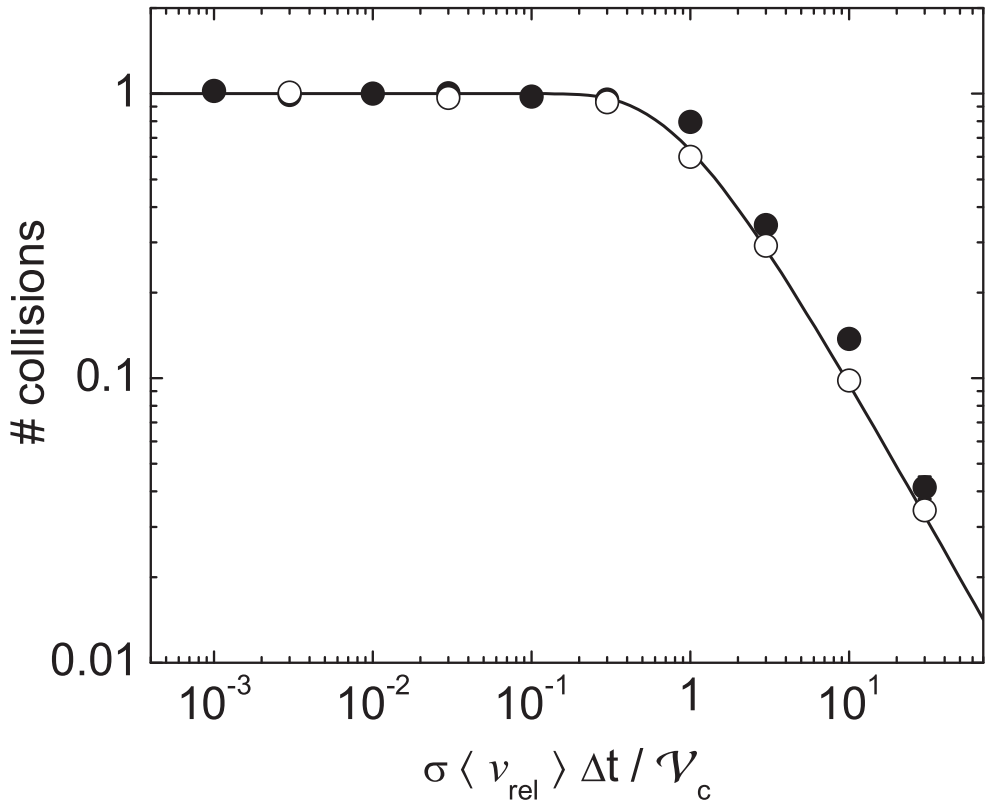

Figure A.1: Effect of bad choice of time-step on the MC simulation. Shown is the number of collisions per calculated collision time as a function of $\langle \tilde{p}_{\rm coll} \rangle$ for a single-species gas in equilibrium. Filled points (•) use $\tilde{p}_{\rm coll}$ and open points (◦) use $1 - \exp(-\tilde{p}_{\rm coll})$ to calculate the collision probability in the simulations. The solid line is just the expected behavior for a Poisson distribution. All simulations used 10^3 particles with an average of 10^{-2} particles per volume $\mathcal{V}_c$.

considered. Although in Ref. [66] we referred to the probability of a cell of volume $\mathcal{V}_c = 4\pi r_c^3/3$ being occupied, this is again not a probability in the conventional sense, as nothing forbids a choice of parameters where the average number of particles per cell volume $\mathcal{V}_c$ is greater than 1. Results from the MC simulations are shown in Fig. A.2. If $\mathcal{V}_c$ is large enough, any given particle will see all $N-1$ of the other particles within the volume. The number of collisions per particle in one collision time will then saturate at $(N-1)\langle\,\tilde{p}_{\rm coll}\,\rangle$, since the calculated collision probability is independent of the positions of the particles. Since we are considering dilute gases, one may expect that in the limit $\mathcal{V}_c \to 0$ there will be no chance for collisions in the simulations, but this is not the case. If the quantity $\tilde{p}_{\rm coll}$ is kept constant, then the time-step $\Delta t \propto \mathcal{V}_c$. This means that for every decrease in $\mathcal{V}_c$, there must be a corresponding increase in the number of times collisions are searched for. This ensures that a constant rate of collisions is maintained. We again conclude that our insistence on keeping $\langle\,n\,\rangle\,\mathcal{V}_c$ around 10^{-3} to 10^{-2} is extremely conservative, and should lead to accurate simulations.

A.2 Transition to Hydrodynamic Behavior

In this section I will use the MC simulations to consider the onset of hydrodynamic behavior in cross-dimensional relaxation (CDR) experiments. Hydrodynamic behavior is generally characterized by a density (or cross-section) so high that a particle undergoes many collisions within a time equal to the trap period. If this happens, the kinetic energy is continuously being re-randomized and the atoms no longer undergo simple harmonic motion in the trap. If one imagines that we begin the CDR experiment with anisotropic energy $\Omega = E_{x,y}/E_z$, then collisions will randomize the relative kinetic energies of colliding atoms before they have had a chance to move very far. The gas will then have isotropic kinetic energy, but the potential (and center-of-mass kinetic) energies will still maintain the

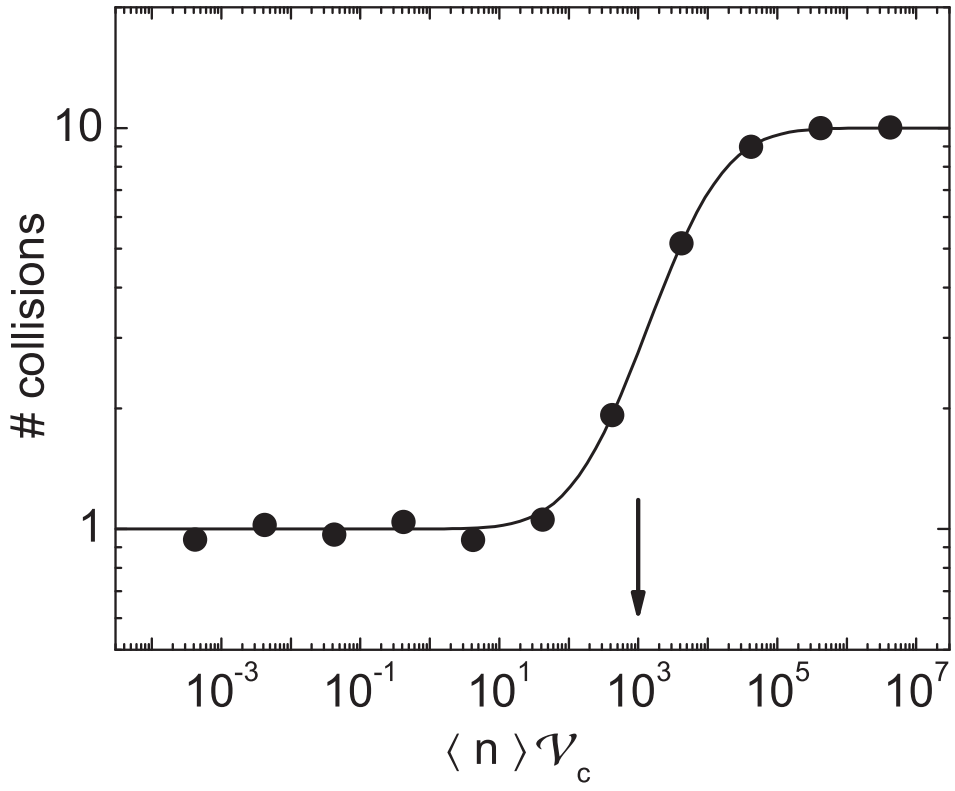

Figure A.2: Effect of bad choice of critical distance of approach on the MC simulation. Shown is the number of collisions per calculated collision time as a function of increasing $\mathcal{V}_c$ for a single-species gas in equilibrium. The curve is just to guide the eye. All simulations used 10^3 particles with $\langle\, \tilde{p}_{\rm coll}\,\rangle = 10^{-2}$. The arrow indicates the point where $\langle\, n\,\rangle\, \mathcal{V}_c = N$.

initial anisotropy Ω. The observed relaxation rate will therefore be slower than in a system with the same collision rate but much higher trapping frequencies.

Our MC simulations typically use atom numbers $\sim 10^4$ to save computation time. These numbers, however, are expected to leave our simulations in the collisionless regime. To determine when a system like ours enters the hydrodynamic regime I ran a series of simulations of ^{87}Rb -^{40}K relaxation with the trapping frequencies fixed to our experimental conditions. The collision rates were varied by either increasing the number of particles, decreasing the temperature (the simulations always use Maxwell-Boltzmann statistics), or increasing the collision cross-sections (with the ratio σ_{bb}/σ_{bf} fixed). Results are shown in Fig. A.3. For these simulations, hydrodynamic behavior was observed to begin for $\langle \Gamma_{\rm coll} \rangle \sim \omega_{z,\rm K}$.

The inset to Fig. A.3 describes the oscillatory behavior which is observed for simulations of CDR in the hydrodynamic regime. An example of the relaxation in this regime is shown in Fig. A.4. Note the 180° phase-shift between oscillations of the axial and radial energies, which means the cloud aspect ratio also oscillates. As the gas goes more deeply into the hydrodynamic regime, the oscillation frequency appears to approach twice the ^{87}Rb axial frequency. The ^{87}Rb axial frequency is the lowest trap frequency in the system, and twice this frequency is the frequency at which kinetic and potential energy are exchanged in the absence of collisions. This oscillatory behavior and the nonlinear dependence of the damping rate on the boson density may be used as a guide in experiments. One should be able to clearly identify whether measurements are performed in the collisionless or hydrodynamic regime.

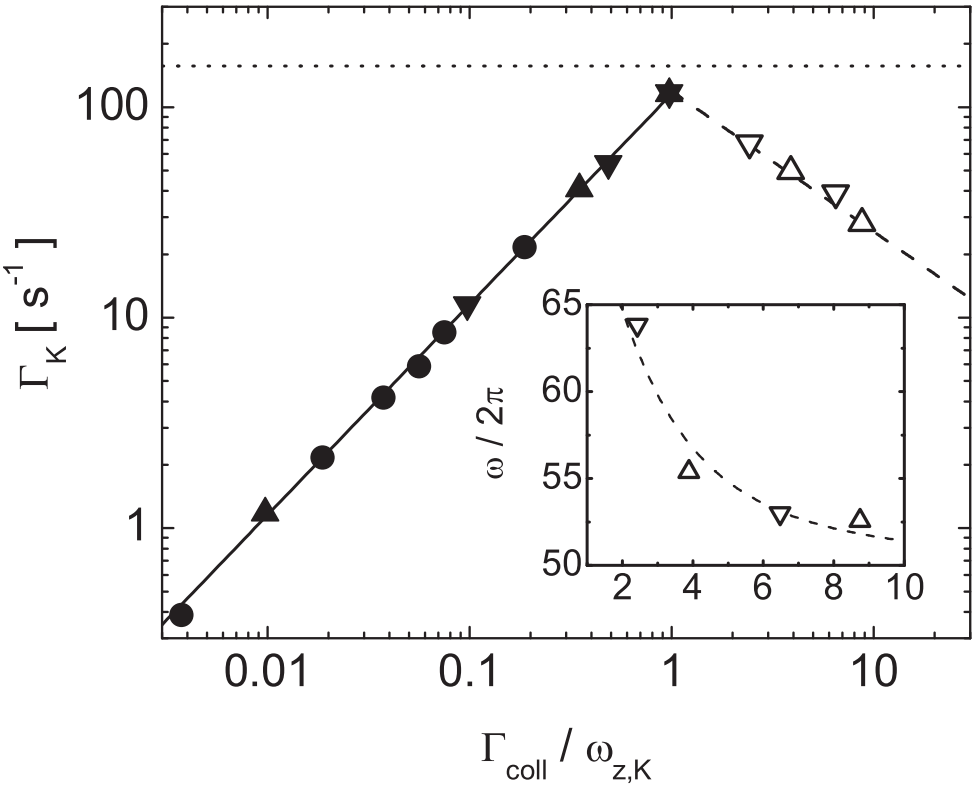

Figure A.3: Nonlinear relaxation rate for CDR due to hydrodynamic effects. Points are from the MC simulations with dots (•) varying the number of atoms, up-triangles (▲) varying the cross-section (with $|a_{bf}/a_{bb}| = 3$ fixed), and down-triangles (▼) varying the temperature. All points used $N_{\rm Rb} = 4\,N_{\rm K}$. The solid line is the collisionless prediction assuming $\beta = 2.0$ for $x \leq 1$, and the dashed line shows a $x^{-2/3}$ decay for $x > 1$, to guide the eye. The dotted line shows the ^{87}Rb axial trap frequency (in rad/s), which is the lowest trap frequency in the system. Relaxation curves corresponding to the open points (Δ, ∇) showed hydrodynamic behavior (see Fig. A.4). Damping rates for these simulations were determined from fits to $E_z(t)$ using damped sines, and neglecting early times. The inset shows the frequency of the hydrodynamic oscillations. For comparison, the dashed curve interpolates between twice the ^{87}Rb and ^{40}K axial frequencies (2×25 Hz and 2×37 Hz, respectively).

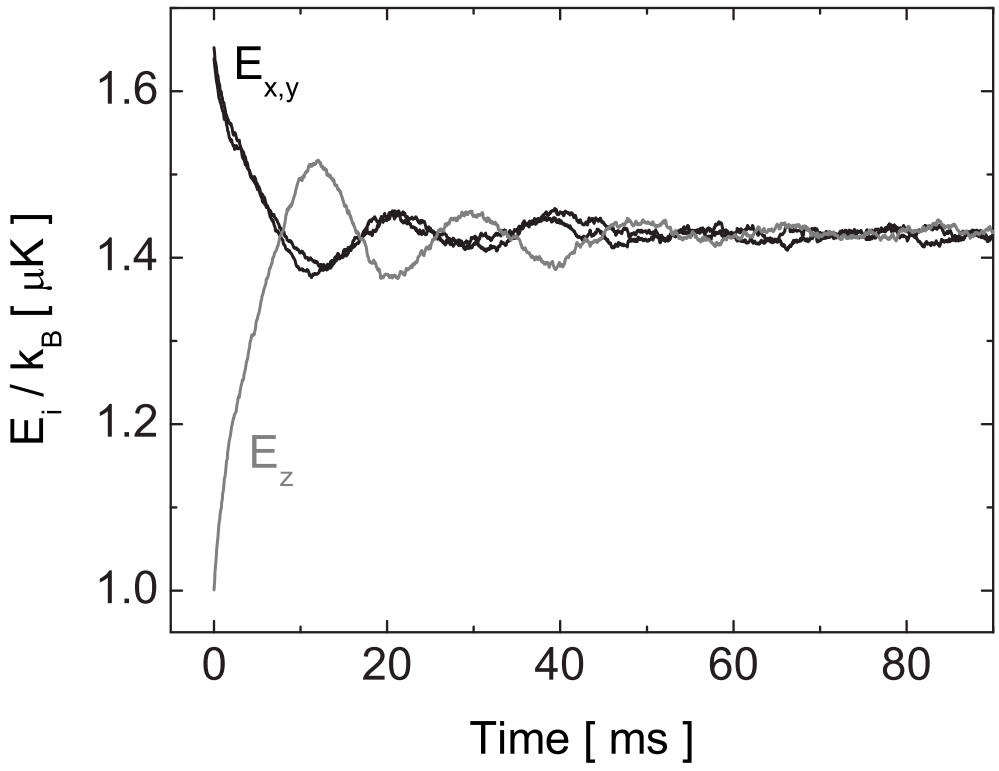

Figure A.4: Signature of hydrodynamic effects on relaxation. Shown is the mean energy per fermion in each direction as a function of time. These curves were taken with $\langle \Gamma_{\rm coll} \rangle = 3.9\,\omega_z$ for ^{40}K.

Appendix B

Cross-dimensional Rethermalization Supplement

Wherein the author leaves a record of various details and equations whose complexity renders them a distraction elsewhere.

B.1 Thermal Averages with Different Anisotropies for Each Species

Although our theory described in Ref. [66] assumes separable Gaussian distributions for each species in each direction, the center-of-mass (CM) and relative velocities are generally correlated if the energy anisotropy is not the same between species. To see this, note that

$$\frac{1}{2}\left(\frac{m_1\,v_{1i}^2}{E_{1i}}+\frac{m_1\,v_{2i}^2}{E_{2i}}\right)=\frac{1}{2}\left(\frac{M\,V_{\mathrm{CM}i}^2}{\epsilon_{\mathrm{CM}i}}+\frac{\mu\,v_{\mathrm{rel}i}^2}{\epsilon_{\mathrm{rel}i}}\right)-\mu\,\delta_i\,V_{\mathrm{CM}i}\,v_{\mathrm{rel}i}\quad , \tag{B.1}$$

where $E_{\sigma i}$ is the mean energy for species σ in the i^{th} direction, and we have defined

$$\begin{aligned}\epsilon_{\mathrm{CM}i} &= (m_1+m_2)\,\frac{E_{1i}\,E_{2i}}{m_2\,E_{1i}+m_1\,E_{2i}}\\ \epsilon_{\mathrm{rel}i} &= \frac{m_2\,E_{1i}+m_1\,E_{2i}}{m_1+m_2}\\ \delta_i &= \frac{E_{1i}-E_{2i}}{E_{1i}\,E_{2i}}\quad .\end{aligned} \tag{B.2}$$

Although the energy anisotropy is the same for each species at the beginning and end of the experiment (Ω and 1, respectively), the fact that α and β are generally different means that the two species will have different anisotropies at intermediate times.

With the definitions above, and using the distribution function $\exp(-H/k_BT)$, one can calculate the following averages:

$$\begin{aligned}
\langle\, v_{\rm rel}\,\rangle &= \sqrt{\frac{2\,E_{{\rm rel}z}}{\pi\,\mu}}\,\left[1+\Omega_{\rm rel}\,Q(\Omega_{\rm rel})\,\right] \\
\langle\, v_{{\rm rel}i}^2\,\rangle &= \frac{E_{1i}}{m_1}+\frac{E_{2i}}{m_2} \\
\langle\, V_{{\rm CM}i}\,v_{{\rm rel}i}\,\rangle &= \frac{(E_{1i}-E_{2i})\,E_{{\rm rel}i}}{m_2\,E_{1i}+m_1\,E_{2i}} \\
\langle\, v_{\rm rel}\,v_{{\rm rel}x}^2\,\rangle &= \frac{1}{\sqrt{2\pi}}\left(\frac{E_{{\rm rel}z}}{\mu}\right)^{3/2}\frac{\Omega_{\rm rel}}{\Omega_{\rm rel}-1}\,\left[\,3\,\Omega_{\rm rel}-2+(3\,\Omega_{\rm rel}-4)\,\Omega_{\rm rel}\,Q(\Omega_{\rm rel})\,\right] \\
\langle\, v_{\rm rel}\,v_{{\rm rel}z}^2\,\rangle &= \sqrt{\frac{2}{\pi}}\left(\frac{E_{{\rm rel}z}}{\mu}\right)^{3/2}\frac{1}{\Omega_{\rm rel}-1}\,\left[\,\Omega_{\rm rel}-2+\Omega_{\rm rel}^2\,Q(\Omega_{\rm rel})\,\right] \\
\langle\, v_{\rm rel}\,V_{{\rm CM}i}\,v_{{\rm rel}i}\,\rangle &= \left(\frac{m_1\,m_2}{m_1+m_2}\right)\frac{E_{1i}-E_{2i}}{m_2\,E_{1i}+m_1\,E_{2i}}\,\langle\, v_{\rm rel}\,v_{{\rm rel}i}^2\,\rangle \quad , \qquad \text{(B.3)}
\end{aligned}$$

where we have introduced the definitions

$$\begin{aligned}
E_{{\rm rel}i} &= \frac{m_2\,E_{1i}+m_1\,E_{2i}}{m_1+m_2} \\
\Omega_{\rm rel} &= \frac{E_{{\rm rel}x}}{E_{{\rm rel}z}} \\
Q(x) &= \begin{cases} \dfrac{\tanh^{-1}\sqrt{1-x}}{\sqrt{1-x}} & , \quad x<1 \\ 1 & , \quad x=1 \\ \dfrac{\tan^{-1}\sqrt{1-x}}{\sqrt{1-x}} & , \quad x>1 \end{cases} \quad . \qquad \text{(B.4)}
\end{aligned}$$

We are now in a position to consider ratios of the type

$$\frac{\langle\, v_{\rm rel}\,v_{{\rm rel}x}^2\,\rangle}{\langle\, v_{\rm rel}\,\rangle\,\langle\, v_{{\rm rel}x}^2\,\rangle} \quad , \qquad \text{(B.5)}$$

which we claimed in Ref. [66] are roughly equal to 4/3 for reasonable anisotropies. As an example of a "reasonable" anisotropy, we take $\Omega = 1.64$, which we used in the CDR measurements and many of the MC simulations. Figure B.1 shows the ratio in Eq.(B.5) as a function of m_1/m_2 for varying anisotropies Ω_1 and Ω_2. In the "worst-case" scenario, where one species maintains $\Omega = 1.64$ and the

other is isotropic, this ratio lies between 1.333 and 1.375 for any choice of masses, corresponding to only a 3% variation. In fact one can show more generally that this ratio is always between 1 and 3/2.

Although it is not immediately evident from Eq.(B.3), one can additionally show that the averages of interest to our theoretical treatment (see Eq.(6) and following in Ref. [66]) are related by

$$\begin{aligned} \frac{\langle\, v_{\rm rel}\, v_{{\rm rel}i}^2 \,\rangle}{\langle\, v_{\rm rel} \,\rangle \langle\, v_{{\rm rel}i}^2 \,\rangle} &= \frac{\langle\, v_{\rm rel}\, V_{{\rm CM}i}\, v_{{\rm rel}i} \,\rangle}{\langle\, v_{\rm rel} \,\rangle \langle\, V_{{\rm CM}i}\, v_{{\rm rel}i} \,\rangle} \\ \frac{\langle\, v_{\rm rel}\, v_{{\rm rel}x}^2 \,\rangle}{\langle\, v_{\rm rel} \,\rangle \langle\, v_{{\rm rel}x}^2 \,\rangle} - \frac{4}{3} &= \frac{4}{3} - \frac{\langle\, v_{\rm rel}\, v_{{\rm rel}z}^2 \,\rangle}{\langle\, v_{\rm rel} \,\rangle \langle\, v_{{\rm rel}z}^2 \,\rangle} \quad . \end{aligned} \tag{B.6}$$

B.2 Analytic Best Fit to Exponential Decay

In Ref. [66] we determined an upper limit β_u for the constant of proportionality β. We saw that the fermion relaxation, described by Eq.(8) in that work, does not generally correspond to pure exponential decay. In Fig. B.2 we compare solutions for the relaxation for light and heavy fermions, neglecting the effects of boson-boson collisions (*i.e.*, assuming $\gamma = 0$ in the language of Ref. [66]). The light fermions begin to relax quickly, and then are held up by the residual anisotropy of the bosons. In contrast the heavy fermions relax slowly at first, and then somewhat more quickly as the energy of the bosons becomes more isotropic. In other words, for heavy fermions the small-τ behavior gives an estimate for β_u that reliably bounds β from above, but for light fermions something more robust is needed.

To determine the best approximation to pure exponential decay, we analytically minimize the integrated squared error

$$\mathrm{err}^2 = \int_0^\infty d\tau \left[\chi_1(\tau) - \exp\left(-\frac{\tau}{\beta_u}\right) \right]^2 \tag{B.7}$$

with respect to the parameter β. Minimization of the error requires $\partial / \partial \beta_u = 0$,

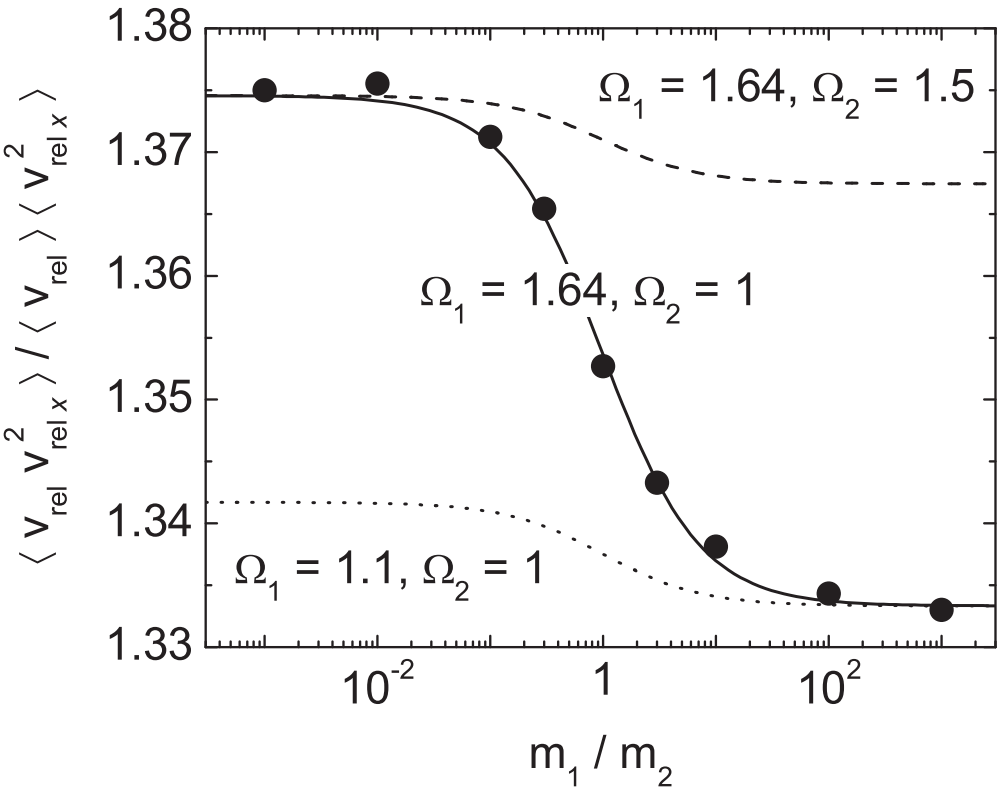

Figure B.1: Effect of energy anisotropies on thermal averages. Shown is the ratio given in Eq.(B.5) as a function of mass ratio m_1/m_2 for different anisotropies. Points are from Monte Carlo integrations, and the solid line is from Eq.(B.3), for the case of $\Omega_1 = 1.64$ and $\Omega_2 = 1$. The dashed and dotted lines are for different anisotropies, as labeled.

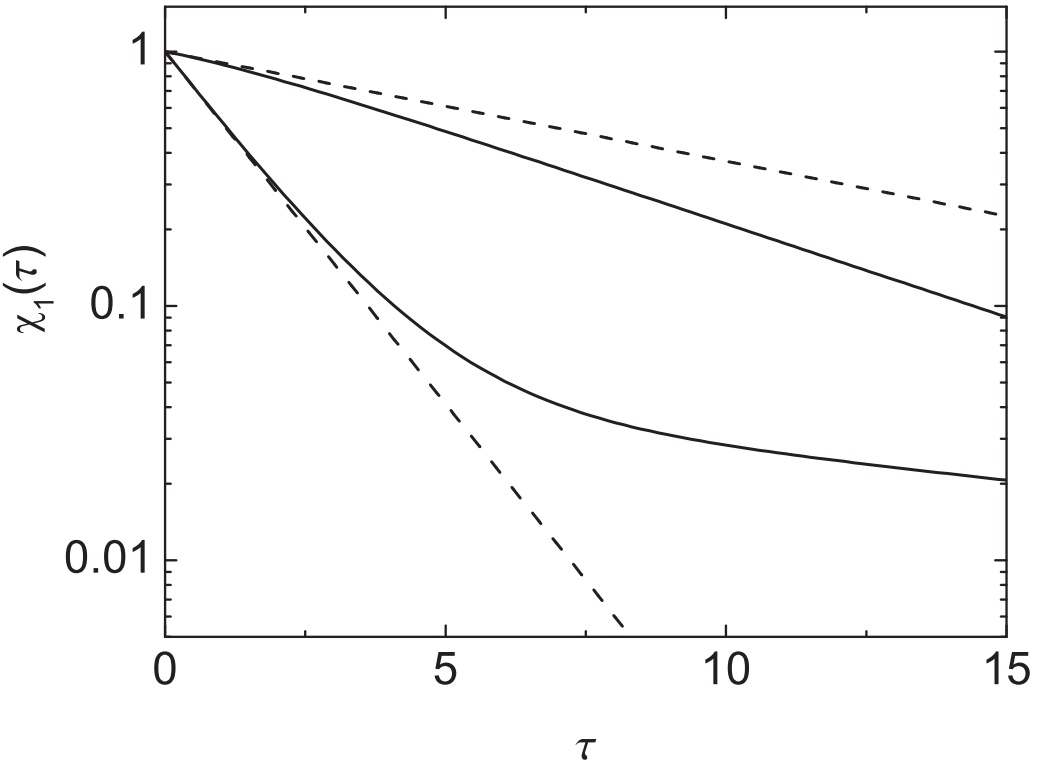

Figure B.2: Fermion relaxation with double exponential decay. Shown is the energy anisotropy of the fermions as a function of time (in units of the mean time τ between collisions). The upper (lower) solid curve is the solution to Enskog's equation from Ref. [66], with masses corresponding to a ^{40}K-^{7}Li (^{6}Li-^{133}Cs) mixture, and with $\gamma = 0$. In each case the dashed line is the exponential decay extrapolated from the small-τ behavior.

so that we need to solve

$$0 = \int_0^\infty d\tau \left[\chi_1(\tau) - e^{-\tau/\beta_u} \right] \tau \, e^{-\tau/\beta_u} \quad . \tag{B.8}$$

Now if we take $\gamma = 0$ in Eq.(8) of Ref. [66], then

$$\chi_1(\tau) = \frac{(1-\eta)(1-2\,\eta)\, e^{-\frac{2}{3}\tau} + \eta\, e^{-\frac{4}{3}\eta\,(1-\eta)\,\tau}}{1-2\,\eta\,(1-\eta)} \quad . \tag{B.9}$$

Carrying out the integral leads to the condition

$$\frac{(1-\eta)(1-2\,\eta)}{(3+2\,\beta_u)^2} + \frac{\eta}{[\,3+4\,\eta\,\beta_u\,(1-\eta)\,]^2} \;=\; \frac{1}{36}\,[\,1-2\,\eta\,(1-\eta)\,] \tag{B.10}$$

The above polynomial equation is solved numerically with a root finder [134], beginning with an initial guess value of β_l in order to obtain the physical solution.

Bibliography

[1] J. J. Sakurai, *Modern Quantum Mechanics* (Addison-Wesley, New York, 1994).

[2] M. P. Marder, *Condensed Matter Physics* (John Wiley & Sons, New York, 2000).

[3] B. DeMarco and D. S. Jin, *Onset of Fermi Degeneracy in a Trapped Atomic Gas*, Science **285**, 1703 (1999).

[4] M. Köhl, H. Moritz, T. Stöferle, K. Günter, and T. Esslinger, *Fermionic Atoms in a Three Dimensional Optical Lattice: Observing Fermi Surfaces, Dynamics, and Interactions*, Phys. Rev. Lett. **94**, 080403 (2005).

[5] M. J. Bijlsma, B. A. Heringa and H. T. C. Stoof, *Phonon exchange in dilute Fermi-Bose mixtures: Tailoring the Fermi-Fermi interaction*, Phys. Rev. A **61**, 053601 (2000).

[6] D. V. Efremov and L. Viverit, *p-wave Cooper pairing of fermions in mixtures of dilute Fermi and Bose gases*, Phys. Rev. B **65**, 134519 (2002).

[7] F. Matera, *Fermion pairing in Bose-Fermi mixtures*, Phys. Rev. A **68**, 043624 (2003).

[8] M. A. Baranov, M. S. Mar'enko, Val. S. Rychkov, and G. V. Shlyapnikov, *Superfluid pairing in a polarized dipolar Fermi gas*, Phys. Rev. A. **66** 013606 (2002).

[9] H. P. Büchler and G. Blatter, *Supersolid versus Phase Separation in Atomic Bose-Fermi Mixtures*, Phys. Rev. Lett. **91**, 130404 (2003).

[10] M. Lewenstein, L. Santos, M. A. Baranov, and H. Fehrmann, *Atomic Bose-Fermi Mixtures in an Optical Lattice*, Phys. Rev. Lett. **92** 050401 (2004).

[11] Throughout this thesis trade names are used for identification purposes only, and do not constitute an endorsement by the author or his institution.

[12] B. DeMarco, H. Rohner, and D. S. Jin, *An enriched ^{40}K source for fermionic atom studies*, Rev. Sci. Inst. **70**, 1967 (1999).

[13] B. DeMarco, *Quantum Behavior of an Atomic Fermi Gas*, Ph.D. thesis, University of Colorado – Boulder (2001).

[14] J. Moore, C. C. Davis, and M. A. Coplan, *Building Scientific Apparatus: a Practical Guide to Design and Construction* (Perseus, Cambridge, MA, 1991).

[15] David R. Lide (Ed.), *CRC Handbook of Chemistry and Physics* (CRC Press, Boca Raton, 1993).

[16] H. Lewandowski, *Coherences and correlations in an ultracold Bose gas*, Ph.D. thesis, University of Colorado – Boulder (2002).

[17] D. J. Griffiths, *Introduction to Electrodynamics* (Prentice Hall, Upper Saddle River, New Jersey, 1989).

[18] W. Petrich, M. H. Anderson, J. R. Ensher, and E. A. Cornell, *Stable, Tightly Confining Magnetic Trap for Evaporative Cooling of Neutral Atoms*, Phys. Rev. Lett. **74**, 3352 (1995).

[19] D. E. Pritchard, *Cooling Neutral Atoms in a Magnetic Trap for Precision Spectroscopy*, Phys. Rev. Lett. **51**, 1336 (1983).

[20] T. Bergeman, G. Erez and H. J. Metcalf, *Magnetostatic trapping fields for neutral atoms*, Phys. Rev. A **35**, 1535 (1987).

[21] Dan M. Stamper-Kurn, *Peeking and poking at a new quantum fluid: Studies of gaseous Bose-Einstein condensates in magnetic and optical traps*, Ph.D. Thesis, Massuchesetts Institute of Technology (2000).

[22] H. J. Metcalf and P. van der Straten, *Laser Cooling and Trapping* (Springer, New York, 1999).

[23] E. Arimondo, M. Inguscio, and P. Violino, *Experimental determinations of the hyperfine structure in the alkali atoms*, Rev. Mod. Phys. **49**, 31 (1977).

[24] R. Williamson, *Magneto-optical trapping of short-lived radioactive isotopes*, Ph.D. thesis, University of Wisconsin – Madison (1997).

[25] J. Goldwin, S. B. Papp, B. DeMarco, and D. S. Jin, *Two-species magneto-optical trap with ^{40}K and ^{87}Rb*, Phys. Rev. A **65** 021402 (2002).

[26] D. Steck, *Quantum Chaos, Transport, and Decoherence in Atom Optics*, Ph.D. thesis, University of Texas – Austin (2001).

[27] L. Ricci, M. Weidemüller, T. Esslinger, A. Hemmerich, C. Zimmermann, V. Vuletic, W. König, and T. W. Hänsch, *A Compact Grating-Stabilized Diode Laser System for Atomic Physics*, Opt. Commun. **117**, 541 (1995).

[28] C. Wieman and L. Hollberg, *Using diode lasers for atomic physics*, Rev. Sci. Inst. **62**, 1 (1991).

[29] K. B. MacAdam, A. Steinbach, and C. Wieman, *A narrow-band tunable diode laser system with grating feedback, and a saturated absorption spectrometer for Cs and Rb*, Am. J. Phys. **60**, 1098 (1992).

[30] M. G. Littman and H. J. Metcalf, *Spectrally narrow pulsed dye laser without beam expander*, Appl. Opt. **17**, 2224 (1978).

[31] G. Ferrari, M.-O. Mewes, F. Schreck, and C. Salomon, *High-power multiple-frequency narrow-linewidth laser source based on a semiconductor tapered amplifier*, Opt. Lett. **24**, 151 (1999).

[32] R. Grimm, M. Weidemüller, and Y. B. Ovchinnikov, *Optical dipole traps for neutral atoms*, Adv. Atom. Mol. Opt. Phys. **42**, 95 (2000); pre-print available at `arXiv:physics/9902072`.

[33] K. Miller, *Trapping and cooling Rubidium in far-off-resonant optical dipole traps*, Ph.D. thesis, University of Colorado – Boulder (2004).

[34] C. Monroe, W. Swann, H. Robinson, and C. Wieman, *Very cold trapped atoms in a vapor cell*, Phys. Rev. Lett. **65**, 1571 (1990).

[35] B. P. Anderson and M. A. Kasevich, *Loading a vapor-cell magneto-optic trap using light-induced atom desorption*, Phys. Rev. A **63**, 023404 (2001).

[36] A. Gallagher and D. E. Pritchard, *Exoergic collisions of cold Na^*-Na*, Phys. Rev. Lett. **63**, 957 (1989).

[37] J. Weiner, V. S. Bagnato, S. Zilio, and P. S. Julienne, *Experiments and theory in cold and ultracold collisions*, Rev. Mod. Phys. **71**, 1 (1999).

[38] L. G. Marcassa, G. D. Telles, S. R. Muniz, and V. S. Bagnato, *Collisional losses in a K-Rb cold mixture*, Phys. Rev. A **63**, 013413 (2000).

[39] T. Walker, D. Sesko, and C. Wieman, *Collective behavior of optically trapped neutral atoms*, Phys. Rev. Lett. **64**, 408 (1989).

[40] W. Petrich, M. H. Anderson, J. R. Ensher, and E. A. Cornell, *Behavior of atoms in a compressed magneto-optical trap*, J. Opt. Soc. Am. B **11**, 1332 (1994).

[41] W. Ketterle, K. B. Davis, M. A. Joffe, A. Martin, and D. E. Pritchard, *High densities of cold atoms in a dark spontaneous-force optical trap*, Phys. Rev. Lett. **70**, 2253 (1993).

[42] K. Dieckmann, *Bose-Einstein Condensation with High Atom Number in a Deep Magnetic Trap*, Ph.D. thesis, University of Amsterdam – Netherlands (2001).

[43] G. Delannoy, S. G. Murdoch, V. Boyer, V. Josse, P. Bouyer, and A. Aspect, *Understanding the production of dual Bose-Einstein condensation with sympathetic cooling*, Phys. Rev. A **63**, 051602 (2001).

[44] S. Inouye, J. Goldwin, M. L. Olsen, C. Ticknor, J. L. Bohn, and D. S. Jin, *Observation of Heteronuclear Feshbach Resonances in a Mixture of Bosons and Fermions*, Phys. Rev. Lett. **93**, 183201 (2004).

[45] E. G. M. van Kempen, S. J. J. M. F. Kokkelmans, D. J. Heinzen, and B. J. Verhaar, *Interisotope Determination of Ultracold Rubidium Interactions from Three High-Precision Experiments*, Phys. Rev. Lett. **88**, 093201 (2002).

[46] B. DeMarco, J. L. Bohn, J. P. Burke, Jr., M. Holland, and D. S. Jin, *Measurement of p-Wave Threshold Law Using Evaporatively Cooled Fermionic Atoms*, Phys. Rev. Lett. **82**, 4208 (1999).

[47] J. P. Burke, Jr., *Theoretical Investigation of Cold Alkali Atom Collisions*, Ph. D. thesis, University of Colorado – Boulder (1999).

[48] A. Derevianko, J. F. Babb, and A. Dalgarno, *High-precision calculations of van der Waals coefficients for heteronuclear alkali-metal dimers*, Phys. Rev. A **63**, 052704 (2001).

[49] F. Dafolvo, S. Giorgini, L. P. Pitaevskii, and S. Stringari, *Theory of Bose-Einstein condensation in trapped gases*, Rev. Mod. Phys. **71**, 463 (1999).

[50] D. A. Butts and D. S. Rokhsar, *Trapped Fermi gases*, Phys. Rev. A **55**, 4346 (1997).

[51] M. Naraschewski and D. M. Stamper-Kurn, *Analytical description of a trapped semi-ideal Bose gas at finite temperature*, Phys. Rev. A **58**, 2423 (1998).

[52] J. E. Williams, *The Preparation of Topological Modes in a Strongly-Coupled Two-Component Bose-Einstein Condensate*, Ph.D. thesis, University of Colorado – Boulder (1994).

[53] J. Goldwin, S. Inouye, M. L. Olsen, B. Newman, B. D. DePaola, and D. S. Jin, *Measurement of the interaction strength in a Bose-Fermi mixture with ^{87}Rb and ^{40}K*, Phys. Rev. A **70**, 021601 (2004).

[54] M. Modugno, F. Ferlaino, F. Riboli, G. Roati, G. Modugno, and M. Inguscio, *Mean-field analysis of the stability of a K-Rb Fermi-Bose mixture*, Phys. Rev. A **68**, 043626 (2003).

[55] C. Ospelkaus, *Quantum degenerate Fermi-Bose mixture with ^{40}K and ^{87}Rb*, seminar presented at JILA, 22 February, 2005.

[56] A. G. Truscott, K. E. Strecker, W. I. McAlexander, G. B. Partridge, and R. G. Hulet, *Observation of Fermi Pressure in a Gas of Trapped Atoms*, Science **291**, 2570 (2001).

[57] M. Brown-Hayes and R. Onofrio, *Optimal cooling strategies for magnetically trapped atomic Fermi-Bose mixtures*, Phys. Rev. A **70**, 063614 (2004).

[58] L. D. Carr and Y. Castin, *Limits of sympathetic cooling of fermions: The role of heat capacity of the coolant*, Phys. Rev. A **69**, 043611 (2004).

[59] L. D. Carr, T. Bourdel and Y. Castin, *Limits of sympathetic cooling of fermions by zero-temperature bosons due to particle losses*, Phys. Rev. A **69**, 033603 (2004).

[60] E. Timmermans, *Degenerate Fermion Gas Heating by Hole Creation*, Phys. Rev. Lett. **87**, 240403 (2001).

[61] E. Timmermans and R. Côté, *Superfluidity in Sympathetic Cooling with Atomic Bose-Einstein Condensates*, Phys. Rev. Lett. **80**, 3419 (1998).

[62] C. Monroe, E. A. Cornell, C. A. Sackett, C. J. Myatt, and C. E. Wieman, *Measurement of Cs-Cs elastic scattering at $T = 30\,\mu K$*, Phys. Rev. Lett. **70**, 414 (1993).

[63] M. Arndt, M. Ben Dahan, D. Guéry-Odelin, M. W. Reynolds, and J. Dalibard, *Observation of a Zero-Energy Resonance in Cs-Cs Collisions*, Phys. Rev. Lett. **79**, 625 (1997).

[64] I. Bloch, M. Greiner, O. Mandel, T. W. Hänsch, and T. Esslinger, *Sympathetic cooling of ^{85}Rb and ^{87}Rb*, Phys. Rev. A **64** 021402 (2001).

[65] A. Simoni, F. Ferlaino, G. Roati, G. Modugno, and M. Inguscio, *Magnetic Control of the Interaction in Ultracold K-Rb Mixtures*, Phys. Rev. Lett. **90**, 163202 (2003).

[66] J. Goldwin, S. Inouye, M. L. Olsen, and D. S. Jin, *Cross-dimensional relaxation in Bose-Fermi mixtures*, Phys. Rev. A **71**, 043408 (2005).

[67] J. L. Roberts, *Bose-Einstein Condensates with Tunable Atom-atom Interactions: The First Experiments with ^{85}Rb BECs*, Ph.D. thesis, University of Colorado — Boulder, 2001.

[68] S. D. Gensemer and D. S. Jin, *Transition from Collisionless to Hydrodynamic Behavior in an Ultracold Fermi Gas*, Phys. Rev. Lett. **87**, 173201 (2001).

[69] A. Marte, T. Volz, J. Schuster, S. Dürr, G. Rempe, E. G. M. van Kempen, and B. J. Verhaar, *Feshbach Resonances in Rubidium 87: Precision Measurement and Analysis*, Phys. Rev. Lett. **89**, 283202 (2002).

[70] H. Wu and C. J. Foot, *Direct simulation of evaporative cooling*, J. Phys. B **29**, L321 (1996).

[71] G. M. Kavoulakis, C. J. Pethick, and H. Smith, *Relaxation Processes in Clouds of Trapped Bosons above the Bose-Einstein Condensation Temperature*, Phys. Rev. Lett. **81**, 4036 (1998).

[72] G. M. Kavoulakis, C. J. Pethick, and H. Smith, *Collisional relaxation in diffuse clouds of trapped bosons*, Phys. Rev. A **61**, 053603 (2000).

[73] G. Modugno, G. Ferrari, G. Roati, R. J. Brecha, A. Simoni, and M. Inguscio, *Bose-Einstein Condensation of Potassium Atoms by Sympathetic Cooling*, Science **294**, 1320 (2001).

[74] G. Ferrari, M. Inguscio, W. Jastrzebski, G. Modugno, G. Roati, and A. Simoni, *Collisional Properties of Ultracold K-Rb Mixtures*, Phys. Rev. Lett. **89**, 053202 (2002).

[75] G. Roati, F. Riboli, G. Modugno, and M. Inguscio, *Fermi-Bose Quantum Degenerate ^{40}K-^{87}Rb Mixture with Attractive Interaction*, Phys. Rev. Lett. **89** 150403 (2002).

[76] F. Ferlaino, R. J. Brecha, P. Hannaford, F. Riboli, G. Roati, G. Modugno, and M. Inguscio, *Dipolar oscillations in a quantum degenerate Fermi-Bose atomic mixture*, J. Opt. B: Quantum Semiclass. Opt. **5**, S3 (2003).

[77] K. Mølmer, *Bose Condensates and Fermi Gases at Zero Temperature*, Phys. Rev. Lett. **80**, 1804 (1998).

[78] R. Roth and H. Feldmeier, *Mean-field instability of trapped dilute boson-fermion mixtures*, Phys. Rev. A **65**, 021603 (2002).

[79] R. Roth, *Structure and stability of trapped atomic boson-fermion mixtures*, Phys. Rev. A **66**, 013614 (2002).

[80] N. Nygaard and K. Mølmer, *Component separation in harmonically trapped boson-fermion mixtures*, Phys. Rev. A **59**, 2974 (1999).

[81] T. Miyakawa, T. Suzuki, and H. Yabu, *Induced instability for boson-fermion mixed condensates of alkali-metal atoms due to the attractive boson-fermion interaction*, Phys. Rev. A **64**, 033611 (2001).

[82] H. Pu, W. Zhang, M. Wilkens, and P. Meystre, *Phonon Spectrum and Dynamical Stability of a Dilute Quantum Degenerate Bose-Fermi Mixture*, Phys. Rev. Lett. **88**, 070408 (2002).

[83] C. P. Search, H. Pu, W. Zhang, and P. Meystre, *Quasiparticle spectrum and dynamical stability of an atomic Bose-Einstein condensate coupled to a degenerate Fermi gas*, Phys. Rev. A **65**, 063615 (2002).

[84] G. Modugno, G. Roati, F. Riboli, F. Ferlaino, R. J. Brecha, and M. Inguscio, *Collapse of a Degenerate Fermi Gas*, Science **297**, 2240 (2002).

[85] X.-J. Liu, M. Modugno, and H. Hu, *Finite-temperature effects on the collapse of trapped Bose-Fermi mixtures*, Phys. Rev. A **68**, 053605 (2003).

[86] S. T. Chui and V. N. Ryzhov, *Collapse transition in mixtures of bosons and fermions*, Phys. Rev. A **69**, 043607 (2004).

[87] S. T. Chui, V. N. Ryzhov, and E. E. Tareyeva, *Stability of the Bose System in Bose-Fermi Mixture with Attraction between Bosons and Fermions*, JETP Lett. **80**, 274 (2004).

[88] A. P. Albus, F. Illuminati, and M. Wilkens, *Ground-state properties of trapped Bose-Fermi mixtures: Role of exchange correlation*, Phys. Rev. A **67**, 063606 (2003).

[89] P. Capuzzi, A. Minguzzi, and P. Tosi, *Collective excitations in trapped boson-fermion mixtures: From demixing to collapse*, Phys. Rev. A **68**, 033605 (2003).

[90] M. E. Gehm, K. M. O'Hara, T. A. Savard, and J. E. Thomas, *Dynamics of noise-induced heating in atom traps*, Phys. Rev. A **58**, 3914 (1998).

[91] R. Jáuregui, *Nonperturbative and perturbative treatments of parametric heating in atom traps*, Phys. Rev. A **64**, 053408 (2001).

[92] D. Guéry-Odelin, F. Zamelli, J. Dalibard, and S. Stringari, *Collective oscillations of a classical gas confined in harmonic traps*, Phys. Rev. A **60**, 4851 (1999).

[93] D. S. Jin, M. R. Matthews, J. R. Ensher, C. E. Wieman, and E. A. Cornell, *Temperature-Dependent Damping and Frequency Shifts in Collective Excitations of a Dilute Bose-Einstein Condensate*, Phys. Rev. Lett. **78**, 764 (1997).

[94] S. Stringari, *Dynamics of Bose-Einstein condensed gases in highly deformed traps*, Phys. Rev. A **58**, 2385 (1998).

[95] Y.-l. Ma and S.-T. Chui, *Analytical expressions for the hydrodynamic excitation spectrum of Bose-Einstein condensates in axially anisotropic traps*, Phys. Rev. A **65**, 053610 (2002).

[96] E. Braaten and J. Pearson, *Semiclassical Corrections to the Oscillation Frequencies of a Trapped Bose-Einstein Condensate*, Phys. Rev. Lett. **82** 255, (1999).

[97] S. K. Yip, *Collective modes in a dilute Bose-Fermi mixture*, Phys. Rev. A, **64**, 023609 (2001).

[98] M. Holland, S. J. J. M. F. Kokkelmans, M. L. Chiofalo, and R. Walser, *Resonance Superfluidity in a Quantum Degenerate Fermi Gas*, Phys. Rev. Lett. **87**, 120406 (2001).

[99] S. Rousseau, A. R. Allouche, and M. Aubert-Frécon, *Theoretical Study of the Electronic Structure of the KRb Molecule*, J. Mol. Spect. **203**, 235 (2000).

[100] R. Landau, *Quantum Mechanics II: A Second Course in Quantum Theory* (John Wiley & Sons, New York, 1996).

[101] H. Friedrich, *Theoretical Atomic Physics* (Springer, Berlin, 1998).

[102] S. Inouye, M. R. Andrews, J. Stenger, H.-J. Miesner, D. M. Stamper-Kurn, and W. Ketterle, *Observation of Feshbach resonances in a Bose-Einstein condensate*, Nature (London) **392**, 151 (1998).

[103] Ph. Courteille, R. S. Freeland, D. J. Heinzen, F. A. van Abeelen and B. J. Verhaar, *Observation of a Feshbach Resonance in Cold Atom Scattering*, Phys. Rev. Lett. **81**, 69 (1998).

[104] J. L. Roberts, N. R. Claussen, J. P. Burke, Jr., C. H. Greene, E. A. Cornell, and C. E. Wieman, *Resonant Magnetic Field Control of Elastic Scattering in Cold ^{85}Rb*, Phys. Rev. Lett. **81**, 5109 (1998).

[105] C. Chin, V. Vuletić, A. J. Kerman, and S. Chu, *High Resolution Feshbach Spectroscopy of Cesium*, Phys. Rev. Lett. **85**, 2717 (2000).

[106] N. Claussen, S. J. J. M. F. Kokkelmans, S. T. Thompson, E. A. Donley, E. Hodby, and C. E. Wieman, *Very-high-precision bound-state spectroscopy near a ^{85}Rb Feshbach resonance*, Phys. Rev. A **67**, 060701 (2003).

[107] C. Chin, V. Vuletić, A. J. Kerman, S. Chu, E. Tiesinga, P. J. Leo, and C. J. Williams, *Precision Feshbach spectroscopy of ultracold Cs_2*, Phys. Rev. A **70**, 032701 (2004).

[108] S. L. Cornish, N. R. Claussen, J. L. Roberts, E. A. Cornell, and C. E. Wieman, *Stable ^{85}Rb Bose-Einstein Condensates with Widely Tunable Interactions*, Phys. Rev. Lett. **85**, 1795 (2000).

[109] E. A. Donley, N. Claussen, S. L. Cornish, J. L. Roberts, E. A. Cornell, and C. E. Wieman, *Dynamics of collapsing and exploding Bose-Einstein condensates*, Nature **412**, 295 (2001).

[110] K. E. Strecker, G. B. Partridge, A. G. Truscott, and R. G. Hulet, *Formation and propagation of matter-wave soliton trains*, Nature **417**, 150 (2002).

[111] L. Khaykovich, F. Schreck, G. Ferrari, T. Bourdel, J. Cubizolles, L. D. Carr, Y. Castin, and C. Salomon, *Formation of a Matter-Wave Bright Soliton*, Science **296**, 1290 (2002).

[112] E. A. Donley, N. R. Claussen, S. T. Thompson, and C. E. Wieman, *Atom-molecule coherence in a Bose-Einstein condensate*, Nature **417**, 529 (2002).

[113] C. A. Regal, C. Ticknor, J. L. Bohn, and D. S. Jin, *Creation of ultracold molecules from a Fermi gas of atoms*, Nature **424**, 47 (2003).

[114] C. Chin, A. J. Kerman, V. Vuletić, and S. Chu, *Sensitive Detection of Cold Cesium Molecules Formed on Feshbach Resonances*, Phys. Rev. Lett. **90**, 033201 (2003).

[115] K. E. Strecker, G. B. Partridge, and R. G. Hulet, *Conversion of an Atomic Fermi Gas to a Long-Lived Molecular Bose Gas*, Phys. Rev. Lett. **91**, 080406 (2003).

[116] K. Xu, T. Mukaiyama, J. R. Abo-Shaeer, J. K. Chin, D. E. Miller, and W. Ketterle, *Formation of Quantum-Degenerate Sodium Molecules*, Phys. Rev. Lett. **91**, 210402 (2003).

[117] J. Cubizolles, T. Bourdel, S. J. J. M. F. Kokkelmans, G. V. Shlyapnikov, and C. Salomon, *Production of Long-Lived Ultracold Li_2 Molecules from a Fermi Gas*, Phys. Rev. Lett. **91**, 240401 (2003).

[118] S. Jochim, M. Bartenstein, A. Altmeyer, G. Hendl, C. Chin, J. Hecker Denschlag, and R. Grimm, *Pure Gas of Optically Trapped Molecules Created from Fermionic Atoms*, Phys. Rev. Lett. **91**, 240402 (2003).

[119] S. Dürr, T. Volz, A. Marte, and G. Rempe, *Observation of Molecules Produced from a Bose-Einstein Condensate*, Phys. Rev. Lett. **92**, 020406 (2004).

[120] J. Herbig, T. Kraemer, M. Mark, T. Weber, C. Chin, H.-C. Nägerl, and R. Grimm, *Preparation of a Pure Molecular Quantum Gas*, Science **301**, 1510 (2003).

[121] J. R. Abo-Shaeer, D. E. Miller, J. K. Chin, K. Xu, T. Mukaiyama, and W. Ketterle, *Coherent Molecular Optics Using Ultracold Sodium Dimers*, Phys. Rev. Lett. **94**, 040405 (2005).

[122] M. Greiner, C. A. Regal, and D. S. Jin, *Emergence of a molecular Bose-Einstein condensate from a Fermi gas*, Nature **426**, 537 (2003).

[123] S. Jochim, M. Bartenstein, A. Altmeyer, G. Hendl, S. Riedl, C. Chin, J. Hecker Denschlag, and R. Grimm, *Bose-Einstein Condensation of Molecules*, Science **302**, 2101 (2003).

[124] M. W. Zwierlein, C. A. Stan, C. H. Schunck, S. M. F. Raupach, S. Gupta, Z. Hadzibabic, and W. Ketterle, *Observation of Bose-Einstein Condensation of Molecules*, Phys. Rev. Lett. **91**, 250401 (2003).

[125] C. A. Regal, M. Greiner, and D. S. Jin, *Observation of Resonance Condensation of Fermionic Atom Pairs*, Phys. Rev. Lett. **92**, 040403 (2004).

[126] M. W. Zwierlein, C. A. Stan, C. H. Schunck, S. M. F. Raupach, A. J. Kerman, and W. Ketterle, *Condensation of Pairs of Fermionic Atoms near a Feshbach Resonance*, Phys. Rev. Lett. **92**, 120403 (2004).

[127] T. Bourdel, L. Khaykovich, J. Cubizolles, J. Zhang, F. Chevy, M. Teichmann, L. Tarruell, S. J. J. M. F. Kokkelmans, and C. Salomon, *Experimental Study of the BEC-BCS Crossover Region in Lithium 6*, Phys. Rev. Lett. **93**, 050401 (2004).

[128] C. Chin, M. Bartenstein, A. Altmeyer, S. Riedl, S. Jochim, J. Hecker Denschlag, and R. Grimm, *Observation of the Pairing Gap in a Strongly Interacting Fermi Gas*, Science **305**, 1128 (2004).

[129] G. Breit and I. I. Rabi, *Measurement of Nuclear Spin*, Phys. Rev. **38**, 2082 (1931).

[130] P. J. Mohr and B. N. Taylor, *CODATA recommended values of the fundamental physical constants: 1998*, Rev. Mod. Phys. **72**, 351 (2000).

[131] T. Loftus, C. A. Regal, C. Ticknor, J. L. Bohn, and D. S. Jin, *Resonant control of elastic collisions in an optically trapped Fermi gas of atoms*, Phys. Rev. Lett. 88, 173201 (2002).

[132] C. Ticknor, C. A. Regal, D. S. Jin, and J. L. Bohn, *Multiplet structure of Feshbach resonances in nonzero partial waves*, Phys. Rev. A **69**, 042712 (2004).

[133] C. A. Stan, M. W. Zwierlein, C. H. Schunck, S. M. F. Raupach, and W. Ketterle, *Observation of Feshbach Resonances between Two Different Atomic Species*, Phys. Rev. Lett. **93**, 143001 (2004).

[134] W. H. Press, S. A. Teukolsky, W. T. Vetterling, and B. P. Flannery, *Numerical Recipes in C* (Cambridge, UK, 1999).

[135] D. Wang, J. Qi, M. F. Stone, O. Nikolayeva, H. Wang, B. Hattaway, S. D. Gensemer, P. L. Gould, E. E. Eyler, and W. C. Stwalley, *Photoassociative Production and Trapping of Ultracold KRb Molecules*, Phys. Rev. Lett. **93**, 243005 (2004).

[136] D. Wang, J. Qi, M. F. Stone, O. Nikolayeva, B. Hattaway, S. D. Gensemer, H. Wang, W. T. Zemke, P. L. Gould, E. E. Eyler and W. C. Stwalley, *The photoassociative spectroscopy, photoassociative molecule formation, and trapping of ultracold* $^{39}K^{85}Rb$, Eur. Phys. J. D **31**, 165 (2004).

[137] W. C. Stwalley, *Improved dissociation energy of the* $^{39}K^{85}Rb$ *molecule*, J. Chem. Phys. **122**, 084319 (2005).

[138] R. V. Hogg and A. T. Craig, *Introduction to Mathematical Statistics* (Prentice Hall, Englewood Cliffs, New Jersey 1995).